VELOCITY DEPENDENCE OF ROTATIONALLY INELASTIC CROSS-SECTIONS FOR $Li_2^*(A^1\Sigma)$ COLLIDING WITH RARE GAS ATOMS

by

Neil Smith

S.B. Massachusetts Institute of Technology
(1977)

Submitted to the Department of
Physics
in Partial Fulfillment of the
Requirements of the
Degree of

DOCTORATE IN PHILOSOPHY

at the

MASSACHUSETTS INSTITUTE OF TECHNOLOGY

January 1983

Signature of author _____
Department of Physics
November 3, 1982.

Certified by _____
Thesis Supervisor

Accepted by _____
Chairman, Departmental Graduate Committee

VELOCITY DEPENDENCE OF ROTATIONALLY INELASTIC CROSS-SECTIONS FOR $Li_2^*(A^1\Sigma)$ COLLIDING WITH RARE GAS ATOMS

by

NEIL SMITH

Submitted to the Department of Physics
on November 3, 1982 in partial fullfillment of the
requirements for the degree of Doctor of Philosophy in
Physics

ABSTRACT

Using laser-induced fluorescence, we have measured absolute rotationally inelastic (RI) collision cross-sections for $Li_2^*(A^1\Sigma)$ colliding with Ne, Ar, and Xe. Measurements for each rare gas were made for initial (and final) vibrational quantum number $v_i = 9$, and initial rotational level $j_i = 8$, 22, and 42. For each j_i, cross-sections were measured for 7 to 8 values of $\Delta \equiv j_f - j_i$, where j_f is the final rotational level and Δ is the collision-induced change in rotational angular momentum (in units of h). Values for Δ range from $\Delta = -20$ ($j_i=42$) to $\Delta = +24$ ($j_i=8$). In addition to the dependence on j_i and Δ, our primary interest in this work is the study of the relative velocity (v_r) dependence of these RI cross-sections $\sigma_{j_i,\Delta}(v_r)$, which was done using a Doppler based velocity selection method known as the "Velocity Selection by Doppler Shift" (VSDS) technique. Using VSDS we have been able to measure $\sigma_{j_i,\Delta}(v_r)$ over a 5-fold range in v_r (a 25-fold range in relative energy) with velocity resolution (for Ar and Xe) comparable to that obtainable using molecular beams techniques. Unlike several previous velocity dependent studies, we have found a rich and widely varying v_r dependence for the $\sigma_{j_i,\Delta}(v_r)$ which depends strongly on j_i and Δ, and in several cases on the rare gas collision partner as well. Theoretically, we have shown that the unique v_r dependence of $|\Delta| = 2$ cross-sections in Li_2^*-Xe can be well explained in terms of large impact parameter - long range interactions. Classical trajectory calculations have been carried out for Li_2^*-Xe using both rigid and vibrating-rotor models and an empirical potential which give very good overall agreement with the v_r dependence and magnitudes of our measured cross-sections. This successful "inversion" of our data substantial information on the Li_2^*-Xe interaction potentials which, like all excited alkali-rare gas potentials, was unknown prior to this work.

TABLE OF CONTENTS

TABLE OF CONTENTS

I. INTRODUCTION

In this work we have measured the relative velocity dependence of the rotationally inelastic (RI) collision cross-section $\sigma_{j_i,\Delta}(v_r)$ for the collision process:

$$^7Li_2^*(v=9, j_i) + X \xrightarrow{v_r} {}^7Li_2^*(v=9, j_f = j_i + \Delta) + X \quad (1.$$

Our notation is as follows: * denotes electronic excitation to the $A^1\Sigma_u^+$ electronic state, v is the initial and final vibrational quantum # (level), j_i and j_f are the initial and final rotational levels respectively, and $\Delta \equiv j_f - j_i$ (also commonly referred to as Δj is the change in rotational level of the Li_2^* molecule due to a collision with a rare gas target atom X, when $Li_2^*(v,j_i)$ and X had an initial relative velocity v_r with respect to one another. The $\sigma_{j_i,\Delta}(v_r)$ are total angle integrated, degeneracy averaged cross-sections, as our experiment is insensitive to scattering angle, and cannot distinguish between individual m_j levels.

In physical terms, the RI collision of eq. 1 can be simply described as follows. A Li_2^* molecule and target atom X approach each other initially with relative velocity (speed) v_r, and in the course of a subsequent collision (or interaction), there is an exchange of orbital ↔ rotational angular momentum (and thus translational ↔ rotational energy), the net magnitude and direction of this exchange determines the magnitude and sign of Δ. This RI process, which is by definition elastic

in the vibrational channel, is a specific case of a more general vibrational-rotational inelastic (VRI) collision process in which both rotational and vibrational levels are changed as a result of the collision. However, since the probability (cross-section) for RI collisions (RIC) is generally large compared to that for VRI collisions (VRIC) (and larger still than that for electronic quenching collisions) it is possible to a good approximation to study RIC independent of, or neglecting, vibrational inelasticity, while the converse is obviously not as true. Thus, a thorough understanding of RIC is basic to a more complete detailed study of VRIC or atom-molecule collision processes in general.

In the past, and at present, there is considerable interest in the study of RI collisions, both experimentally[1-5] and theoretically.[6,7] The experimental work has covered a wide range of experimental techniques (such as molecular beams, time of flight measurements, cell experiments, use of IR and optical laser induced fluorescence detection), but most of it has not focused specific attention on measurement of the relative velocity or energy dependence of RI cross-sections and/or rate constants, and in many cases only velocity averaged quantities have been measured. Previous experiments most relavent to this work are velocity dependence studies in Na_2^*-Xe[1] and HF-Ne,Ar,Kr[5], and measurements of velocity averaged rate constants for $Li_2^*(A^1\Sigma)$-He,Ar,Xe.[4]

Much of the theoretical work in RIC has gone into developing sim-

plifying approximations[6,7] to the exact close-coupling equations, such as the Coupled States, j_z conserving, l_z conserving, and Infinite Order Sudden approximations,[7] as well as various semi-classical[7] approximation methods, and finally classical trajectory methods.[7] However, virtually all of the exact or approximate quantum calculations schemes have been applied to ground state,light mass, low j_i collision systems[6] (where they are most valid and where ab-initio potential surfaces might be available) which are quite disimilar to our Li_2^*-X system studied here. With few exceptions,[8] previous calculations by any method, like the previous eperimental work, have not addressed themselves to the question of the velocity dependence of $\sigma_{j_i,\Delta}(v_r)$.

Another approach used to describe RIC is that of theoretical-empirical scaling laws, which predict all RI cross-sections $\sigma_{j_i,\Delta}(v_r)$ given given only a smaller subset $\sigma_{j,-j}$, or in some cases only a few parameters. Two examples of such scaling laws which have proven useful in the past are the empirical Statistical Power Gap (SPG) law,[9] and the Energy Corrected Sudden (ECS) scaling theory,[10] which when combined with SPG to form a scaling law ECS-P[9] can predict, as SPG itself can, all $\sigma_{j_i,\Delta}$ given only 3 or 4 parameters. Though these "laws" do not have firm theoretical foundations, their great simplicity, proven applicability,[3] and analytical form which can exhibit explicit dependence of $\sigma_{j_i,\Delta}(v_r)$ on j_i, Δ, and to some extent v_r (for ECS-P) allow for a greater qualitative, physical understanding of RIC, something which the

more exact formal theoretical methods (being numerical calculation schemes) cannot do.

Referring back to the subject of this work (eq. 1), we have measured $\sigma_{j_i,\Delta}(v_r)$ in Li_2^*-X for X = Ne, Ar, and Xe for j_i = 8, 22, and 42, and for 7 to 8 values of Δ for each j_i, covering a range of Δ = -20 (j_i = 42) to Δ = +24 (j_i = 8). Using the "Velocity Selection by Doppler Shift" (VSDS) technique (discussed in detail in chap.II) we have obtained measurements of $\sigma_{j_i,\Delta}(v_r)$ over a 5:1 range of relative velocity v_r (for $.75 \leq v_r/s_p \leq 4$, with $s_p \equiv \sqrt{\frac{kT}{m_{Li_2}}} = 7.23 \times 10^4$ cm/sec for our experimental cell temperature of T = 880°K), with a velocity resolution as good as $.4s_p$ in the case of Li_2^*-Xe.

The present Li_2^*-Xe study represents a 2 fold increase in resolution, range of Δ, and overall quality and reliability of data and results over earlier VSDS measurements in Na_2^*-Xe,[1] due to a lower molecule-atom mass ratio, as well as greater signal collection and improved experimental and analysis techniques (which apply to the Li_2^*-Ne,Ar data as well). Furthermore, the present VSDS results for Xe and Ar have at least as good resolution and relative error as those obtained by Barnes et. al.[5] in HF-He,Ar,Kr using molecular beams, and in addition cover a 2.5:1 greater v_r range, a much greater range of j_i and Δ, and yield absolute (as opposed to relative) cross-sections. Unlike the previous Na_2^*-Xe and HF-X studies which showed that for most j_i,Δ the $\sigma_{j_i,\Delta}(v_r)$ were relatively insensitive to v_r, our Li_2^*-X results show a

marked dependence of $\sigma_{j_i,\Delta}(v_r)$ on the relative velocity v_r, which varies significantly depending on both j_i and Δ (especially true for Li_2^*-Xe.

Following a description of our apparatus and experimental proceedure and analysis, we will present in chap.III results of our measurements of $\sigma_{j_i,\Delta}(v_r)$, along with discussion of these results and qualitative explanations of the more interesting aspects of their v_r dependence. We will also present our data in context of the previously mentioned SPG and ECS-P scaling laws. In chap.IV, we will show how semiclassical 1^{st} order time dependent perturbation theory can satisfactorilly explain the unique v_r dependence of the $\sigma_{j_i,\pm 2}(v_r)$ for Li_2^*-Xe. We will further present and discuss classical trajectory calculations using an empirical potential which give fairly good quantitative agreement with the measured velocity dependence of the $\sigma_{j_i,\Delta}(v_r)$ for Li_2^*-Xe. Effects of vibrational inelasticity additionally be discussed via trajectory calculations.

We feel the work presented here represents the most accurate, comprehensive, and probably interesting measurements of the v_r (as well as j_i, and Δ) dependence of RI cross-sections to date.

II. VSDS

The "Velocity Selection by Doppler Shift" (VSDS) technique[1] is an experimental method which allows measurement of the velocity dependence of collision processes when one collision partner (referred to as the primary) is in a (laser) excited state prior to collision with the target partner. It has been made possible with the development of single-mode tunable dye lasers, and can be performed on systems under fixed temperature equilibrium cell conditions, thus avoiding the use of the more traditional and more experimentally difficult methods, such as molecular beams machines and mechanical velocity selectors.

The basic idea behind VSDS is rather simple; if one shines a single mode laser of frequency ν into the system in order to excite a transition (in the primary species) of resonant frequency ν_o, then only the primary particles with velocity

$$v_L = \frac{(\nu-\nu_o)}{\nu} c \simeq \frac{(\nu-\nu_o)}{\nu_o} c \qquad (1.$$

along the laser beam axis will be excited on resonance due to the 1st order Doppler shift (eq. 1); v_L is thus referred to as the laser-selected velocity. As $(\nu-\nu_o)/\nu$ is typically 10^{-5}, we replace ν by ν_o in eq. 1 with very negligible error, and thus the laser selected velocity v_L is proportional to the detuning $\delta\nu = (\nu-\nu_o)$. Thus, the experimenter can select one velocity component of the excited primary collision

partner velocity $\vec{v}_p$, say v_{pz}, (laser axis $\equiv \hat{z}$ axis) by simply controlling the detuning $\delta\nu$ of the tunable excitation laser with $v_{pz} = v_L = c\delta\nu/\nu_o$.

Of course, selecting v_{pz} does not determine the relative collision velocity $\vec{v}_r \equiv \vec{v}_p - \vec{v}_t$ ($\vec{v}_t \equiv$ target velocity), but it does allow control of the relative velocity probability distribution, which will depend on v_{pz} as a parameter. If as in our experiment, the collision partners are enlcosed in an oven, or cell at thermal equilibrium at some constant temperature T, then after excitation, v_{pz} is precisely determined at $v_{pz} = v_L$; the target velocity $\vec{v}_t$ and the other primary velocity components v_{px} and v_{py}, which are not selected, will all be independently distributed according to the equilibrium Maxwell-Boltzman (M-B) velocity distribution at temperature T. Under such conditions, one can mathematically derive (App. A) the resulting conditional probability distribution $P(v_r|v_{pz}=v_L)$ for finding a primary-target collision pair with relative velocity (speed) $v_r = |\vec{v}_r|$ given that $v_{pz} = v_L$. The result is

$$a.\quad P(v_r|v_L) = \frac{v_r}{2\sqrt{r+1}}\, e^{-\frac{\left(v_r^2-(r+1)v_L^2\right)}{2(r+1)}}\left[\operatorname{erf}\left(\frac{v_r+(r+1)v_L}{\sqrt{2r(r+1)}}\right)+\operatorname{erf}\left(\frac{v_r-(r+1)v_L}{\sqrt{2r(r+1)}}\right)\right] \qquad (2.)$$

$$b.\quad r \equiv m_p/m_t\,, \quad P(v_r|v_L) = P(v_r|v_{pz}=v_L)$$

In eq. 2 and as will be done throughout the remainder of the thesis (unless otherwise indicated), all velocities are dimensionless, and expressed in terms of the thermal unit $s_p \equiv \sqrt{\frac{kT}{m_p}}$. The probability

Fig. 1 Relative velocity probability distribution for the ideal VSDS experiment; v_L = laser selected velocity.

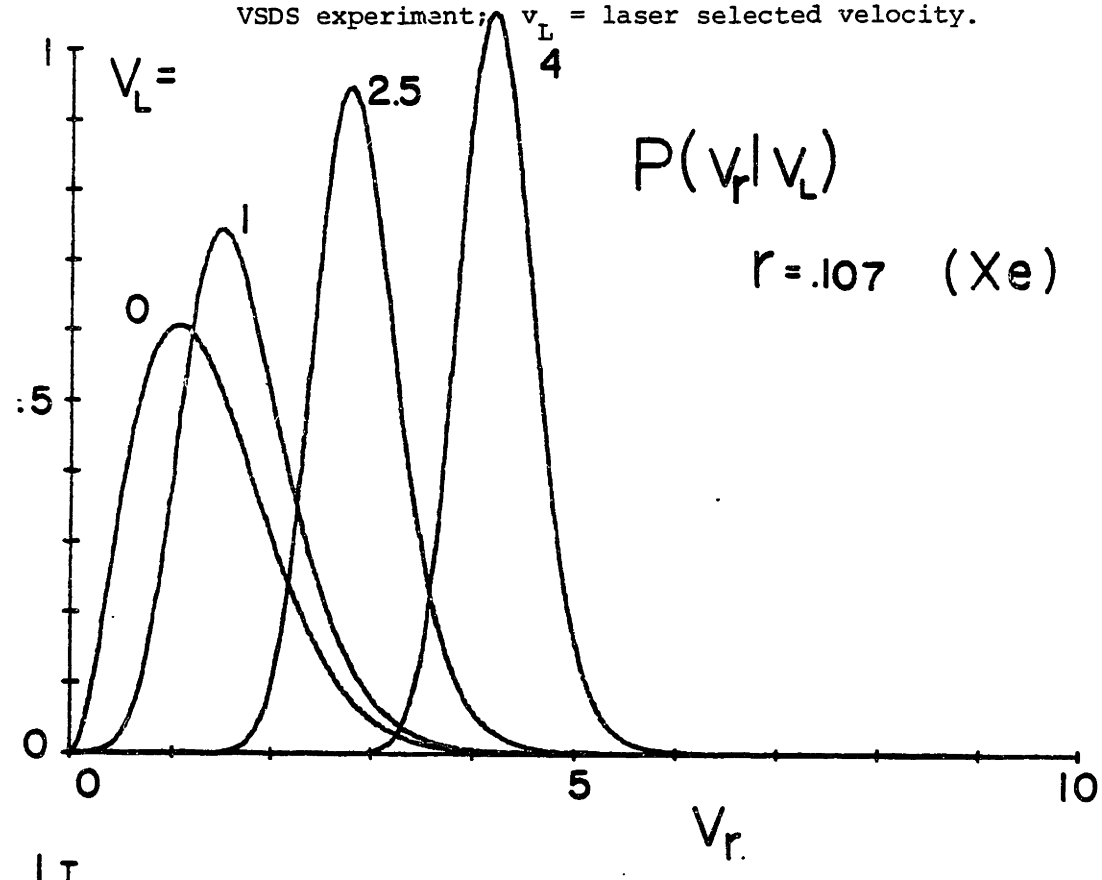

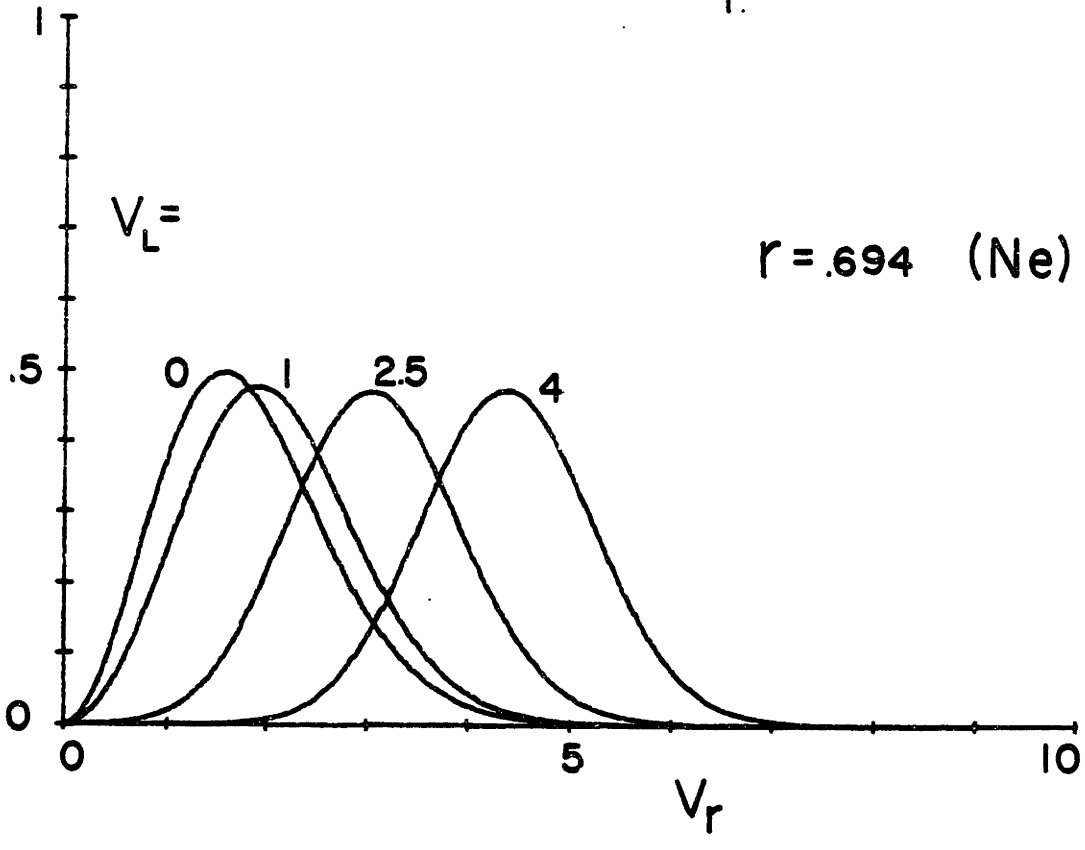

distribution $P(v_r|v_L)$ of eq. 2 is completely determined by the single paramter r, the ratio of primary mass to target mass. The width of $P(v_r|v_L)$ decreases monotonically with decreasing r (e.g. increasing m_t, fixed m_p), because $\vec{v}_t$ has a broader distribution then $\vec{v}_p$ (since $v_{pz} = v_L$ is exactly specified) and since $|\vec{v}_t|_{aver} \propto m_t^{-1/2}$ the $\vec{v}_t$ contribution to $\vec{v}_r$ decreases relative to $\vec{v}_p$, resulting in a narrower distribution in v_r, for any given v_L. In fig. 1 , are plots of $P(v_r|v_L)$ for several v_L and for r = .1067 and r = .694, corresponding to the mass ratios for Li_2^*-Xe and Li_2^*-Ne respectively. In app. B fig. 7 is a plot of $P(v_r|v_L)$ for r = .3502, which is almost identical to the Li_2^*-Ar mass ratio which = .3505.

In the above discussion of VSDS velocity selection, we have assumed that it is possible to laser select v_{pz} <u>precisely</u> equal to v_L; in other words, an infinitely narrow line width, or resonance. Mathematically, this would mean that $p(v_{pz};v_L) = \delta(v_z-v_L)$ where $p(v_{pz};v_L)$ is the probability of finding an excited primary with $\hat{z}$ velocity v_{pz}, <u>given</u> that the excitation laser is detuned to select velocity v_L (eq. 1). We refer to this case as the <u>ideal</u> VSDS experiment.

However, in reality, the resonance, or linewidth is not infinitely narrow, but has the well known Lorentzian lineshape[12]
$= \frac{\Gamma}{\pi}(\Gamma^2+(v_{pz}-v_L)^2)^{-1}$ in velocity categorized by a HWHM Γ. The resulting probability distribution $p(v_{pz};v_L)$ will then be the product of the Lorentzian linewidth x $\exp(-v_{pz}^2/2)$, which is just the M-B probability distribution in v_{pz} for ground state primary particles prior to excita-

Fig. 2 Primary velocity probability distribution along the z (laser) axis. Γ = Lorentzian HWHM in units of s_p.

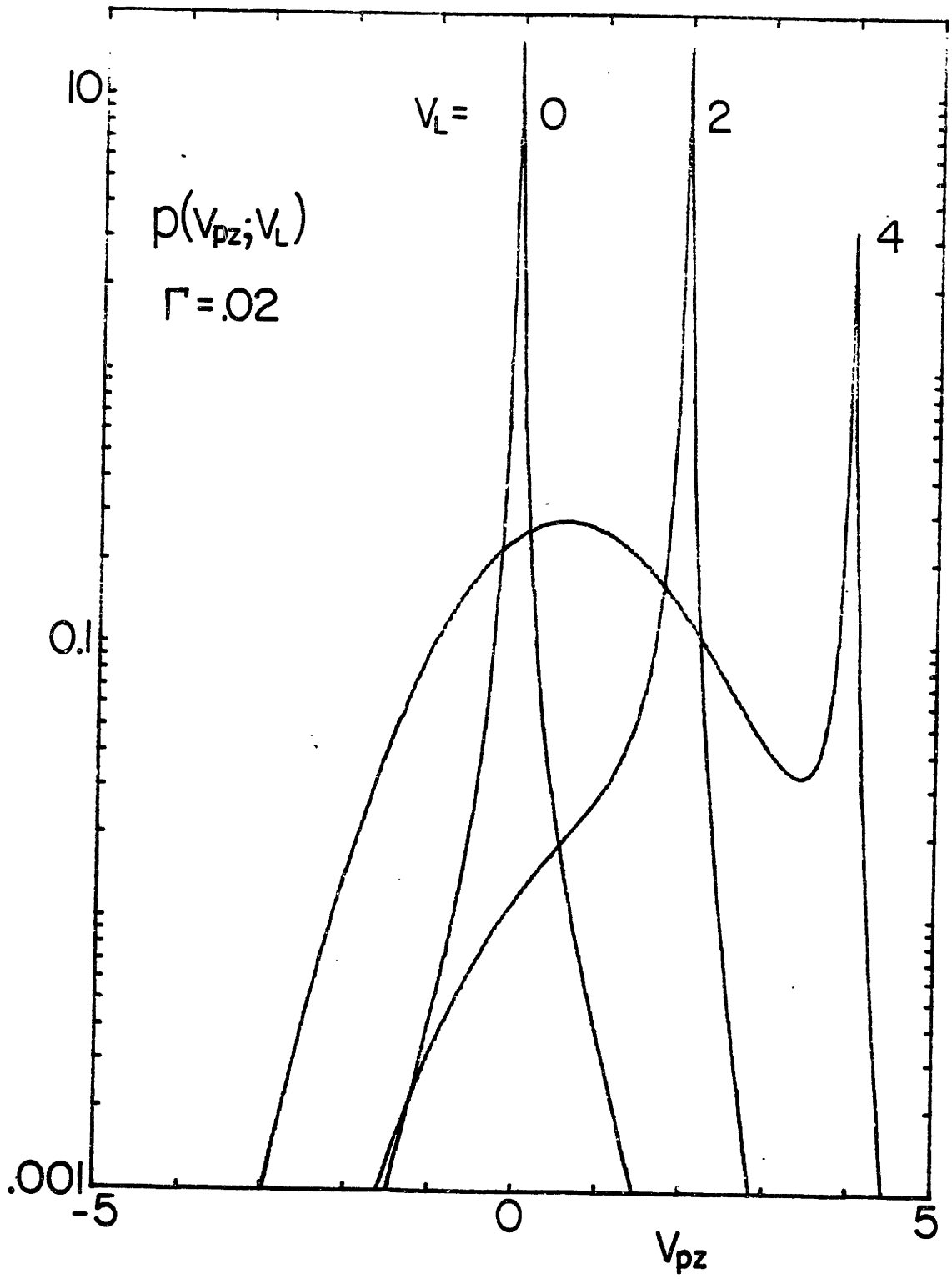

tion. We then have that

$$a.\quad p(v_{pz};v_L) = e^{-v_{pz}^2/2}\,\frac{\Gamma/\pi}{\Gamma^2+(v_L-v_{pz})^2}\,V^{-1}(v_L;\Gamma) \qquad (3.$$

$$b.\quad V(v_L;\Gamma) = \int_{-\infty}^{\infty} dv_{pz}\, e^{-v_{pz}^2/2}\,\frac{\Gamma/\pi}{\Gamma^2+(v_L-v_{pz})^2}$$

Since we have chosen to work in dimensionless velocity variables, Γ as expressed in Eq. 3 is actually the ratio of Lorentzian HWHM (in velocity) to the Doppler width $s_p = \sqrt{\frac{kT}{m_p}}$. The physical origins of the width Γ, such as natural linewidth, as well as pressure (collisional) broadening and laser power broadening, are not of primary importance here; our only real concern is that $p(v_{pz};v_L)$ can be described by eq. 3, categorized by a single constant Γ which we assume independent of v_{pz} or v_L. (That $p(v_{pz};v_L)$ is well represented by eq. 3 has been well verified experimentally by our data, as will be shown in chap. III). The function $V(v_L;\Gamma)$ is the well known Voigt profile function, and assures normalilzation of $p(v_{pz};v_L)$. In fig. 2 we show plots of $p(v_{pz};v_L)$ for several v_L, taking $\Gamma = .02$ (as discussed in chap. III, a typical value found experimentally). We shall further discuss the effects of having $p(v_{pz};v_L) \neq \delta(v_{pz}-v_L)$ below.

Having determined the <u>conditional</u> probability distribution $P(v_r|v_{pz})$ (eq. 2) and the v_{pz} probability distribution $p(v_{pz};v_L)$ (eq. 3), we can immediately express the <u>bi-variable</u> probability distribution $P'(v_r,v_{pz};v_L)$, which is the probability density for finding a laser excited primary-target collision pair which have relative velocity = v_r,

and simultaneously having the primary $\hat{z}$ velocity = v_{pz}, given that the excitation laser is detuned to laser select velocity v_L (eq. 1). The result is simply[13]

$$P'(v_r, v_{pz}; v_L) = P(v_r|v_L)\,p(v_{pz}; v_L) \qquad (4.$$

Finally, the non-ideal VSDS probability distribution for finding a laser-excited primary-target collision pair which have relative velocity v_r, which we'll call $P_o(v_r; v_L)$ is given by

$$P_o(v_r; v_L) = \int_{-\infty}^{\infty} P'(v_r, v_{pz}; v_L)\, dv_{pz} \qquad (5.$$

In principle, $P_o(v_r; v_L)$ is what is needed to be known in order to properly analyze a VSDS experiment; unfortunately, it cannot be expressed analytically. However, as will be discussed below, for the case $\Gamma \ll 1$, knowledge of $P(v_r|v_{pz})$ (eq. 3) will be sufficient in practice.

In a VSDS experiment, as with many other methods used to study collisional processes, what is directly accessible to experimental measurement is $\overline{k} \equiv \overline{v_r \sigma(v_r)}$, where the "——" represents an average over relative velocity, $\sigma(v_r)$ is the orientation averaged cross-section for the collisional process under study, and $\overline{k}$ is the velocity, orientation averaged rate constant. We specify orientation average since the VSDS experiment is not sensitive to the orientation of $\vec{v}_r$, but only $v_r = |\vec{v}_r|$ (in the case of RIC, the orientation averaging corresponds to an averag-

ing over m_j). Since VSDS allows for control of the v_r distribution by selection of v_L, we specify $\bar{k} = \bar{k}(v_L)$. The experimentally measured $\bar{k}(v_L)$ can be mathematically expressed with the help of eqs. 4 and 5. We have

$$a.\quad \bar{k}(v_L) = \int_0^\infty P_o(v_r; v_L) k(v_r)\, dv_r = \int_0^\infty v_r \sigma(v_r)\, dv_r \int_{-\infty}^\infty P'(v_r, v_{pz}; v_L)\, dv_{pz}$$

$$b.\quad \bar{k}(v_L) = \int_{-\infty}^\infty p(v_{pz}; v_L) \left[\int_0^\infty v_r \sigma(v_r) P(v_r | v_{pz})\, dv_r\right] dv_{pz} \qquad (6.$$

where we have switched the order of integration is going from 6.a to 6.b. Equation 6.b is a central result in VSDS theory, as it gives the explicity relationship between the experimentally measured $\bar{k}(v_L)$ and the cross-section $\sigma(v_r)$, which is what is desired to be determined.

We consider for further analysis the special, but important practical case $r \ll 1$. Equation 6.b is rewritten as follows:

$$a.\quad \bar{k}(v_L) = \int_{R_1} dv_{pz}\, p(v_{pz}; v_L) \bar{k}_i(v_{pz}) + \int_{R_2} dv_{pz}\, p(v_{pz}; v_L) \bar{k}_i(v_{pz})$$

$$\int_{R_1} dv_{pz} \equiv \int_{v_L-\delta}^{v_L+\delta} dv_{pz} \quad , \quad \int_{R_2} dv_{pz} \equiv \int_{-\infty}^{v_L-\delta} dv_{pz} + \int_{v_L+\delta}^{\infty} dv_{pz} \qquad (7.$$

$$b.\quad \bar{k}_i(v_{pz}) = \int_0^\infty dv_r\, v_r \sigma(v_r) P(v_r | v_{pz})$$

The quantity $\bar{k}_i(v_{pz})$ (eq. 7.b) is identically the ideal VSDS velocity averaged rate constant, that would be measured in an ideal VSDS experiment; this can be immediately verified by letting $p(v_{pz};v_L) \rightarrow \delta(v_{pz}-v_L)$ (the ideal VSDS limit) in eq.6.b. In eq.7.a, $\bar{k}(v_L)$ is written as the sum of two contributions. The first comes from region R_1 of v_{pz} space, corresponding physically to those primaries excited on or near resonance with v_{pz} in a region $\pm\delta$ about $v_{pz} = v_L$; these primaries are considered as velocity selected. The second contribution from region R_2 (everything outside R_1) is due to primaries excited off resonance by the asymptotic Lorentz tail (far wing) of the resonance lineshape, and are thus not velocity selected. The parameter δ is as yet unspecified; it is required $\delta \gtrsim 3\Gamma$ (so $\delta^2 >> \Gamma^2$) so that in region R_2 the Lorentzian part of $p(v_{pz};v_L)$ has assumed its asymptotic Lorentz tail form, $\propto (v_{pz}-v_L)^{-2}$. It is also understood that δ is small enough so region R_1 does not include any contributions from off-resonant non velocity-selected primaries (which by definition belong in R_2), especially when these contributions become important, i.e. at "large" v_L when off-resonant primaries with relatively small v_{pz} excited by the Lorentz tail, become comparable or greater in number to those excited on resonance at $v_{pz} \approx v_L$ (the Gaussian tail of the M-B distribution vanishes much faster than the Lorentzian tail). This happens at sufficiently large v_L when the narrow Lorentzian peak of $p(v_{pz};v_L)$, at $v_{pz} = v_L$ with FWHM = $2\Gamma \ll 1$, is well outside the much broader Gaussian peak of

$p(v_{pz};v_L)$ with maximum at $v_{pz} = 0$. In this limit, $p(v_{pz};v_L)$ approaches the following limiting form:

$$p(v_{pz};v_L) \simeq \left[e^{-v_L^2/2} \frac{\Gamma/\pi}{\Gamma^2+(v_L-v_{pz})^2} + \frac{\Gamma/\pi\, e^{-v_{pz}^2/2}}{v_L^2} \right] N^{-1}(v_L;\Gamma) \quad (8.$$

The first term of eq. 8 is the R_1 contribution to the probability density $p(v_{pz};v_L)$; it is sharply peaked at $v_{pz}=v_L$ and as expected, represents "fast" velocity selected primaries. The 2nd term is the R_2 contribution; it is relatively broad (width ~ 2) with maximum at $v_{pz} = 0$, and represents primaries which are "slow", thermally (M-B) distributed, and obviously <u>not</u> velocity selected. We can now define an <u>upper limit</u> to δ, by choosing the R_1-R_2 boundary at the minimum between the maximums of the R_1 and R_2 terms in eq. 8. In this region $p(v_{pz};v_L) \propto \exp(-v_{pz}^2/2) \times (v_L-v_{pz})^{-2}$ (since $\Gamma \ll 1$, and $\delta^2 \gg \Gamma^2$, by definition), so setting $\frac{d}{dv_{pz}} p(v_{pz};v_L) = 0$, we find the minimum at $v_{pz}^o = \frac{1}{2}(v_L + \sqrt{v_L^2-8})$ and so $\delta_{max} \equiv v_L - v_{pz}^o = \frac{1}{2}(v_L - \sqrt{v_L^2-8})$. The minimum doesn't exist for $v_L < \sqrt{8} \simeq 2.8$ (see fig. 2), which means that the limit of eq. 8 has not been truly reached for $v_L < \sqrt{8}$. Since δ_{max} depends on v_L, and decreases monotonically for $v_L > \sqrt{8}$, the choice $\delta_{max} = \delta_{max}(v_{Lmax})$ (where v_{Lmax} is the largest v_L for which meaningful velocity selection can be achieved) will guarantee δ is not chosen too large. As will be seen below, $v_{Lmax} \simeq 4$, and so $\delta_{max}(v_L=4) \simeq \underline{.6}$ is a reasonable upper bound for δ.

For $\Gamma \ll 1$, $p(v_{pz};v_L)$ in region R_1 becomes fairly negligable $|v_{pz}-v_L| \gtrsim 3\Gamma$, regardless of δ, $\bar{k}_i(v_{pz})$ may be removed from inside the R_1 integral in eq. 7.b and replaced with $\bar{k}_i(v_L)$, resulting in the following equation.

$$a.\ \bar{K}_i(v_L) = \bar{f}^{-1}(v_L,\delta)\left[\bar{K}(v_L) - \int_{R_2} dv_{pz}\, p(v_{pz};v_L)\,\bar{K}_i(v_{pz})\right] \qquad (9.$$

$$b.\ f(v_L,\delta) = \int_{R_1} dv_{pz}\, p(v_{pz};v_L) \simeq \bar{f}^{-1}(v_L,\Gamma)\left[\frac{e^{-v_L^2/2}}{\pi}\left(\tan^{-1}\left(\frac{\delta}{\Gamma}\right)\left(2-(v_L^2-1)\right)+\Gamma\delta(v_L^2-1)\right)\right]$$

The $\bar{k}_i(v_L)$ on the LHS of eq. 9.a is more exactly a velocity smoothed (over a region $\sim \pm 2\Gamma$ about v_L) version of the real $\bar{k}_i(v_L)$, but for $\Gamma \ll 1$, the distinction is generally of little consequence in practice. The function $f(v_L,\delta)$ is the integrated probability over region R_1, and is the fraction of primaries which are velocity selected with $v_{pz} \simeq v_L$; $1-f(v_i;\delta)$ is just the fraction of primaries which are non velocity selected. If $f(v_L,\delta) \simeq 1$, then $\int_{R_2} dv_{pz} p(v_{pz};v_L) \to 0$ and eq. 9.a shows that $\bar{k}_i(v_L) \simeq \bar{k}(v_L)$, which must obviously be the case, since $f(v_L,\delta) = 1$ means all primaries are velocity selected. The second term on the RHS of eq. 9.a can be considered as the <u>correction</u> to $\bar{k}(v_L)$ to yield the desired $\bar{k}_i(v_L)$; this "Lorentz tail" correction simply subtracts contributions to $\bar{k}(v_L)$ from non velocity selected primaries in region R_2. Eq. 9.a can be solved to good approximation by replacing

$\bar{k}_i(v_L)$ with the (presumably) known $\bar{k}(v_L)$, and if necessary, solved iteratively from that point (more on solving eq. 9.a. below). The correction cannot be neglected when f is significantly < 1; to examine the question more quantitatively, $f(v_L,\Delta)$ is tabulated in Table 1 as a function of v_L, for a wide range of Γ, and for $\delta = 4\Gamma$ and $\delta = .5$, which are appropriate lower and upper bounds for δ, as discussed earlier. (The approximation to $f(v_L,\delta)$ in eq. 9.b, used for Table 1, is obtained by 3rd order expansion about v_L of the $\exp(-v_{pz}^2/2)$ factor of $p(v_{pz};v_L)$; $V(v_L;\Gamma)$ is obtained as described in the appendix of Appendix B.)

It is seen that results for $f(v_L,\delta)$ for $\delta = 4\Gamma$ or $\delta = .5$ differ by $\leq$ 20%, even though δ may vary by as much as a factor of 100. This rather dramatic insensitivity of $f(v_L,\delta)$ to δ (for $\Gamma<<1$) provides strong justification that the concept of distinct regions R_1 and R_2 of velocity-selected and non-selected primaries is well founded; any choice of δ such that $4\Gamma \leq \delta \leq \delta_{max}$ will not, in principle have consequential bearings on results obtained. However, while it follows form eq. 9.a that $\lim_{\Gamma\to 0}\bar{k}(v_L) \to \bar{k}_i(v_L)$ for any δ, for $\delta = 4\Gamma$, $\lim_{\Gamma\to 0} f(v_L,\delta=4\Gamma) \to .84$ (see Table 1), which is logically (not mathematically) inconsistent with the meaning of the ideal VSDS limit $\Gamma\to 0$, and so the choice of a constant δ, independent of Γ which yields $\lim_{\Gamma\to 0} f(v_L,\delta) \to 1.0$ is probably a more physically reasonable definition of region R_1.

Further, as source of experimental error (especially random noise) in a measured $\bar{k}(v_L)$ will be amplified by $f^{-1}(v_L,\delta)$ in the $\bar{k}_i(v_L)$

Table II.1 - $f(v_L, \Gamma)$

v_L	$\Gamma = .1$		$\Gamma = .03$		$\Gamma = .02$		$\Gamma = .01$		$\Gamma = .003$		$\Gamma = .001$	
	$\delta = 4\Gamma$	$\delta = .5$	$\delta = 4\Gamma$	$\delta = .5$	$\delta = 4\Gamma$	$\delta = .5$	$\delta = 4\Gamma$	$\delta = .5$	$\delta = 4\Gamma$	$\delta = .5$	$\delta = 4\Gamma$	$\delta = .5$
0.0	.90	.93	.86	.98	.86	.99	.85	1.0	.85	1.0	.84	1.0
1.0	.86	.91	.85	.97	.85	.98	.85	.99	.84	1.0	.84	1.0
2.0	.76	.79	.81	.93	.81	.95	.83	.97	.84	.99	.84	.99
2.5	.62	.65	.75	.87	.78	.91	.81	.95	.83	.99	.84	.99
3.0	.40	.43	.61	.69	.67	.79	.75	.89	.82	.97	.83	.98
3.5	.18	.19	.37	.44	.46	.54	.59	.70	.75	.89	.81	.96
4.0	.05	.05	.13	.15	.17	.21	.29	.34	.53	.63	.71	.84
4.5	.01	.01	.02	.03	.03	.04	.07	.08	.18	.22	.38	.46
5.0	.001	.001	.003	.004	.004	.005	.008	.01	.03	.03	.08	.09

obtained by the Lorentz tail correction (eq. 9.a); choosing $\delta = \delta_{max}(v_{Lmax})$ (e.g. $\delta = .5$, for $v_{max} \simeq 4.5$) will increase $f(v_L,\delta)$ for any v_L (admittedly, as was already seen, not by much) and thus reduces this problem (potentially serious for v_L near v_{Lmax}) as much as possible. The cost of this, in principle is in resolution; for $\Gamma \ll 1$, this will not be of practical importance. Thus on these considerations, we recommend the choice $\delta \simeq \delta_{max}(v_{Lmax})$ (typically $\simeq .5$); inspection of fig. 2 (especially at large v_L when it is most important) shows the choice $\delta = .5$ very reasonable.

Referring back to Table 1, (and restricting attention to $\delta = .5$, as discussed above) the following conclusions can be drawn:

1. for $v_L \leq 2.5$, $f(v_L,.5) \gtrsim .9$, and so $\bar{k}(v_L) \simeq \bar{k}_i(v_L)$ (at least for $\Gamma < .1$).

2. $\underline{3.5} \leq v_{Lmax} < 5$, where v_{Lmax} is the largest v_L where it is practically possible to obtain $\bar{k}_i(v_L)$. Even if measurement of $\bar{k}(v_L)$ for $v_L \gtrsim 5$ where possible (and it almost certianly is not, as is seen in chap III) in this v_L range $f \to 0$ very rapidly, (even for $\Gamma \simeq .001$), making the Lorentz tail correction both absolutely imperative and yet enormously unstable, and impossible to apply. We have found, in the present Li_2^* work, and in past VSDS work in Na_2^*-Xe[1], $v_{Lmax} \simeq 4$ as a realistic value.

3. For $\Gamma \gtrsim .1$, the velocity selection is rather rapidly deteriorating, especially for $v_L \gtrsim 2.5$. In fact, for $\Gamma = .25$,

$\delta_{min} \geq 3\Gamma = .75$ is larger than $\delta_{max} \simeq .5$, and the method for Lorentz tail corrections described here breaks down, requiring a more exact (and thus more difficult) deconvolution of eq. 6.b to obtain $\bar{k}_i(v_L)$.

We now re-write eq. 9.a in the more practical form, useful for application to real VSDS data $\bar{k}(v_L)$, measured over a region $0 \leq v_L \leq v_{Lmax}$ (by definition $\bar{k}(-v_L) = \bar{k}(v_L)$).

$$a.\ \bar{K}_i^1(v_L) = f^{-1}(v_L,\delta)\left[\bar{K}(v_L) - \int_{-v_{Lmax}}^{v_L-\delta} P(v;v_L)\bar{K}(v)dv\right]$$

$$b.\ \bar{K}_i^n(v_L) = f^{-1}(v_L,\delta)\left[\bar{K}(v_L) - \int_{-v_{Lmax}}^{v_L-\delta} P(v;v_L)\bar{K}_i^{n-1}(v)dv\right] \qquad (10.$$

$$c.\ \bar{K}_i(-v_L) = \bar{K}_i(v_L)$$

$$d.\ \delta \simeq \tfrac{1}{2}\left(v_{Lmax} - \sqrt{v_{Lmax}^2 - 8}\right),\ \delta = .5 \text{ is generally recommended}$$

Firstly, we point out that when going from eq. 9.a. to eq. 10.a, contributions from that part of R_2 for $v_L+\delta \leq v \leq \infty$ have been neglected; this will generally <u>always</u> be an excellent approximation (even for $v_L = 0$, where it is <u>maximum</u>) since the integral of the probability over this region $= \frac{1}{2}(1-f_1(0,\delta)) < .01$ (see Table 1) and thus quite negligible. Similarly, neglect of R_2 contributions for $v < -v_{Lmax}$ (if $v_{Lmax} > 3$) also results in negligable error (see fig.). Lastly, $\bar{k}_i(v)$ has been replaced by $\bar{k}(v)$ in the integral term for $\bar{k}_i^1(v_L)$, the 1st iteration approximation to $\bar{k}_i(v_L)$; this is also generally a very good approximation since here $p(v;v_L) \propto e^{-v^2/2}(v_L-v)^{-2}$ becomes negligable for $|v| \gtrsim 2.5$

and $|v_L - v| \geq .5$, and as concluded earlier $\bar{k}(v) \approx \bar{k}_i(v)$ for $|v| \leq 2.5$. The scheme for calculating the n^{th} iteration approximation $\bar{k}_i^n(v_L)$ is given by eq. 10.b, but generally only 2 iterations will be necessary (see App. B - fig. 4 and discussion).

As a further point of interest, we consider the large v_L limit, as expressed by eq. 8 noting that as $v_L \to \infty$, $V(v_L;\Gamma) \to \sqrt{\frac{2}{\pi}}\,\Gamma/v_L^2$. Eq. 8 then shows $\lim_{v_L \to \infty} p(v_{pz};v_L) \to \frac{1}{\sqrt{2\pi}} \exp(-v_{pz}^2/2)$, which is just a (M-B) thermal velocity distribution; this implies that

$$\lim_{V_L \to \infty} \bar{k}(v_L) \longrightarrow \langle k \rangle_{MB} \qquad (11.$$

where $\langle\ \rangle_{M-B}$ represents an average over relative velocity for a true (M-B) thermal velocity distributions in <u>all</u> velocity components. This limit, in which $\bar{k}(v_L)$ becomes <u>independent</u> of v_L has been observed experimentally[ ] in far wing line broadening studies in Na atoms. For sufficiently large v_L, ($v_L \geq 4$ say) when eq. 8 becomes valid, the behavior of $\bar{k}(v_L)$ can be expressed somewhat more exactly as

$$\bar{k}(v_L) \simeq f(v_L)\bar{k}_i(v_L) + (1 - f(v_L))\langle k \rangle_{MB}\ ,\ v_L \gtrsim 4 \qquad (12.$$

As $v_L \to$ infinity, in eq. 12, $f_1(v_L) \to 0$ (as we know) and eq. 11 is recovered.

We have now described in detail a method to obtain $\bar{k}_i(v_L)$ from the experimentally measurable $\bar{k}(v_L)$, for the practical case $\Gamma \ll 1$. The final

and most important stage of VSDS analysis is determining the cross-section $\sigma(v_r)$ from $\bar{k}_i(v_L)$. These two quantities are mathematically related by the following integral equation (see eq.7.b)

$$\bar{k}_i(v_L) = \int_0^\infty dv_r \, P(v_r|v_L) v_r \sigma(v_r) \qquad (13.$$

In Appendix A, it is shown that this integral equation (with $P(v_r|v_L)$ given by eq. 2) can be exactly mathematically inverted (deconvoluted) using Fourier transforms to yield $\sigma(v_r)$ given $\bar{k}_i(v_L)$. Formally, the deconvolution may be expressed as (see eq. III.8, Appendix A)

$$\sigma(v_r) = \frac{e^{\left(\frac{v_r^2}{2(r+1)}\right)}}{v_r^2\sqrt{r+1}} \left\{ \mathcal{F}^{-1}\left[2\pi i \kappa e^{\left(\frac{2\pi^2 r \kappa^2}{r+1}\right)} \mathcal{F}\left[e^{-v_L^2/2} \bar{k}_i(v_L); \kappa \right]; \frac{v_r}{r+1} \right] \right\} \qquad (14.$$

$$\mathcal{F}[f(x);\kappa] \equiv \int_{-\infty}^{\infty} e^{2\pi i \kappa x} f(x) dx, \quad \mathcal{F}^{-1}[g(\kappa);x] \equiv \int e^{-2\pi i \kappa x} g(\kappa) d\kappa$$

where $\mathcal{F}[f(x);\kappa]$ is the Fourier transform of $f(x)$, with κ as the transform variable (similarly for the inverse transform $\mathcal{F}^{-1}$). Eq. 14 firmly proves that knowledge of $\bar{k}_i(v_L)$ is <u>sufficient</u> to determine $\sigma(v_r)$, establishing that the VSDS technique is able (in principle) to yield measurement the velocity dependence of the cross-section $\sigma(v_r)$. The fact that in reality $\bar{k}_i(v_L)$ can only be measured for $v_L \leq v_{Lmax}$ has been numerically shown by example (see sec. IV, Appendix B) not to prohibit

determination of $\sigma(v_r)$ for a similarly limited range $v_r \leq v_{Lmax}$. This is quite reasonable since $\bar{k}_i(v_L)$ for $0 \leq v_L \leq v_{Lmax}$ ($v_{Lmax} \simeq 4$ say) contains practically <u>all</u> "information" available on $k(v_r)$ for $0 \leq v_r \leq v_{Lmax} - 1$ (see fig. and eq. 13), and $\bar{k}_i(v_L)$ for v_L near v_{Lmax} contains much "information" on $k(v_r)$ for $v_{Lmax} + 1 \gtrsim v_r \gtrsim v_{Lmax}$.

This concludes the discussion of the mathematical theory and analysis of the VSDS method. Application of the formal, mathematical deconvolution of eq. 14 to real experimental data is discussed at length in Appendix A, and is further detail in Appendix B, as applied to a previous Na_2^*-Xe VSDS experiment. Further review and discussion of the VSDS technique, as applied to the present Li_2^*-X data, will be given in the next chapter.

III. Experiment.

1. Apparatus

The apparatus used for the present Li_2^*-X VSDS experiment is shown schematically in fig. and is basically the same as that used in previous Na_2^* experiments[1,3.a], with the notable exception of a new Li oven and vacuum system, and somewhat different collection optics.

The Li oven, shown in fig. 2, is a linear piece of 304 stainless steel tubing with 1.5" O.D. and 1/16" wall thickness, with 3 layers of 304 stainless steel mesh (#100 mesh) surrounding the inside wall; the mesh is used as a wick to return liquid Li (cooled from the vapor) to the hot central region of the oven vice capillary action.[14]. The oven is heated by an ARi 115 volt co-axial electric heating cable, which is coiled around and brazed to the central section of oven pipe, referred to as the hot region, or zone. To provide a more uniform temperature distribution over the hot region, a 304 stainless steel insert (fig. 2) was used to increase thermal conductivity, due to the large increase in cross-sectional area for heat flow. The insert was surrounded with another 3 layers of mesh along its inside wall, and 1 to 3 layers along it outside wall as shown in fig. 2; the continuous layers of mesh from outside to inside of the insert (through a 1/16" lengthwise slot) allowed for circulation (by wick action) of molten Li form the oven to the inside central region of the insert, providing a steady supply of liquid Li (and thus Li_2 vapor) to this central hot zone, which is the

Fig. 1 Schematic of the apparatus used for the present experiment.

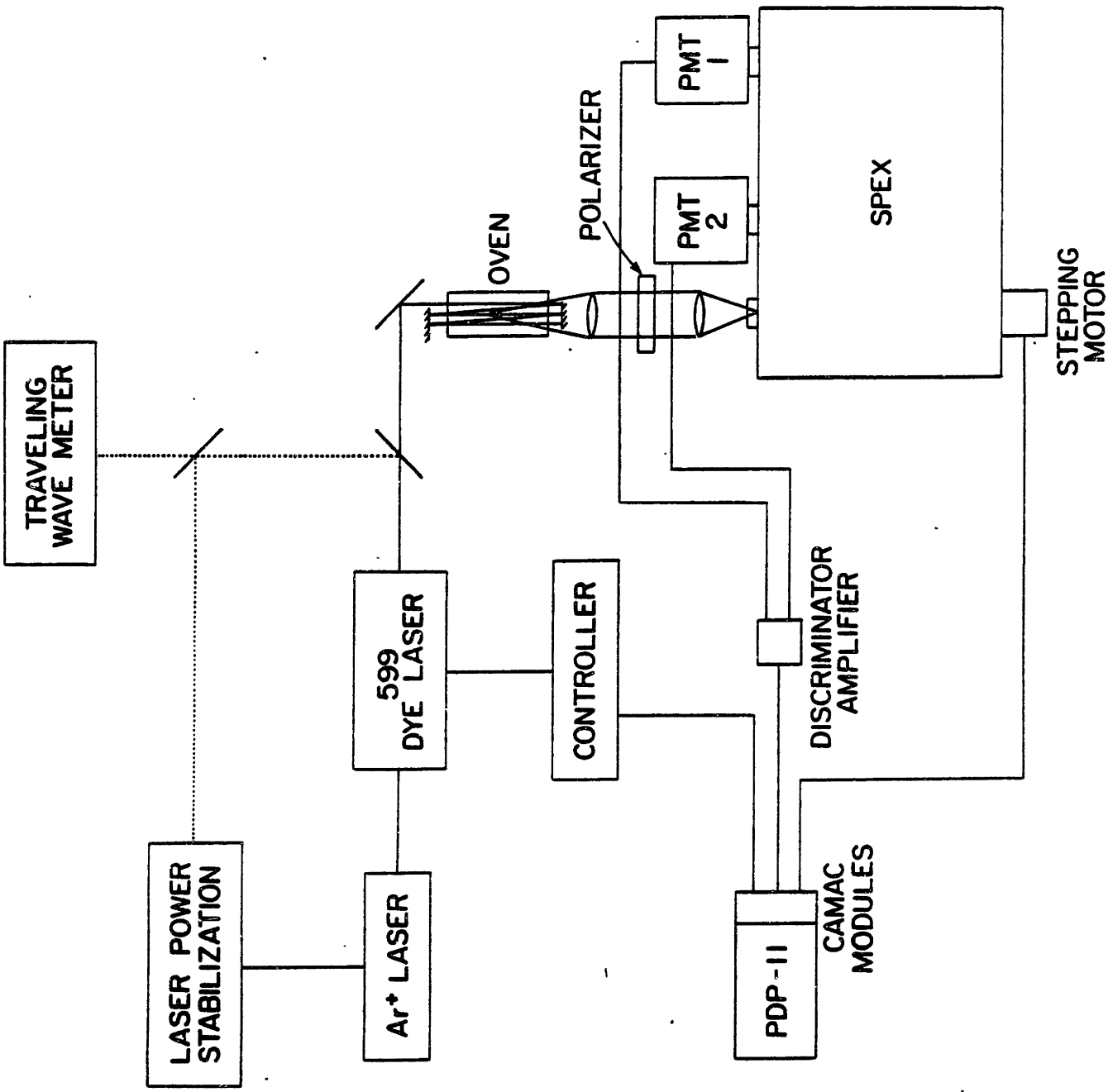

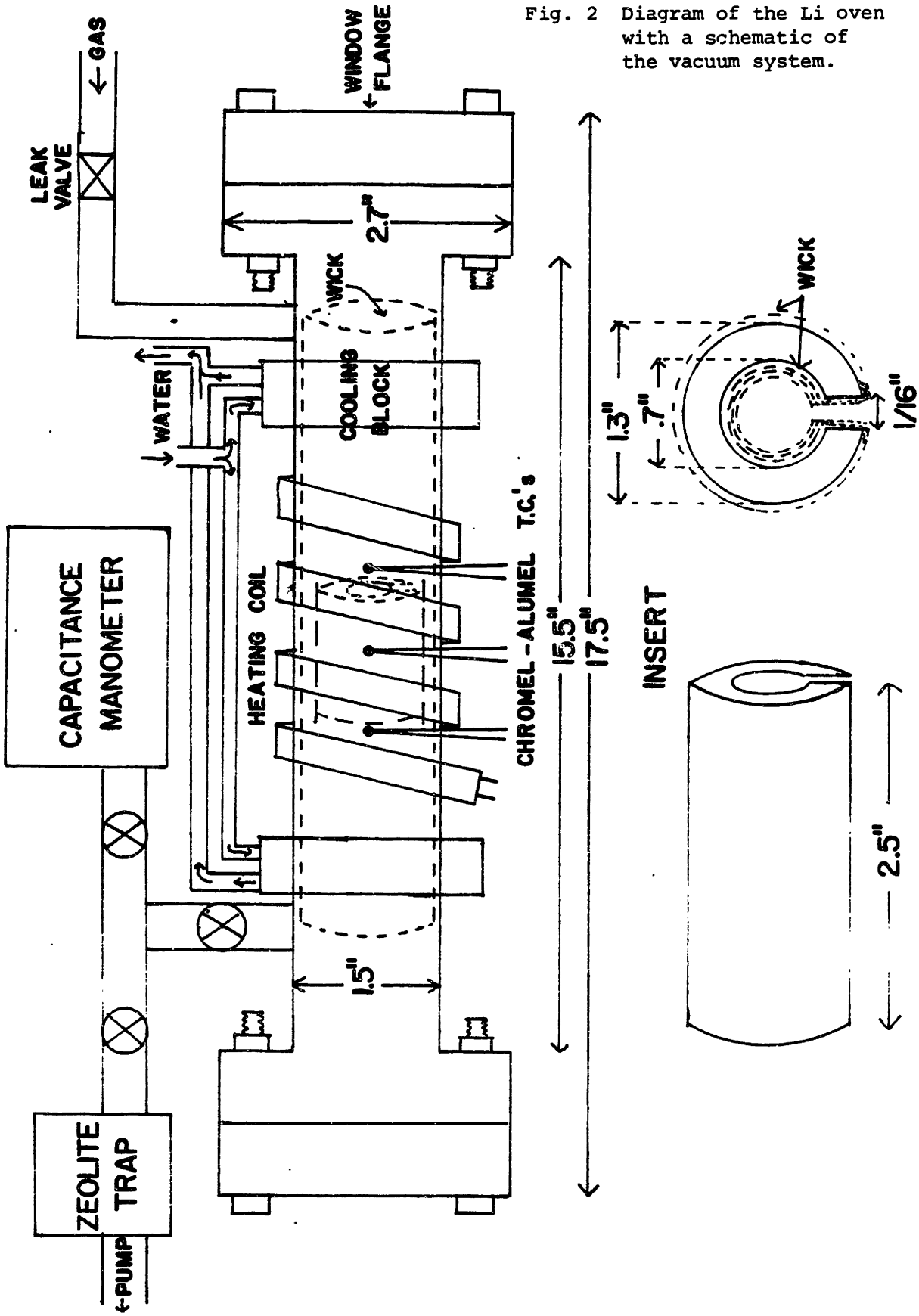

Fig. 2 Diagram of the Li oven with a schematic of the vacuum system.

interaction region for the experiment where signal is collected. The tight fit of the insert as well as molton Li in the wicks provide good thermal contact between the insert and the oven walls.

We measured the temperature distribution of the insert (under experimental operating conditions of T $\sim$ 600°C and 1 torr background gas) using an Omega type K chromel-alumel thermocouple (within Omega electronic ice point) enclosed in a 1' long 1/16" O.D. stainless steel sheath, which was inserted from one end of the oven using a specially made flange with a partially drilled out ultra torr fitting, allowing translational capability of the thermocouple probe through the fitting while still making a vacuum seal. The tip of the probe was placed along the inside wall of the insert wick, the molten Li in the wick providing good thermal contact. For readings of the 575°C, 615°C on the central outside oven thermocouple (see fig. 2) the insert temperature was found to be 582°C, 626°C at the center, dropping most by $\simeq$20°C at either edge. As discussed below, the depth of focus our collection optics is $\simeq$30cm, and over this length the insert temperature varies <10°C, thus only a .5% variation in $s_p \equiv \sqrt{\frac{kT}{m}}$, the thermal velocity unit characterizing the velocity distribution of the Li_2 vapor. Our experimental measurement of s_p is typically good to < 2%, and thus the variation of insert temperature is negligible; in practice we can simply use the measurement of the outside central thermocouple and add 11°K to determine the exper-

imental temperature.

The oven is covered with 2 layers of ≈ 1/2" thick thermal insulation, and requires about 200 watts of continuous power to maintain an equilibrium temperature at 600°C. The oven was initially loaded with about 10 grams of isotopically pure (> 99%) ^{7}Li, and after ∿ 200 hours of use, we have not observed any decay of signal due to loss of Li to the cooler outside region of the oven, indicating the wick circulation system is functioning well. Visual inspection also shows the inside insert wick to to be well wet with liquid Li.

Our vacuum system is quite simple, as is shown schematically along with the oven in fig. 2. We use a Granville-Phillips series 203 variable leak valve, and an MKS Baratrun 10-torr capacitance manometer (which measures absolute pressue) to measure target gas pressure. Under experimental condition we have found the pressure to drift < 2μ in the course of run times of ∿ 15 min, when the oven is isolated from the pump and the gas input.

Our collection optics consists of two plano-convex lens for collection and re-focussing of signal fluorescence onto our monochromator entrance slit; the net magnification of the two lens is approximately unity, and the collection system as a whole has a relative apperture of approximately f/8, to match the f/7.8 optics of the monochromator. In addition, a plane linear polarizer mounted on a graduated rotatable mount, is placed between the two lens, and allows selection of the

polarization of measured fluorescence (more on this later). The lens, polarizer, and one end mirror are all alligned on an optical bench supported on the oven table.

We employ a multiple pass mirror system to bounce the excitation laser beam back and forth through the oven, typically 6-7 passes, with each pass only marginally overlapping; this system can provide up to a factor of 5 increase in signal over that of a single pass system, as Li_2 vapor density under our experimental conditions results in relatively small absorption of the laser beam. The multiple pass system requires a well collimated laser beam, which was accomplished by using a 2x beam expanding telescope adjusted to focus somewhere during the middle passes. The mirrors are located a few cm outside the end windows of the oven; both mirrors and windows have broad band dielectric coatings which give 99+% reflection and transmission respectively, to increase the efficiency of the multiple pass system.

With our present geometry, we collect fluorescence radiated in a cone of width $\approx 10^\circ$ about the laser beam, with the exception of that blocked by the 12mm x 5mm multiple pass mirror on the collection side of the oven, which was cut down to minimize blockage. The optical depth of our collection optics (for beam diameter $\approx$ 2 m.m. >> slit width $\approx 150\mu$) is approximately given by 2(f/#)(beam diamter) $\approx$ 30 m.m., as mentioned earlier. Assuming 6 multiple passes, this would indicate an effective interaction region of $6\pi(1\text{m.m.})^2(30\text{m.m.}) \approx .5\ \text{cm}^3$, and whose shape is a

vertical "ribbon" of width ≈ 2 m.m., height ≈ 1 cm, length ≈ 3 cm. An image of the fluorescence is focused onto the vertical entrance slit of the monochromator by the collection optics.

Other parts of our equipment used during the experiment are basically the same as used previously, and are described in sec. II of Appendix B (and/or ref. 3.a), with the exception of a travelling wave meter (home built in our lab) which was very useful in measuring dye laser frequency for tuning to specific transitions of interest. The wave meter measures frequency by counting interference fringes between the source beam and a co-linear, stabilized He-Ne reference laser, and was accurate to a few gigahertz.

We used Rhodamine-B laser dye in our dye laser, since we were exciting transitions in Li_2 of wavelength 6300-6500Å; ≈ 4 watts all lines pump power with our Argon ion pump laser resulted in 30-40 mw single mode dye laser power. The dye laser power was electronically stabilized to better than 2% using an electronic servo-system which adjusted the pump laser power to maintain a constant dye laser output as measured by the dye laser reference cavity.

2. Experimental Procedure - Spx

We employ two basic stages of experimental measurement when performing a complete VSDS experiment. The first preliminary step is the absolute measurement of the velocity averaged rate constants $\bar{k}^o \equiv \bar{k}(v_L=0)$, measured when the excitation laser frequency is fixed on

resonance, or line center. We refer to this stage as a spx experiment (named after our Spex monochromator) and the $\bar{k}^{o}$, or more specifically, the $\bar{k}^{o}_{j,\Delta}$, as spx data. The second stage is the heart of our experiment and is what we more often are referring to when speaking of a VSDS experiment. In this VSDS stage the $\bar{k}_{j,\Delta}(v_L)$ are measured (in relative units only) as a function of v_L, and as stated in chapter II, it is these measurements that can be used to determine $\sigma_{j,\Delta}(v_r)$.

From the point of view of this work, the purpose of the spx experiment is simply to allow for normalization, in absolute units, of the otherwise unnormalized VSDS results for $\bar{k}_{j,\Delta}(v_L)$ (as will be seen, the spx data are also useful for determining multiple collision corrections to the raw VSDS results). However, the spx experiment results for $\bar{k}^{o}_{j,\Delta}$ are of considerable experimental interest in their own right, as there has been numerous experimental measurements of the $\bar{k}^{o}_{j,\Delta}$ in a variety of systems,[2-4] including many done in our lab.[3] Descriptions of the experimental equipment and procedures used to measure the $\bar{k}^{o}_{j,\Delta}$ by us in the past, and in the present work, have been previously described in detail.[3.a] Similarly, most of the experimental procedures used for VSDS experiments are described in App. B, which refers to our earlier VSDS work on Na_2^*. In this section, we will review the more important details of our experimental procedure, and discuss changes or improvements made from past methods.

In fig.3 is an outline of the scheme by which laser induced

Fig. 3 Laser Induced Fluorescence (LIF) measurement scheme.

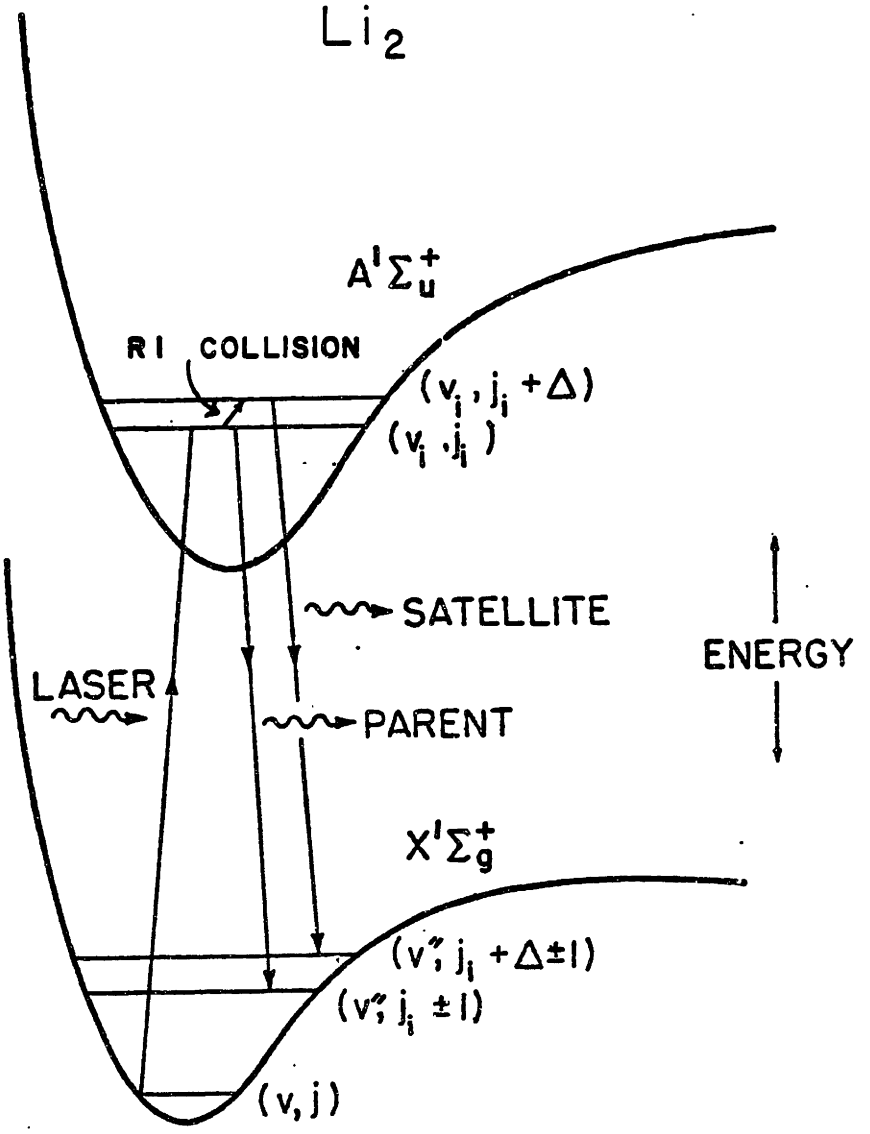

fluorescence (LIF) is used to measure excited state rate constants, as applied to the present work of RI rate constants in Li_2^*-X. A single frequency laser is used to excite a transition from the ground state $Li_2(v,j_i\pm1)$ to a <u>single</u> rovibronic level $Li_2^*(v_i,j_i)$ in the $A'\Sigma$ electronic state for electric dipole, Σ-Σ transitions transitons, there is the section rule[15] $j \rightarrow j\pm1$. The excited $Li_2^*(v_i,j_i)$ may, or may not undergo an RI collision to level $Li_2^*(v_i,j_i+\Delta)$ before radiatively decaying back down to the ground state $Li_2(v'',j_i+\Delta\pm1)$, with $\Delta = 0$ implying no collision. If $n_\Delta(t)$ is the number density of $Li_2^*(v_i,j_i+\Delta)$ molecules, then in the steady state, <u>single collision</u> limit, the rate equations for $\Delta \neq 0$ are (n_t = target gas density)

$$a.\quad \frac{dn_\Delta}{dt} = \bar{K}_{j_i,\Delta}\, n_t n_o - n_\Delta/\tau = 0 \qquad (1.$$

$$b.\quad \bar{K}_{j_i,\Delta} = \frac{1}{n_t \tau}\left(\frac{n_\Delta}{n_o}\right)$$

In eq. 1.a, the first term represents the rate of population of the $(v_i,\ j_i+\Delta)$ level due to RI collisions between $Li_2^*(v_i,j_i)$ and the target gas; this experimentally defines the velocity averaged rate constant $\bar{K}_{j_i,\Delta}$. The second term represents radiative decay out of the excited state, with τ = the radiative lifetime. As $I_\Delta \propto n_\Delta/\Gamma$, where I_Δ is the radiative intensity for transitions $Li_2(v_i,j_i+\Delta) \rightarrow Li_2(\ v'',\ j_i+\Delta\pm1)$ (any v"), and assuming the transition rate Γ is independent[16,17] of Δ then eq. 1.b, which follows directly from eq. 1.a. shows that

$$\bar{K}_{j_i,\Delta} = \frac{1}{n_t \tau}\left(\frac{I_\Delta}{I_o}\right) \qquad (2.$$

Equation 2 is of fundamental importance, for it relates the velocity averaged rate constant $\overline{k}_{j_i,\Delta}$ to the experimentally measurable intensity ratio I_Δ/I_o. Further, in VSDS terms, the LIF scheme which led to eq. 2 is independent of selected velocity laser detuning and thus v_L(ea.II.1). Consequently the result is valid as a function of v_L, which can be explicity written as

$$\overline{k}_{j_i,\Delta}(v_L) = \frac{1}{n_t \tau}\left[\frac{I_\Delta(v_L)}{I_o(v_L)}\right] \qquad (3.$$

Eq. 3 is the basic relation we seek, for it gives the experimental prescription for determining $\overline{k}_{j_i,\Delta}(v_L)$; to measure the intensity ratio $I_\Delta(v_i)/I_o(v_L)$ as a function of v_L (laser detuning). This procedure may be realized experimentally with a tunable dye laser and a spectrometer.

Eq. 3 is not strictly correct, as it does not take into account the possibility of multiple collisions (which will be discussed below), but its implication that I_Δ/I_o is the basic experimental quantity to measure is still valid. Throughout the remainder of this work, we will refer to the level (v_i,j_i) as the parent level, $(v_i,j_i+\Delta)$ as a satellite level, are the intensities I_o, I_Δ as parent and satellite line intensities respectively, (and also as parent lines and satellite lines, as in the spectroscopic sense).

As can be seen from the above discussion, in a spx experiment we wish to measure parent and satellite line intensities $I_o(v_L=0)$, $I_\Delta(v_L=0)$ (and their ratios) with dye laser frequency fixed at line center

(resonance) for the transition of interest. This is done by shining our dye laser into the Li oven, and scanning the monochromator to measure fluorescence intensity as a function of fluorescence frequency. The monochromator is scanned electronically by computer software control in discrete steps; at each step, fluorescent intensity measured with photo-multiplier tube (PMT) 1 for a specified time (typically .2 sec) is stored in counts/sec in computer disk files.

In fig. 4 we show a typical fluorescent scan for Li_2^*-Ar $j_i = 22$, which we refer to as a spx scan. For each parent or satellite level, there result two parent or satellite lines corresponding to the transitions $(v_i, j_i+\Delta) \rightarrow (v'', j_i+\Delta\pm1)$, with the "+" referred to as the P line, and the "-" as the R line (in the usual spectroscopic notation); P, R (Δ) lines used later for VSDS are identified in fig. 4. With experience, most RI satelite lines can be identified by inspection of the spx scan; in any event they can be unambiguously assigned using line position predicted using the Dunham coefficients for $Li_2(X\Sigma)$ and $Li_2^*(A\Sigma)$ determined by Kusch and Hessel,[18] whose predictions have been found to be accurate to $\sim$.1 cm^{-1}. As P and R lines are equivalent for the analysis, results for P, R parent-satellite intensity ratios are generally averaged together; when significant deviations exist, the smaller ratio is used since the larger value is most likely due to an interferng foregin line adding intensity to the satellite. Line intensities from spx scans were measured as the sum of the 3 largest measured

Fig. 4 Fluorescent spectrum (spx scan) for parent level v_i=9, j_i=22, with 1.0 torr Argon.

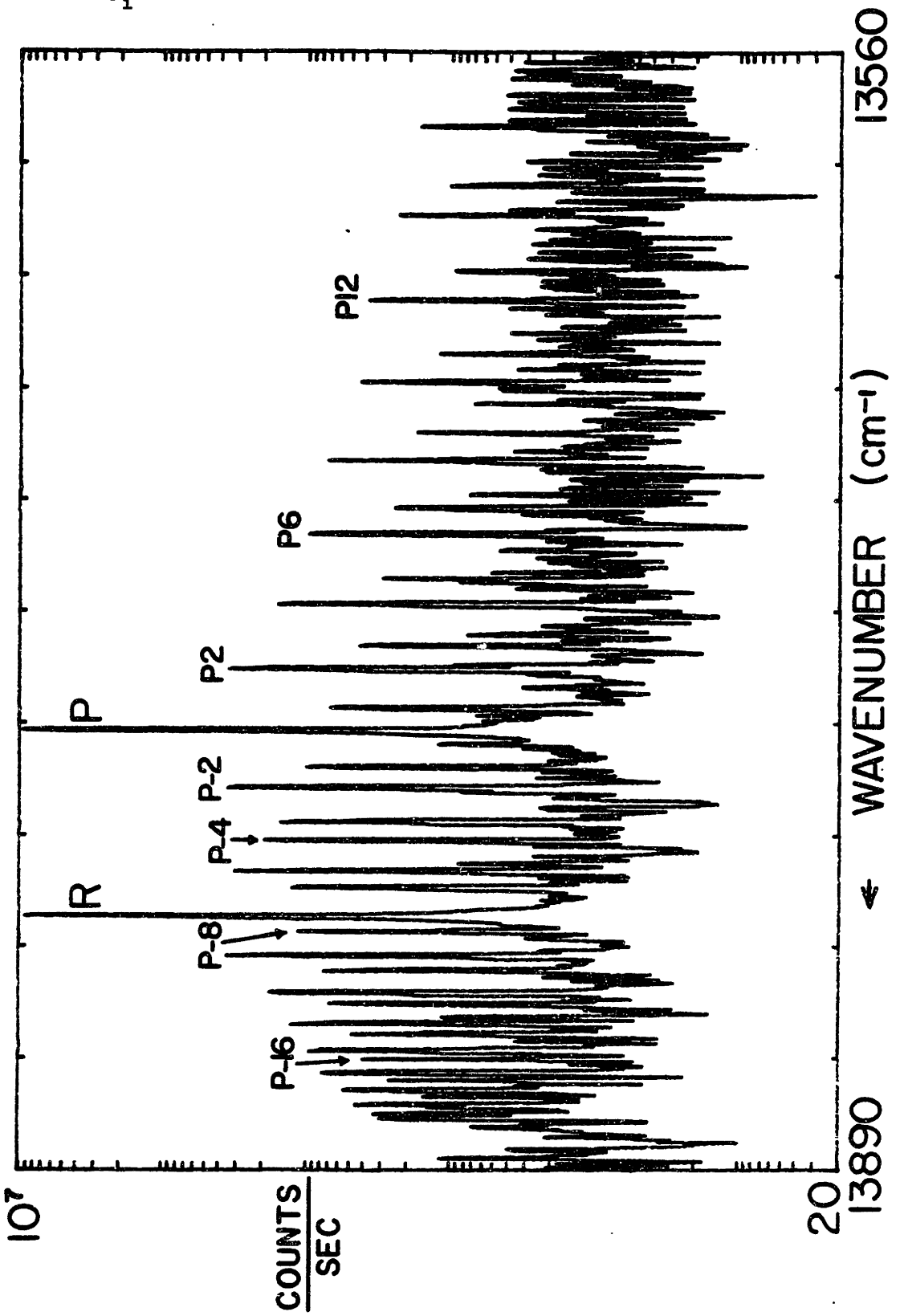

points on each line peak.

For all spx and VSDS measurements made for the present Li_2 experiment, we used (refering to fig.) v = 1, v_i = 9, and v" = 7. The transition 1→9 was used for excitation since it had a low initial ground state vibrational level (and thus a sizeable Boltzmann factor), and a fairly large Franck-Condon factor[18] (for increased transition probability and thus greater upper state population). In addition the excitation frequency for all j_i was in the tuning range of our Rhodamine-B laser dye.

The 9 → 7 fluorescence band seemed to be an ideal choice for analysis purposes: it was far from the excitation band 9→1, which had large background problems due to scattered laser light entering the monochromator, it had a relatively large Franck-Condon factor (for increased signal), while the neighboring 9→6, 9→8 bands had much smaller Franck-Condon factors thus minimizing possible interference between bands. In addition, comparison with other bands both experimentally and theoretically (using predicted line positions) showed that overlapping of different P, R satellites was nonexistent for v" = 7, given the actual $\simeq 1$ cm^{-1} resolution of the monochromator corresponding to slit sizes $\leq 150\mu$ used in practice. This last point was not always true for other possible choices of v". Given all these points in its favor, no other choice for v" other than v" = 7 was considered. In table 1, we outline the transitions used for excitation and fluorescence used for

Table III.1 - LIF Measurement Scheme

v_i, j_i	Excitation Level (Ground State) v, j	Transition Frequency (cm^{-1})	Analysis Fluorescence Band $v_i \rightarrow v''$	Fluorescence Frequency Range (cm^{-1})
9,8	1,9	15,806	9 → 7	13,560 - 13,890
9,22	1,21	15,754	9 → 7	13,560 - 13,890
9,42	1,43	15,401	9 → 7	13,380 - 13,890

the present experiment.

We will next briefly preview the analysis of spx experimental data, some of the results of which will again be used for VSDS correcting procedures. A more detailed analysis of the rate equations[3.a] for this system yields the following relationships between $\bar{k}^{o}_{j,\Delta}$ and the measured intensity ratios $R_{\Delta,\Delta'} \equiv I_{\Delta}/I_{\Delta'} = I_{\Delta}/I_{o} \div I_{\Delta'}/I_{o}$.

$$a.\ \bar{K}_{j_i,\Delta} = \frac{1}{n_t \tau'} R_{\Delta,0} + R_{\Delta,0}\left[\sum\left(\bar{K}^{o}_{j_f,\Delta} - R_{\Delta-\Delta',\Delta'}(1-\delta_{\Delta,\Delta'})\bar{K}^{o}_{j_f-\Delta',\Delta'}\right)\right] \quad (4.$$

$$b.\ \frac{1}{\tau'} = \frac{1}{\tau} + n_t \bar{K}_q \qquad c.\ j_f \equiv j_i + \Delta$$

with $\Delta = 0$ refering to the parent line (v_i, j_i), and τ' = effective lifetime, with $\bar{k}_q \equiv$ average rate constant for "quenching" collisions (e.g. VRI, electronic quenching) which remove population from the $(v_i, j_i+\Delta)$ levels (we assume no back transfer in this case). The first term in eq. 4a is just that of eq. 3 (with $\tau' \to \tau$) and represents the single collision limit $n_t \to 0$. The second term is the multiple collision correction, physically representing contributions to the $(v_i, j_i+\Delta)$ level from collisions to and from other <u>satellite</u> levels. Eq. 4a cannot be solved as is, as a solution would require knowledge of $\bar{k}^{o}_{j,\Delta}$ for $j \neq j_i$, which are only measured indirectly as multiple collision effects. However, <u>assuming</u> the substitution $n_t \tau' \bar{k}^{o}_{j,\Delta} = f(j,\Delta)T_{\Delta}$ for some <u>pre-specified</u> function $f(j,\Delta)$ only <u>constrained</u> such that $f(j,\Delta) = 0$ for $\Delta > N^{+}$, or $\Delta < -N^{-}$, (and from physical considerations, $\Delta < -j$), with the

unknown T_Δ depending on Δ <u>only</u> (not j), then eqs. 4a can be rewritten in the following matrix form:

$$\sum_{\substack{\Delta'=-N^- \\ \Delta'\neq 0}}^{N^+} \left[R_{\Delta-\Delta',\Delta'}\, f(j_t-\Delta',\Delta') - f(j_t,\Delta') \right] T_{\Delta'} = 1 \quad (5.$$

$$-N^- \leq \Delta \leq N^+, \quad \Delta \neq 0$$

The constraint on $f(j,\Delta)$ assumes $\bar{K}_{j,\Delta} = 0$ for "large" Δ RI collisions ($-\Delta > N^-, \Delta > N^+$) for the purposes of multiple collision corrections, and in a sense these collisions are now absorbed into $\bar{K}_q$. The $\frac{1}{2}(N^-+N^+)$ equations of eq. 5 can be solved algebraically for the $\frac{1}{2}(N^-+N^+)$ unknowns T_Δ ($-N^- \leq \Delta \leq N^+$) provided we choose $(N^++N^-) <$ both $<N^-_{max}$ <u>and</u> N^+_{max}, where $-N^-_{max} \leq \Delta \leq N^+_{max}$ is the experimental range where $R_{\Delta,0}$ has been measured. In practice, we generally take $N^- = N^-_{max} - 4$, $N^+ = N^+_{max} - 4$ and assume reasonable estimates for the unknown $R_{\Delta,0}(\Delta < -N^-, \Delta > N^+)$ required in eq. 5; we have found that results for $\bar{K}^o_{j_i,DELTA}$ using this procedure are quite insensitive to these estimates.(3.a)

In the spx experiments done for this work, spx data were taken at 5 different target gas pressures p_t = .25, .50, .75, 1.0, 2.0 torr; at each p_t, we solved eq. 5 for each T_Δ ($-N^- \leq \Delta \leq N^+$) and subsequently fit T_Δ as a function of p_t (in torr) to the form

$$T_\Delta(p_t) = t_\Delta p_t (1+t_q p_t)^{-1}$$

$$\text{with} \quad f(j_i,\Delta)\, t_\Delta = \left(\frac{n_t}{p_t}\right) \gamma \bar{K}^o_{j_i,\Delta} \quad , \quad t_q = \left(\frac{n_t}{p_t}\right)\gamma \bar{K}_q \quad (6.a)$$

where t_Δ, t_q are free parameters[3.a] in this non-linear fit, and $(\frac{n_t}{p_t}) = 1.10 \times 10^{16} \frac{cm^{-3}}{torr}$ at T = 880°K. Results for t_q at each Δ are averaged together to obtain $\langle t_q \rangle$ (since we found no systematic dependence of t_q on Δ) and the T_Δ are refit to the form (we now exclude the 2.0 torr point from the fit)

$$b.\ T_\Delta = t_\Delta p_t \left(1 + \langle t_q \rangle p_t\right)^{-1} \qquad (6.$$

where now t_Δ is the only free parameter. Having finally determined t_Δ form eq. 6b, and using τ = 18 nsec,[16] we can immediately solve for $\bar{k}^o_{j_i,\Delta}$

$$c.\ \bar{K}^o_{j_i,\Delta} = 5.05 \times 10^9 f(j_i,\Delta) t_\Delta \ cm^3 sec^{-1} \qquad (6.$$

$$-N^- \leq \Delta \leq N^+$$

As in past work,[3] we initially take f(j,Δ) = 1, which is equivilant to assuming (for multiple collision correction purposes only) that $\bar{k}^o_{j_i,\Delta} \propto t_\Delta$ depends only on Δ, independent of j_i (note that at 1 torr p_t, multiple collision effects are generally <15%, so $\bar{k}^o_{j_i,\Delta}$ is still primary determined by the measured $R_{\Delta,O}$, regardless of choices and assumptions for f(j,Δ)). However, in this work we then fit the results obtained (eq. 6.c) for $\bar{k}^o_{j_i,\Delta}$ to a power law[9] of the form $k^o_{j_i,\Delta} = aR_\Delta(T)N(j_i,j_f)\Delta E^{-\alpha}$, where $\Delta E = |E_{jf} - E_{ji}|$ is the change in rotational energy. $N(j_i,j_f)$ is a statistical spin factor,[9] and $AR_\Delta(t)$ is a thermally averaged ratio of final to initial density of

translational states.[3.a,9] We try $N(j_i, j_f) = N_o = \frac{2j_i+1}{2j_+1}$ and $N_\Delta = 2j_f+1$ corresponding to selection rules[9] $\Delta m_j = 0$, Δm unrestricted respectively. Comparing fits using N_o, N_Δ, we keep the one with lower χ^2, along with the fitted value for α, and repeat the above analysis procedure (starting from eq. 5) using $f(j,\Delta) = R_\Delta N(\Delta E)^{-\alpha}$; now t_Δ may be though of as a "correction" to the power law, assumed to depend on Δ only. In practice we find these second, and a priori more accurate results differ, with rare exception, on the order of <5% (i.e. within error) from the initial results with $f(j,\Delta) = 1$, giving us increased confidence in our multiple collision correction procedure.

We conclude our review of the procedure and analysis of this preliminary stage of the VSDS experiment by presenting, in Tables , our measured results for $\bar{k}^o_{j_i,\Delta}$ for L^*_{i2}-Ne, Ar, Xe j_i = 8, 22, and 42. These values, of course, will be used to normalize our VSDS measurements for $\sigma_{j_i,\Delta}(v_r)$ in absolute units, but they will not be considered for further discussion here; analysis of the $k^o_{j_i,\Delta}$, especially in terms of previously successful fitting laws,[9] will be the subject of a future publication.[19]

Table III.2 - Velocity Averaged Rate Constants

$\bar{k}^{o}_{j_i,\Delta}$ (10^{11} cm^3/sec)

j_i	Δ	Xe	Ar	Ne
8	-2	8.38 ± .65	8.38 ± .65	8.38 ± .65
	-6	8.38 ± .65	5.05 ± .43	4.91 ± .43
	-4	17.0 ± 1.4	12.3 ± 1.0	10.3 ± .87
	-2	40.4 ± 3.9	33.1 ± 3.3	21.4 ± 2.2
	+2	41.8 ± 3.8	37.5 ± 3.5	24.1 ± 2.4
	+6	15.0 ± 1.1	10.4 ± .87	11.8 ± .90
	+12	5.35 ± .41	5.78 ± .42	5.56 ± .41
	+18	2.05 ± .18	2.84 ± .22	2.82 ± .21
	+24	0.69 ± .08	0.91 ± .10	1.07 ± .10
22	-16	1.61 ± .12	1.85 ± .12	1.73 ± .11
	-8	6.89 ± .40	6.25 ± .37	6.08 ± .36
	-4	12.5 ± .79	10.9 ± .68	10.8 ± .69
	-2	25.9 ± 1.8	22.7 ± 1.6	19.5 ± 1.4
	+2	22.6 ± 1.5	20.5 ± 1.4	18.7 ± 1.3
	+6	5.35 ± .32	6.07 ± .36	6.31 ± .38
	+12	1.72 ± .11	2.08 ± .13	2.16 ± .14
42	-20	0.95 ± .09	1.21 ± .10	1.21 ± .10
	-16	1.26 ± .11	1.64 ± .13	1.61 ± .14
	-8	2.28 ± .17	3.19 ± .24	3.54 ± .28
	-4	5.08 ± .38	6.41 ± .49	7.03 ± .55
	-2	10.5 ± .84	13.9 ± 1.0	15.3 ± 1.2
	+2	9.21 ± .72	11.8 ± .89	13.4 ± 1.0
	+6	1.97 ± .16	2.31 ± .19	3.20 ± .23
	+12	0.35 ± .05	0.53 ± .06	0.55 ± .06

3. Experimental Procedure - VSDS

In this section we will review our experimental method for taking VSDS data, as well as the necessary correction and analysis procedures needed to finally obtain $\sigma(v_r)$. Descriptions of our equipment (as in fig. 1) not given here may be found in ref. 3.a, and also to a lesser extent in App. B, which details the VSDS analysis procedures as applied to previous Na_2^*-Xe measurements. We will review these proceedures here, and also discuss the several additions and improvements in our technique used for the present Li_2^* experiment.

As stated earlier, the experimental quantity of interest in VSDS is the ratio of measured satellite to parent line intensities $I_\Delta(v_L)/I_o(v_L)$ as a function of laser detuning (i.e. v_L). Satellite intensity is measured by PMT 1 (see fig. 1) mounted at the exited slit of our Spex double monochromator. Parent line intensity is measured with PMT 2, which is fixed to a horizontal linear translational mount attached atop an "optics tower" to whose base (mounted inside the Spex) is attached a 7μ thick, 8% reflecting pellicle beam splitter which reflects light to the first focus of the double monochrometor (i.e. converging light already dispersed by the Spex's first grating), up and out of the monochromator and through a ∿150μ slit mounted directly in front of the PMT 2 housing window and thus also fixed w.r.t. the translator. (The height of the tower was adjusted so the slit was ≈ at the focus of the diffracted light). Translation capability allows for a frequency tuning of range

$\approx \pm 150\ cm^{-1}$ about the Spex frequency (seen by PMT 1). Fine tuning of the Spex, and then the tower, is done (with laser at line center) by maximization of satellite and parent photon counts. We point out that the simultaneous measurement of $I_\Delta(v_L)$, $I_o(v_L)$ which we employ assures that the intensity ratio I_Δ/I_o is insensitive to drift or fluctuations in experimental conditions (in practice, Li_2^* density or laser power).

Having set the Spex and tower, we measure $I_\Delta(v_L)$ and $I_o(v_L)$ as a function of laser detuning by scanning our Coherent 599 dye laser $\approx \pm 5$ GHz about line center (as 1 velocity unit $s_p = 1.1$ GHz at $T = 880°K$, this corresponds to $v_L \approx \pm 4.5$). Scanning is computer controlled by our PDP-11/20 computer, using a CAMAC output register and a 12 bit D. to A. converter which outputs a linear ramp voltage to the 599 frequency controller which in turn is used to accomplish frequency detuning. We generally make intensity measurements at 200 discrete laser frequency points. The results are stored on computer disk files in our PDP-11/34 computer for future analysis. (Fig. 1 shows the "path" of the data collection.) This scanning procedure is repeated 3 to 4 times at each of two pressures, usually 1.0 torr and 0.2 torr, for each $\overline{k}_{j,\Delta}(v_L)$ to be measured. Over all measurements taken, the cell temperature used was in the range 600-610°C; over the course of a single I_Δ/I_o measurement, temperature varied only $\lesssim 1°K$. Laser power for these measurements was in the range 25-40 m.w. single mode, depending on how well the 599

was "cooperating" at the time.

Before proceeding with the above measurement procedure, we make a rather thorough check for possible interference to our parent, and especially satellite lines by foreign parents and satellites - those originating from levels other than (v_i, j_i) which are accidentally excited by the laser, as well as possible fluorescence from levels populated by VRI collisions from (v_i, j_i). This interference (unwanted fluorescence inside the resolution of the Spex) with satellite lines is potentially the most serious source of systematic error for VSDS measurements. This problem is much more serious at large detunings, where parent and satellite lines are considerably down in intensity (by a factor $\sim$ 500 at v_L = 4). Thus even small intensity foreign lines (comparitively negligible at line center) can be an intolerable source of error.

In addition to previous precautions,[1] in the present work we also ran computer searches, using calculated line frequencies, to predict the occurence and magnitude of interference problems (for any prospective choice of v, v_i, j_i, and v" (see fig. 3), although v = 1, v" = 7 were already considered solid choices for reasons discussed earlier. The searches consisted of determination of foreign parent lines (v_f, j_f) with excitation frequencies within $\pm.4$ cm^{-1} ($\approx \pm 12$ GHz, of the desired parent (v_i, j_i) resonance frequency, and finally checking for all possible interfering parent, satellite lines $(v_f, j_f+\Delta)$ whose fluorescence frequencies were within ± 2 cm^{-1} (for $\approx$ 150 μ Spex slits, extinction is

$\sim$ 1000 for detuning of 2 cm^{-1} at our wavelengths) of the fluorescence frequencies of specified Δ $(v_i, j_i+\Delta)$ satellites (assuming v" = 7). An extinction factor $e(v_L)$ (predicted ratio of foreign/desired satellite line intensities) was calculated, for each Δ (both P,R cases) assuming ground state populations $\propto (2j+1)e^{-E(v,j)/kT}$, Voigt profile lineshapes (eq. II.3) (these determine upper state (v_f, j_f) populations), and a power law for $\overline{K}_{j,\Delta}$ (which can then determine $(v_f, j_f+\Delta)$ populations); $e(v_L)$ was calculated for detuning corresponding to v_L = 0 and ±4. Given $e(v_L)$, the also calculated fluorescent frequency difference between foreign and desired lines, the known (by measurement) Spex instrumet function, and tabulated Franck-Condon factors,[18] we can accurately predict the source and magnitude of possible interference over the scan width of our measurements, and save potentially huge amounts of time relative to <u>experimentally</u> determining whether a partiuclar excitation level (v_i, j_i) or satellite line $(v_i, j_i+\Delta) \rightarrow (v", j_i\pm1)$ is a good choice or not. It was in fact this method by which we chose specifically j_i = 8, 22, 42 (and to a somewhat lesser extent v_i = 9) for use as low, medium, high j_i, since these cases appeared to suffer least from interference compared with other j_i checked.

Lastly, we point out that intensity measurements for negative or positive v_L (red or blue detuning), as well as for P or R lines, are in principle equivalent, so all that is necessary for VSDS is one clean side of either a P or R fluorescence line. When both $\pm v_L$ sides are

good, they are averaged together for improved signal/noise. We feel that the new computer search procedure, to aid in picking optimal choices for v_i, j_i and Δ (P or R), is an important reason for the improvement in range (especially in Δ) and quality of the present Li_2^*-Xe data over that of the earlier Na_2^*-Xe measurements of App. B.

For all measuremetns taken we kept our polarizer (see Fig.) alligned at 55° ($P_2(\cos 55°) \approx 0$) from the axis of laser polarization (determined easily by null measurement). This is because the dipole radiation intensity emitted by Li_2^* perpendicular to the excitation laser polarization axis is expressible[12] as $I(\theta) = \frac{1}{4\pi} I_T(1 + \beta P_2(\cos\theta))$, where θ is the angle between laser polarization and radiation polarization directions; we assume there is no other mechanism for allignent besides the laser polarization. The parameter β depends on the allignment, or m_j distribution of the Li_2^*, and I_T is the total angle integrated intensity. By measuring fluorescent instensity at polarization direction such that $P_2(\cos\theta) = 0$ (i.e. $\theta = 55°$) our measurements are rendered <u>insensitive</u> to the m_j distribution (possibly different for satellite and parent) or its changing with v_L. $I(55°) = \frac{1}{4\pi} I_T$ should thus be proportional to population density of n_Δ of $Li_2^*(v_i, j_i+\Delta)$, independent of β.

4. VSDS Analysis

In this section we discuss corrections and analysis applied to the measured raw intensity ratios to obtain $\bar{K}(v_L)$, the Lorentz tail

correction (described in Chap. II) applied to $\bar{k}(v_L)$ to yield $\bar{k}_i(v_L)$ (eq. II.13) and finally the deconvolution of $\bar{k}_i(v_L)$ to obtain $\sigma(v_r)$, the level specific cross-section at a particular relative velocity. All data processing is done by computer software (implemented on our PDP-11/34), and requires direct interaction by the experimentalist with the computer.

4.1. Data Averaging

The 3 to 4 repetitions of all VSDS scans measured are done for the purposes of averaging to improve signal/noise ratio; this is preferable to a single scan of longer counting time as the latter is more sensitive to long term drifts in experimental conditions, and more likely to result in failed scans due to laser problems. To properly average scans, line center ($\delta\nu = 0 = v_L$) must be accurately determined, so each scan can be precisely centered and alligned w.r.t. another to insure averaging points corresponding to equal detuning $\delta\nu$. This is done using the Lamb dip ($\simeq$ 5%, at 1 torr p_t) in our parent lineshape $I_o(\delta nu)$ which results from the slight overlapping of the counter-propagating beams of our multiple bounce scheme (sec. III.1). As $I_o(\delta\nu\simeq 0) \sim 10^6$ counts/sec, counting noise ($\propto\sqrt{I_o}$) will not obscure the Lamb dip, whose minimum (line center) is located by triangular extrapolation from adjacent points, to within $\sim \pm 5$ MHz($v_L \sim .005$). This method to find line center is simple, systematic, and at least 3 times more accurate than the previously used method of finding the centroid of the entire parent

profile. Next, original scans (200 points here) are restored in a standardized array of 128 equi-spaced points (interpolating when necessary), with ficticious point 63.5 defined as $v_L = 0$; this experimental velocity scale is referred to as channel number #, with $0 \leq \# \leq 127$, and and $v_L=0 \leftrightarrow \# = 63.5$. It is now that points of equal # (both parent and satellite lines) are averaged. The averaged results for $I_o(\#)$ and $I_\Delta(\#)$ are now stored for further analysis. (We have, and will use #, v_L, $\delta\nu$ interchangably, with $v_L = c\delta\nu/\nu_o$ (eq. II.1)).

During the averaging process, about 10% of each raw scan (5% at each end) corresponding to $4 < |v_L| < 4.5$ is discarded, since VSDS analysis at these large v_L is a practical impossibility. After averaging, a pulse overlap correction $\propto(1 + I/5x10^7)$ is made to account for the finite temporal resolution of our discriminator amplifiers (50 MHz), and is at most $\sim$ 2% (for $I_o(v_L\approx0)$).

4.2. Background Subtraction

For the next step of the analysis, we subtract estimated background signal from both $I_o(v_L)$ and $I_\Delta(v_L)$; the source of background noise being PMT dark counts (typically $\sim$ 30 counts/sec for thermo-electrically cooled RCS C31034 PMT's), and foreign line fluorescence (as discussed earlier), both of which are generally negligible for the parent lineshape. Inputting initial guesses (based on dark count measurements) for parent and satellite background into our analysis program, these backgrounds are then subtracted, and the resulting ratio $R_\Delta(v_L)$ =

$I_\Delta(v_L)/I_o(v_L)$ is displayed on a storage slope, the left ($-v_L$) side on top of the right ($+v_L$) side for ease of comparison. Substantial foreign line interference in the satellite line results in a much enlarged $R_\Delta(v_L)$ on the offended side, which can be quickly seen by inspection, and this side is then discarded for further analysis.

For the largest $|\Delta|$ measurements, satellite intensity in the wings was down far enough so that for $v_L > 3.5$, $I_\Delta(v_L) \sim$ dark counts, and so an accurate background subtraction is crucial to avoid very large ($\sim$100%) error in $R_\Delta(v_L)$ at the large v_L. This was done by adjusting the background to give the large v_L limit of $R_\Delta(v_L)$ predicted by the Lorentz tail effect; applying results of eq. II.12 and Table II.1 (for typical Γ = .02 and δ = .5)

$$a.\quad R_\Delta(v_L \simeq 4) \simeq \tfrac{1}{5} R_{\Delta i}(v_L \simeq 4) + \tfrac{4}{5} \langle R_\Delta \rangle_{MB} \qquad (7.$$

$$b.\quad \langle R_\Delta \rangle_{MB} \simeq \int R_\Delta(v_L)\, e^{-v_L^2/2}\, dv_L$$

(We set v_L =4 in eq. 7.a as we can, from experience, choose that position of our raw scans such that # = 0, 127 correspond to v_L = -4, 4 ± .01 respectively, and we apply eqs. 7 at or near the endpoints of our averaged data scans; accurate velocity calibration is done later, as described in the succeeding section). We feel we can, by visual inspection of $R_\Delta(v_L)$ for $0 \leq v_L \leq 3$ (where $R_\Delta(v_L) \approx R_{\Delta i}(v_L)$), estimate $\langle R_\Delta \rangle_{MB}$

to <10%, and $R_{\Delta i}(v_L \simeq 4)$ to <30% (by extrapolation assuming reasonably behaved $k(v_r)$); thus we can estimate $R_\Delta(v_L \simeq 4)$ to <15% by eq. 7.a. Our background guess is then re-adjusted until $R_\Delta(v_L \simeq 4)$ equals the estimated value (noise here is substantial, so an approximate eyeball fit of R_Δ near the $v_L = 4$ is then required).

In those cases when this procedure is important (i.e. signal/noise ~ 1), noise is too great to allow practical use of the $R_\Delta(v_L)$ data for $v_L \simeq 4$, but we have confidence in our results for $R_\Delta(v_L)$ data for $v_L \leq 3.5$ for all Δ. We feel that the above method is the most accurate way of determing the real background (at larger v_L where its knowledge is most important), and gives the most accurage values of $R_\Delta(v_L)$ possible under the circumstances; possible small satellite interference due to foreign lines can also be approximately eliminated by this procedure. Finally, we point out that usually the biggest observed deviations between $R_\Delta(v_L \simeq 4)$ and $R_{\Delta i}(v_L \simeq 4)$, where the background procedure of eqs. 7 is most subject to error, are for $\Delta = |2|$ where $I_\Delta(v_L)$ is always large enough so background corrections are in fact unimportant.

4.3. Voigt Fitting

The next stage of VSDS anlaysis, one of the most important ones, is fitting the parent lineshape to a Voigt profile function $V(v_L;\Gamma)$; that $I_o(v_L) \propto V(v_L;\Gamma)$ follows from eq. II.3, since $V(v_L;\Gamma)$ was defined as the total integrated probability, over all v_{pz}, for finding excited molecules with v_{pz} (and any v_{px}, v_{py}) given fixed v_L. The Voigt fits

determine the conversion factor from arbitrary unit # to the natural VSDS velocity unit $s_p = \sqrt{\frac{kT}{m_{Li2}}}$, and provide a method of determining Γ, which is used for the Lorentz tail correction. The fits are done using a programmed non-linear least squares fitting routine[20] (we assign errors $\propto .01 I + \sqrt{I}$, the $\sqrt{I}$ appropriate for Poisson statistics) and $V(v_L,\Gamma)$ is determined by an approximation accurate to .1% described in Appendix B.

Our fitting function has the form

$$a.\quad I_0(\#) = mV(v_L;\Gamma) = \frac{m\Gamma}{\pi}\int_{-\infty}^{\infty} dv\, \frac{e^{-v^2/2}}{\Gamma^2 + (v_L - v)^2} \qquad (8.$$

$$b.\quad X = \# - 63.5\ , \quad V_L = \frac{X}{S}\left(1 + \frac{aX}{63.5}\right)$$

with fitted parameters m (magnitude in counts/sec), s (dimensionless and equivalent to s_p measured in channel number #), Γ (ratio of Lorentzian to Doppler width), and a (asymmetry parameter to allow for non-linearity of frequency with # of our laser scans). In eq. 8.b, v_L is the usual, dimensionless (in s_p) laser selected velocity; for VSDS analysis, the actual value of s_p (in say, cm/sec) need not be known, only the conversion between s_p and laser detuning $\delta\nu$ (measured in channel # here). Of course, for $a \neq 0$, s and # are not precisely $\propto v_L$ or $\delta\nu$ but their meaning for this discussion seems clear, with a the maximum deviation (at the end points # = 0, 127) between actual v_L and that determined assuming v_L

= (#-63.5/s; we assumed (eq. 8b) a simple quadratic correction term for the nonlinearity.

We first decided to include an asymmetry parameter when close inspection of $I_o(v_L)$ on semi-log plots showed a slightly asymmetric lineshape, as though the laser detuning varied more rapidly on the blue side compared to the red side of the lineshape. Coherent's own specifications give the 599 a scan linearity (not further defined) good to 2% (we find a = .03 ± .01.

However, more sophisticated theories on collision redistribution of radiation[12] predict a small frequency red shift $\varepsilon(\delta\nu)$ which generally increases with detuning $\delta\nu$, which then would also qualitatively predict the observed asymmetry. If $\varepsilon(\delta\nu)$ varies linearly with $|\delta\nu|$, the resulting asymmetry would in fact be described by the non-linear correction of eq. 8b, and could be corrected for. However, these collisional effects would be sensitive to both choice of target (significantly larger for Xe, than for Ne) and would very roughly linearly with target pressure p_t; we have found "a" to be systematically independent witin error of both target and p_t (table 3), indicative of a very consistent, systematic apparatus type effect; we feel non-linearity of the laser is in fact the cause, and that otherwise the simple Lorentzian lineshape theory we have used in our VSDS analysis is quite sufficiently accurate. Lastly, we point out that this effect is at most only 3%, and that our measured ratio $R_\Delta(v_L)$ was essentially insensitive to it, since $R_\Delta(v_L)$

varies much less rapidly with v_L than does $I_o(v_L)$.

Depending on whether we use the left (case 1), right (case 2) or both (case 3) sides of $R_\Delta(v_L)$ for analysis, we Voigt fit $I_o(v_L)$ on the corresponding sides(s); using a non-zero asymmetry factor gave agreement within error for fitted values of s and Γ regardless of which side, or sides were fit. From eq. 8.b, the maximum v_L for which we have measurements, v_{Lm} is given by $|v_{Lm}| = \frac{63.5}{s}(1+a)$ for cases 2,3, and $\frac{63.5}{s}(1-a)$ for case 1. We now re-define $s' \equiv \frac{63.5}{v_{Lm}}$, and $I_o(v_L)$, $I_\Delta(v_L)$, $R_\Delta(v_L)$ are now re-stored (using interpolation when necessary) on a new linearized scale #, with $v_L = \frac{1}{s'}(\#-63.5)$ $0<\#<127$. For case 3, results at equal $|v_L|$ are averaged together (when possible, except for v_L near $\pm v_{Lm}$), and in all cases results are symmetrized so $R_\Delta(-v_L) = R_\Delta(v_L)$, similarly for $I_o(v_L)$, $I_\Delta(v_L)$. In fig.5 we show plots of $I_o(\#)$, $I_\Delta(\#)$ and $R_\Delta(\#)$ (averaged and symmetrized) for the case $\Delta = 2$, $j_i = 22$, Xe; in fig.6 we plot $I_o(\#)$ as well as its now linearized Voigt fit (i.e. $s \to s'$, $a \to 0$) on a semi-log plot, where it can be seen that the Voigt profile gives an excellent description of our parent lineshape.

Results for the Voigt fit parameters s, Γ, and a , averaged over all j_i, Δ_i, are presented in table 3 , along with standard deviations. As noted before, a has no obvious systematic dependence on either the target gas or its pressure, p_t. Systematic increase of Γ with p_t (largest for Xe) is well expected;[12] the rather small observed p_t dependence (from collisional broadening Γ_c) perhaps results from significant

Fig. 5 Parent, satellite, and intensity ratio for j_i=22, Δ=2, Xe.

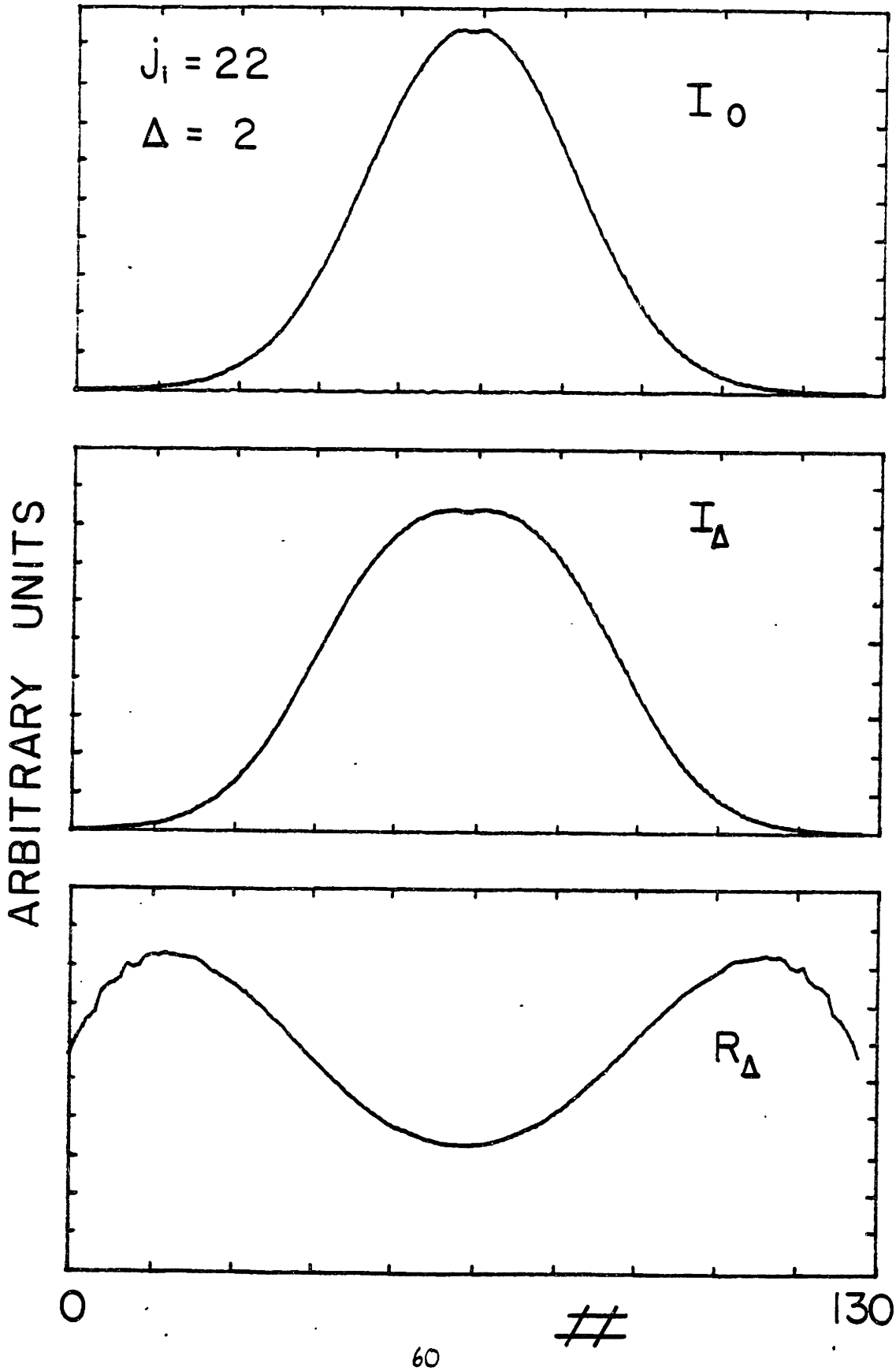

Fig. 6 Semi-log plot of the parent line-shape of fig. 5, along with a Voigt profile fit (circles).

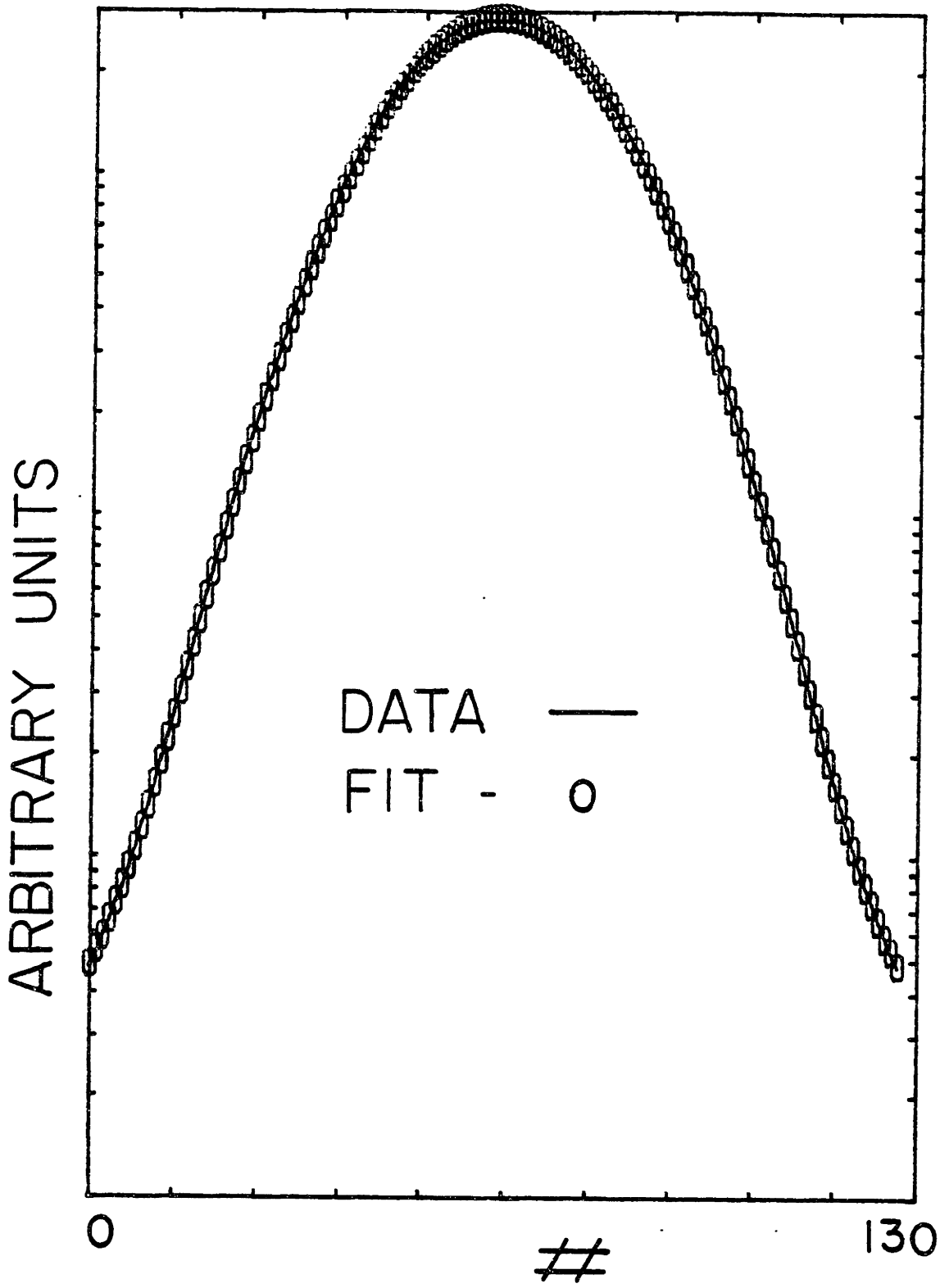

Table III.3 - Voigt Fit Parameters

Target Gas	Pressure (torr)	Γ	a	s
Xe	1.0	.020 ± .002	.034 ± .01	16.1 ± .2
	0.2	.018 ± .003	.028 ± .01	16.3 ± .2
Ar	1.0	.020 ± .002	.029 ± .01	16.2 ± .2
	0.2	.019 ± .003	.027 ± .01	16.4 ± .2
Ne	1.0	.019 ± .003	.029 ± .01	16.2 ± .2
	0.2	.019 ± .003	.030 ± .01	16.3 ± .2

power broadening Γ_p, since for lifetime τ = 18 nsec, natural broadening $\Gamma_n = (4\pi\tau\nu_o s_p)^{-1} \simeq .004$, with $\Gamma \simeq \Gamma_n + \Gamma_c + \Gamma_p$.

4.4. Multiple Collision Correction

Referring back to the multiple collisions analysis of section III.2, then the result of eq. 4, as a function of v_L, may be cast in the following form

$$\overline{K}_{j_i,\Delta}(v_L) \simeq \frac{1}{n_r \tau} R_\Delta(v_L)\left[1 + P_t\left(c\,\overline{K}_{j_f}(v_L) + \langle t_q\rangle(v_L)\right)\right] \quad (9.$$

$$j_f = j_i + \Delta$$

The term $\overline{K}_{j_f}(v_L)$ comes from the [ ] term on the RHS of eq. 4a, and represents the correction due to multiple collisions. Assuming that $\overline{K}_{j,\Delta}$ decreases rapidly with Δ, as is in fact the case, then [ ] is approximately proportional to $\overline{K}_{j_f} \equiv \Sigma_\Delta \overline{K}_{j_f,\Delta}$ (the total rate out of level j_f) with proportionality constant c. The term $\langle t_q \rangle$ is the quenching rate (per radiative lifetime per torr) as in eqs. 6.a, 6.b, as a function of v_L. The v_L dependence of the total rate constant $\overline{K}_j(v_L)$ is dominated by the $\overline{K}_{j,\pm\Delta)}(v_L)$ for small Δ <6, thus making it possible to estimate the v_r dependence of $K_j,(v_r)$ from $K_{j,\pm\Delta}(v_r)$ $|\Delta| \leq 6$, which can in turn be smoothly approximated from inspection of $\overline{K}_{j\pm\Delta}(v_L)$. However, while we can approximate $K_{j_i}(v_r)$ from our data, the correction term requires $\overline{K}_{j_f}(v_r)$; we assume that the difference is unimportant. For small $|\Delta|$, this is a very good approximation, and our data for j_i = 8, 22, 42 show it is also good even for large $|\Delta|$. Additionally, we note

that these corrections are always < 20%.

Unfortunately, we have no direct way of knowing the velocity dependence of the quenching term t_q in eq. 9, which is expected to be primarily due to vibrationally inelastic collisions. We arbitrarily assume its v_r dependence to be the same as $K_j(v_r)$. Thus, our multiple collision correction takes the form

$$a.\quad R_\Delta^2(v_L) = R_\Delta(v_L)\left[1 + p_t(\epsilon + \langle t_q\rangle)\frac{\bar{f}_i(v_L)}{\bar{f}_i(v_L=0)}\right] \qquad (10.$$

$$b.\quad f_1(v_r) = v_r\,,\quad f_2(v_r) = v_r(1 - v_r/12)\,,\quad f_3(v_r) = v_r(1 - v_r/8)$$

where R_Δ^2 is the multiple collision now corrected ratio, ϵ is the fractional multiple collision correction at $v_L = 0$ and $p_t = 1$ (torr). Both ϵ and $\langle t_q\rangle$ at $v_L = 0$ are known from our solutions to the rate equations for our spx data (sec. III.2). The $f_i(v_r)$ i = 1, 2, 3 are the simple choices we use to approximate the v_r dependence of $\bar{K}(v_r)$. The choice is made to reproduce the small $|\Delta|$ behavior of $\bar{K}_{j_i,\Delta}(v_L)$ for each individual data set. The relatively small magnitude of this correction does not warrant a more complex approximations to $K_j(v_r)$. Generally, f_1 was used for Xe, and f_2, f_3 were used for Ar, Ne. $\bar{f}_i(v_L)$ is a VSDS velocity average (as eq. II.b with Γ = .02) of $f_i(v_r)$ numerically integrated and stored on computer ($\bar{f}_i(v_L)$ is <u>not</u> the ideal VSDS average (Γ=0) as incorrectly reported in App. B.) We have ignored in the above analysis

any collision induced changes in the Li_2^* velocity distribution.

We have generally found $|\varepsilon| \leq .15$ and $\langle t_q \rangle = \langle t_q \rangle = .13 \pm .03$ Xe, and $.04 \pm .02$ for Ne, Ar, <u>independent</u> of j_i, resulting in an overall correction of <20% for all cases. Finally, we point out that the multiple collision correction is important for VSDS only to the extend that $\bar{f}_i(v_L)$ <u>changes</u> with v_L (at most $\frac{\bar{f}_1(v_L \simeq 3)}{\bar{f}_1(v_L=0)} \simeq 2$), since a constant $\bar{f}_i$ in eq. 10.a gives a constant correction factor which is irrelevant as all VSDS results are finally normalized using the $\bar{k}^o_{j_i,\Delta}$ measured form the spx data.

4.5. Lorentz Tail Correction

As discussed in detail in chap. III, the Lorentz tail correction is to account for and remove contribution to $\bar{k}(v_L)$ from molecules with essentially a thermal velocity distribution which are excited off resonance. It is generally important only at larger $v_L \geq 3$. Applying eq. II.10 to the present discussion, we have

$$a.\quad R'^3_\Delta(v_L) = \bar{f}^{-1}(v_L,\Gamma)\left[R^2_\Delta(v_L) - \int_{-3}^{v_L-\delta} p(v;v_L) R^2_\Delta(v)\,dv\right]$$

$$b.\quad R^3_\Delta(v_L) = \bar{f}^{-1}(v_L,\Gamma)\left[R^2_\Delta(v_L) - \int_{-3}^{v_L-\delta} p(v;v_L) R'^3_\Delta(v)\,dv\right] \qquad v_L \geq 0 \qquad (11.$$

$$c.\quad R_\Delta(-v_L) = R_\Delta(v_L)$$

Here, $R^3_\Delta(v_L)$ is now the Lorentz tail corrected ratio using a 2 iteration correction procedure, with $R'^3_\Delta(v_L)$ the intermediate 1st iteration result, the probability distribution $p(v_i,v_L)$ as in eq. II.3, and $f(v_L,\Gamma)$ the fraction of velocity selected Li_2^* (eq. II.9b and Table II.1);

we used $\delta = .5$ for all the Li_2 data, and Γ as determined by the Voigt fits discussed previously. Eqs. 11 are integrated numerically by computer, with R^2_Δ, R'^3_Δ, R^3_Δ stored by # with $0 \leq \# \leq 127$ and $v_L = (\#-63.5)v_{Lm}/63.5$; we replace the lower limit of the integrals with $v_L = -3$, which is effectively $-\infty$ given how rapidly $p(v,v_L)$ vanishes for $v_L \geq 0$ and $v \leq -3$.

The Lorentz tail correction amplifies noise in the ratio $R^2_\Delta(v_L)$ by a factor $f^{-1}(v_L;\Gamma)$, and we find $v_{Lmax} \approx 4$ as the largest v_L where $\bar{k}_{j,\Delta}(v_L)$ can be recovered with meaningful accuracy. The severity of noise in $R^3_\Delta(v_L)$ depends on Δ, but in general $3.5 \leq v_{Lmax} \leq 4$ for all the Li_2^*-Xe data.

4.6. Li Atom Correction

Correction steps 1-5 described above are all performed separately for VSDS data at two different pressures (typically 1.0 torr and 0.2 torr). To remove contributions from Li_2^*-Li collisions (at T = 880°K, the equilibrium vapor pressure[21] $p_{Li} \approx .04$ torr, with $p_{Li_2} < .02\ p_{Li}$) the data at high (p_{t1}) and low (p_{t2}) target gas pressure (but same p_{Li}) are subtracted.

$$R^4_\Delta(v_L) = \frac{1}{P_{t1}-P_{t2}}\left[R^3_\Delta(v_L,P_{t1}) - R^3_\Delta(v_L,P_{t2})\right] \quad (12.$$

The ratio $R^*_\Delta(v_L)$ is now in principle the intensity ratio measured in an ideal VSDS experiment at unit target pressure p_t = 1 torr. We then have

$$\overline{K}^i_{j_i,\Delta}(v_L) = \frac{1}{n_t \tau} R^4_\Delta(v_L) \qquad (13.$$

as the ideal VSDS velocity averaged rate constant (chap. II, $\overline{k}_i \to \overline{k}^i$). In practice, the unnormalized $R^*_\Delta(v_L)$ (scaled for convenience) are used for analysis, with the $\overline{k}^i_{j_i,\Delta}(v_L)$ in absolute units determined from

$$\overline{K}^i_{j_i,\Delta}(v_L) = \overline{K}^o_{j_i,\Delta} \frac{R^4_\Delta(v_L)}{R^4_\Delta(v_L=0)} \qquad (14.$$

with the $\overline{k}^o_{j_i,\Delta}$ measured in earlier spx experiments (Table III.2).

This completes the raw data analysis and correction procedure. The $R^*_\Delta(v_L)$, along with error bars (Poisson counting noise plus an assumed error of 20% the magnitude of the multiple collisions and Lorentz tail correction) at each point are stored on computer files, which can then be input into our deconvolution program, which is the next step in the analysis. For further discussion, we let $\overline{k}^i_{j_i,\Delta}(v_L) \to \overline{k}_{j_i,\Delta}(v_L)$ (except when otherwise noted) and $\overline{k}(v_L)$ and $R^*(v_L)$ will be used interchangeably.

4.7. Deconvolution

As stated earlier in chap. II, it is possible in principle to determine $\sigma(v_r)$ given $\bar{k}_i(v_L)$ (= $\bar{k}(v_L)$ for notational convenience), the formal mathematical deconvolution being given by eq. II.14. Methods of practical application of the formal result have been discussed in Apps. A and B; we will review them here, as well as improvements and changes in our deconvolution procedure made for this work.

To mathematically describe our data $\bar{k}(v_L)$ for deconvolution purposes, we linearly least square fit the $\bar{k}(v_L)$ to an even polynominal function:

$$a.\ \bar{K}(v_L) = \sum_{n=0}^{N} b_n P_n(v_L)$$

$$b.\ P_n(v_L) = \sum_{m=0}^{n} c_{mn} v_L^{2m} \qquad (15.$$

$$c.\ \sum_{\#} \delta_{\#}^{-2} P_m(v_L) P_n(v_L) = 0 \ , \ m \neq n$$

where $\delta_{\#}$ is the error assigned to the "#" data point; we again use $v_L = \frac{v_{Lm}}{63.5}$ (#-63.5) and # interchangeably (sec. III.4.3). We choose an <u>even</u> polynomial series since mathematically $\bar{k}(v_L) = \bar{k}(-v_L)$; additionally, odd powers of v_L cannot be solved for by our analytic deconvolution method. As our data have already been symmetrized, we need only fit $\bar{k}(v_L)$ for $v_L > 0$ (# > 64).

The polynomials P_n of eqs. 15 are mutually orthogonal polynomials[22], defined to within an overall scaling factor by eqs.

15.b and 15.c, with c_{nm} generated by recursion relations given in ref.22. Least squares fitting with the orthogonal P_n's is preferable over simpler expansion in powers of v_L, i.e. $\sum_{n=o}^{n} a_n v_L^{2n}$, as determining the a_n requires inversion of an $(N+1)x(N+1)$ matrix which becomes highly ill-conditioned as N increases (the b_n are determined immediately by orthogonality using eqs. 15.a, 15.c). The P_n are also preferable to standard orthogonal polynomials (e.g. Legendre Polynomials) as they allow for least squares minimization of

$$\sum_{\#} \left[\bar{K}(v_L) - \sum_{n=o}^{N} b_n P_n(v_L) \right] \delta_{\#}^{-2} \qquad (16.$$

where the $\delta_{\#}$'s are the optimal weights for our data, not weights associated with the standard polynomials themselves (the set $\delta_{\#}$ determine the $c_{n,m}$ in eq. 15.b). Finally, the b_n (unlike the a_n) are statistically independent, making statistical and error analysis considerably simpler.

Having fit the experimental $\bar{K}(v_L)$ to the form of eq. 15.a, use of eq. B.8 of App. A, along with eq. 15.b above, yield the following result for the deconvoluted cross-section $\sigma(v_r)$

$$\sigma(v_r) = \sum_{p=o}^{N} \frac{v_r^{2p-1}}{(2p+1)!} \sum_{n=p}^{N} b_n \sum_{m=p}^{n} c_{nm} \frac{(2m)! \left(\frac{-r}{2}\right)^{m-p} \left[(2m+1)(r+2(m-p))\right]}{r(m-p)!} \qquad (17.$$

with $r = m_{Li_2} \div m_X = .107, .351, .697$, for X = Xe, Ar, Ne respectively. It is seen that an even power series representation of $\bar{k}(v_L)$, of order 2N, yields another 2Nth order even power series for $k(v_r) = v_r\sigma(v_r)$, only with different coefficients. Both fitting (eq. 15.a) and deconvolution (eq. 17) are carried out by our PDP 11/34 computer, the program requiring active participation by the experimentor, with fitting and deconvolution results observed on storage scopes for visual inspection.

The basic limitation of our deconvolution procedure is lack of complete information on $\bar{k}(v_L)$, due to the limited range ($0 \leq v_L \leq v_{Lmax} \approx 4$) over which experimental measurement is possible, as well as uncertainty in the measured $\bar{k}(v_L)$ due to systematic and especially random error, or noise (in principle, exact deconvolution requires exact $\bar{k}(v_L)$ for $0 \leq v_L \leq \infty$). As discussed in chap. II, and in further detail in App. B, limited measurement of $\bar{k}(v_L)$ over only a finite v_L range tends only to limit the range over which $\sigma(v_r)$ can be recovered, and not to further limit the accuracy of the deconvoluted $\sigma(v_r)$ over that limited v_r range. We have consistently found with both real data and numerically generated examples (App. B) that measurement of $\bar{k}(v_L)$ for $0 \leq v_L \leq 4$ will allow recovery of $\sigma(v_r)$, via eq. 17, for approximately $.7 \leq v_r \leq 4$, with accuracy limited primarily by error in $\bar{k}(v_L)$, and not the finite v_L range. This is true regardless of the fact that our fit to $\bar{k}(v_L)$ (eq. 15.a) is generally completely unrealistice for $v_L > v_{Lmax} \approx 4$, thus confirming earlier statements (chap. II, App. B) that

$\overline{k}(v_L)$, $v_L > 4$ is rather insensitive to $k(v_r)$ for $v_r < 4$, and visa versa.

The approximate (it depends somewhat on r) lower bound of .7 for meaningfully recoverable v_r is due to the rather considerable insensitivity of $\overline{k}(v_L)$ to $k(v_r)$ for $v_r \leq .5$, where the integrated $P(v_r|v_L)$ (see fig. II.1) is very small, $<< 1$ (even for $v_L = 0$).

The primarly limitation of accuracy and resolution of our deconvoluted $\sigma(v_r)$ is error in our measurement of $\overline{k}(v_L)$, especially noise. Structure such as narrow peaks or rapid oscillations in $k(v_r) = v_r\sigma(v_r)$ will appear with very greatly reduced magnitude in $\overline{k}(v_L)$ due to convolution with $P(v_r|v_L)$, and can be partially or completely obscured by noise. The deconvolution problem of recovering the real strucutre or behavior of $\sigma(v_r)$ without generating artificial structure from noise is manifest in the choice of N, or the number of polynomial terms (=N+1) kept in our fit to $\overline{k}(v_L)$ (eq. 15.a). Too many polynomial terms generally causes the fit to follow noise structure in $\overline{k}(v_L)$, resulting usually in highly unrealistic large amplitude oscillations in the deconvolution result. Use of too few terms results in loss of both accuracy and resolution of both the fit and deconvolution.

In past work (App. B), we used a statistical test to determine when a fit coefficient b_n had a more than x% chance (typically $1 \leq x \leq 5$) of being found non-zero due <u>solely</u> to noise or uncertaintly in $\overline{k}(v_L)$, the actual value of b_n in fact being identically zero. We generally found that there existed an N_o such that b_n was statistically significant at

the (1-x)% confidence level for practically all $N < N_o$, and relatively few or no $N > N_o$; in such a case we used $N = N_o$ in our fit to $\bar{k}(v_L)$ (eq. 15.a).

For the present study in Li_2^*, we still employed this statistical test, but used N_o only as a guide, and visually inspected deconvolution results for several N greater than N_o. We then generally found that there existed a range of (typically 3) values $N_1 \leq N \leq N_2$ for which deconvolution results were essentially the same to within error. However, for $N > N_2$ noise induced oscillations rapidly became large. For our final fit, we usually chose $N = N_2$, and always $N \geq N_1$; this procedure typically resulted in a value N_2 which exceeded N_o by 1 or 2 for Ne, and 2 to 3 for Ar and Xe, though sometimes by as much as 5 in the latter case. We feel justified in using these extra terms by the fact that our statistical test on b_n assumes random, normal, uncorrelated errors at each data point, while contributions to the total assigned error from multiple collision and Lorentz tail corrections (dominant at large v_L) are smoothly correlated; thus our data are in fact less noisy than the errors indicate, resulting in an overly conservative choice of $N = N_o$ by the statistical test. As the velocity resolution δv_r of the deconvolution varies roughly as 1/N, choosing N_2 over N_o allows setting a smaller lower bound on δv_r; we feel that the rough invarience of our result with several $N \leq N_2$ indicates a real smoothness of $\sigma(v_r)$ itself.

An additional step in the deconvolutions employed with all the

present Li_2^*-Xe data was use of an artifical extension of $\bar{k}(v_L)$ (of typical length = 1 velocity unit) past v_{Lmax}, where again, v_{Lmax} is the largest v_L where we feel $\bar{k}(v_L)$ is meanifully accurate. The extension was done by first fitting $\bar{k}(v_L)$ for $0 \leq v_L \leq v_{Lmax}$, and then adding an approximately linear (in v_L) extension of the data with matched value and slope at $v_L = v_{Lmax}$ of the first fit. (N and v_{Lmax} were slightly varied so to give a slope which gave the "best" eyeball extrapolation of the data). This extrapolation of the measured $\bar{k}(v_L)$ to $v_L \approx 5$ was done solely to control behavior of the fitting function (eq. 15.a) immediately outside of v_{Lmax}; deconvolution results for $v_L > 4$ are never used. The extension method, in addition to having an intuitive appeal, appeared to give more reasonable results for $\frac{d\sigma(v_r)}{dv_r}$ for $3.5 \leq v_r \leq 4$. We emphasize that it was repeatedly found that use of the extension only negligably influenced deconvolution results for $\sigma(v_r)$ when $v_r < 3.5$, and caused changes generally well within error for all $v_r \leq 4$, again confirming earlier statements to this effect. Errors assigned to the extended region were fairly large, so the fit would not "try" too hard to fit this section.

The statistical independence of the fit coefficients b_n (eq. 15.a) allows a simple evaluation of the error in the deconvolution results caused by initial measurement error in the $\bar{k}(v_L)$ (App. B, eqs. 19,20). However, for the present work, errors were assigned by an empirical formula designed in part to reproduce the observed pattern of percentage error given by the former procedure of App. B, with $N = N_o$. This was

done to avoid the overly large error bars generated by the earlier statistical method as a result of using $N_2 > N_o$ (i.e. keeping b_n the tests "think" are less well known than in actuality), as well as to eliminate the somewhat oscillatory N dependent nature of the statistically calculated error bars. The present error assignment method was also designed so that error bars reflect the size of deviations observed in deconvolution results as N varies between N_1 and N_2; their size is generally conservatively large in this regard. We assume the latter error assignment method is more reflective of the error of our method due to the inexactness and non-uniqueness of our deconvolution results.

Information about $\sigma(v_r)$ in regards to velocity thresholds (primarily for $\Delta > 0$ cases) is in fact known prior to deconvolution. Using the method of Lagrange mutlipliers, our fitting program was also adapted to perform least squares fits for the b_n constrained so that the deconvolution result for $k(v_r) = v_r\sigma(v_r)$ vanish at one, or two distinct points v_{r1}, v_{r2}.

For practically all of the $\Delta < 0$ data, the constraint $v_{r1} = v_{r2} = 0$ was examined, but not kept for final results. We found that either χ^2 (goodness) of the fit significantly worsened, or much more often that the constrained deconvolution had oscillation problems, tending to simply oscillate about the smoother deconvolution, and agreeing to within error bars for all $v_r > .7$ in any case. When both constrained and unconstrained results were in good agreement, we again generally kept the

unconstrained deconvolution.

Considerably more use of the constraint technique was made in analysis of the $\Delta > 0$ data, the constrained deconvolution results being kept roughly 50% of the time. For smaller velocity thresholds ($v_{th} < 1$), the constraint $v_{r1} = v_{r2} \approx \frac{2}{3} v_{th}$, with 2/3 being typical, was used. We use the factor 2/3 as a compromise to allow for the finite resolution of our deconvolution method. As no finite polynomial could exactly reproduce the sharp cutoff behavior at the velocity threshold, this will put less "strain" on our constrained fits. We point out that in practically all cases for which this constraint was used, the natural <u>unconstrained</u> fits yielded deconvolutions which <u>also</u> attempted to reproduce threshold behavior by going through zero at finite $v_r \leq v_{r1} \leq v_{th}$; in all cases the χ^2 (goodness) of the fits differed insignificantly, and visual inspection found constrained and unconstrained results in agreement to well within error for $v_r > \max(.7, v_{th})$. For virtually all other $v_{th} \leq 1$ cases, constrained and natural results agreed well enough to make the constraint superfluous. We also point out that having $\sigma(v_r)$ become negative for $v_r < v_{r2}$ does not significantly effect results for $\sigma(v_r)$ when $v_r > v_{th}$, since $\bar{k}(v_L)$, and thus the fit to it, are quite insensitive to $\sigma(v_r)$ for $v_r \lesssim .6$.

For the largest threshold ($v_{th} > 1.1$) cases, the alternative constraint $v_{r1} = 0$, $v_{r2} \approx .8\, v_{th}$ (".8" again being typical) was also occasionally tried.This type constraint attempts to reproduce threshold

behavior while also keeping the deconvoluted $\sigma(v_r)$ near zero. This can prevent the deconvolution from becoming too negative for large enough v_r (though still $< v_{r2}$) where the negative values could conceivably have a causal effect on deconvolved results for $v_r > v_{th}$. Without exception, all natural deconvolutions for $v_{th} > 1$ did go through zero at some $v_r < v_{th}$. When kept, constrained results had essentially equal χ^2 fits to $\bar{k}(v_L)$ as did natural fits; both deconvoluted $\sigma(v_r)$ agreed quite well for $v_r > v_{th}$, with deviations between them always well within error bars; it was however felt that the constrained deconvolutions were more realistic for v_r near v_{th}. In cases where the natural deconvolutions were kept, they always went through zero at $v_r > \frac{2}{3} v_{th}$, and thus it was felt that they determined (resolved) the threshold behavior sufficently well to make use of the constraint unnecessary.

Generally speaking, the value of the constraint technique is that it provides a way to include known information (from basic considerations such as energy conservation) in the fitting procedure, allowing the constrained fit to very slightly deviate from the natural least squares fit, and thus "ignoring" the small noise errors in $\bar{k}(v_L)$ (at low v_L) which can yield unphysical behavior for $\sigma(v_r)$ at low $v_r < v_{th}$. Of course, constrained results being usually negative for $v_r < v_{r2}$ are still not realistic for $v_r < v_{th}$, but the constraint can in a sense increase resolution of deconvoluted results by representing threshold behavior more accurately and also by often allowing for a few extra fit-

ting terms, since constrained fits will not always follow noise or error in $\overline{k}(v_L)$ as closely as natural fits might. We re-emphasize that the constraint method provides only a "fine tuning" of our deconvolution results, and that in most cases the data, VSDS method, and our deconvolution method were of sufficient accuracy and resolution to find and predict velocity threshold behavior without the use of constraint techniques; constrained results were always discarded when the quality of the fits and/or the deconvolutions were inconsistent with natural results.

4.8. Velocity Resolution

While velocity resolution of the $\overline{k}(v_L)$ can be readily determined by the width (in v_r) of $P(v_r|v_L)$, it is not so simple to assign a resolution width δv_r to our deconvoluted results. To an extent, it must depend on the form of $k(v_r)$. Any $k(v_r)$ expressible as an even polynomial of finite order could in principle be deconvoluted from the corresponding $\overline{k}(v_L)$ exactly using our method. However, we note that given N distinct values of $k(v_r)$ for $0 < v_r < v_{max}$, it would require in general at least a 2Nth order <u>even</u> polynomial to interpolate or represent these N values. Alternatively, given a 2Nth order even polynomial, it can in general represent only N+1 distinct values over the finite interval $0 < v_r < v_{max}$. Thus, we may then define an approximate deconvolution resolution as $\delta v_r = \frac{v_{max}}{N+1}$. We found N (as defined last section) to be usually in the ranges of 9-11 for Xe, 8-10 for Ar, and 6-8 for Ne, so

taking $v_{max} = 4$, we find that the above criteria gives resolutions of $\delta v_r = .4, .45, .6$ for Xe, Ar, Ne respectively.

The above approach fails (at least in a direct sense) to account for any mass ratio r dependence of δv_r, which is crucial in determining $P(v_r|v_L)$ and thus the natural VSDS resolution of $\bar{k}(v_L)$ - see fig. II.1. An alternative method to define δv_r was to assume a δ-function rate constant $k(v_r) = k_o\delta(v_r-v_o)$, for which $\bar{k}(v_L) = k_oP(v_o|v_L)$, and then use our deconvolution procedure to attempt recovery of $k(v_r)$. The finite polynomial could not of course, reproduce the delta function $\delta(v_r-v_o)$, but it did approximate it with a large peak centered at $v_r \approx v_o$, with smaller oscillatory peaks surrounding it; we then define the FWHM of the central peak as $= \delta v_r$. Using $v_{max} = 4$, $v_o = 2$, we fit and deconvoluted $\bar{k}(v_L) = cP(v_o|v_L)$ with N = 9, 10, 12 for Ne, Ar, Xe respectively which are similar to typical values used for our data. We found the FWHM $\delta v_r = .45, .55, .75$ for Xe, Ar, Ne respectively, which are in fact fairly similar to values obtained by the previous definition, though somewhat larger.

Thus, given the rather good agreement for estimates of δv_r by the two above definitions, we can assume the following estimations for δv_r to be "best" estimates of the velocity resolution for our deconvolution procedure applied to the present data.

$$\delta V_r = \begin{cases} .4, Xe \\ .5, Ar \\ .7, Ne \end{cases} \qquad (18.$$

These δv_r estimates are typical, the actual resolution being perhaps slightly better (worse) at larger (smaller) v_r. We emphasize that the resolutions δv_r in eq. 18 are $\gtrsim$ 3 times better than the "natural" VSDS resolution (FWHM of $P(v_r|v_L)$) at corresponding v_L (fig. II.1). The δv_r can be interpreted as being the FWHM of some $\simeq$ symmetric probability distribution function $f(x)$, with maximum at $x=0$; the convolution of $f(x)$ with the real $\sigma(v_r)$ would then yield in our deconvolution result for $\sigma(v_r)$.

5. Results for $\bar{k}_{j_i,\Delta}(v_L)$

In figs. 7-15, we present our final results for the ideal VSDS velocity averaged rate constants $\bar{k}^i_{j_i,\Delta}(v_L)$ (which we hereafter refer to as $\bar{k}_{j_i,\Delta}(v_L)$). We have actually plotted $\bar{k}_{j_i,\Delta}(v_L) \div \bar{k}^o_{j_i,\Delta}$, the $\bar{k}^o_{j_i,\Delta} \equiv \bar{k}_{j_i,\Delta}(v_L=0)$ can be found in table III.2 of chap. III. This is convenient for both discussion and presentation purposes; it allows simple inspection and comparison of the v_L dependence of the $\bar{k}_{j_i,\Delta}(v_L)$ independent of the overall magnitude of the $\bar{k}^o_{j_i,\Delta}$, and also facilitates the graphing together of the $\bar{k}_{j_i,\Delta}(v_L)$ for any j_i, Δ, without scaling problems.

The $\bar{k}(v_L)$ have considerable information content in their own right. The basic trends in the v_r dependence of $k(v_r)$ and thus $\sigma(v_r)$ can be qualitatively estimated by simple inspection of the $\bar{k}(v_L)$. They are also, of course, free of any deconvolution errors. As was done in the first VSDS work,[23] the $\bar{k}(v_L)$ can be plotted v.s. $\bar{v}_r(v_L)$ (average relative velocity) to obtain a "first order" approximation to $k(v_r)$. However, as shown in App. B, this method is considerably inferior in both range and resolution to the deconvolution approach.

It is seen from an inspection of $\bar{k}_{j_i,\Delta}(v_L)$ in figs. 7-15 that the v_r dependence of $\sigma_{j_i,\Delta}(v_r)$ has a rather dramatic dependence on both j_i and Δ, and in many cases on the choice of target gas as well. This variation with j_i,Δ is much more pronounced than that observed in Na_2^*-Xe (App. B) or HF-Ne,Ar,Kr[5], and is made more

Fig. 7 Velocity averaged rate constants for $j_i = 8$, Xe.

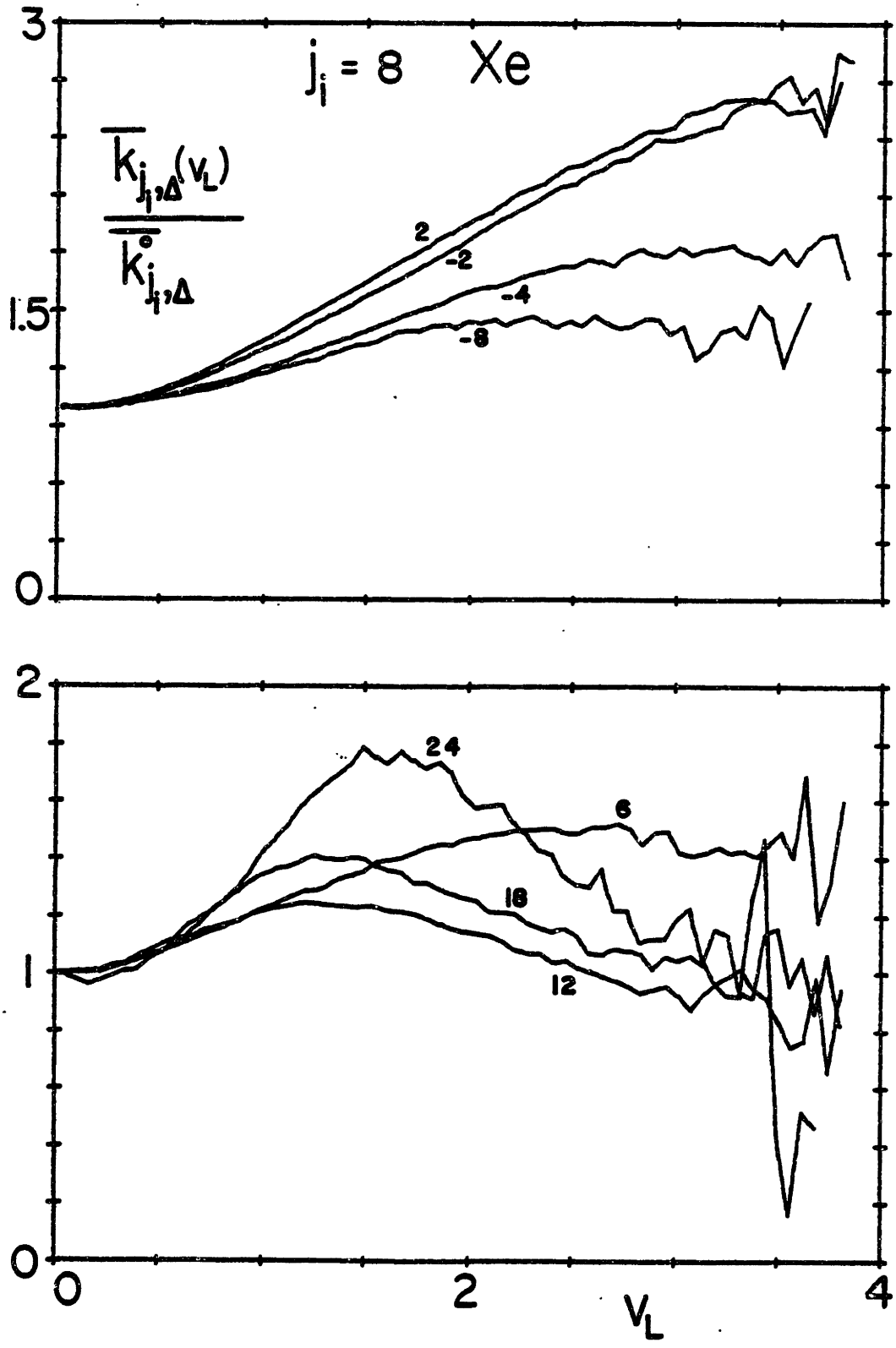

Fig. 8 Velocity averaged rate constants for j_i = 22, Xe.

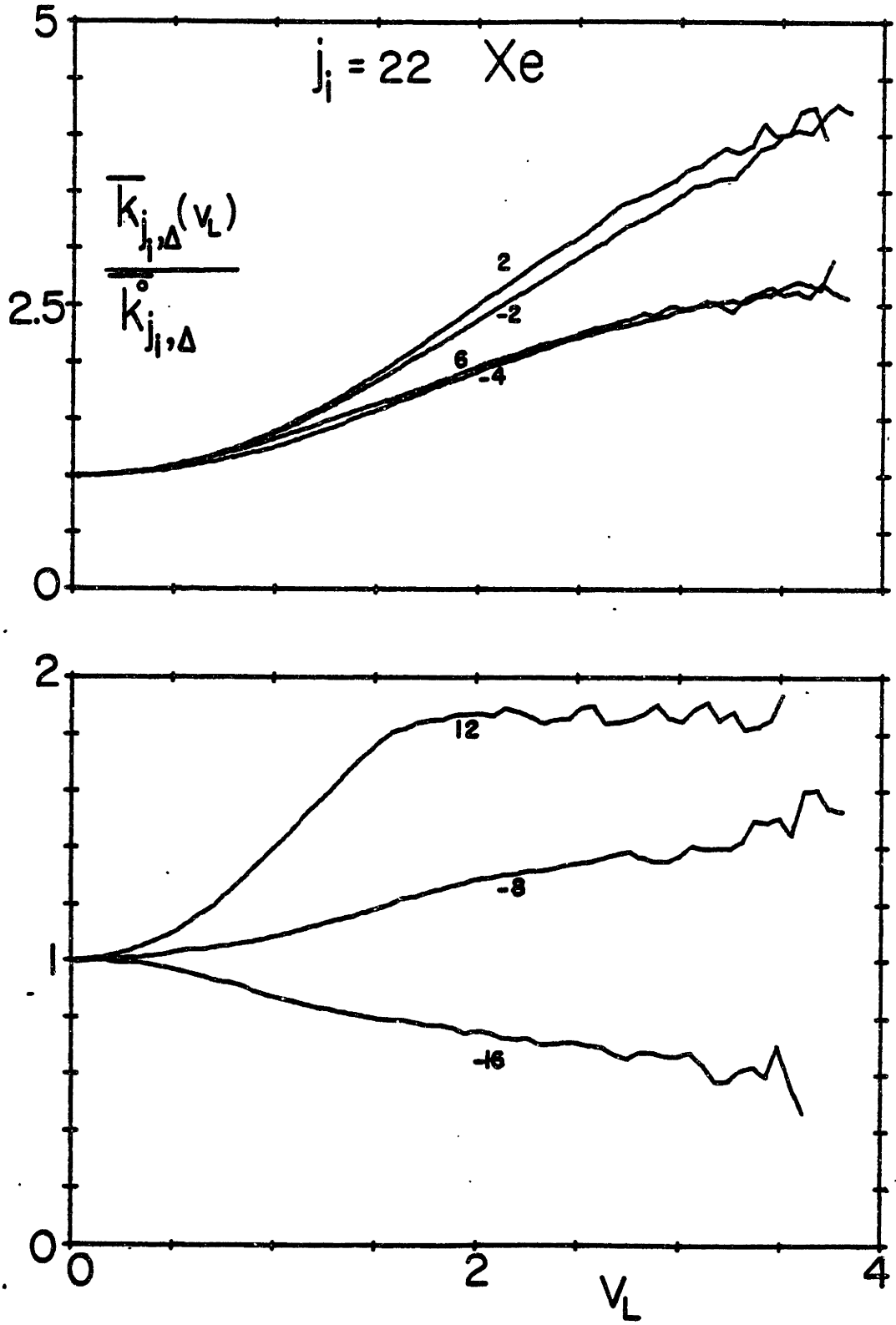

Fig. 9 Velocity averaged rate constants for j_i = 42, Xe.

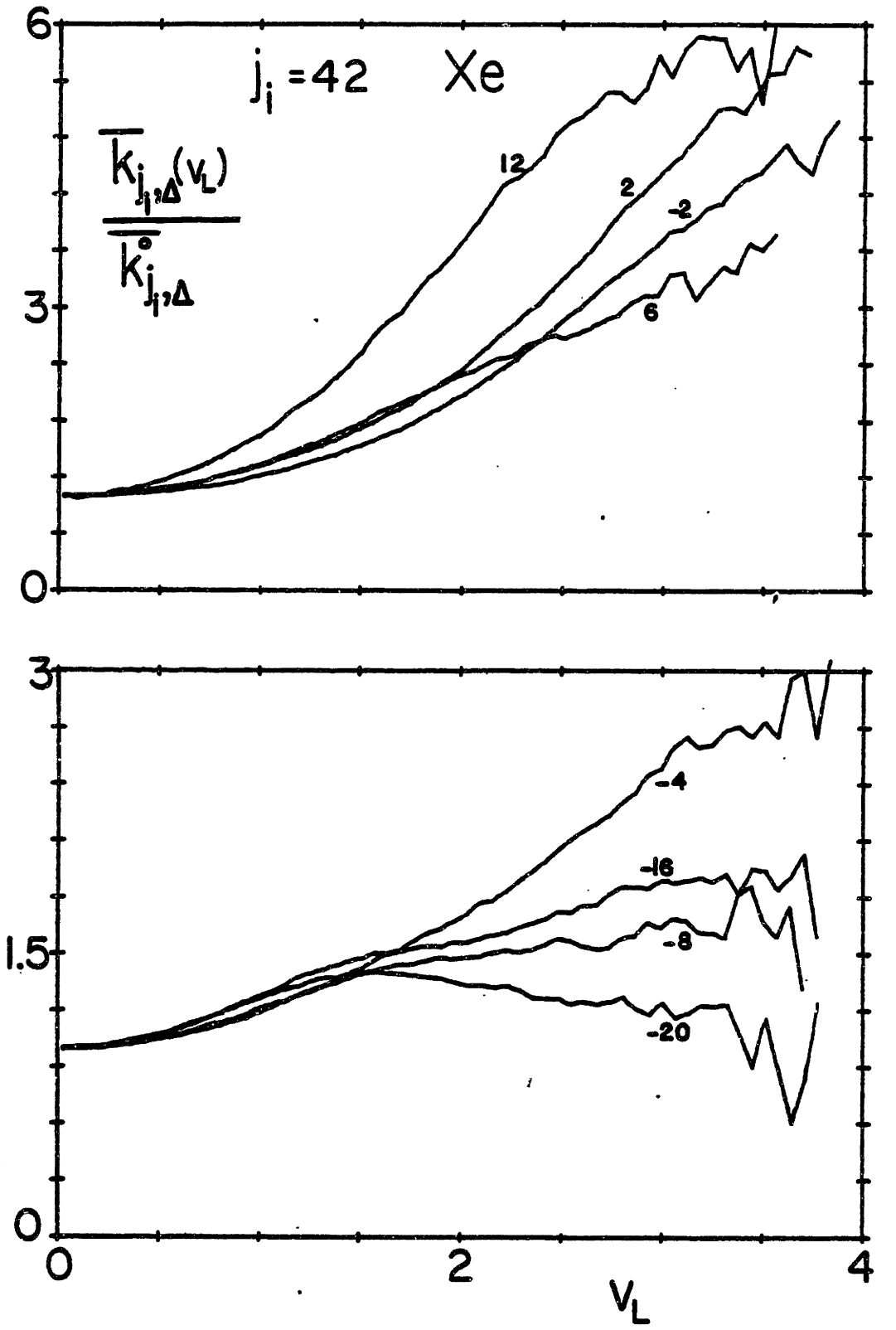

Fig. 10 Velocity averaged rate constants for $j_i = 8$, Ar.

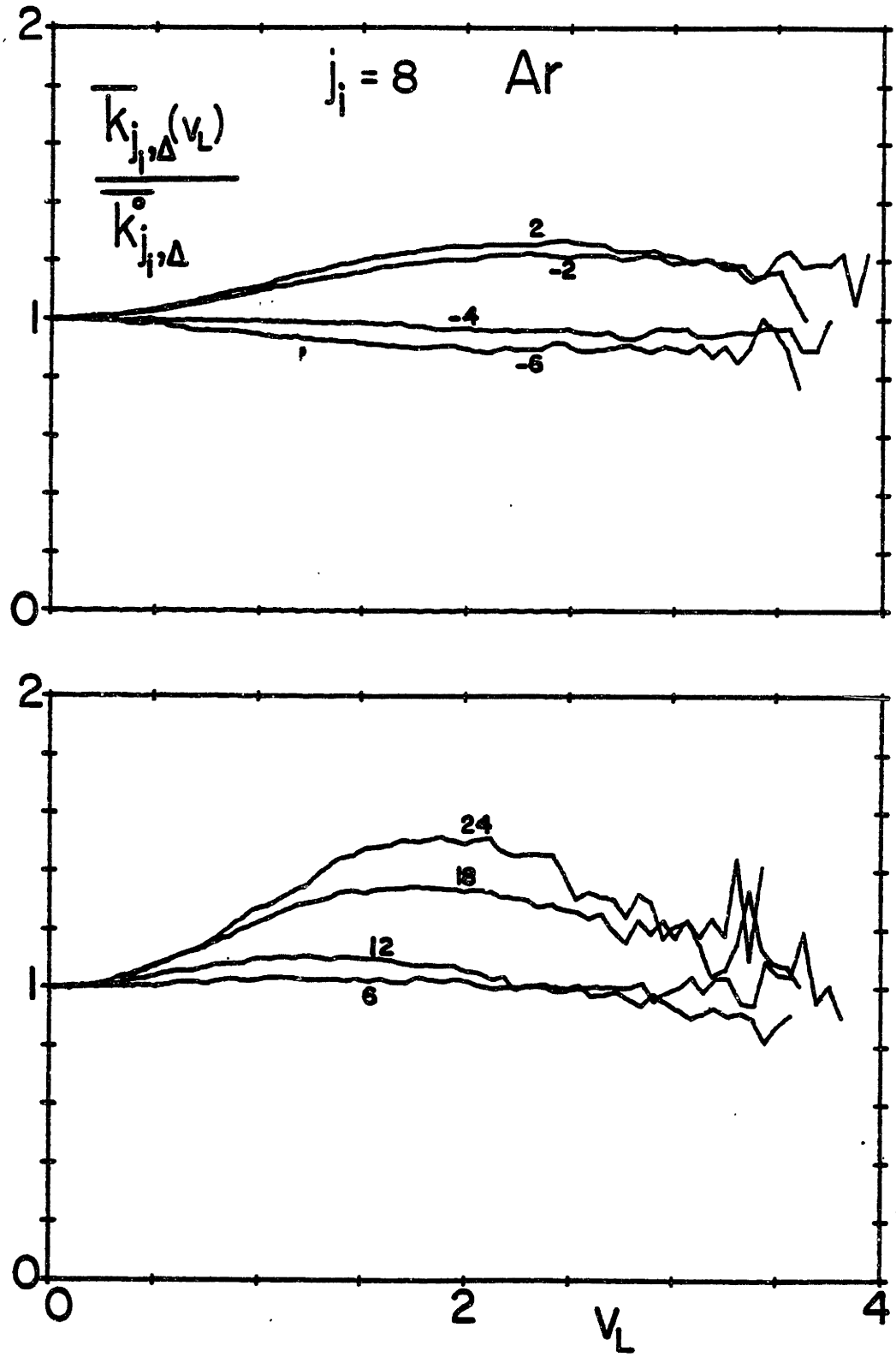

Fig. 11 Velocity averaged rate constants for j_i = 22, Ar.

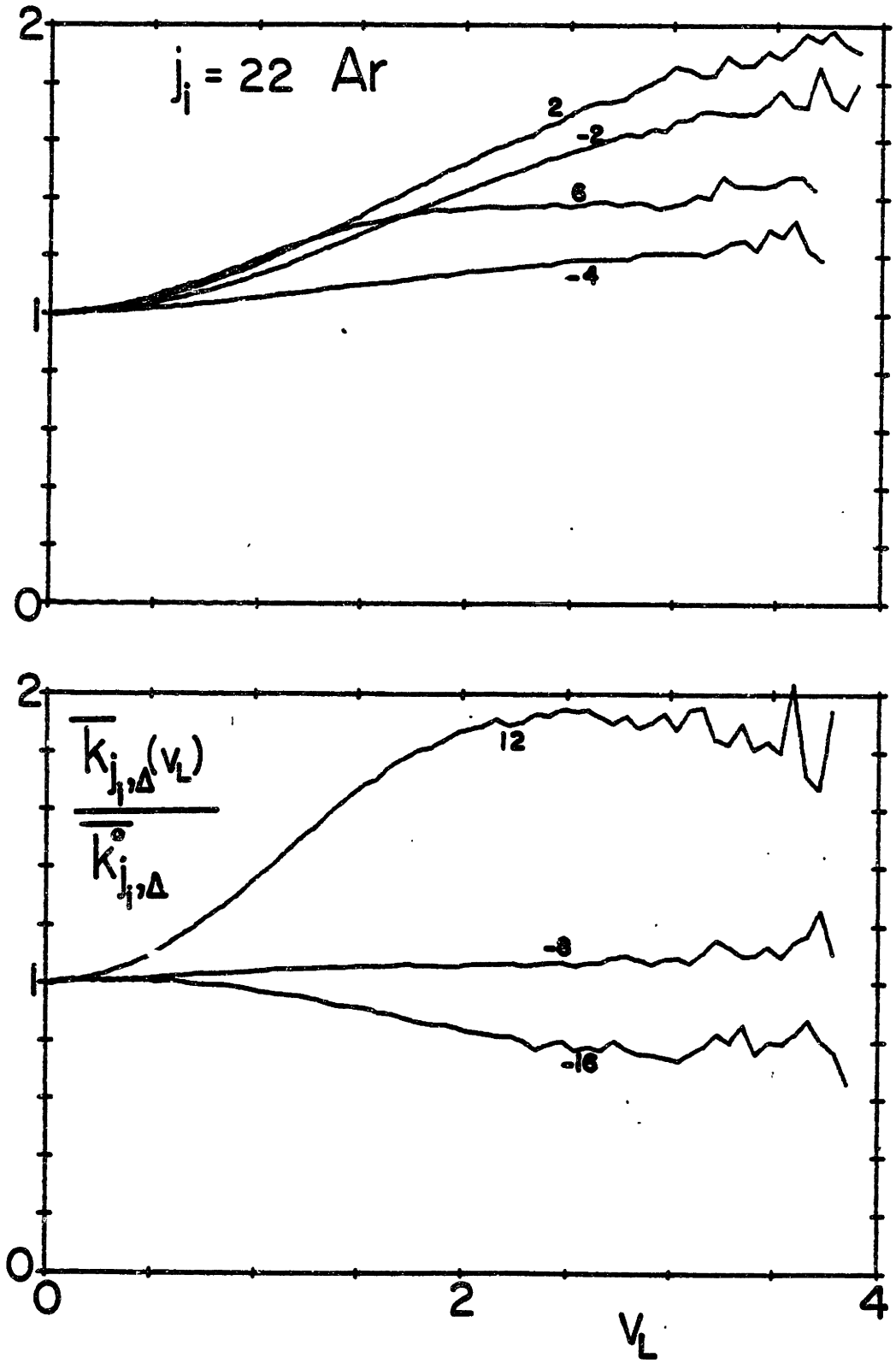

Fig. 12 Velocity averaged rate constants for j_i = 42, Ar.

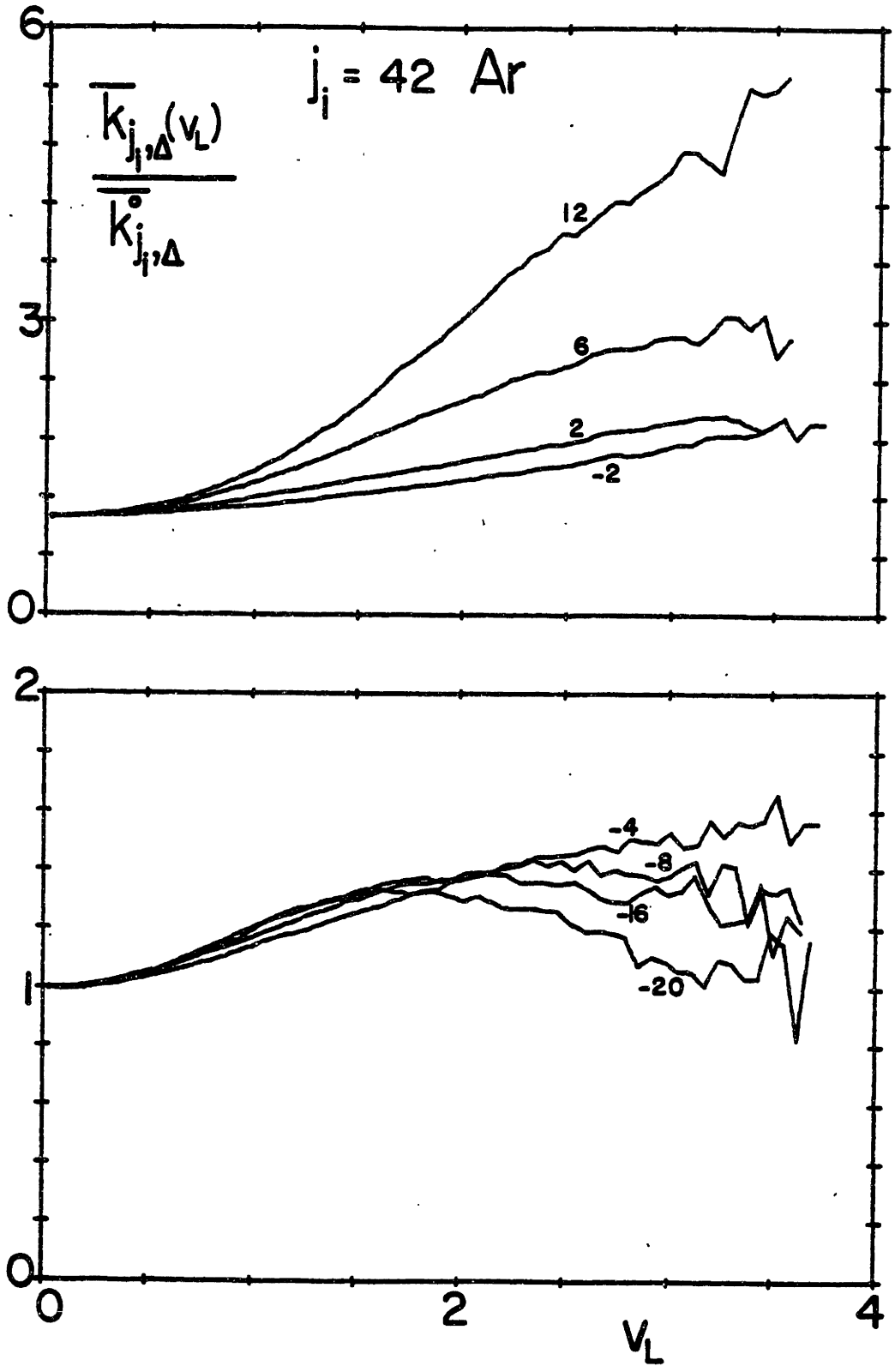

Fig. 13 Velocity averaged rate constants for j_i = 8, Ne.

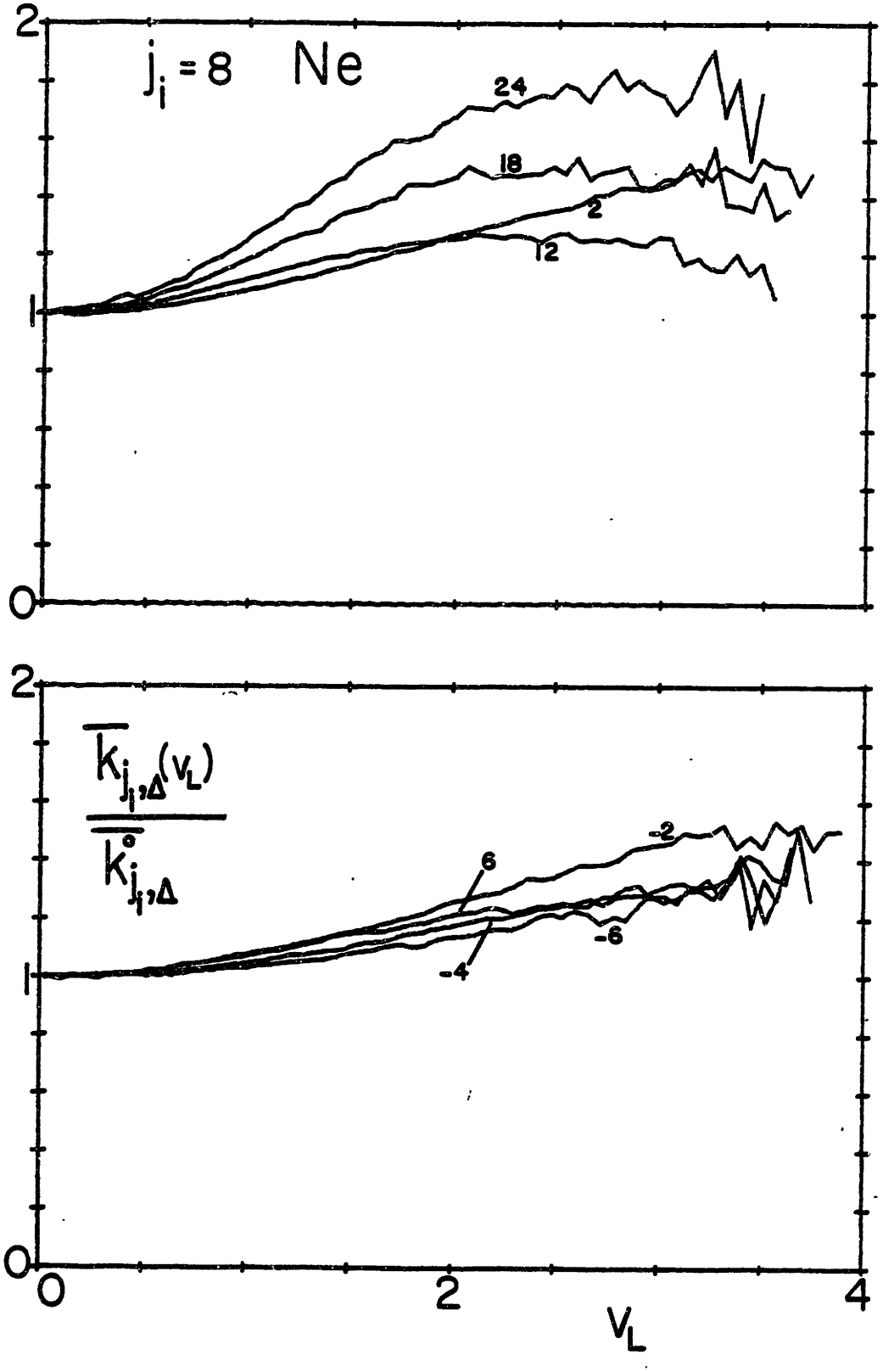

Fig. 14 Velocity averaged rate constants for j_i = 22, Ne.

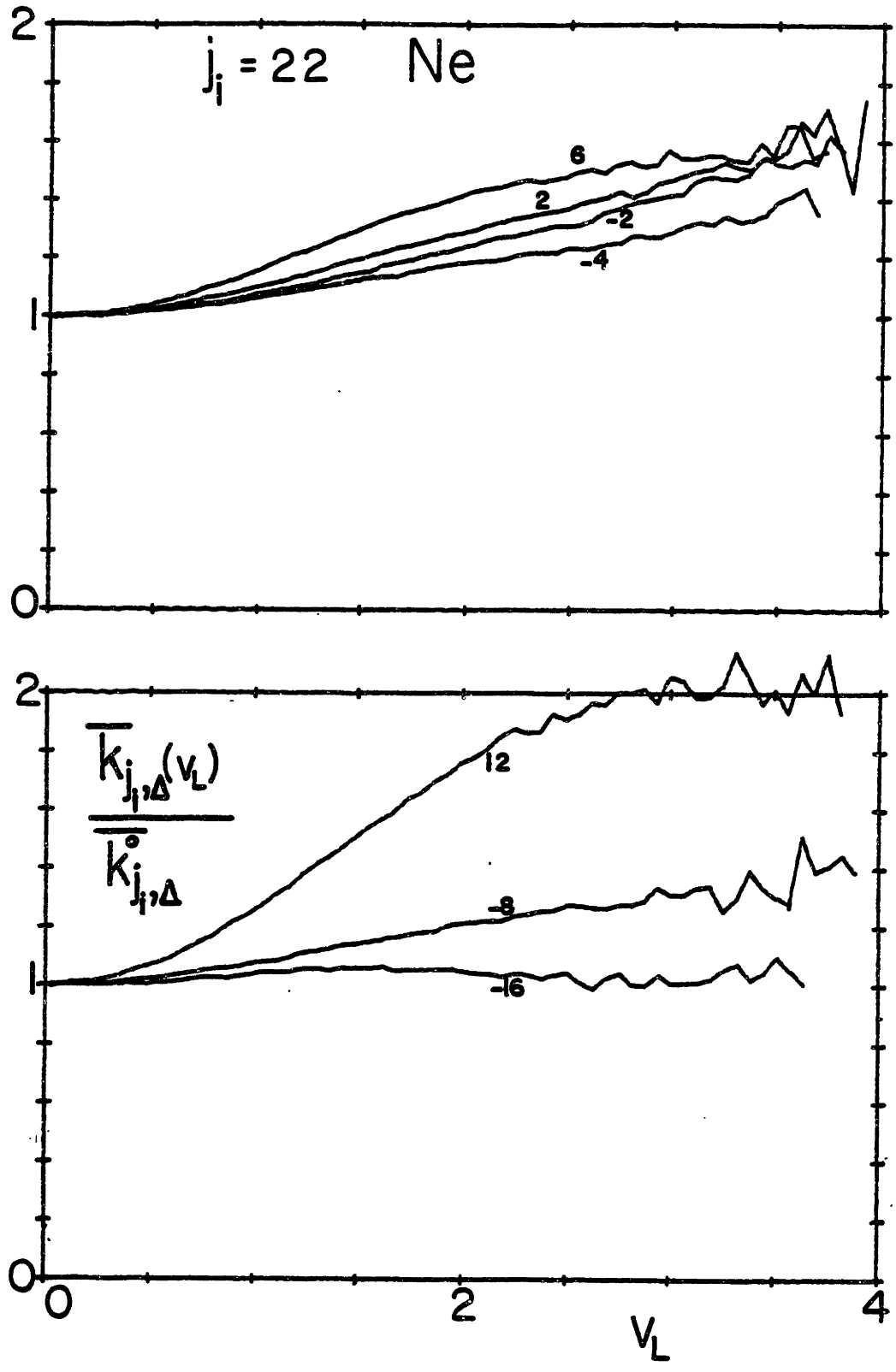

Fig. 15 Velocity averaged rate constants for j_i = 42, Ne.

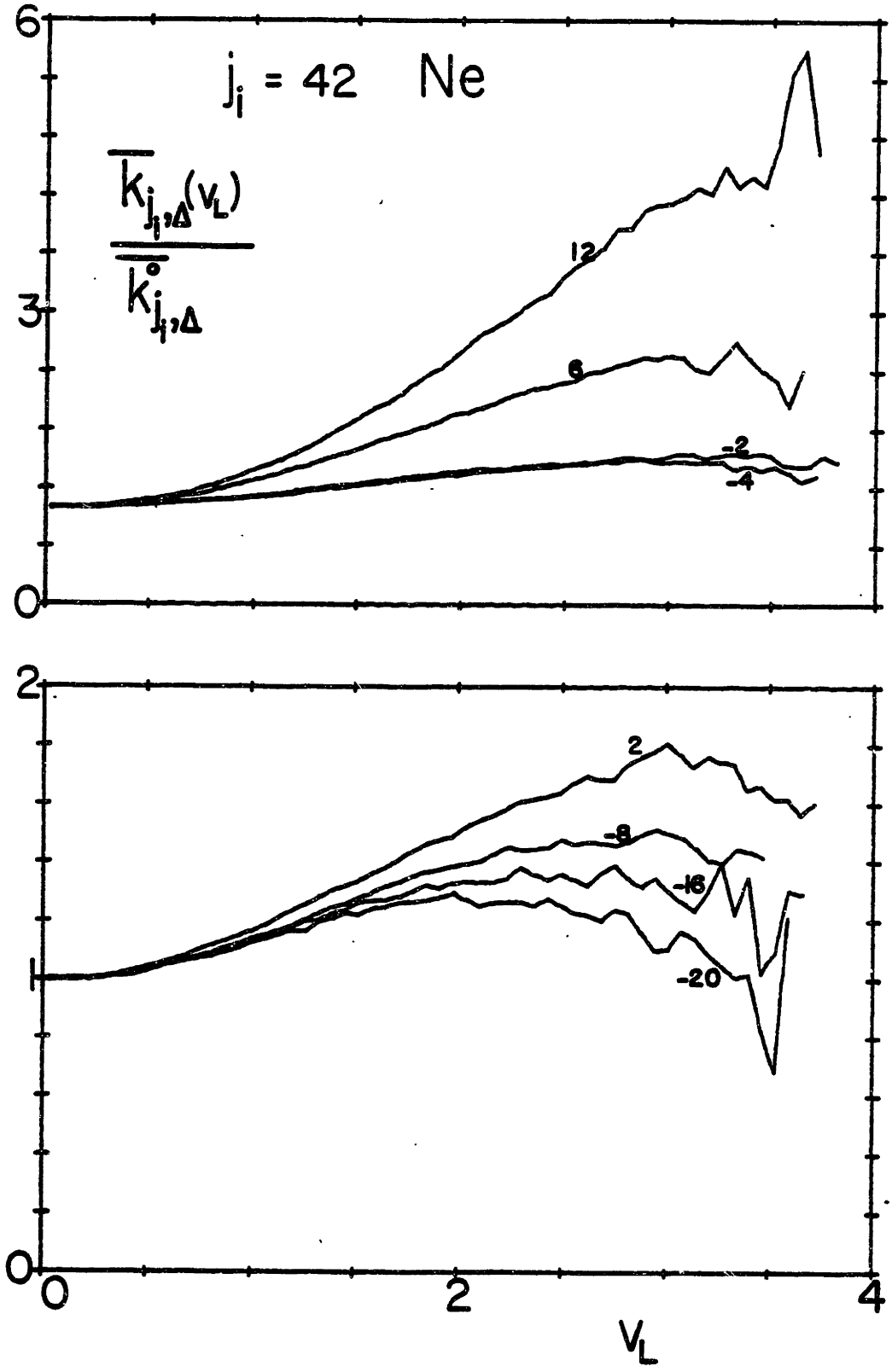

dramatic because this study covers a considerably greater range of Δ.

For the majority of j_i,Δ combinations the v_L dependence of $\overline{k}_{j_i,\Delta}(v_L)$ is not heavily dependent on the choice of rare gas target atom. There are however, a number of very noticable and interesting exceptions. An example is the $\overline{k}_{j_i,\pm2}(v_L)$, whose v_L dependence for Xe is markedly different than for Ar or Ne, the latter two being fairly similar. The rapid rise in $\overline{k}_{j_i,\pm2}(v_L)$ for Li_2^*-Xe, particularly for j_i = 22 and 42, is in fact a result of a $\sigma_{j_i,\pm2}(v_r)$ that strongly increases with v_r. This results, we believe, from a <u>reduction</u> of rotational <u>averaging</u> of the torque from the <u>long</u> range, <u>anisotropic</u> forces between Li_2^* and Xe at <u>large</u> impact parameters, as v_r increases relative to the rotational speed of Li_2^*. Thus, the $\overline{k}_{j_i,\pm2}(v_L)$ seem to give clear evidence of a large, significantly anisotropic long range Li_2^*-X potential, which is considerably stronger for X = Xe than Ar or Ne. The difference between Xe and Ar or Ne is perhaps more than expected based on measured[24] rare gas polarizabilities in the ratio of 27:11:3 for Xe, Ar, Ne respectively. This steeper rise in $\overline{k}_{j_i,\Delta}(v_L)$ for Xe, than for Ar or Ne, is also evident for Δ = -4 and +6, though to a smaller degree. On the other hand, the very steep rise in $\overline{k}_{42,12}(v_r)$ for all target atoms is probably the result of the <u>threshold</u> for this large j_i, large $+\Delta$ collision, which occurs for $v_r \approx 1.5$ and which significantly reduces $\overline{k}_{42,12}(v_L)$ at low v_L. The idea of "torque averaging" has been discussed elsewhere[25], and semi-quantitative discussion of the $\Delta = \pm2$ results will be given in

Another rather interesting example of target atom dependence is $\overline{k}_{22,-16}(v_L)$. For Xe and Ar this has a distinct maximum at v_L=0 while for Ne, there is a somewhat less distinct minimum. The data for Ar and Xe imply that $\sigma_{22,-16}(v_r) \sim v_r^{-p}$ with $p > 1$, since $\sigma(v_r) \propto v_r^{-1} \rightarrow k(v_r) =$ constant, which yields a constant flat $\overline{k}(v_L)$; the exponent "p" appears to be definitely greater for Xe, in comparison with Ar. Even for Ne, however, $\overline{k}_{22,-16}(v_L)$ is quite nearly flat, implying $\sigma_{22,-16}(v_r) \sim v_r^{-p}$ with p less than, but near 1 (with possible exception at very low v_r). This unusually rapid increase in $\sigma_{22,-16}(v_r)$ as $v_r \rightarrow 0$[26] (never observed previously) is not generally characteristic of large -Δ collisions, as can be immediately seen for the $\overline{k}_{42,-20}(v_L)$ for all three rare gas targets.

By far the most unusual target atom dependence of $\overline{k}(v_L)$ can be seen for the $j_i = 8$, $\Delta = -4, \pm 6$ data, where the $\overline{k}_{8,\Delta}(v_L)$ for Ar are much flatter than for the corresponding cases in either Xe and Ne. In particular, the $\overline{k}_{8,-6}(v_L)$ is maximal at $v_L = 0$ for Ar (similar to $\overline{k}_{22,-16}(v_L)$). Thus it is even qualitatively different from $\overline{k}_{8,-6}(v_L)$ for Ne, and even more so for Xe. (Similarly, for $\overline{k}_{22,-8}(v_L)$, the Ar data are considerably flatter than for Ne and Xe, which in fact appear rather similar). On the other hand, for $j_i = 8$, $\Delta = +12, +18, +24$, the Ar and Xe data are quite similar, with Ne also sharing similar characteristics,

only not decreasing at larger v_L as rapidly as for Ar, Xe.

The above observation is unexpected in that intuitively one would expect the Ar data for $\bar{k}_{j_i,\Delta}(v_L)$ to behave as an intermediate between Ne and Xe, since Ar lies roughly midway between Ne and Xe in both mass and polarizability. For the majority of the j_i,Δ cases, this seems to hold true, at least roughly speaking. Perhaps only for the case $j_i = 42$ does the Ar data resemble that of Ne distinctly more than that of Xe.

We point out that an excellent example of the Lorentz tail correction can be seen by comparing the shape for $v_L > 3$ of the $j_i = 22$, $\Delta = -2$ intensity ratio R_Δ of fig. 5 (prior to correction), and the Lorentz tail corrected $\bar{k}_{22,-2}(v_L)$ in fig. 8. The turning down of R_Δ for $v_L \gtrsim 3.5$ is just as expected based on eqs. 7. We also point out however that this is a somewhat extreme example. The Lorentz tail correction is usually considerably smaller for most other j_i,Δ.

Finally, we have up until now negected considering <u>elastic</u> velocity changing collisions between Li_2^*-X which might limit the velocity selectivity of VSDS. Collisions which <u>substantially</u> change $\vec{v}_p$ <u>prior</u> to RI collisions must require hard, short range interactions whose rate constants we expect to be similar in size to the $\bar{k}_{j_i,\Delta}$ for larger $|\Delta|$, i.e. $\sim 10 \times 10^{-13}$ cm^3/sec. For $p_t = 1.$ torr, these type collisions occur only $\sim .01$ times per lifetime, a seemingly negligable effect. The widely different, non-flat v_1 dependences seen in figs. 7-15, and the success of our deconvolutions to resolve known thresholds (discussed next section) give (we believe) solid empirical "proof" that VSDS velocity selection is working well.

6. Results for $\sigma_{j_i,\Delta}(v_r)$

We now turn our attention to, and present the deconvoluted results for the absolute RI cross-sections $\sigma_{j_i,\Delta}(v_r)$ for Li_2^*-Xe, Ar, Ne, which are at the heart of this experimental investigation. The large range and number of j_i and Δ covered by our measurements, as well as the widely different velocity dependences and magnitudes of the $\sigma_{j_i,\Delta}(v_r)$ make brief yet clear informative presentation of these data a very difficult task. We have chosen to present the deconvoluted $\sigma_{j_i,\Delta}(v_r)$ grouped by target gas, j_i, and (usually) the sign of Δ. Many results have been scaled by convenient factors as indicated, to provide a more graphic presentation of the v_r dependence of the smaller magnitude cross-sections, while still allowing a choice of σ (y axis) scale large enough to include the larger $\sigma(v_r)$. These scale factors generally divide the scale of the σ axis integrally or half-integrally to provide easy ability to read cross-section magnitudes from the graphs.

Although we present continuous curves for all results (calculated from eq. 17), it is perhaps worth pointing out that it is the <u>value</u> of $\sigma(v_r)$ at any v_r which has <u>physical</u> meaning and in which we have confidence. It <u>cannot</u> be assumed that higher derivatives $\frac{d^n\sigma(v_r)}{dv_r^n}$ are accurately represented by these deconvolution curves. The slope $\frac{d\sigma(v_r)}{dv_r}$ should usually be semi-quanitatively correct (best for Xe, worst for Ne) with a possible <u>exception</u> at or near the endpoints $v_r \approx .7$ or $v_r \approx 4$. Slow, small amplitude wiggles or oscillations which are either

noise induced or result from convergence problems of the finite polynomials are generally easily distinguishable from real maxima-minima; the size of the 3 representative error bars usually given will clarify the above cases and points.

To avoid confusion, we emphasize that the error bars shown are not data points. They are presented to display the approximate magnitude and v_r dependence of the estimated uncertainty in our continuous (in v_r) deconvolved results for $\sigma_{j_i,\Delta}(v_r)$ - see sec. III.4.7 for further discussion on the choice of error bars. We also point out that all deconvolution curves are additionally subject to an overall normalization error due to uncertainty in the absolute magnitude of the $\overline{K}^o_{j_i,\Delta}$ - see table III.2 and eq. 14.

For discussion purposes, we will concentrate most of the attention on the Li_2^*-Xe results. In our opinion these are the most interesting. They are also the results for which deconvolutions have the best resolution (as discussed in III.4.8) and reliability. Results for Ar and Ne will be commented on mainly to the extent that they exhibit interesting differences from the Xe results or from each other.

$$j_i = 8$$

Xe

Considering fig. 16, we see that the $\sigma_{8,\pm2}(v_r)$ are quite similar, with a rapid rise for $v_r < 1$, a broad roughly flat plateau for $1.5 < v_r < 3$, and a slow but definite fall-off for $v_r > 3$. This v_r dependence

Fig. 16 RI cross-sections for j_i = 8, Xe as a function of relative velocity.

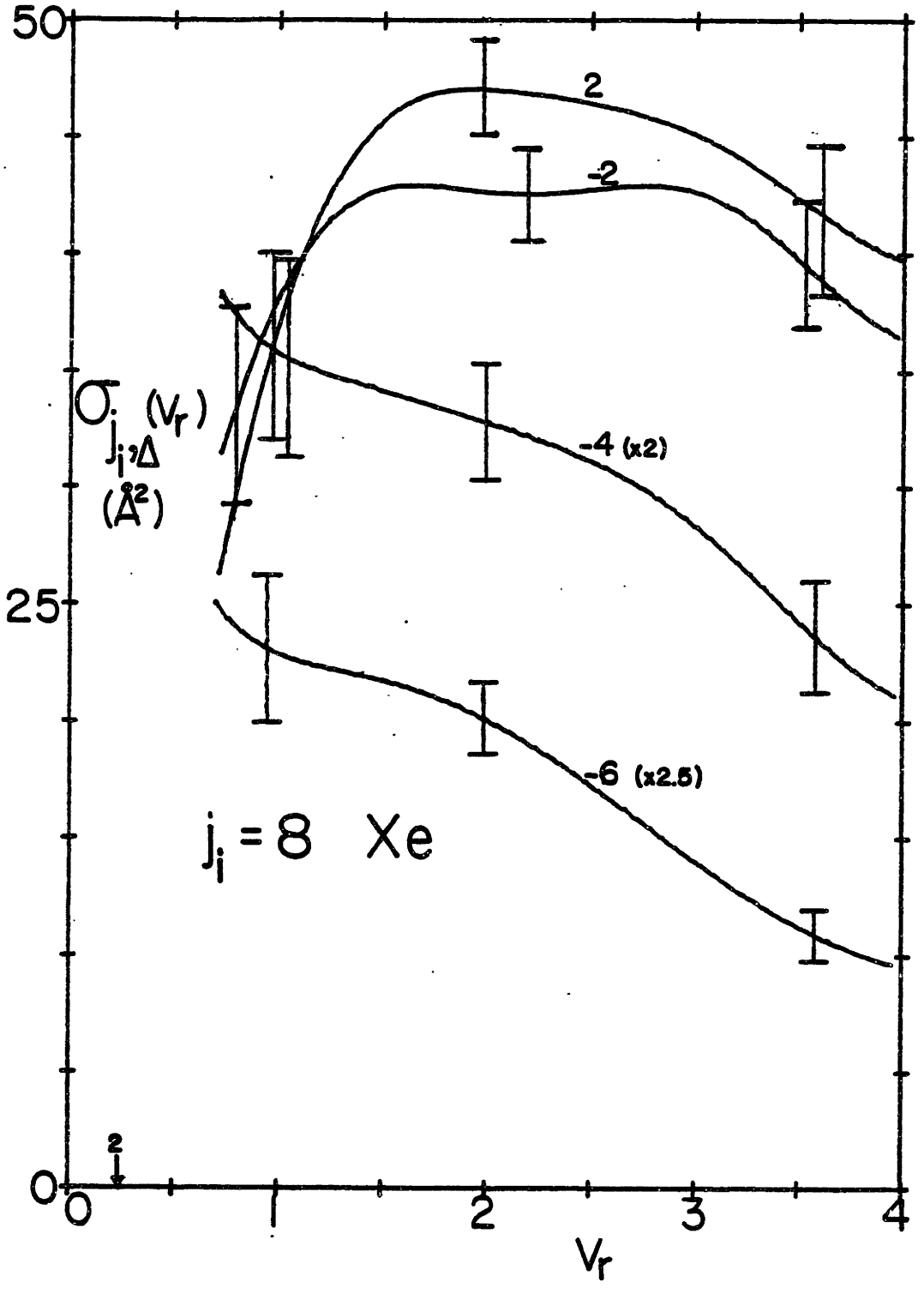

Fig. 17 RI cross-sections for j_i = 8, Xe as a function of relative velocity.

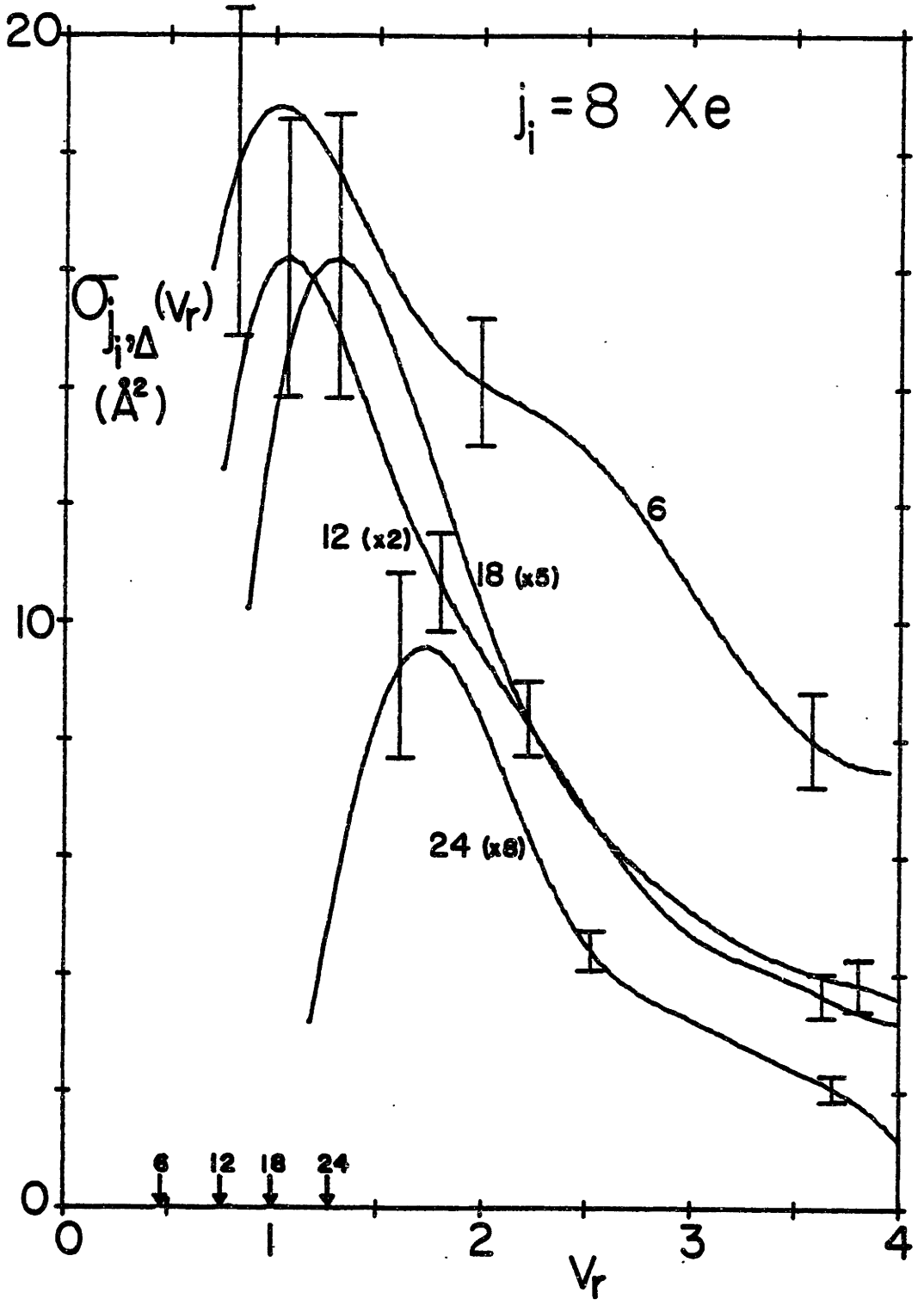

can in fact be explained on the basis of dominant long range (R^{-6}) interactions. The rapid increase results from the decrease in "torque averaging" as v_r increases relative to an approximately constant rotational speed (as discussed in III.5), and the decrease with v_r at large v_r (in the rotationally "sudden" limit) going like $v_r^{-2/5}$. (We will discuss the $|\Delta| = 2$ cases in more quantitative detail in chap. IV). The $\sigma_{8,\pm2}(v_r)$ are remarkably large, being close to 50 $Å^2$ each over the flat regions. The $\sigma_{8,-4}(v_r)$ and $\sigma_{8,-6}(v_r)$ appear similar in v_r behavior, though $\Delta = -6$ is definitely decreasing more rapidly with v_r, roughly like v_r^{-1} for $v_r > 2$.

The $\sigma_{8,+\Delta}(v_r)$ of fig. 17 all appear to have the characteristic of a very rapid rise after threshold velocity v_{th} (indicated by arrows just above the v_r axis), followed by a varingly rapid decrease with increasing v_r. Our deconvolutions reveal the threshold behavior in the curves for $\Delta = \pm18, +24$ even though we have not constrained the results. $\sigma_{8,24}(v_r)$ actually re-crosses zero at $v_r \simeq .5$ (not shown) in an attempt to "hug" or oscillate about $\sigma=0$.) The deconvolutions are positive for some $v_r < v_{th}$, but this is certainly not unexpected given the very sharp rising behavior and finite resolution ($\delta v_r \simeq .4$) of the deconvolution method. We expect that the peak heights for $\sigma_{8,+\Delta}(v_r)$ ($\Delta \geq 6$) are likely to be a lower bound to the real values because of smoothing due to finite resolution. Even so, the $\sigma_{8,+\Delta}(v_r)$ exhibit a sharp fall-off with v_r after the maxima, the rapidity of which increases strongly with

increasing Δ; for $2 < v_r < 4$, $\sigma_{8,6}(v_r) \propto v_r^{-1}$, while $\sigma_{8,24}(v_r) \propto v_r^{-3}$. (The exponent "3" from $\sigma_{8,24}(2) \div \sigma_{8,24}(4) \simeq 7 \propto 2^3$.) A possible explanation for these sharply decreasing cross-sections is that as v_r increases, more large +Δ channels become energetically possible, decreasing the probability of transfer to any single j_f level. This v_r dependence may also be evidence of more VRI collisions occuring at higher velocity, which reduce the pure RI cross-secion.

Ar,Ne

For $\Delta > 12$, the Ar and Ne results (figs. 19,21) are similar to Xe in both v_r dependence and magnitude, with maxima shifted to slightly higher v_r (v_{th} is larger as a consequence of the smaller reduced mass). They are also somewhat broader, especially in Ne, due at least in part to the lower resolution δv_r. For $\Delta = +6$, we have the anomolous behavior discussed in III.5. Ne qualitatively resembles Xe (the rise in $\sigma_{8,6}(v_r)$, $v_r > 3$ for Ne is probably a deconvolution artifact), while Ar shows no maximum at all, behaving roughly $\propto v_r^{-1}$ for all $v_r > .7$.

In figs. 18,20 we again see this anomolous behavior. Results for all Δ decrease more rapidly with v_r for Ar than for Ne. The $\Delta = -4, -6$ results increase with decreasing v_r much more rapidly than for Xe. The $\Delta = \pm 2$ results do not show the behavior of Xe which we attributed to long range interactions. Instead they decrease approximately monotonically with increasing v_r, with a significantly diminishing magnitude in going from Xe → Ne as expected. Ar decreases anomolously faster at

Fig. 18 RI cross-sections for $j_i = 8$, Ar as a function of relative velocity.

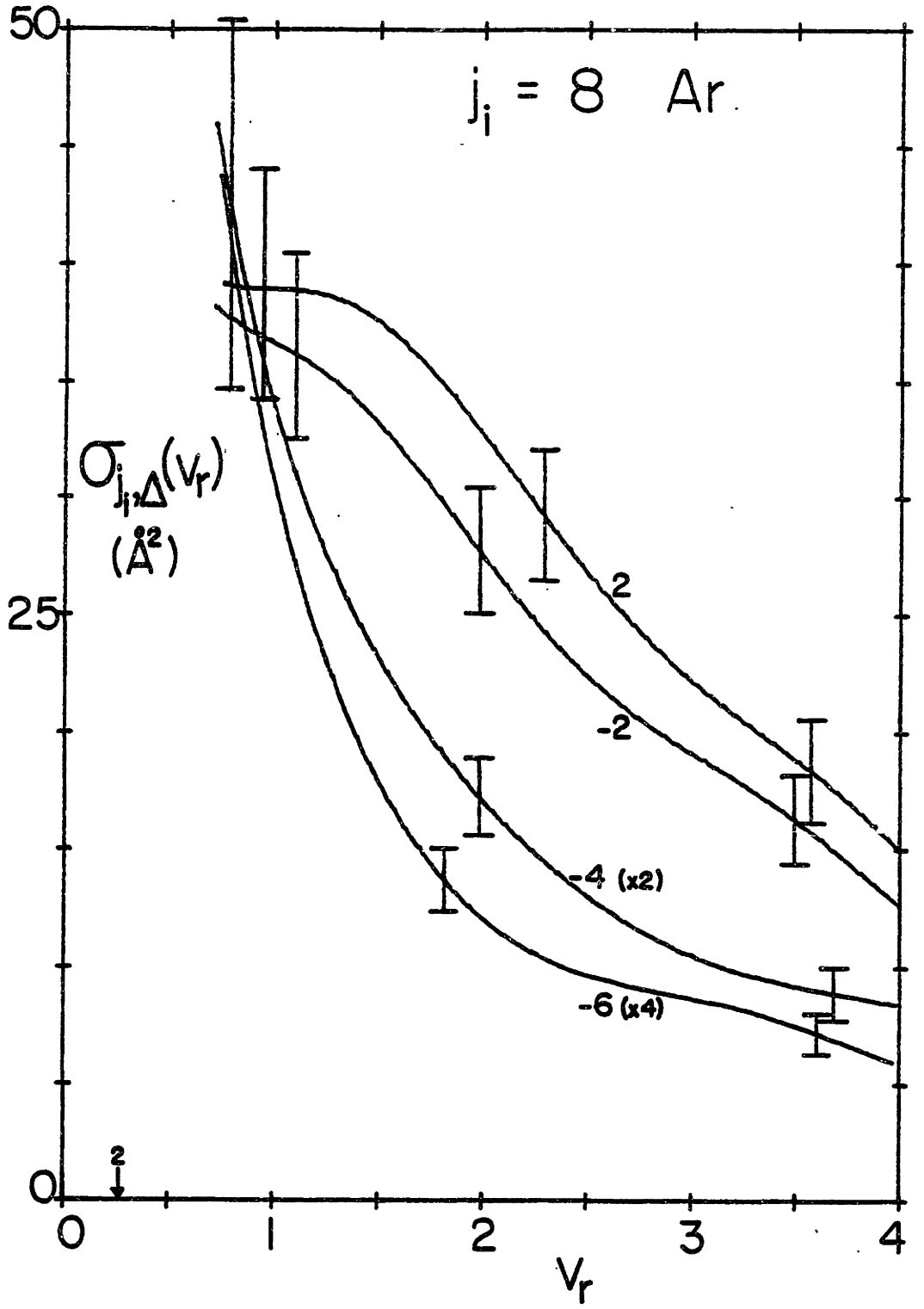

Fig. 19 RI cross-sections for j_i = 8, AR as a function of relative velocity.

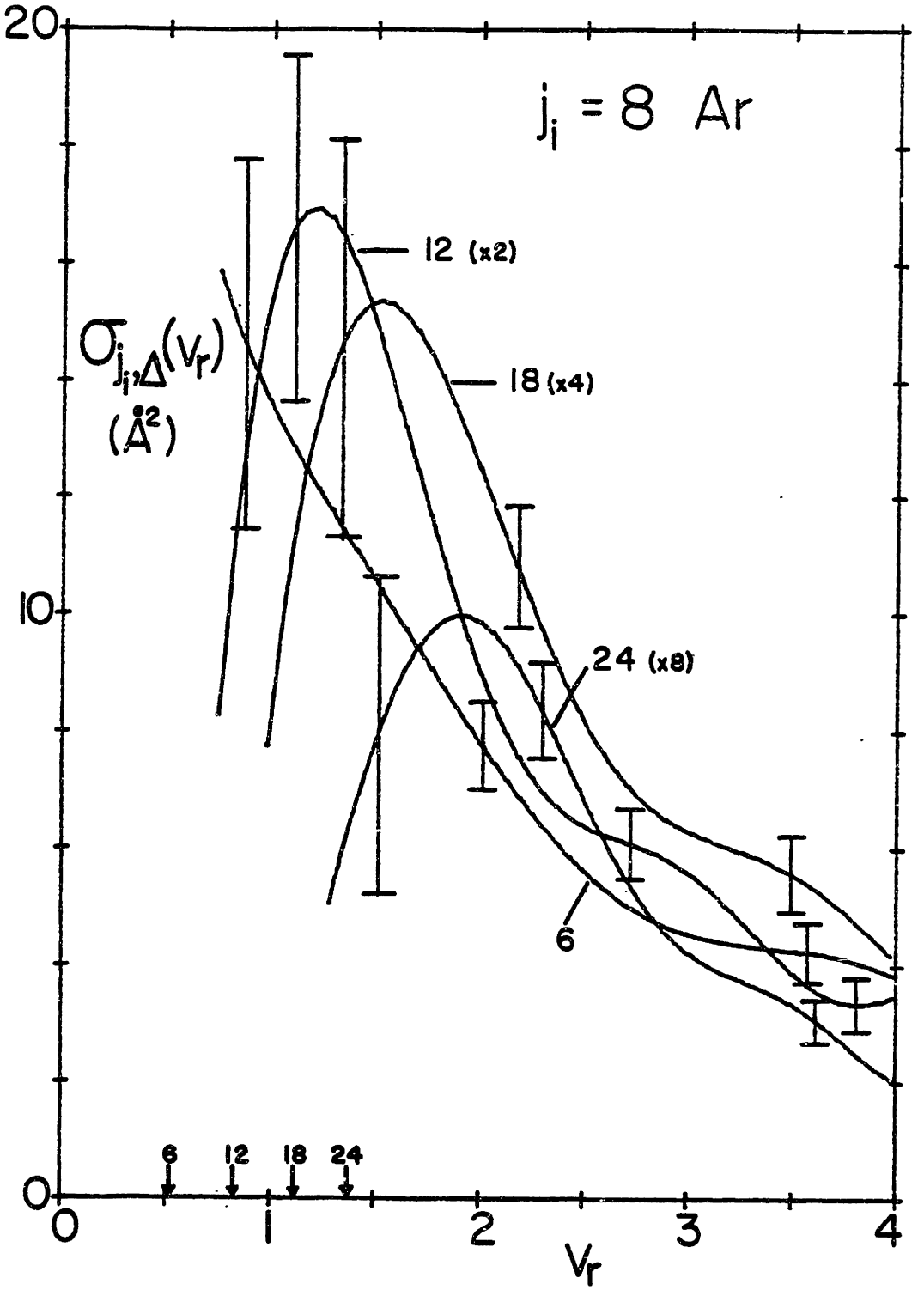

Fig. 20 RI cross-sections for j_i = 8, Ne as a function of relative velocity.

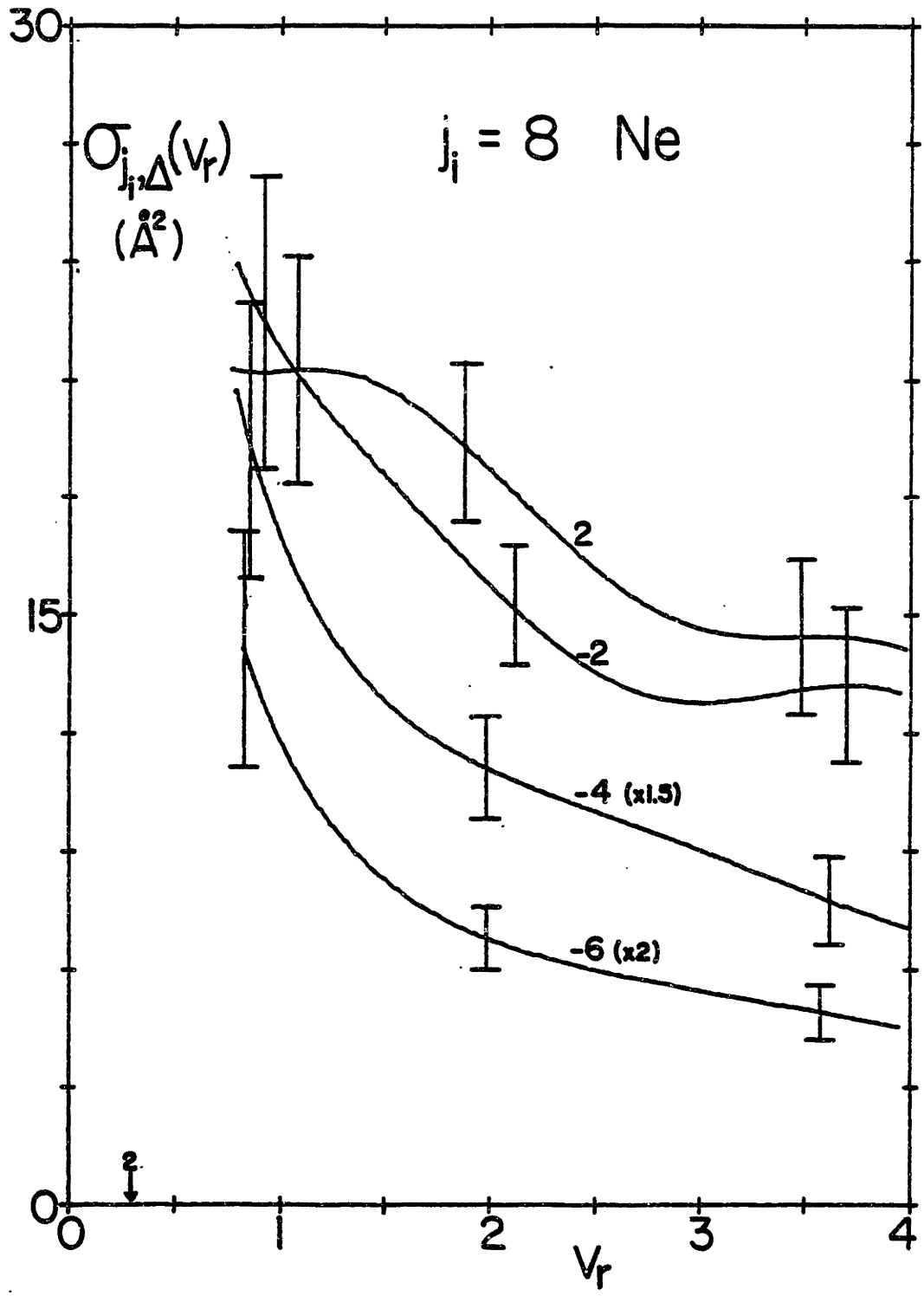

Fig. 21 RI cross-sections for j_i = 8, Ne as a function of relative velocity.

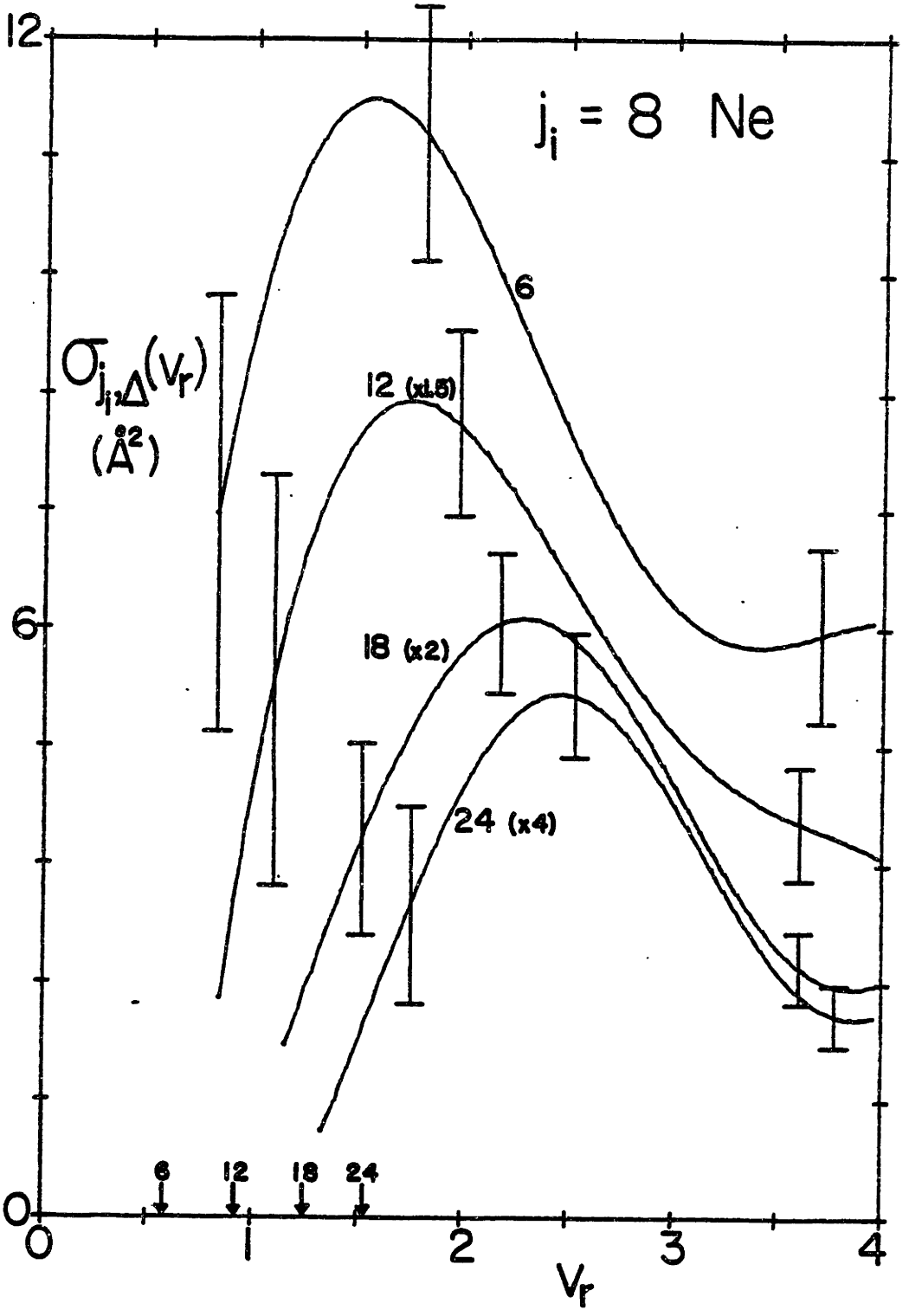

larger v_r than does Ne. (This latter conclusion can be confirmed from inspection of the $\bar{K}_{8,\pm2}(v_L)$). We have not found any simple explanation for this behavior.

$$j_i = 22$$

Xe

The $\sigma_{22,\Delta}(v_r)$ for Xe are perhaps the most interesting results obtained in the present Li_2^*-X study, exhibiting the widest variation in size and shape of the $\sigma_{j_i,\Delta}(v_r)$ with v_r and Δ. The shapes of the $\sigma_{22,\pm2}(v_r)$ (figs. 22,23) are unique amoung our measured cross-sections. They show a dramatic rise (by a factor of > 3) in cross-section with increasing v_r for $v_r < 3$. This is a beautiful example of what we belive is the long range "torque averaging" effect which will be discussed further in chap. IV. The $\sigma_{22,-4}(v_r)$ (fig. 23) also shows what might be a slight trace of this behavior. It has a steady but slow rise for $v_r >$ .7, peaking at $v_r \approx 2.5$, and then slowly rolls off with increasing v_r. The $\Delta = +6$ (fig. 22) cross-section is an even more subtle example of this behavior, rising rapidly after threshold to a roughly flat plateau, (like $\sigma_{8,-2}(v_r)$ -Xe) with a slow fall-off for $v_r > 3$. The fact that this behavior is so much less pronounced for $\Delta = -4$ or $\Delta = +6$ than for $\Delta = \pm2$, as well as the fact that the peak values for $\sigma_{22,\pm2}(v_r)$ are so much larger than σ for $\Delta = -4$ or +6 is strong evidence that (at least for $v_r \gtrsim 2$) essentially <u>only</u> $|\Delta| = 2$ collisions are occuring at large impact parameters ($\gtrsim$ 7Å - see chap. IV). The large impact parameter

Fig. 22 RI cross-sections for j_i = 22, Xe as a function of relative velocity.

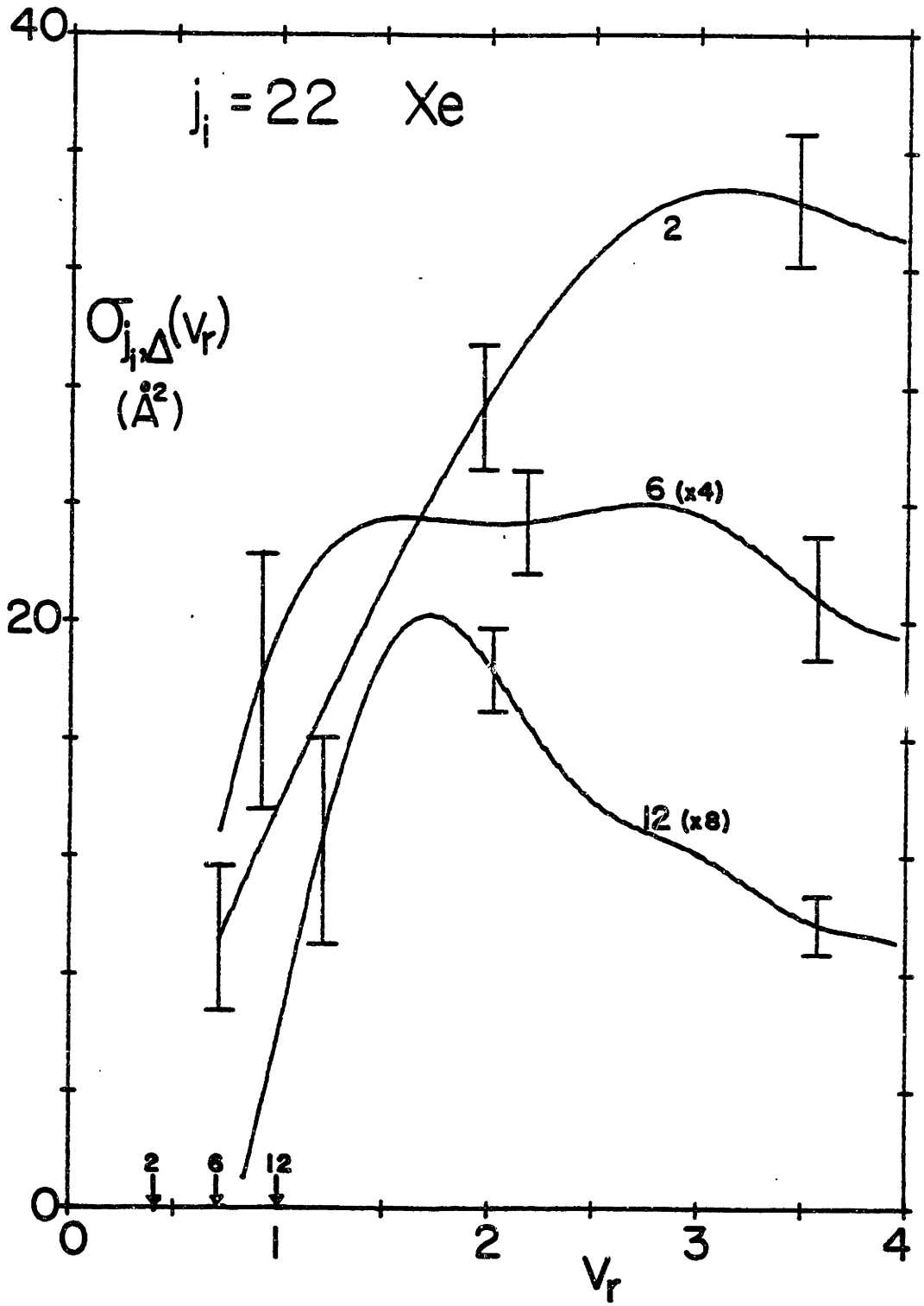

Fig. 23 RI cross-sections for j_i = 22, Xe as a function of relative velocity.

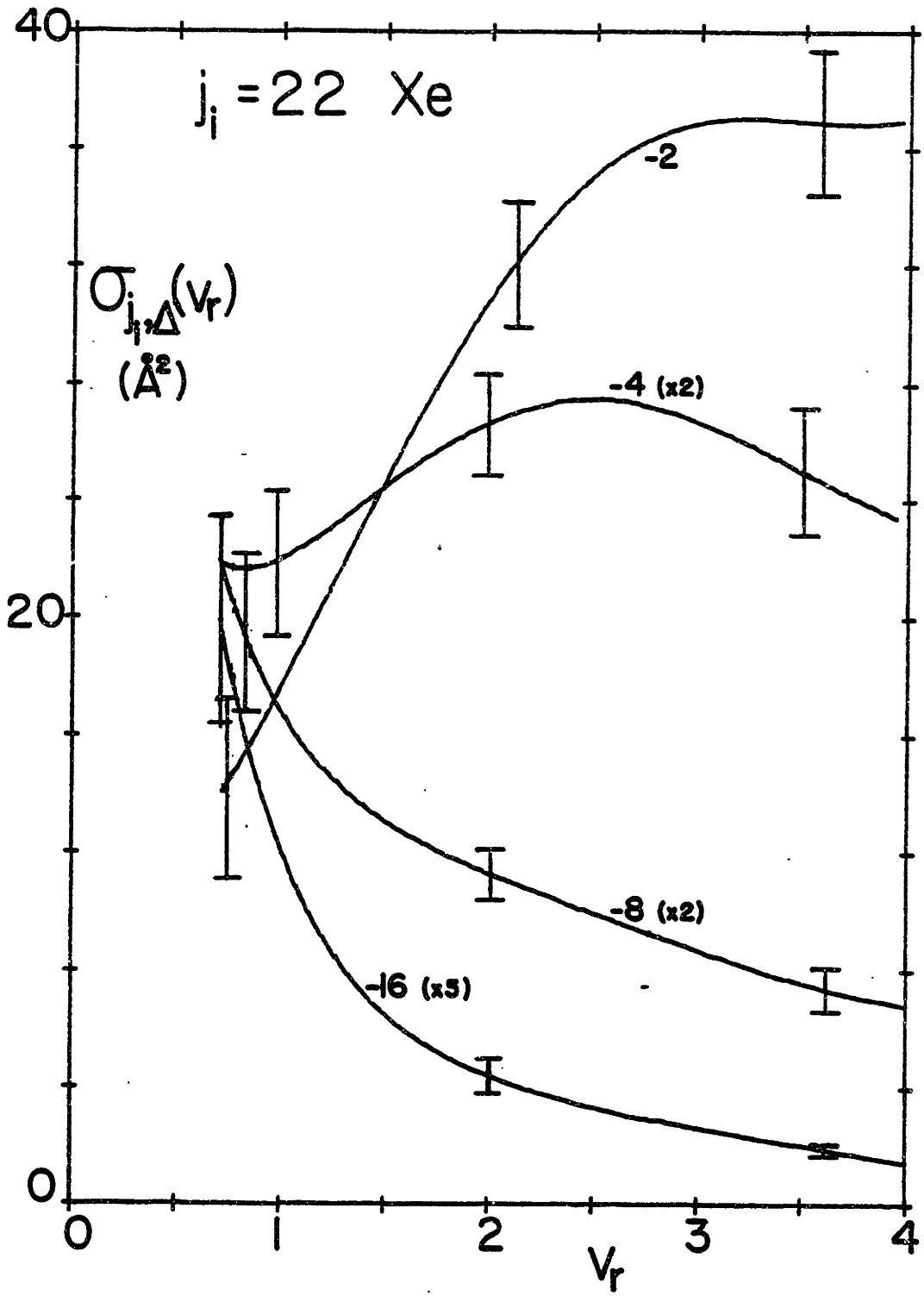

collisions result in large cross-sections and should be the the ones for which torque averaging of long range forces becomes important. The behavior of $\sigma_{22,12}(v_r)$ with v_r (also fig. 22) is in fact quite similar to that of the large $+\Delta$ cross-sections for $j_i = 8$, with the characteristic rapid rise for $v_r > v_{th}$ ($v_{th} = 1.0$ here, and is nicely resolved by the natural deconvolution), and then the sharp fall-off for larger v_r, in this case $\sim v_r^{-1}$ similar to $\sigma_{8,12}(v_r)$, and for probably the same reasons (see discussion of $j_i = 8$ $\Delta > 6$, Xe).

Fig. 23 also displays results for $\sigma_{22,-8}(v_r)$ and $\sigma_{22,-16}(v_r)$, both of which show a dramatic increase in cross-section as v_r decreases for <u>all</u> recoverable v_r. For $.7 \leq v_r \leq 4$, we find $\sigma_{22,-8}(v_r) \sim v_r^{-2/3}$ and $\sigma_{22,-16}(v_r) \sim v_r^{-3/2}$. These power law exponents were simply estimated by ratios of $\sigma(v_r=.7) \div \sigma(v_r=4)$, but they do give a fairly accurate description of the functional dependence on v_r over the velocity range measured. A simple plausible explanation for the v_r dependence of $\sigma_{22,-8}(v_r)$ can be given by noting that for a long range R^{-6} attractive potential (realistic for Li_2^*-X) the cross-section for overcoming the centrifugal barrier ($\propto R^{-2}$) may be straightforwardly shown to vary as $v_r^{-2/3}$; once overcoming the centrifugal barrier, the Li_2^* and Xe can then experience the forces of their strong, short range repulsive interaction potential, which must be responsible for most or all of the larger Δ collisions.

This simple picture should also apply to the $\Delta = -16$ case, which in

fact varies more rapidly with v_r by near a full power of v_r^{-1}. This large difference between $\sigma_{22,-8}(v_r)$ and $\sigma_{22,-16}(v_r)$ is not attributable to a deconvolution error or artifact, as is clearly shown by comparison of $\bar{k}_{22,-8}(v_L)$ and $\bar{k}_{22,-16}(v_L)$ in fig. 23; as discussed in III.5, $\bar{k}_{22,-16}(v_L)$ shows that $\sigma_{22,-16}(v_r)$ must vary significantly more rapidly than v_r^{-1}. It is apparent then, that the unusually dramatic v_r dependence of $\sigma_{22,-16}(v_r)$ must have its origin in more complicated dynamical effects than simply crossing a centrifugal barrier. It may result in part from closing (at low v_r) of other T-R as well as T-V channels, together with the fact that for small v_r the large increase in final translational energy accompanying large negative Δ RI collisions significantly increases the relative final density of translational states - see also discussion for Ar,Ne $j_i = 22$, $\Delta = -16$. Finally, we point that our deconvolution method is unable to determine whether this v_r^{-p}, $p > 1$ behavior continues as $v_r \to 0$.

Ar,Ne

For the $j_i = 22$ data, the Ar and Ne results are distinguishable from each other, as well as from Xe results. For $\Delta = +6, +12$, the Ar, Ne results are, however, fairly similar. Maxima for Ne occur at larger v_r than for Ar (or Xe, as generally tends to be the case whenever a maximum occurs for all 3 target gases); for both gases the $\sigma_{22,6}(v_r)$ falls $\sim v_r^{-1}$ for $v_r > 2$. This is significantly different from $\Delta = +6$ results

Fig. 24 RI cross-sections for j_i = 22, Ar as a function of relative velocity.

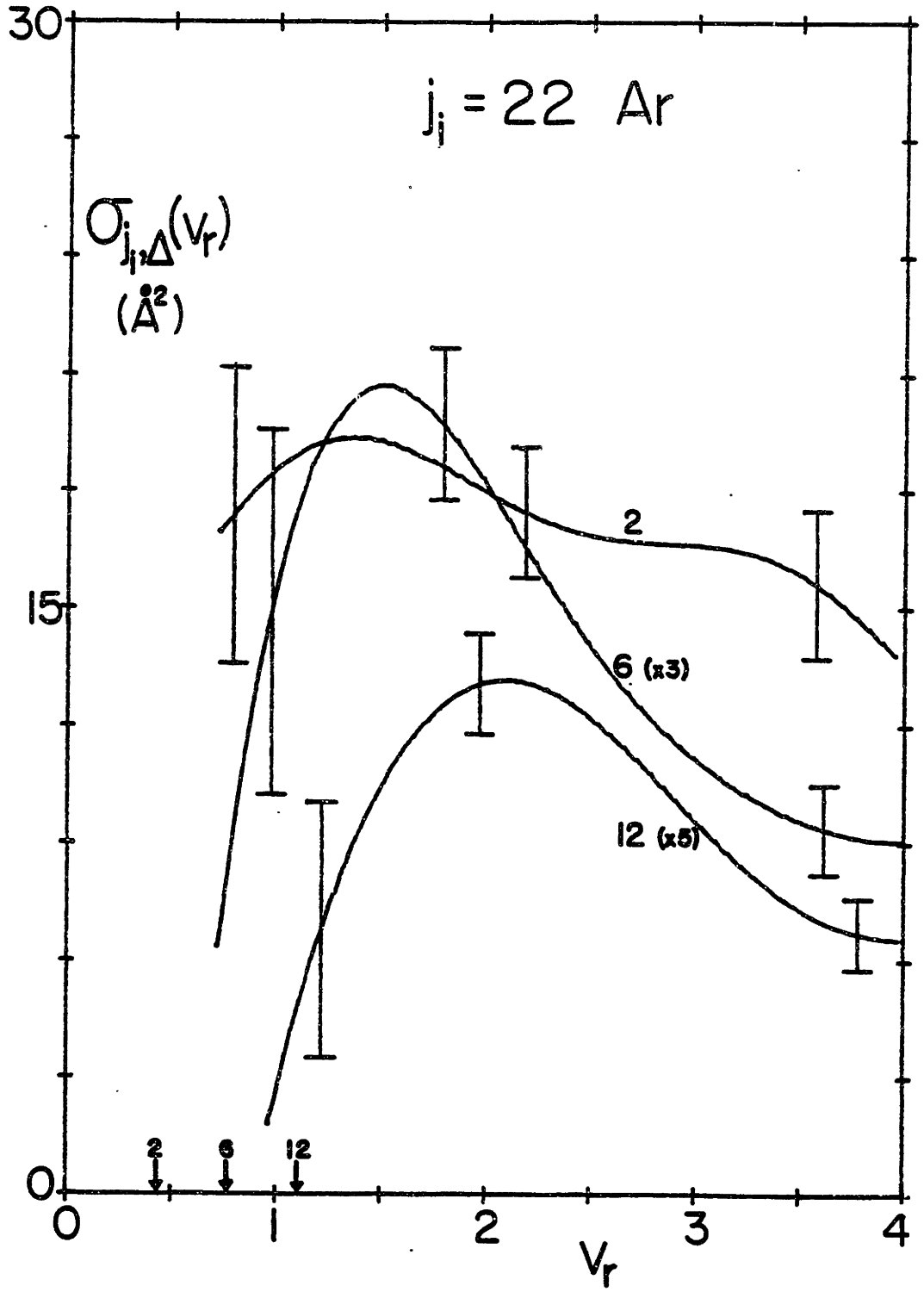

Fig. 25 RI cross-sections for j_i = 22, Ar as a function of relative velocity.

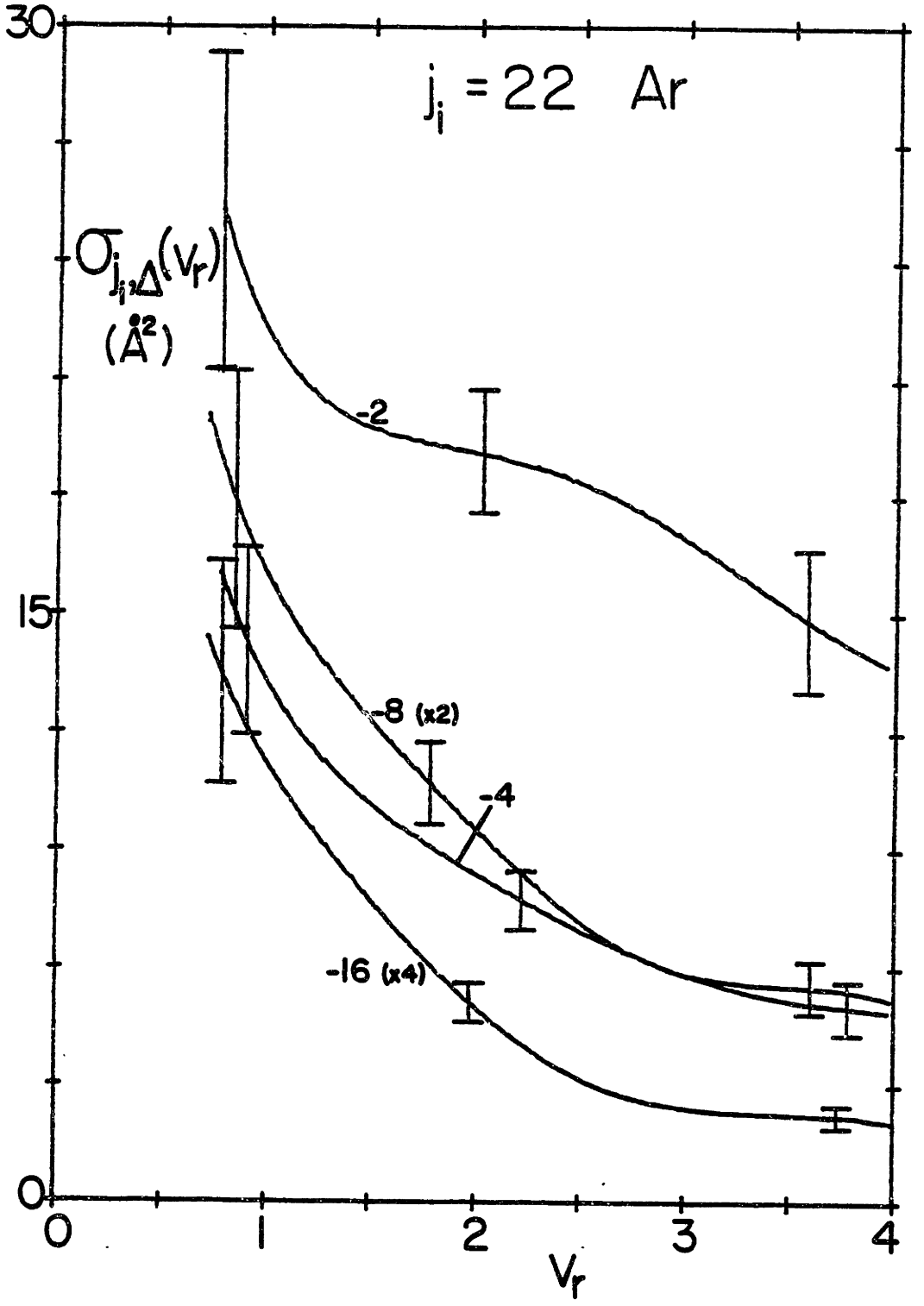

Fig. 26 RI cross-sections for j_i = 22, Ne as a function of relative velocity.

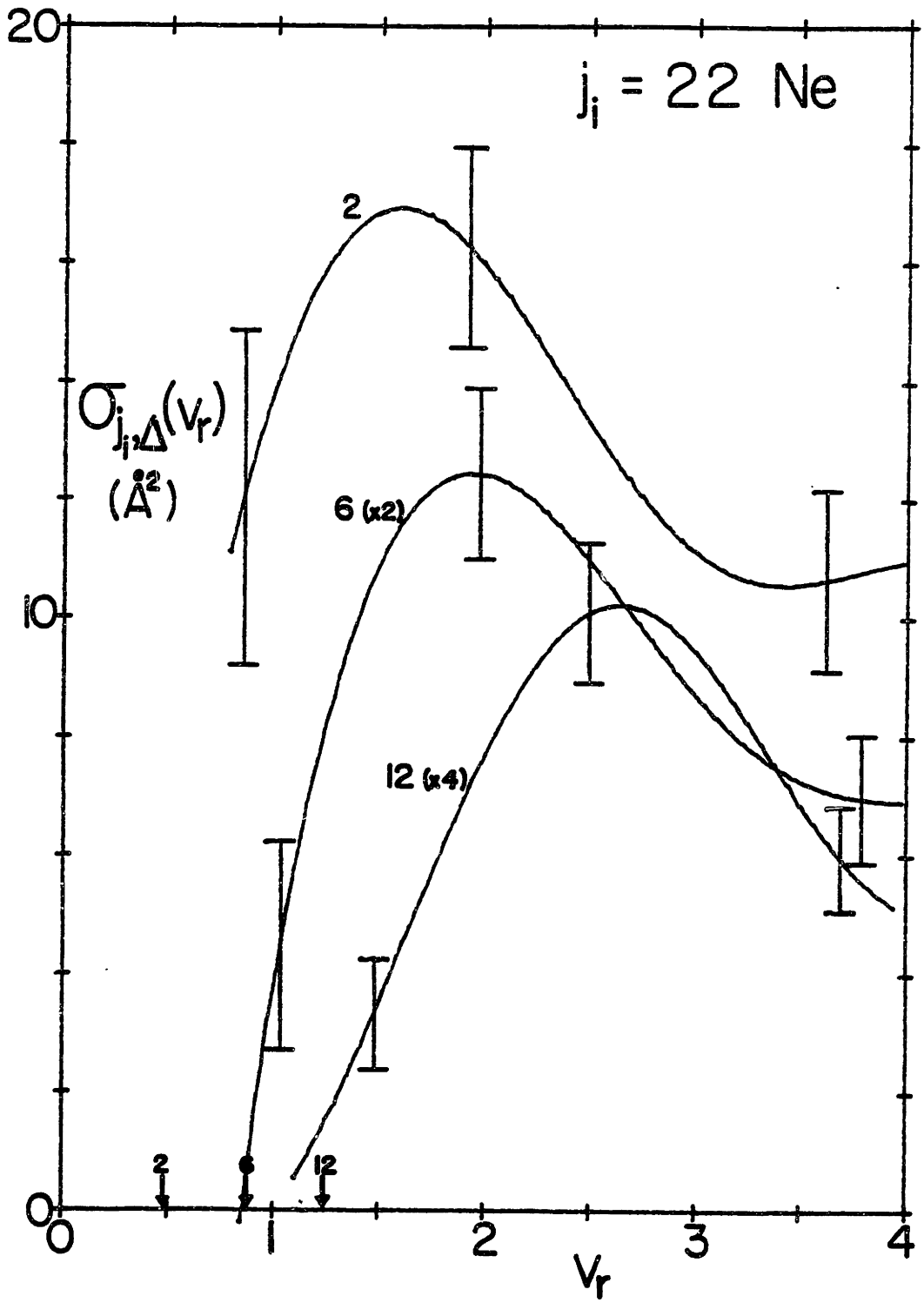

Fig. 27 RI cross-sections for j_i = 22, Ne as a function of relative velocity.

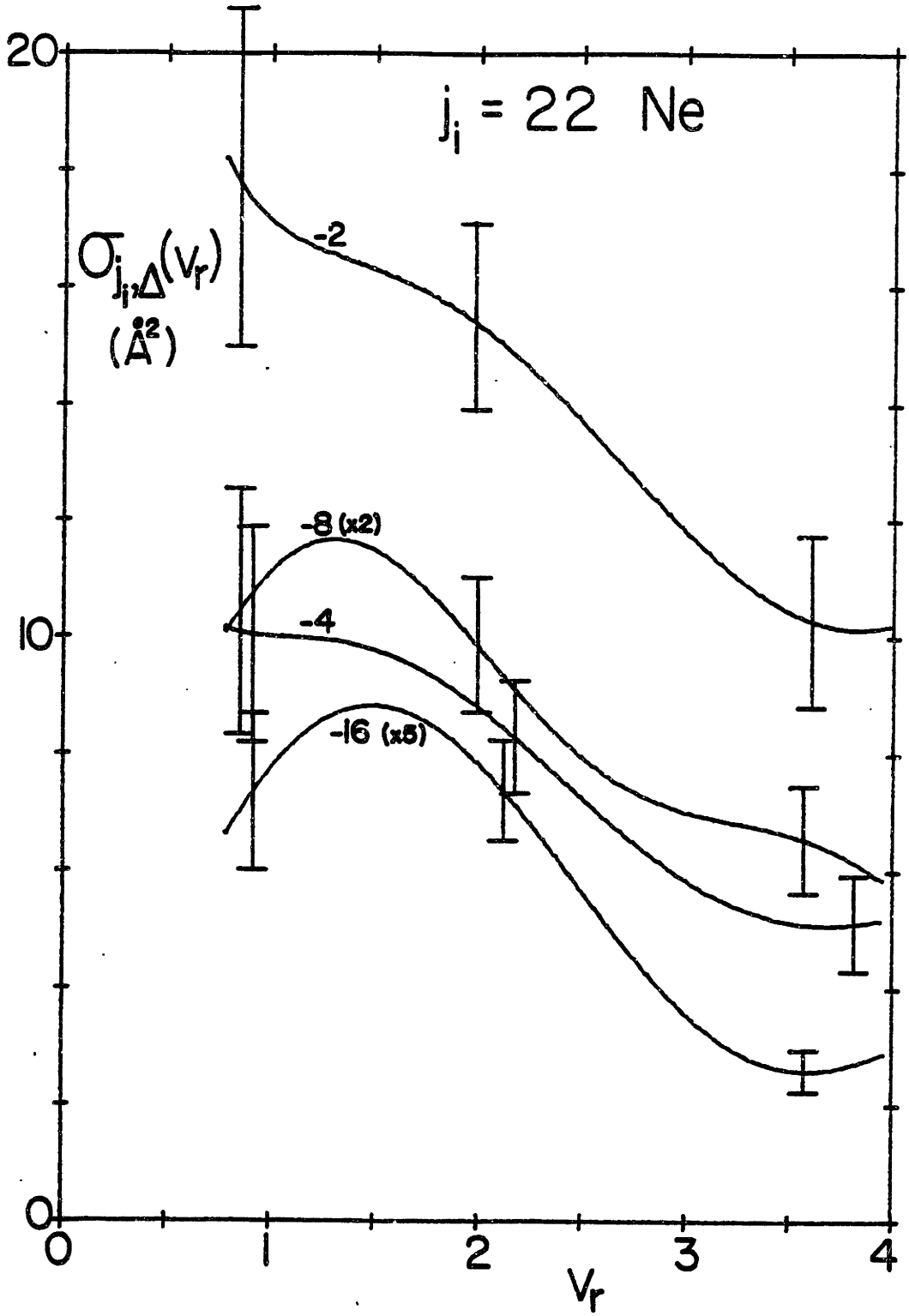

for Xe.

For $\Delta = +2$, $\sigma_{22,2}(v_r)$ for Ne shows a rather pronounced maximum at $v_r \approx 1.5$, followed by a significant decrease as v_r increases (the slight upturn for $v_r > 3.5$ probably a deconvolution artifact.) The $\Delta = +2$ cross-section for Ar, in contrast, shows a quite flat, somewhat ill-defined maximum at $v_r \approx 1.25$, followed by a very gradual decrease in $\sigma_{22,2}(v_r)$ as v_r increases. Neither result exhibits the "torque averaging" behavior characteristic of the $|\Delta| = 2$ data for Xe. We believe this strongly indicates a significantly weaker long range attraction in Li_2^*-Ar,Ne compared to Li_2^*-Xe. This assertion is also supported by the steadily decreasing magnitude of the "average" value (at $v_r = 2$, say) of $\sigma_{22,\pm 2}(v_r)$ going from Xe → Ne. Referring now to figs. 24-27, the $\Delta = -2$ cross-section is rather similar for Ne, Ar (though quite different from $\Delta = +2$ at lower v_r) and once again greatly different in behavior and smaller in size than for Xe.

For $\Delta = -4$, the Ne, Ar results are similar in magnitude and shape, exept at low v_r where $\sigma_{22,-4}(v_r)$ for Ne shows signs of a leveling off, suggestive of a barely resolved maximum. We make the last statement in light of the apparent trend for large $-\Delta$ cross-sections in Ne, which for $\Delta = -8, -16$ show distinct maxima near $v_r \approx 1.5$, and for $v_r < 1$ actually exhibit a positive "threshold like" behavior (we point out that these results are obtained from natural, unconstrained fits). The low $v_r < 1.5$ dependence for $\Delta = -8$ and especially $\Delta = -16$ in Ne is in sharp con-

trast to that of Ar, Xe, which show the rapidly increasing (with decreasing v_r) behavior at all measured velocities, as discussed in detail for the $j_i = 22$ Xe data; $\sigma_{22,-16}(v_r)$ in Ar also varies more rapidly than v_r^{-1} at lower v_r, but definitely not as rapidly as Xe. This contrasting behavior between Ne and Ar or Xe suggests that the unusual low v_r behavior for $\sigma_{22,-16}(v_r)$ in Ar, Xe results from collisions where at sufficiently low v_r the Li_2^*-Xe, Ar can be drawn together even from relatively larger impact parameters, becoming quasi-bound for relatively long times until a large rotational → translational energy transfer occurs, breaking apart the complex. The significantly weaker long range attraction in Li_2^*-Ne, and the correspondingly shallower well-depth are unable to efficiently attract and "trap" the Li_2^*-Ne for orbiting to occur. At larger relative velocities ($v_r > 2$), where orbiting and complex formation is probably far less likely, all three target gases show qualitatively similar behavior for $\Delta = -16$. All decrease rapidly with increasing v_r. (See also the discussion for $j_i = 42$, large $-\Delta$ results).

$j_i = 42$

Xe

Although it was stated earlier that the Xe data and results for $j_i = 22$ were probably the most interesting and/or unusual, $j_i = 42$ is certainly a close second, allowing an examination of the effect of high rotational speed of Li_2^* on the magnitude and v_r dependence of the $\sigma_{42,\Delta}(v_r)$. We define the reduced duration $\tau \equiv$ (rotational angular

frequency) x (collision time) = $(\frac{2Bj}{\hbar})$ $(\frac{b}{v_r s_p})$ with rotational constant B (=.44, v=9), impact parameter b, and $s_p = \sqrt{\frac{kT}{m_p}}$ (= 7.23 x 10^4 cm/sec) our usual velocity unit, with v_r dimensionless as always; τ equals the rotation in radians that the Li_2^* in rotational level j undergoes in a collision time $\frac{b}{v_r s_p}$. Assuming a typical, realistic value of b = 6Å, and a mid-range value of $v_r = 2$, we find $\tau = 3.3$, a value of virtually[27] unprecedented large size for all past RIC studies. Thus, our $j_i = 42$ data allow the best opportunity to date for studying RI collisions in the near adiabatic limit $\tau >> 1$.

Considering fig. 28, we see a rather unusual shape for the $\sigma_{42,\pm2}(v_r)$ results, which for $v_r > 1.5$ are almost identical.The cross-section rises sharply with increasing v_r. Once again, we believe that this is due to reduction of "torque averaging" (i.e. lowering τ) as v_r increases relative to the rotational speed $\propto j_i$). In fact, the $\sigma_{42,\pm2}(v_r)$ for $2 \leq v \leq 4$ behave quite similarly to $\sigma_{22,\pm2}(v_r)$ for $1 \leq v_r \leq 2$ (both increase $\simeq$ linearly with v_r, by a factor of $\simeq 2$), corresponding, to almost equal values of τ (since $\tau \propto j/v_r$), giving very solid support to our contention that torque averaging, of which τ is obviously an accurate measure, is responsible for most of the v_r behavior of the $|\Delta| = 2$ cross-sections for Li_2^*-Xe. Over certain v_r ranges $\sigma_{j_i,\pm2}(v_r)$ is approximately a function of τ only[25] to within a v_r independent scale factor (more on this chap. in IV). However, considering $\sigma_{42,\pm2}(v_r)$ for $v_r < 1.5$, (especially for $\Delta = -2$ - no threshold effects), the torque

Fig. 28 RI cross-sections for j_i = 42, Xe as a function of relative velocity.

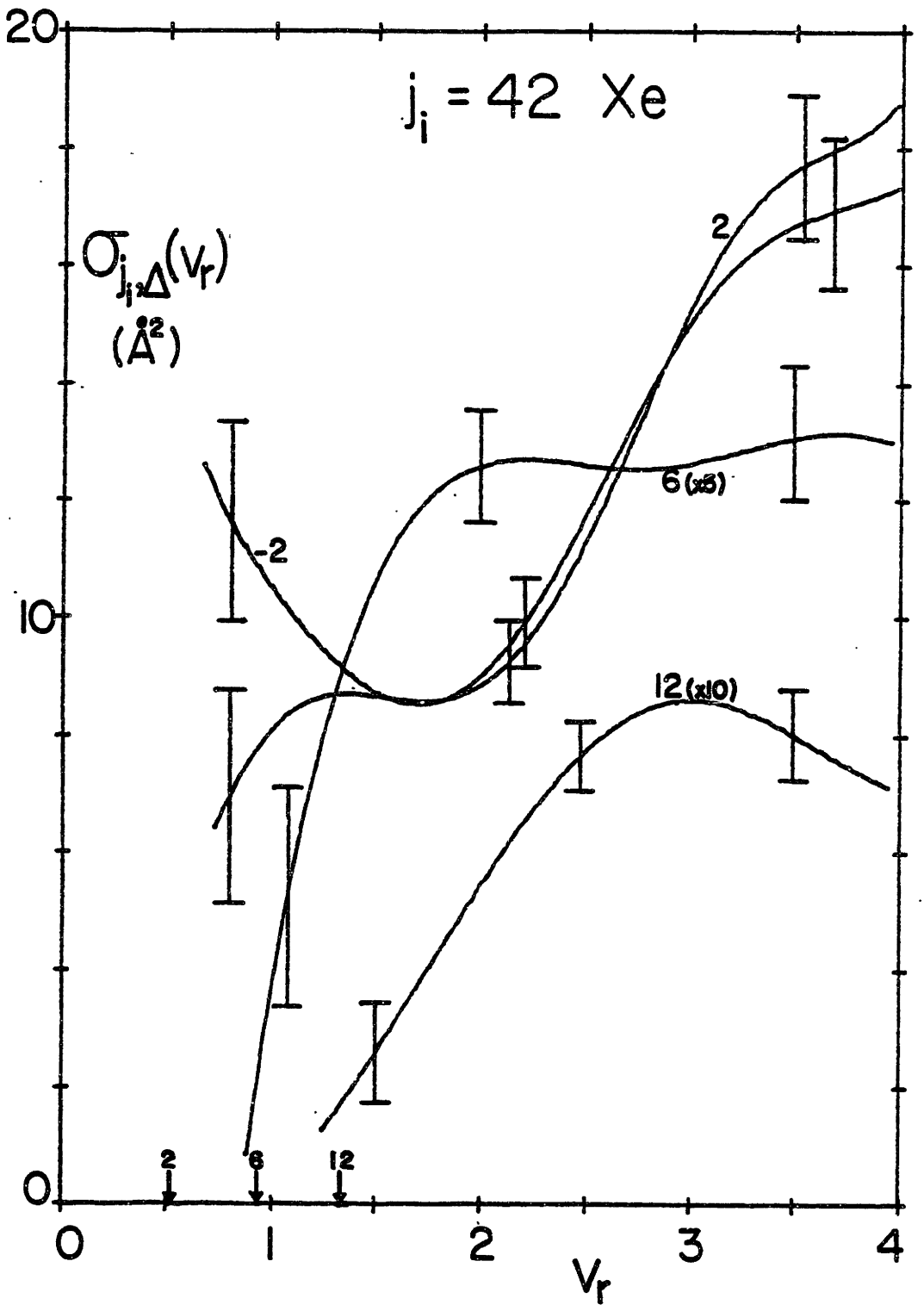

Fig. 29 RI cross-sections for j_i = 42, Xe as a function of relative velocity.

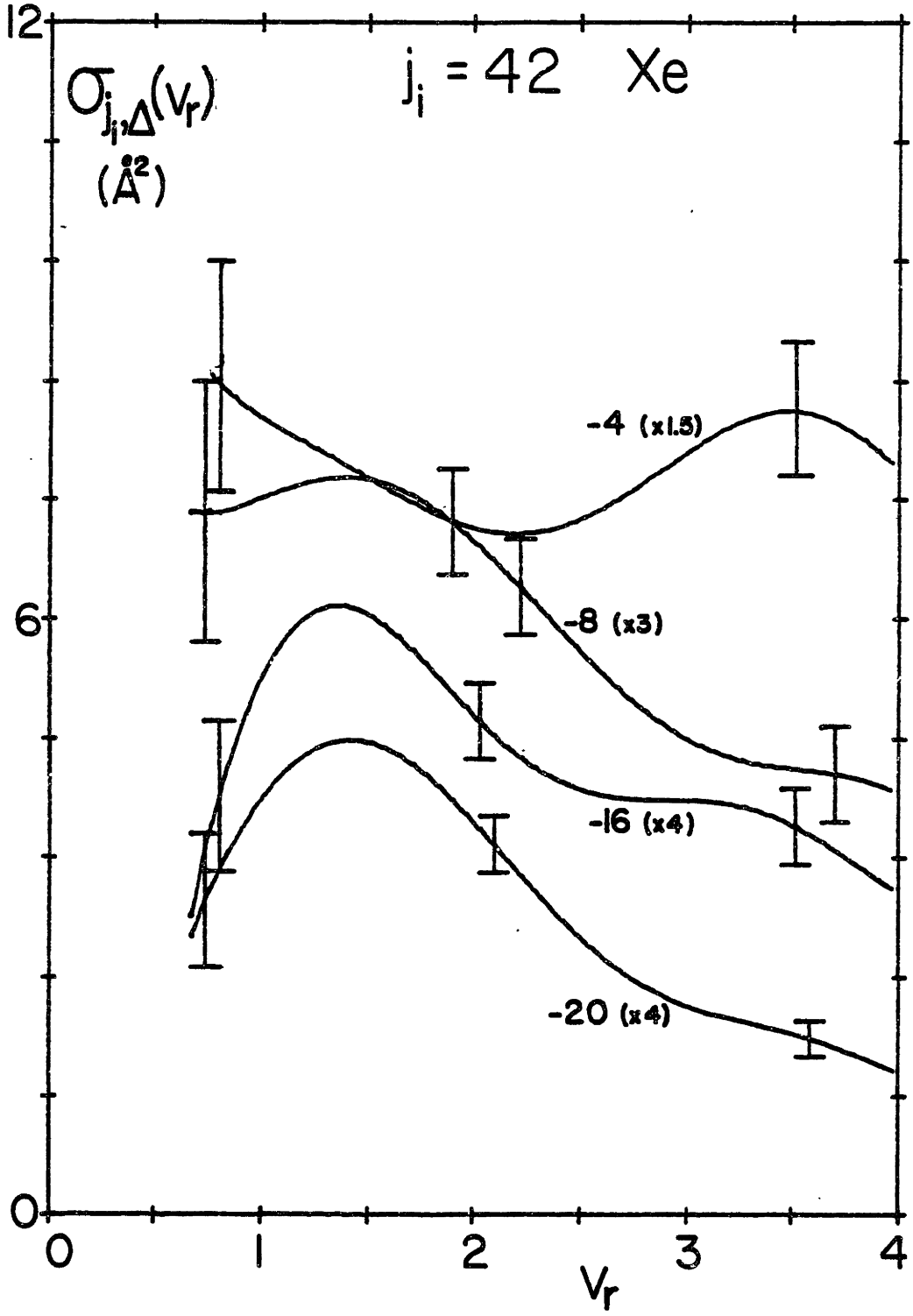

averaging behavior gives way to a v_r dependence more typical of low v_r behavior of $\sigma_{j_i,-2}(v_r)$ in Ar (see $\sigma_{8,-2}$, $\sigma_{22,-2}$, $\sigma_{42,-2}$ in figs. 18,25,30). A simple but very plausible explanation for this is that the torque averaging effect (generally important for long range large b collisions) has become sufficiently great at high j_i, low v_r (i.e. large τ) as to effectively eliminate the possibility of $|\Delta| = 2$ collisions occurring at long range. In this limit the entire contribution to the $\Delta = -2$ cross-section would now come from short range colisions. Comparison of large $|\Delta|$ collision cross-sections for Ar and Xe (which are undoubtably due to hard short-range collisions) in fact show that the v_r dependence of these cross-sections are quite similar, for all j_i.

Referring again to fig. 28, the $\sigma_{42,6}(v_r)$ is quite similar in behavior (though smaller in magnitude) to $\sigma_{22,6}(v_r)$ (fig. 22), rising rapidly for $v_r > v_{th}$ and otherwise basically constant. The case $j_i = +12$, $\Delta = 42$ has the largest threshold velocity of any RIC process measured in this experiment ($v_{th} = 1.32$ for Xe), and the threshold behavior was well represented by this unconstrained deconvolution. However, in a somewhat subtle contrast with previous large $+\Delta$ cases ($j_i = 8$, $\Delta > 12$, $j_i = 22$, $\Delta = 12$), the rise in $\sigma_{42,12}(v_r)$ for $v_r > v_{th}$ seems definitely slower and more gradual, similar to the rising behavior for $|\Delta| = 2$, $j_i = 22$ and 42. It is highly unlikely that this is due to the same long range torque averaging effect. Instead, thinking classically in terms of rotating dumbells and hard spheres, we suggest that the

rapid rotational motion of Li_2^* for $j_i = 42$ coupled with a low relative velocity does not easily allow the Xe to strike the Li_2^* at high torque orientations. This tends to result in collisions off the ends, top, and bottom of the molecule, with torques either small in magnitude or $\perp$ to $\vec{j}_i$, both cases inefficient for large $|\Delta|$ RI collisions. This effect obviously becomes less important as v_r increases, hence the rising behavior of $\sigma_{42,12}(v_r)$ with increasing v_r may be thought of as a reduction of "torque prevention" at high j_i.

In fig. 29, it is seen that for $j_i = 42$, the torque averging effect, although greatly reduced, is still large enough even to effect the behavior of $\sigma_{42,-4}(v_r)$, which like $\Delta = -2$ has a minimum near $v_r = 2$, followed by a rise in cross-section as v_r increases, over $2 \leq v_r \leq 3.5$.

A very (at first) unexpected result, considering the v_r^{-p}, $p > 1$ low v_r dependence of $\sigma_{22,-16}(v_r)$ is the strong decrease, or perhaps even <u>vanishing</u> of $\sigma_{42,-16}(v_r)$ and $\sigma_{42,-20}(v_r)$ at low $v_r < 1$; this behavior is hinted at, but not yet obvious for $\sigma_{42,-8}(v_r)$. One can give a simple, classical explanation of this by again evoking the rotating dumbell, hard sphere picture, and using the "torque prevention" concept mentioned earlier for $\Delta = +12$. For $j_i = 42$, $v_r = 1$ (and again taking $b = 6\text{Å}$), we find $\tau = 6.6 >> 1$, and for purposes of argument we will consider the limit $\tau \to \infty$. In this limit, it becomes impossible for the Xe atom to get in close to Li_2^* to strike it at a high torque orientation (e.g. like a bat (Li_2^*) hitting a baseball (Xe)), i.e. "torque prevention". Instead,

the Li_2^* appears like a cylindrically symmetric spinning "disk", the short range anisotropy about the j_i axis (spin axis) being effectively averaged to zero by the very fast rotation. In this limit, we must have by symmetry that the torque $\vec{T} \perp \vec{j}_i$, and since $\vec{j}_f \equiv \vec{j}_i + \int \vec{T} dt$, it then follows that $|\vec{j}_f| > |\vec{j}_i|$ and thus $\Delta > 0$. Thus in the high j_i, low v_r (large τ) limit, there is, classically speaking, an approximate dynamical constraint prohibiting - Δ (and especially large - Δ) collisions from occuring. In other words, there exists an effective velocity threshold (for given j_i) for v_r below which - Δ (for given Δ) collisions "cannot" happen. This behavior is well reflected by the $\sigma_{42,-16}(v_r)$, $\sigma_{42,-20}(v_r)$ at low v_r, while at large v_r these large - Δ collisions take on the typical large $|\Delta|$ behavior of rapid decrease with increasing v_r. We point out that while v_r, the initial relative velocity can be arbitrarily small, the attractive well of Li_2^*-Xe (almost certainly $\sim$ several hundred cm^{-1}[28]) will increase the effective relative velocity prior to collision. This is possibly why the dynamical constraint on large -Δ collisions is not seen for $j_i = 22$ at a corresponding v_r of $(\frac{22}{42})(1.5) \approx .75$, (since for $j_i = 42$, this effect begins at $v_r \approx 1.5$). Lastly, the complex-forming orbiting collisions used as a plausible explanation for $\sigma_{22,-16}(v_r)$, would probably be inhibited from occuring for large enough j_i, another consequence of "torque prevention ".

Fig. 30 RI cross-sections for j_i = 42, Ar as a function of relative velocity.

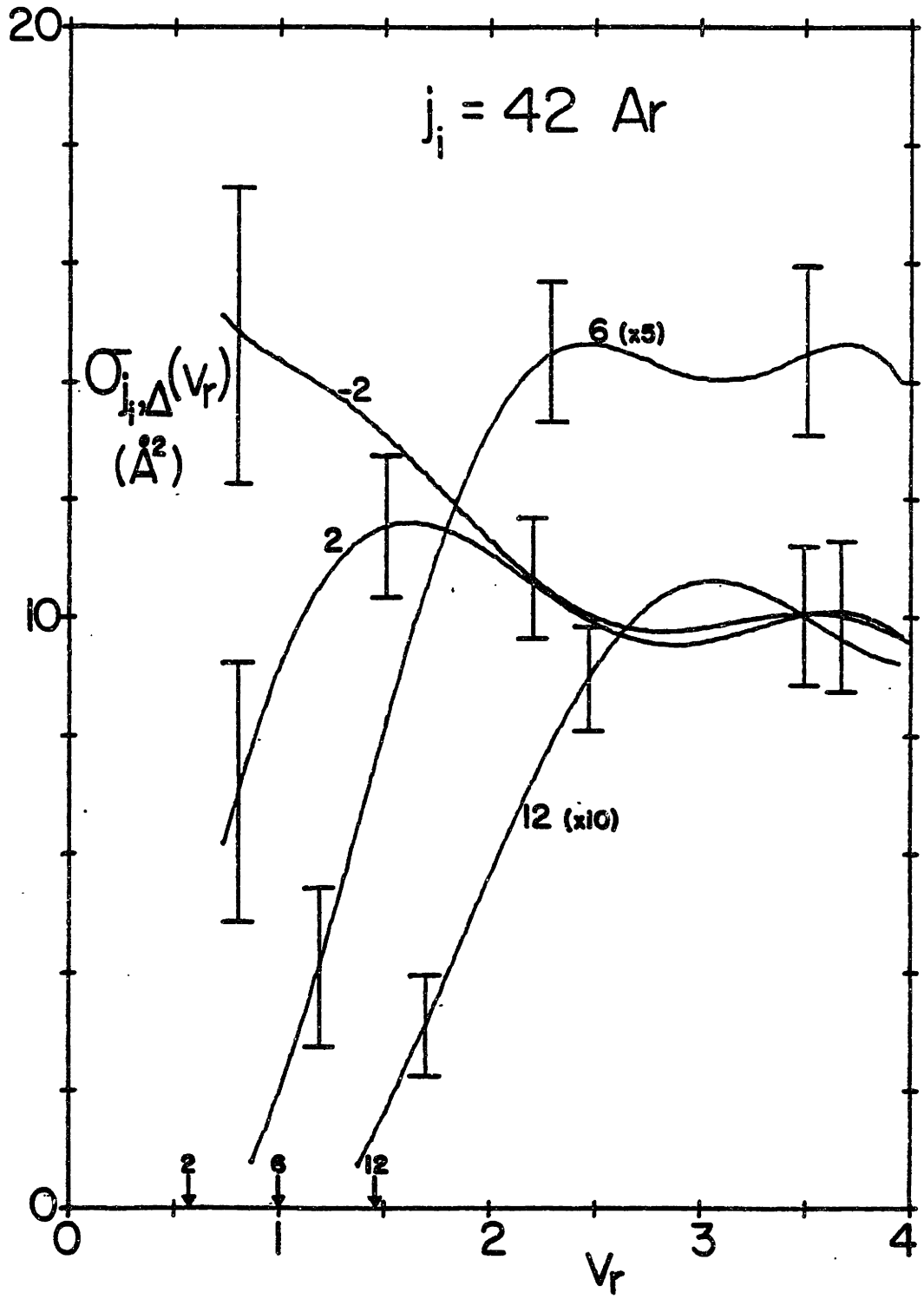

Fig. 31 RI cross-sections for j_i = 42, Ar as a function of relative velocity.

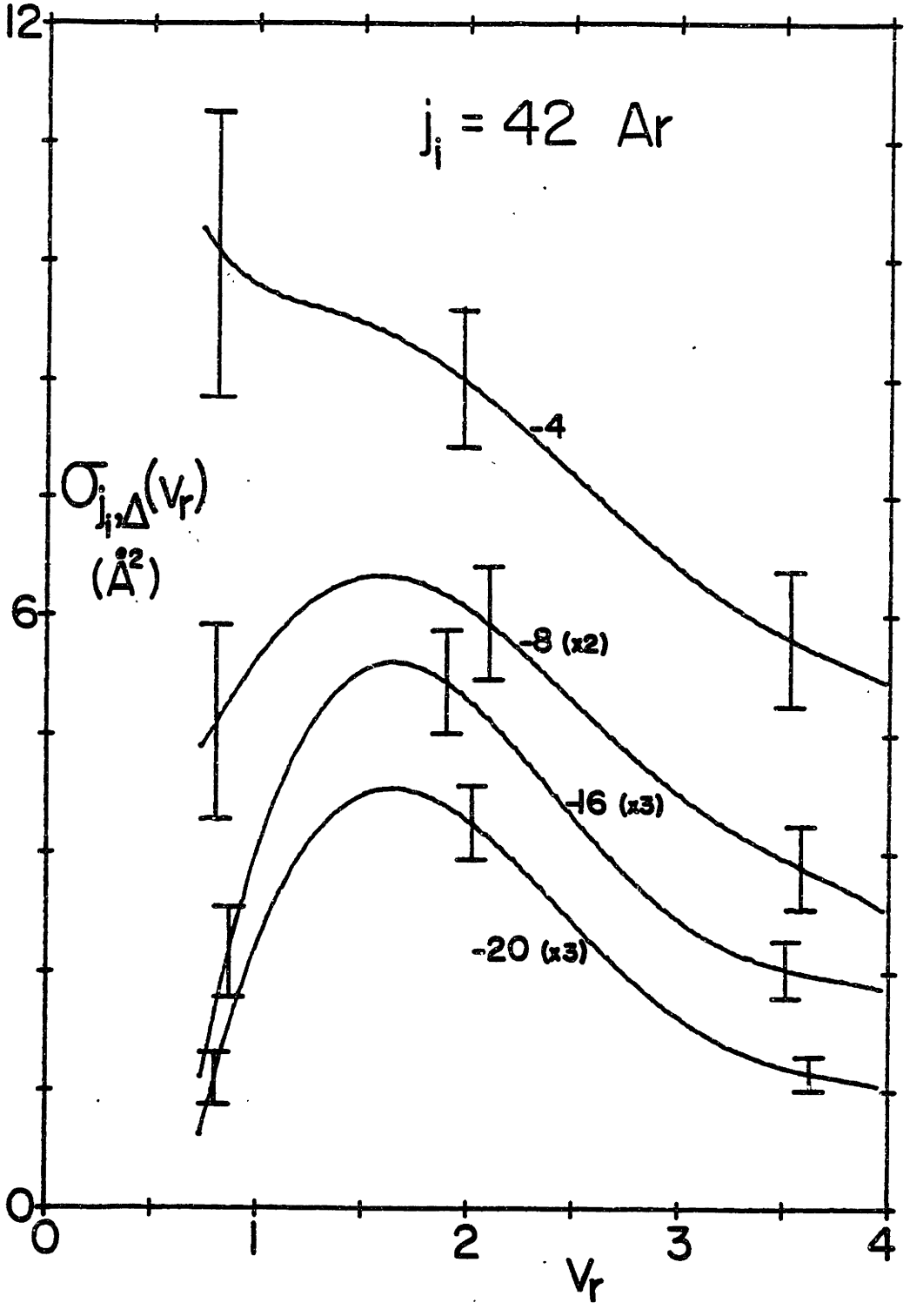

Fig. 32 RI cross-sections for j_i = 42, Ne as a function of relative velocity.

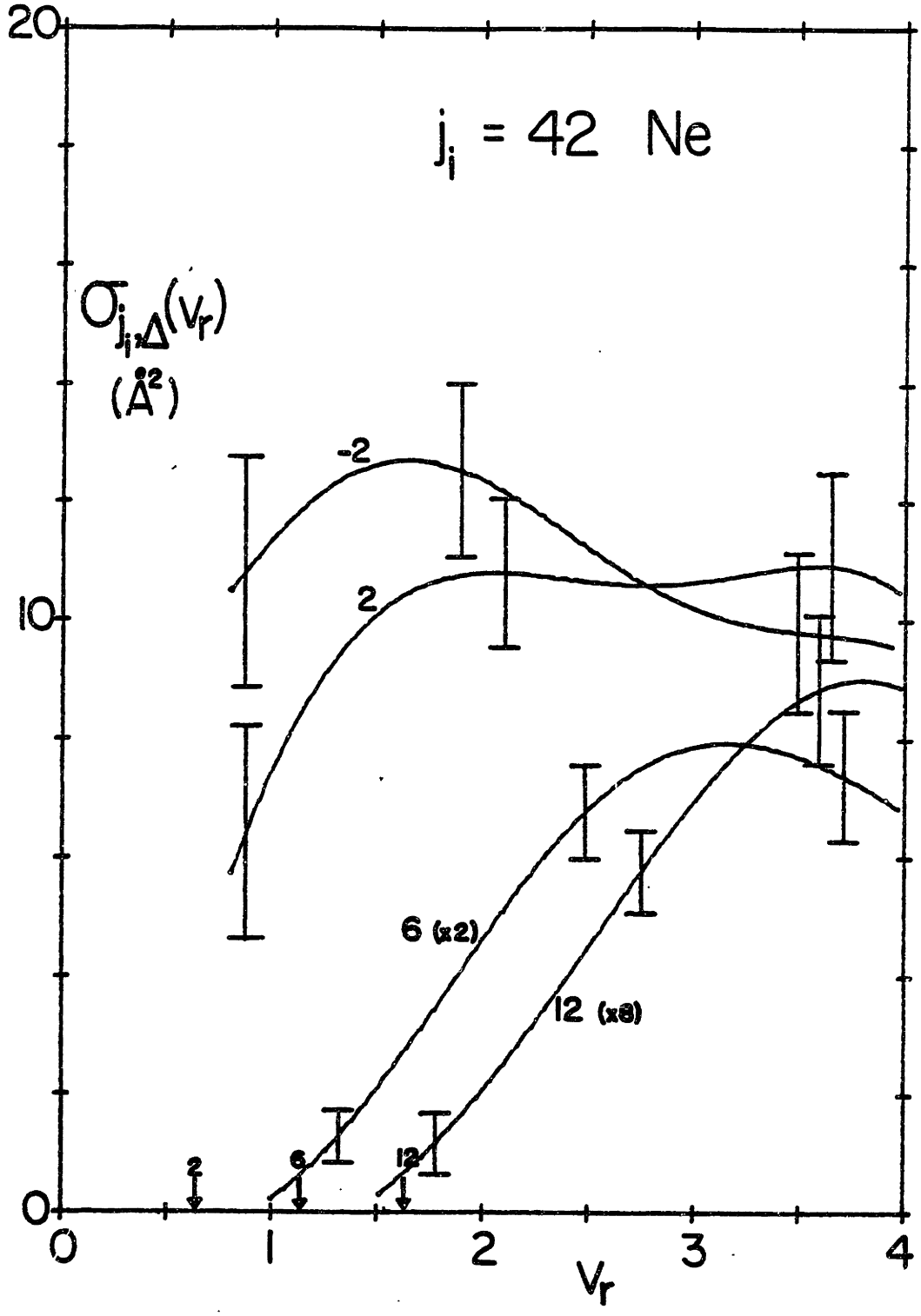

Fig. 33 RI cross-sections for j_i = 42, Ne as a function of relative velocity.

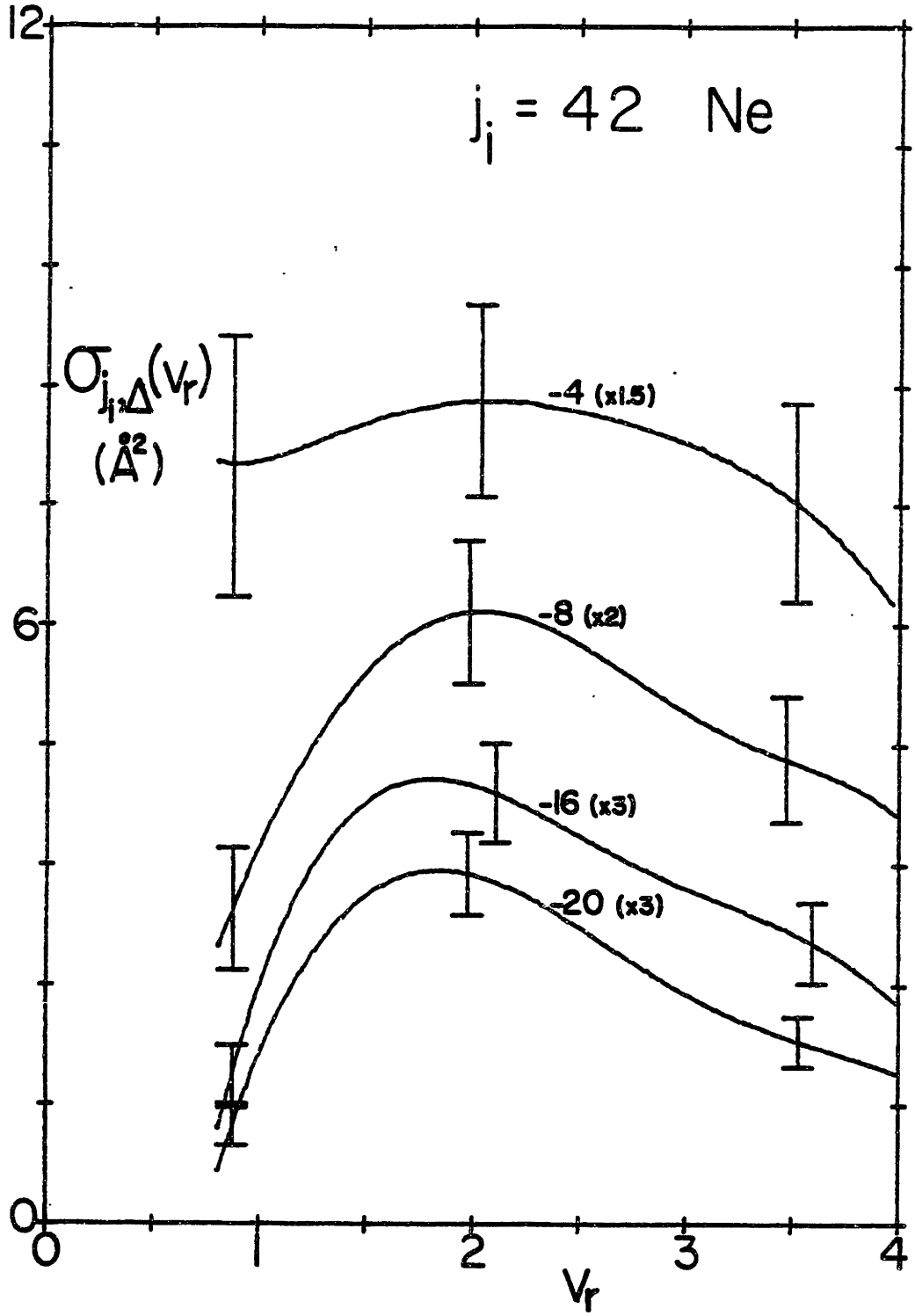

Ar,Ne

The $\sigma_{42,\pm2}(v_r)$ for Ar (fig. 30) are similar to those of Xe in the sense that the $\Delta = \pm2$ cross-sections are almost identical for $v_r > 2$ and diverge at lower v_r. They are much more similar to Xe $\Delta = -4$ in v_r dependence (especially the $\Delta = -2$ case), and probably for the same reason, i.e. a very reduced but observable torque averaging effect. Even the $\sigma_{42,\pm2}(v_r)$ in Ne (fig. 32) fall off at high v_r much more slowly than typical $|\Delta| = 2$ Ne cross-sections at $j_i = 8$ and 22. The $\Delta = +6, +12$ cross-sections for Ar and Xe are quite similar in shape, but $\sigma_{42,6}(v_r)$ for Ne has a slower rise for $v_r > v_{th}$, characteristic of $\sigma_{42,12}(v_r)$, which is similar for Ne, Ar, and Xe. Referring to figs. 31,33, the $\Delta = -8, -16, -20$ cross-sections for both Ne and Ar are quite similar to those of Xe, exhibiting the dynamical threshold behavior for large $-\Delta$ discussed earlier for the Xe case. This effect is apparently more important (i.e. higher "threshold") in going from Xe → Ne. A vestige of this effect appears in Ne for $\Delta = -2, -4$ also.

Summary

The most significant conclusion one can draw about Li_2^*-X RI cross-sectons, after examination of our results for $\sigma_{j_i,v_r}(v_r)$, is that there are no simple conclusions. Earlier studies in Na_2^*-Xe[1] and HF-Ne,Ar, Kr[5] showed predomiantely (though not entirely - see App. B) constant cross-sections independent of velocity. Our work has contrastingly found that there is substantial v_r dependence which depends significantly on

j_i and Δ. There is no doubt that a good deal of physics can be revealed by our Li_2^*-X data. Such examples include the simple, but dramatic "torque averaging" effect for $|\Delta| = 2$ in Xe (and lack thereof in Ar, Ne), the "torque prevention" dynamical threshold behavior for $j_i = 42$, large negative Δ, and in partiuclar the rapid increase of $\sigma_{22,-16}(v_r)$ at low v_r (Ar and especially Xe), as well as the very rapid decrease of $\sigma_{8,24}(v_r)$ at large v_r. The anomolous behavior (that is, in comparison with Xe and Ne) of $\sigma_{8,\Delta}(v_r)$ $|\Delta|<6$ for Ar belies any simple classical explanation like those which we have offered to describe some of the more interesting aspects of our data. While these explanations may be only partially applicable to the data at hand, the effects are real. Together these models, as well as all our results, certainly provide insight into the dynamics of RI collisions. Moreover, the data contain a great deal of information about the Li_2^*-X potentials (see chap. IV), which at present are not known at all.

A troublesome aspect of our results for $\sigma_{j_i,\Delta}(v_r)$ is that the strong, widely varying velocity dependences they exhibit are inconsistent with the simple power law[9] descriptions of RIC used so successfully in the past both on velocity averaged rate constants and also for previous $\sigma_{j_i,\Delta}(v_r)$ data[1,5]. We will now consider in more detail the question of fitting $\sigma_{j_i,\Delta}(v_r)$ to known fitting laws.

7. Fitting Laws

Two relatively simple scaling-fitting laws which have proven applicability[3,9] to a wide range of RI collision systems are the empirical Statistical Power Gap law[9] (SPG), and the Energy Corrected Sudden-Power law (ECS-P) developed from the Energy Corrected Sudden (ECS) scaling theory of DePristo et. al.[10] combined with a special case of the SPG law. The SPG fitting law is expressed as

$$a.\ k_{j_i,\Delta} = k_0\sqrt{1-\frac{2\Delta E}{\mu v_r^2}}\,N_\lambda(j_i,j_f)\,|\Delta E|^{-\alpha}$$

$$b.\ j_f = j_i+\Delta,\quad N_\lambda(j_i,j_f) = \sum_{m_f=-j_f}^{j_f}\sum_{m_i=-j_i}^{j_i}\delta(m_f-m_i),\quad \delta(x)=\begin{cases}1, & |x|\le\lambda\\ 0, & \text{else}\end{cases} \qquad (19.$$

$$c.\ \Delta E \equiv E(v_i,j_f)-E(v_i,j_i)$$

with parameters k_o, λ, α determiend by fit only, having no theoretical justification. It predicts that $k_{j_i,\Delta}(v_r)$ varies as a power of the change in rotational energy ΔE, the magnitude otherwise determined solely by statistical factors: the density of final translation as well as spin states, with N_λ the spin degeneracy factor (averaged over m_i, summed over m_f) assuming the selection rule $|\Delta m| < \lambda$; the factor k_o is assumed to be independent of j_i, Δ, and is therefore just an overall scale factor. We should point out that the SPG law has been applied predominantly to velocity averaged data (e.g. $\overline{k}^{o}_{j_i,\Delta}$) with all quantities dependent on v_r in Eq. 19 (including in principle, k_o, α, and λ) replaced by velocity averaged values.

The more complicated ECS-P is

$$a.\ K_{j_i,\Delta}(v_r') = (2j_i+1)\frac{v_r}{v_r'}\sum_{J=|\Delta|}^{j_>+j_<}(2J+1)\begin{pmatrix} j_i & j_< & J \\ 0 & 0 & 0\end{pmatrix}^2 |A^J_{j_>}|^2 K_{J\to 0}(v_r)$$

$$b.\ A^J_{j_>} = \frac{1+\tau_{j_<}^2/6}{1+\tau_{j_>}^2/6},\quad \tau_j = \left(\frac{2Bj}{\hbar}\right)\frac{l_c}{v_r s_\varphi},\quad j_> = \max(j_i, j_<) \qquad (20.$$

$$c.\ v_r' \equiv v_r\sqrt{1+\left(\frac{2(1+\tau)B}{kT\,v_r^2}\right)\left(J_>(J_>+1) - J_i(J_i+1)\right)}$$

$$d.\ k_{j\to 0} \equiv k_{J,-J} = k_0\left[J(J+1)\right]^{-\gamma}$$

with fitted parameters k_0, γ and l_c, l_c having the interpretation of the "average" collision length (impact parameter), or range of the potential; again, k_0, γ and l_c may in general depend on v_r, though the greater their independence on v_r, the greater the utility of this approach. Eqs. 20.a,b express results of the ECS theory (derived for $\Delta < 0$, but usable for $\Delta > 0$ through micro-reversibility - eq. 20.c), with A an "adiabatic correction factor" derived[10] to approximately account for the rotation of the molecule during a collision. In eq. the parameter τ expresses the importance of rotational effects (sec. III.6); in the sudden limit $\tau\to 0$, we have $A \to 1$ and eq. 20.a reverts to a well known sudden scaling law commonly derived form the Infinite Order Sudden (IOS) approximation[7]. Eq. 20.d is a special case of the power law of eq. 19, for a rigid rotor in the energy sudden limit ($\mu v_r^2 >> \Delta E$) with unrestricted Δm.

It has in fact been shown[29] that SPG is mathematically equivalent

in many cases (provided τ not too large) to the more complicated, but theoretically justifiable ECS-P, which does not require any arbitrary restrictions on Δm; it has also been found[30] for experimental Na_2^*-Xe data that SPG failed, while ECS-P succeeded, in fitting the entire data set when j_i = 100 data (large τ) was included in the fits. In light of these above statements, we will focus attention only on ECS in regards to fitting our present Li_2^*-X data, and but mention however, that SPG was found to successfully fit the velocity dependent data of Barnes et. al.[5] with α relatively independent of v_r.

First attempts at fitting our Li_2^*-X data at several v_r with ECS-P showed obvious systematic deviations between data and fit, especially for j_i = 8, with χ^2/ν in the range 4-9, indicating average deviations 2 to 3 times the size of our assigned error bars (which include both deconvolution and spx normalization errors). This agreement was definitely worse than that obtained using ECS-P on Na_2^*-Xe VSDS data (average $\chi^2/\nu < 2$ - see App. B), though errors assigned to those data were generally somewhat larger. Referring back to the j_i = 8 data, the nonlinearity of log-log plots of $\sigma_{8,\Delta}(v_r)$ v.s. $|\Delta|$, especially for j_i = 8, Xe, v_r = 1 (see fig. 34) suggested we try the alternative

$$\sigma_{J\to 0} = \sigma_0 [J(J+1)]^{-\gamma} e^{-\theta J(J+1)} \qquad (21)$$

referring to ECS plus eq. 21 as ECS-EP (the "E" for exponential). A similar term was found necessary earlier for velocity averaged I_2^*-He

data,[31] the reason given for the exponential cut-off of $\sigma_{j\to o}$ at sufficiently large j was a dynamical constaint imposed by limited maximum orbital angular momentum transferable to rotation. One would then expect the paramter θ to decrease roughly as v_r^{-1}; however the ECS-EP fits show θ to have similar values for both $v_r = 1$ and $v_r = 3$ (table 4), and also to be fairly independent of target gas (and thus reduced mass), thus clouding the interpretation of the θ parameter. In any case, its inclusion reduced χ^2/ν by about a factor of 2, and it was thus decided to continue use of ECS-EP to fit our data set. The predictions of the fit results for $v_r = 1, 3$ are plotted as curves in figs. 34-36, along with the corresponding experimental data points (evaluated at v_r' of eq. 20.c); error bars (not shown) are approximately 1 (1.5) times the size of the symbols for $v_r = 3$ (1) respectively. A tabulation of fitted values for k_o, γ, θ, and l_c as a function of v_r are given in table 4.

Inspection of figs. 34-36 shows that the ECS-EP can describe the general variation of $\sigma_{j_i,\Delta}$ with j_i,Δ quite well, at both $v_r = 1$, $v_r = 3$, and thus presumably over the v_r range of our experiment. The only <u>systematic</u> deviation between data and fit appear to occur for $j_i = 42$; here ECS-EP definitely <u>underestimates</u> the $\sigma_{42,\pm 2}(v_r=1)$ while <u>overestimating</u> $\sigma_{42,12}(v_r = 1)$, and again then <u>underestimates</u> both $\sigma_{42,-16}(v_r = 3)$ and $\sigma_{42,-20}(v_r=3)$. These $j_i = 42$ data provide the most most rigorous test of the adiabatic correction factor A of any data we know of, and it is not too surprising that ECS-EP is less than perfect in this case; espe-

Fig. 34 RI cross-sections for Xe, v_r = 1 and 3, with ECS-EP fits (lines).

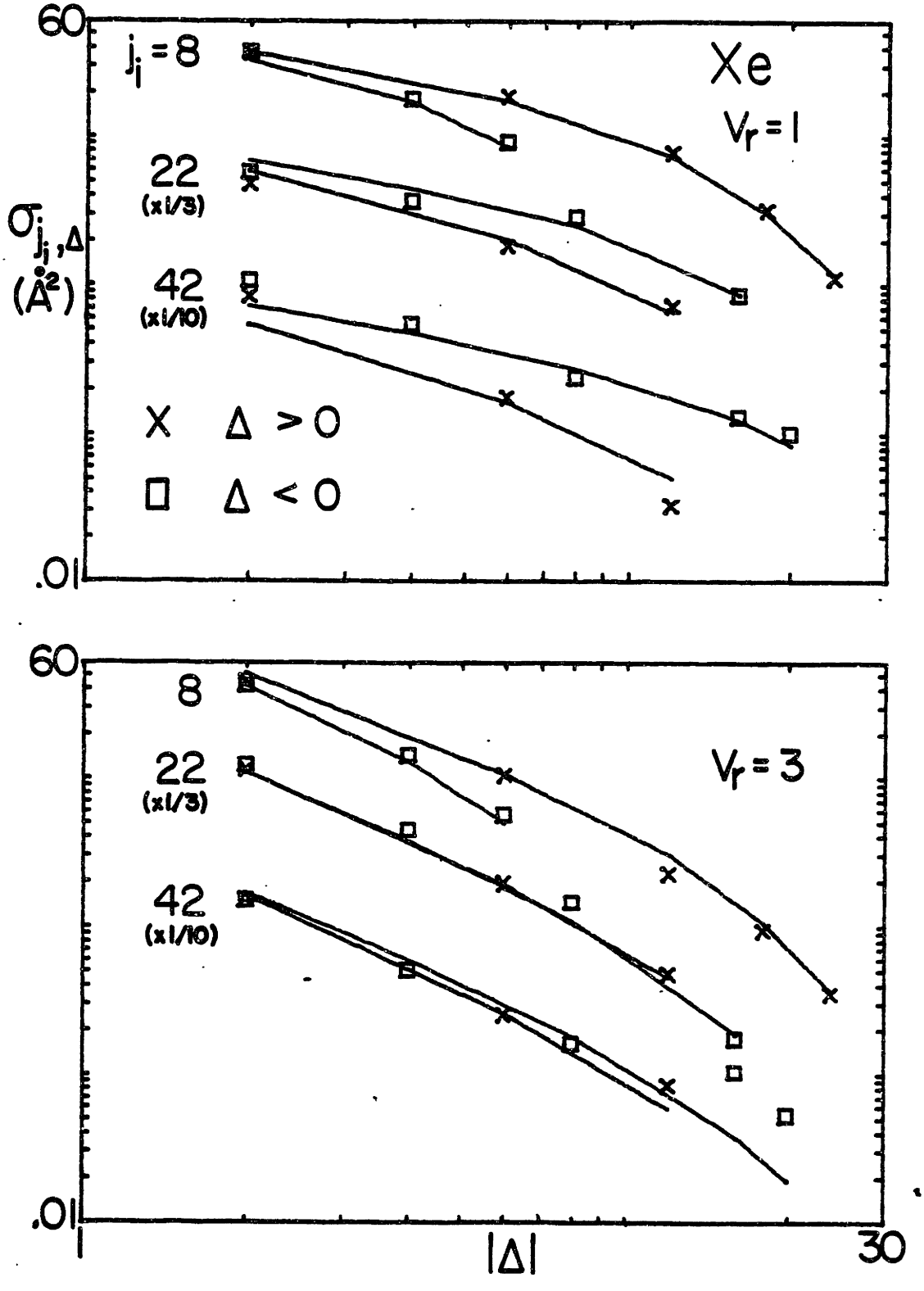

Fig. 35 RI cross-sections for Ar, v_r = 1 and 3, with ECS-EP fits (lines).

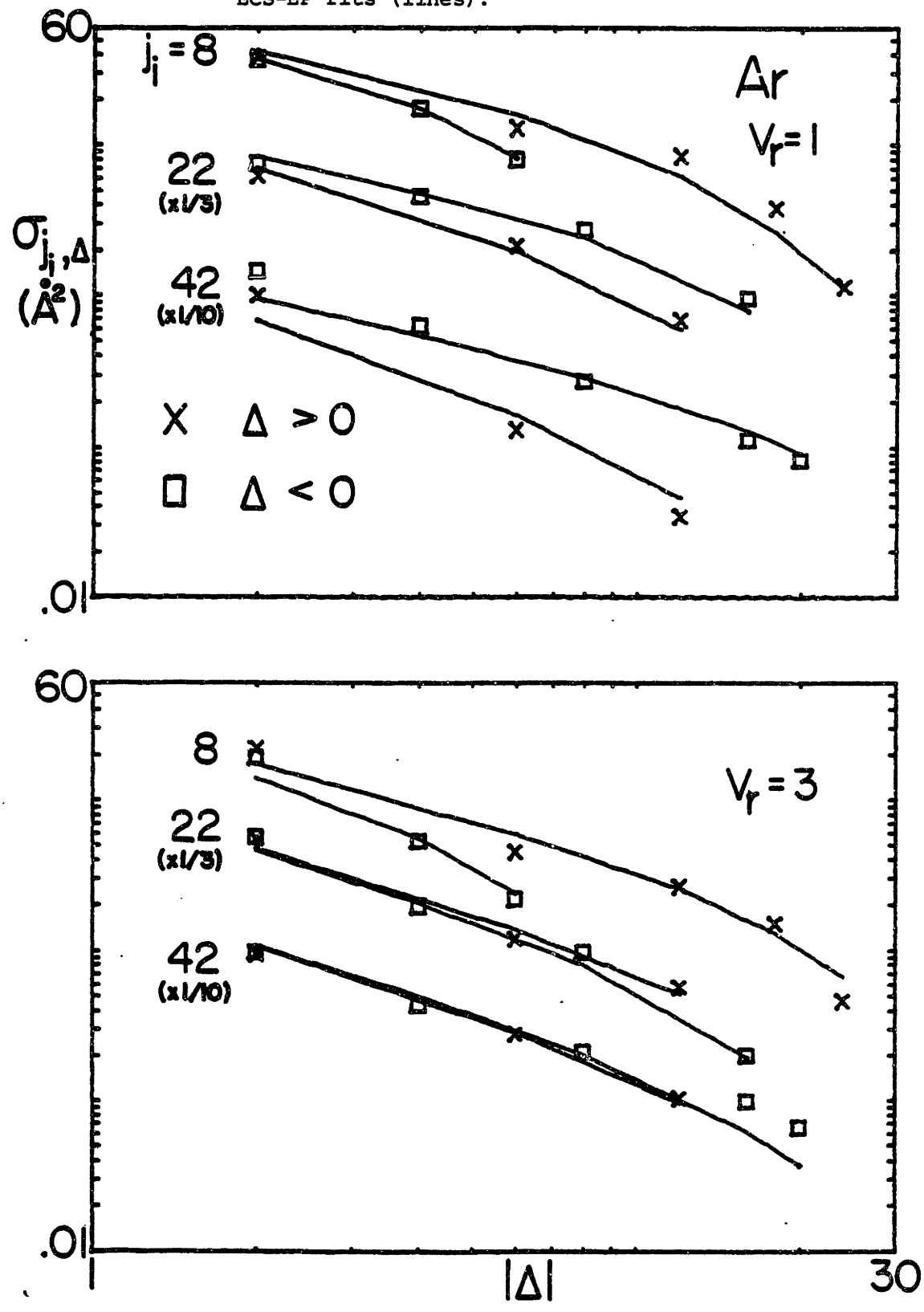

Fig. 36 RI cross-sections for Ne, v_r = 1 and 3, with ECS-EP fits (lines).

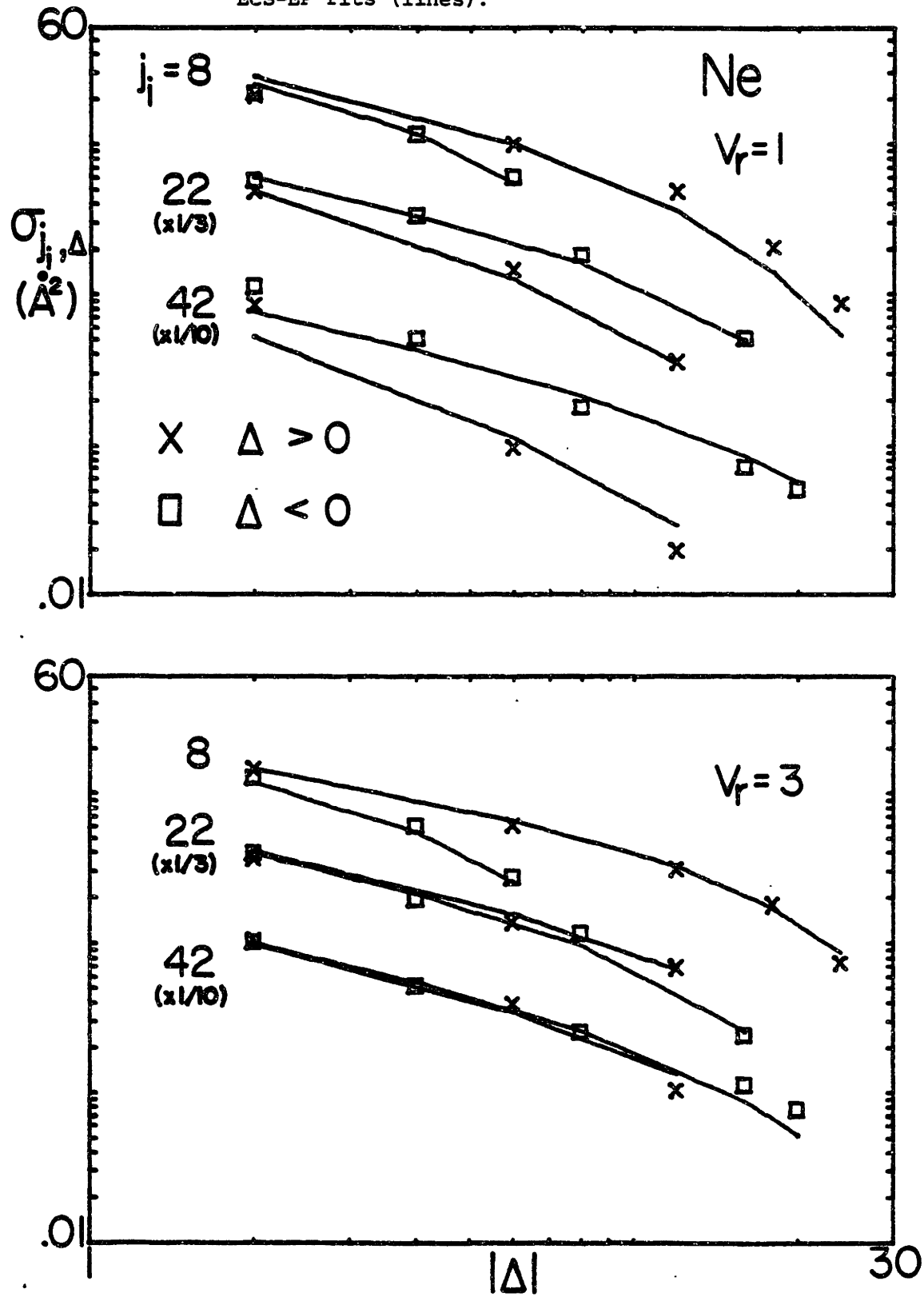

Table III.4 - ECS-EP Fit Parameters

Target Atom	v_r	k_o (10^{11} cm^3/sec)	γ	θ (x10^3)	l_c (Å)	χ^2/ν
	.75	16.0±3	.451±.1	2.99±.7	2.49±.2	1.93
	1.0	36.0±4	.698±.06	1.79±.6	3.06±.2	1.85
	1.5	76.1±6	.926±.04	1.33±.3	4.17±.2	2.61
Xe	2.0	87.2±6	.951±.04	2.23±.3	5.36±.2	4.45
	2.5	122.±9	1.06±.04	2.40±.3	6.23±.3	4.85
	3.0	171.±12	1.20±.03	2.04±.3	6.56±.3	5.12
	3.5	173.±13	1.25±.03	2.03±.3	6.75±.3	4.68
	.75	46.2±9	.612±.10	5.98±.9	2.25±.2	2.92
	1.0	61.9±6	.845±.06	1.23±.3	2.89±.2	1.61
	1.5	84.4±4	.973±.05	.431±.2	3.45±.2	1.99
Ar	2.0	63.5±3	1.07±.04	.120±.1	3.72±.3	2.56
	2.5	57.0±4	.962±.04	.975±.2	3.25±.3	3.58
	3.0	33.1±2	.994±.04	1.08±.2	3.46±.4	3.09
	3.5	32.5±3	1.02±.04	1.28±.3	3.49±.5	2.86
	1.0	41.8±5	.844±.07	1.46±.4	2.62±.2	1.55
	1.5	38.4±4	.878±.06	.725±.3	3.47±.2	2.33
Ne	2.0	31.1±3	.872±.05	.646±.2	3.75±.2	1.93
	2.5	23.6±2	.854±.05	.799±.3	3.50±.3	1.08
	3.0	18.0±2	.826±.05	1.34±.3	2.84±.5	.973
	3.5	17.4±2	.843±.05	1.72±.3	2.55±.7	1.24

cially since the A factor was only obtained after use of rather crude, simplistic assumptions[25]. There is no guarantee of the accuracy of eq. 21 either. Exclusion of the $j_i = 42$ from fits did, in fact result is significant improvements in χ^2/ν, by about a factor of 2. However, we also note that after exclusion of the $j_i = 8$ data, it was found that ECS-P described the remaining $j_i = 22, 42$ data with comparable accuracy ($\chi^2/\nu < 3$), thus further confusing the issue.

As it is not of primary interest to this work, we will not further discuss the fitting of our data to well-known fitting laws. We will however, further discuss the idea of an adiabatic correction factor, in regards to "torque averaging" later in chap IV. With this in mind, we now consider the velocity dependence of the fit parameter l_c, which according to the ECS theory[10], is approximately an "average" impact paramter. As τ in eq. 20.b was derived[10] assuming straight-line trajectories at impact parameter l_c, with an assumed (long range) potential of R^{-6}, it is quite reasonable to expect a strong relationship between the v_r dependence of l_c, and the "torque averaging" concept discussed earlier for long range collisions, primarily $|\Delta| = 2$.

This is in fact beautifully demonstrated in fig. 37 where we plot fitted values of l_c as a function of v_r. As speculated earlier in sec.III.6, the range of the Li_2^*-Xe potential (persumably related to l_c) is considerably larger than that for Li_2^*-Ar,Ne. These latter two appeared to be quite similar in this regard, as is roughly confirmed in

Fig. 37 Fitted values for the ECS parameter l_c, as a function of relative velocity.

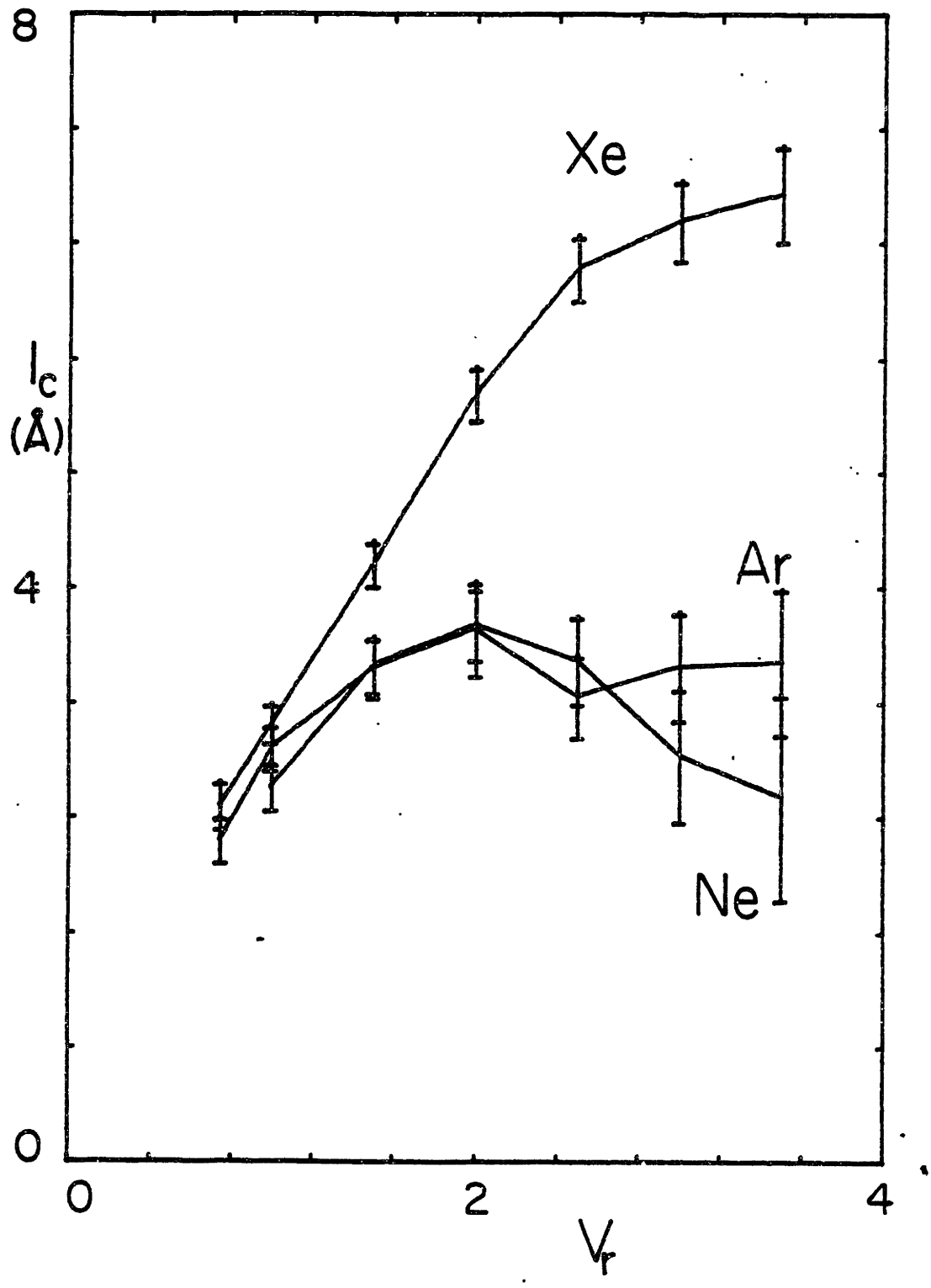

fig. 37. The v_r dependence of l_c appears quite similar to that for $\sigma_{22,\pm2}(v_r)$ for the corresponding target gas. In fact, we find $\sigma_{22,-2}(v_r) \approx 2\pi l_c$ to a good approximation, as if the cross section came from an annulus of radius $\approx l_c$, and width $\approx 1\text{Å}$, as might be expected if long range forces dominate $|\Delta| = 2$ collisions. (For $j_i = 8$, torque averaging is much less important at most v_r, while for $j_i = 42$, short range contributions cannot be neglected). We note that a qualitatively similar v_r dependence of l_c, for Li_2^*-Xe was found for Na_2^*-Xe (App. B - fig. 15), where some torque averaging was observed for $j_i = 66$, which for given v_r and τ, is equivalent to $j_i = 27$ for Li_2^*-Xe.

The above discussion leads us to a final, somewhat puzzling question. If the value and v_r dependence of l_c is closely related to the long range potential, "torque averaging", and $|\Delta| = 2$ collisions (as it appears to be), why then does this l_c value work well even for large $|\Delta|$ which can only result from hard, short range collisions with physically smaller average impact parameters? A possible mathematical (though not very physical) answer is that for large $|\Delta|$ the numerator of the factor A^2 in eq. 20.b becomes more comparable in size to the denominator, thus making A^2 less sensitive to the value of l_c.

IV. Calculations

1. Semi-Classical Results for $\Delta = -2$

We believe the unique velocity dependence of the $\sigma_{j_i,\pm 2}(v_r)$ for Xe is the result of sufficiently strong anisotropic long range forces between Li_2^*-Xe, coupled with rotational averaging of the long range torque (i.e. "torque averaging" - see chap III.6) which decreases the cross-section as v_r decreases (and τ increases). That the $|\Delta| = 2$ cross-section in Xe is dominated by "soft", large impact parameter collisions is evidenced by the large size of $\sigma_{j_i,\pm 2}(v_r)$ - generally $\approx 40\text{Å}^2$ at large v_r where torque averaging is unimportant, and more than twice the size of the next largest cross-section $\sigma_{j_i,-4}$. Further, "torque averaging" is not significantly observed for Li_2^*-Ar, Ne which have significantly smaller polarizabilities and hence considerably weaker long range interactions.

As the leading anisotropic long range potential term goes like[4,28] $C_6 R^{-6} P_2(\cos\gamma)$ (γ = angle between position vector $\vec{R}$ and internuclear axis $\vec{r}$), only $|\Delta| = 2$ matrix elements are non-zero to first order. Conversely, the large magnitude for $\sigma_{j_i,\pm 2}$ as well as the fact that the ratio $\sigma_{j_i,-2} \div \sigma_{j_i,-4}$ is greater than 2 indicate that 1st order terms dominate the long range collision process. The above considerations indicate that the long-range $|\Delta| = 2$ collisions are amenable to simple theoretical treatment, such as a semi-classical calculation where the relative motion is treated classically using a straight line

trajectory approximation, the rotational motion treated quantally, and the dynamics solved by 1st order quantum-mechanical time-dependent perturbation theory. We shall presently attempt this calculation for $\Delta = -2$, so to avoid any considerations of velocity threshold effects present for $\Delta = +2$.

The potential for calculation purposes is taken to be

$$a.\ V(\vec{R},\vec{r}) = \tfrac{3}{2} C_6 R^{-6} (\hat{R}\cdot\hat{r})^2,\ R\equiv|\vec{R}|, r\equiv|\vec{r}| \qquad (1.$$

$$b.\ \vec{R}(t) = (X,Y,Z) = (b, v_r t, 0),\ \vec{r} = (x,y,z)$$

where $\vec{r}$ is the rotor axis and with constant terms of $P_2(R\cdot\hat{r})$ dropped for convenience. The classical relative motion $\vec{R}(t)$ (eq. 1.b.) corresponds to a straight line trajectory with constant relative velocity $\vec{v}_r = v_r\hat{y}$; without loss of generality we let the relative motion take place in the x-y plane of some space-fixed set of coordinate axis.

We consider a transition by RI collision from state $|j,m\rangle$ to state $|j-2,m'\rangle$, with m,m' are projections of $\vec{j}$ along the space fixed z axis. The transition (scattering) amplitude for this collision, as a function of impact paramter b, is given in 1st order by [32]

$$a.\ S^{J}_{m,m'} = \frac{1}{\hbar}\int_{-\infty}^{\infty} \langle j-2,m'|V(\vec{R}(t),\vec{r}|j,m\rangle e^{-(E(j)-E(j-2))\hbar^{-1}t}\,dt$$

$$b.\ \xrightarrow{\text{eq.1}} = \frac{1}{\hbar}\int_{-\infty}^{\infty}\frac{3}{2}\frac{C_6}{R^6(t)}\left\langle j-2,m'\left|\left(\frac{x}{r}\right)^2X^2+\left(\frac{y}{r}\right)^2Y^2+2\left(\frac{xy}{r^2}\right)XY\right|j,m\right\rangle e^{-2i\omega t}\,dt \qquad (2.$$

$$\omega = (2\hbar)^{-1}[E(j)-E(j-2)],\ R(t) = \sqrt{b^2+v_r^2t^2}$$

$$c.\ \xrightarrow{q=\frac{v_rt}{b}} = \frac{3C_6}{2\hbar v_r b^5}\left[\left\langle\left(\frac{x}{r}\right)^2\right\rangle_{m,m'}\int_{-\infty}^{\infty}\frac{e^{i\alpha q}\,dq}{(1+q^2)^4}+\left\langle\left(\frac{y}{r}\right)^2\right\rangle_{m,m'}\int_{-\infty}^{\infty}\frac{q^2e^{i\alpha q}\,dq}{(1+q^2)^4}-2\left\langle\left(\frac{xy}{r^2}\right)\right\rangle_{m,m'}\int_{-\infty}^{\infty}\frac{qe^{i\alpha q}\,dq}{(1+q^2)^4}\right]$$

$$d.\ \left\langle \left(\frac{x}{r}\right)^2 \right\rangle_{m,m'} \equiv \left\langle j-2,m' \left| \left(\frac{x}{r}\right)^2 \right| j,m \right\rangle, \text{ etc.}, \quad \alpha \equiv 2w\left(\frac{b}{v_r}\right) = 2\gamma \qquad (2.$$

In eq. 2.b, ω is the analogue to the classical rotation frequency of the rotor, and for $E(j) \propto j(j+1)$, $\omega \approx 2Bj/h$. Thus τ in eq. 2.d has its usual meaning of angular rotations per collision time b/v_r, for given b (see III.6, $j_i = 42$ discussion). The dimensionless integrals in eq. 2.c can be solved analytically, using complex residue methods. The results are

$$a.\ \int_{-\infty}^{\infty} \frac{e^{i\alpha q}\,dq}{(1+q^2)^4} = \frac{5\pi}{16} e^{-\alpha}\left(1+\alpha+\frac{2}{5}\alpha^2+\frac{\alpha^3}{15}\right)$$

$$b.\ \int_{-\infty}^{\infty} \frac{2q e^{i\alpha q}\,dq}{(1+q^2)^4} = \frac{i\pi}{8} e^{-\alpha}\left(\alpha+\alpha^2+\frac{\alpha^3}{3}\right) \qquad (3.$$

$$c.\ \int_{-\infty}^{\infty} \frac{q^2 e^{i\alpha q}\,dq}{(1+q^2)^4} = \frac{\pi}{16} e^{-\alpha}\left(1+\alpha-\frac{\alpha^3}{3}\right)$$

Since we measure only degeneracy averaged cross-sections, we wish to calculate the transition probability

$$a.\ P_{j,-2} = \frac{1}{2j+1} \sum_{m=-j}^{j} \sum_{m'=-j+2}^{j-2} \left| S^j_{m,m'}(b) \right|^2 \qquad (4.$$

$$b.\ \sigma_{j,-2} = \int 2\pi b P_{j,-2}(b)\,db$$

for comparison with our experimental results. To this end, we define the following quantity Q

$$Q = \frac{4}{45}(2j+1)(2j-3)\begin{pmatrix} j & 2 & j-2 \\ 0 & 0 & 0 \end{pmatrix}^2 = \frac{2}{15}\frac{j(j-1)}{(2j-1)} \qquad (5.$$

It can then be shown by expressing x^2, y^2, xy in terms of spherical harmonics[33.a] Y_2^m, and using angular momentum addition formalism[33.b] that

$$a.\ \sum_{m,m'} \left| \left\langle \left(\frac{x}{r}\right)^2 \right\rangle_{m,m'} \right|^2 = \sum_{m,m'} \left| \left\langle \left(\frac{y}{r}\right)^2 \right\rangle_{m,m'} \right|^2 = Q$$

$$b.\ \sum_{m,m'} \left\langle \left(\frac{x}{r}\right)^2 \right\rangle^*_{m,m'} \left\langle \left(\frac{y}{r}\right)^2 \right\rangle_{m,m'} = \sum_{m,m'} \left\langle \left(\frac{y}{r}\right)^2 \right\rangle^*_{m,m'} \left\langle \left(\frac{x}{r}\right)^2 \right\rangle_{m,m'} = \frac{-Q}{2} \qquad (6.$$

$$c.\ \sum_{m,m'} \left| \left\langle \left(\frac{xy}{r^2}\right) \right\rangle_{m,m'} \right|^2 = \frac{3}{4} Q$$

$$d.\ \sum_{m,m'} \left\langle \left(\frac{x}{r}\right)^2 \right\rangle^*_{m,m'} \left\langle \left(\frac{xy}{r^2}\right) \right\rangle_{m,m'} = \sum_{m,m'} \left\langle \left(\frac{y}{r}\right)^2 \right\rangle^*_{m,m'} \left\langle \left(\frac{xy}{r^2}\right) \right\rangle_{m,m'} = 0$$

Finally, gathering results from eqs. 2.c, 3, 5, and 6, it can be shown (after some straight-forward but tedious algebra) that $P_{j,-2}$ in eq. 4.a is expressable as

$$a.\ P_{j,-2}(b) = f^2(\gamma) P^s_{j,-2}(b)$$

$$b.\ f^2(\gamma) = e^{-4\gamma}\left[1 + 4\gamma + 8\gamma^2 + \frac{32}{3}\gamma^3 + \frac{208}{21}\gamma^4 + \frac{128}{21}\gamma^5 + \frac{128}{63}\gamma^6\right] \qquad (7.$$

$$c.\ P^s_{j,-2}(b) = \frac{c}{v_r^2 b^{10}}(2j-3)\begin{pmatrix} j & 2 & j-2 \\ 0 & 0 & 0 \end{pmatrix}^2, \quad c = \frac{21\pi^2 C_6^2}{1{,}280\hbar^2}$$

with c (eq. 7.c) absorbing all non v_r, b, j dependent constants.

The quantity $P^s_{j,-2}(b)$ is the <u>transition probability in the sudden limit</u>, i.e. when $\tau \to 0$, and $f(\tau)$ is the analogue of the "adiabatic correction factor" $A(\tau)$ of the ECS scaling law (eqs. 20). In fact, eqs.7 are

identical in form to the (1^{st} order limit) ECS theory with $\sigma^{s}_{j,-2}(v_r) \propto v_r^{-2/5}$ (a result earlier obtained[34] classically), with $A^2(\tau) \to f^2(\tau)$, and $l_c \to \bar{b}$ being adjustable parameters representing "average" impact parameters. The only discrepancy is the differing mathematical behavior of $f^2(\tau)$ and $A^2(\tau) = (1+\tau^2/6)^{-2}$; although both factors decrease monotonically with increasing τ, for $\tau \to 0$, $f^2(\tau) \to 1-\frac{16\tau^4}{21}$ while $A^2(\tau) \to 1-\tau^2/3$, and for $\tau \to \infty$, $f^2(\tau) \propto e^{-4\tau}$ while $A^2(\tau) \propto \tau^{-2}$. These differences are not unexpected since while we give a rigourous (to 1^{st} order) derivation valid only for $|\Delta|=2$ to obtain[35] $f(\tau)$, the authors of ref.10 make substantial assumptions in order to derive a more general $A(\tau)$ approximately valid for all Δ.

To finally obtain $\sigma_{j,-2}(v_r)$, eq. 7.a must be integrated over b (as in eq. 4.b), keeping in mind that this perturbation calculation is strictly only valid in the large b limit when $P_{j,-2}(b) \ll 1$. For simplicity we define $\bar{b}$ such that $P^{s}_{j,-2}(\bar{b}) = 1$ and take $\bar{b}$ as the lower limit to the impact parameter integration:

$$\bar{b} = V_r^{-1/5}\left[C(2j-3)\begin{pmatrix} j & 2 & j-2 \\ 0 & 0 & 0 \end{pmatrix}^2\right]^{1/10} \simeq C^{1/10} V_r^{-1/5} \qquad (8.$$

with the neglibable j dependence of [ ] in eq. 8 being ignored.

Similar to the derivation in ref. 10, we can treat $f^2(\tau)$ as a "small" (in the sense that $f^2(\frac{2\omega b}{v_r})$ varies much more slowly that b^{-10} for $b \simeq \bar{b}$) correction <u>factor</u> to the sudden result, it then being assumed that the relatively slow variation of $f^2(\tau)$ near $b = \bar{b}$ allows for the

removal of the $f^2(\tau)$ factor from inside the integral over b and then evaluating it at $\tau = \frac{2\omega\bar{b}}{v_r}$. However, in our theory $f^2(\tau) \propto e^{-4\tau}$, and so for a given b and large enough τ this assumption must break down, resulting in a smaller effective b where $|\Delta|=2$ is the dominent collision process with 2^{nd} order effects still small. In other words, severe torque averiging can significantly reduce the effective range of the anisotropic potential. To approximately account for this effect, we propose the following modification for evaluating $f^2(\tau)$ when taken outside the integral over b:

$$\gamma = \frac{2\omega b'}{v_r} \quad , \quad b' = \bar{b} f^{1/5}\left(\frac{2\omega b'}{v_r}\right) \qquad (9.$$

The modification of eq. 9 (obtainable by setting $P_{j,-2}(b')=1$) compensates for the otherwise overestimation of torque averaging effects at large τ due to the then decreased range of the anisotropic potential and thus lower effective $\bar{b}$; we still however use $\bar{b}$ for integration purposes when evaluating the $P^s_{j,-2}$ contribution to the cross-section. As a check for consistancy, we note from eq. 9 that provided $f^2(\tau)$ is not $\ll 1$ (severe torque averaging), $b' \simeq \bar{b}$ as should be expected. This theoretical modification of $\bar{b} \to b'$ is physically analogous to the reduction as v_r decreases of the ECS parameter l_c (see fig. III.37).

Using the above new prescription for pulling $f^2(\tau)$ outside the impact parameter integral, we can easily integrate eq. 7.a over b from

$\bar{b}$ (eq. 8) to ∞, which yields the following result:

$$a.\ \sigma^{s}_{j,-2}(v_r) = \sigma_o(2j-3)\begin{pmatrix} j & 2 & j-2 \\ 0 & 0 & 0 \end{pmatrix}^2 f^2(\tau)\, v_r^{-2/5} \qquad (10.$$

$$b.\ \tau = \frac{2wb'}{v_r}\,,\quad b' = \bar{b} f^{1/5}\left(\frac{2wb'}{v_r}\right)\,,\quad w = \frac{2Bj}{\hbar}$$

As the v_r dependence of $\sigma^{s}_{j,-2}$ is now given explicitly in eq. 10.a, we will for simplicity ignore the mild $v_r^{-1/5}$ dependence of $\bar{b}$ as in eq. 8, and for eq. 10.b and for all further discussion take $\bar{b}$ to be a constant adjustable parameter of our theory. Eq. 10.b itself must be solved for b' numerically. The constant σ_o bears the units of cross-section, with v_r taken dimensionless as usual.

Unfortunately, the above calculation for the $\Delta = 2$ collisions must fail at sufficiently low v_r because the long range attraction pulling together collison partners, coupled with the substantial torque averaging ($f^2(\tau) \ll 1$), which occurs increasingly with lower v_r will together effectively eliminate long range contributions to $\sigma_{j,-2}(v_r)$ and short range collision must then dominate the $|\Delta| = 2$ cross-section. Reasonable estimates to the short range, low v_r contribution to $\sigma_{j,-2}(v_r)$ can be obtained empirically from observation of our $\sigma_{j,-4}(v_r)$ results. Short range collisions are obviously less Δ dependent than long range ones, and as $\Delta = -4$ is the next closest case to $\Delta = -2$, and as the much smaller $\Delta = -4$ long range contribution does not obscure its short range

behaivor, the $\sigma_{j,-4}(v_r)$ can be expected to yield a good approximation to both the v_r dpendence and magnitude of the short range contribution to $\sigma_{j,-2}(v_r)$. Employing this method for j_i = 8, 22, we see from figs. 16 and 23 that $\sigma_{8,-4}(v_r)$ and $\sigma_{22,-4}(v_r)$ are constant to a good (and certainly sufficient for these purposes) approximation, both of magnitude in the range of 12-15 Å^2; we then assume that short range contributions to Δ = -2 are also independent of v_r for j_i = 8, 22.

For j_i = 42, we can actually observe the short range contribution to $\sigma_{42,-2}(v_r)$ directly, since as pointed out in III.6, the long range contribution to $\sigma_{42,-2}(v_r)$ at low v_r (where we are interested anyway) has been effectively reduced to zero by severe torque averaging. The low $v_r < 1.5$, presumably short range behavior of $\sigma_{42,-2}(v_r)$ appears to be $\sim v_r^{-p}$ with $0 < p < 1$, a conclusion that might have also been reached from $\sigma_{42,-4}(v_r)$. The relatively large velocity thresholds for j_i = 42, all $+\Delta$, combined with the observed "dynamical threshold" (see discussion in III.6) seen for larger $-\Delta$, would roughly mean that at low $v_r < 1$ only small $-\Delta$ RI collision channels are open; the result would be that a large fraction of Li_2^*-Xe collisions which overcome the centrifugal barrier and experience short range forces will end up with Δ = -2. This would predict, as indicated earlier, a cross-section $\propto v_r^{-2/3}$, not at all inconsistant with what is in fact observed for $\sigma_{42,-2}(v_r)$ at low v_r. We then assume $\sigma_{42,-2}(v_r) \propto v_r^{-2/3}$, and note from fig. 28 that $\sigma_{42,-2}(v_r) \approx 10/v_r^{2/3}$ Å^2 would not be a bad approximation for $v_r < 1.5$.

Thus, our final analytical approximation to $\sigma_{j,-2}(v_r)$ is given by

$$a.\ \sigma_{j,-2}(v_r) = \sigma_0\left[\frac{3j(j-1)}{2(2j+1)(2j-1)}\right] f^2(\gamma)\, v_r^{-2/5} + \sigma_1^j v_r^{-p}$$

$$b.\ p = 0 \text{ if } j = 8 \text{ or } 22,\quad p = \tfrac{2}{3} \text{ if } j = 42. \qquad (11.$$

$$c.\ \gamma = \frac{2\omega b'}{v_r},\quad b' = \bar{b} f^{1/5}\left(\frac{2\omega b'}{v_r}\right),\quad \omega = \frac{2Bj}{\hbar}$$

with $f^2(\tau)$ given by eq. 7.b, the 3-j symbol of 10.a written out explicity, with 5 free parameters σ_0, $\bar{b}$, and the three σ_1^j; the scale factor σ_0 also available theoretically from C_6 (see eq. 9.b), though its numerical value depends somewhat on the definition of $\bar{b}$. We point out the 5 parameters appearing in eqs. 11 are asumed to have no v_r dependence unlike the parameters appearing in the ECS theories at the end of chap. III.

In fig. 1 we show the "best" fit results using eq. 11 (dashed curves) along with the corresponding experimental result for $\sigma_{j,-2}(v_r)$; we used $\sigma_0 = 135\text{Å}^2$ $\sigma_1^8 = 13\text{Å}^2$, $\sigma_1^{22} = 14\text{Å}^2$, $\sigma_1^{42} = 11\text{Å}^2$, and $\bar{b} = 6.7\text{Å}$, all obtained by "eyeball" trial and error fitting. We consider theory and experiment to be in excellent agreement, with deviations always within expected error for each j_i and all v_r shown. Further, the values for the σ_1^j are all in fine agreement with their previous empirically estimated values from $\sigma_{8,-4}$, $\sigma_{22,-4}$ and $\sigma_{42,-2}$ (as one would hope), and the value $\bar{b} = 6.7\text{Å}$ is in excellent agreement with the large v_r "sudden

Fig. 1 Experimental results for $\sigma_{j_i,-2}(v_r)$ (solid lines) and theoretical predictions-fits (dashed lines) of eq. 11.

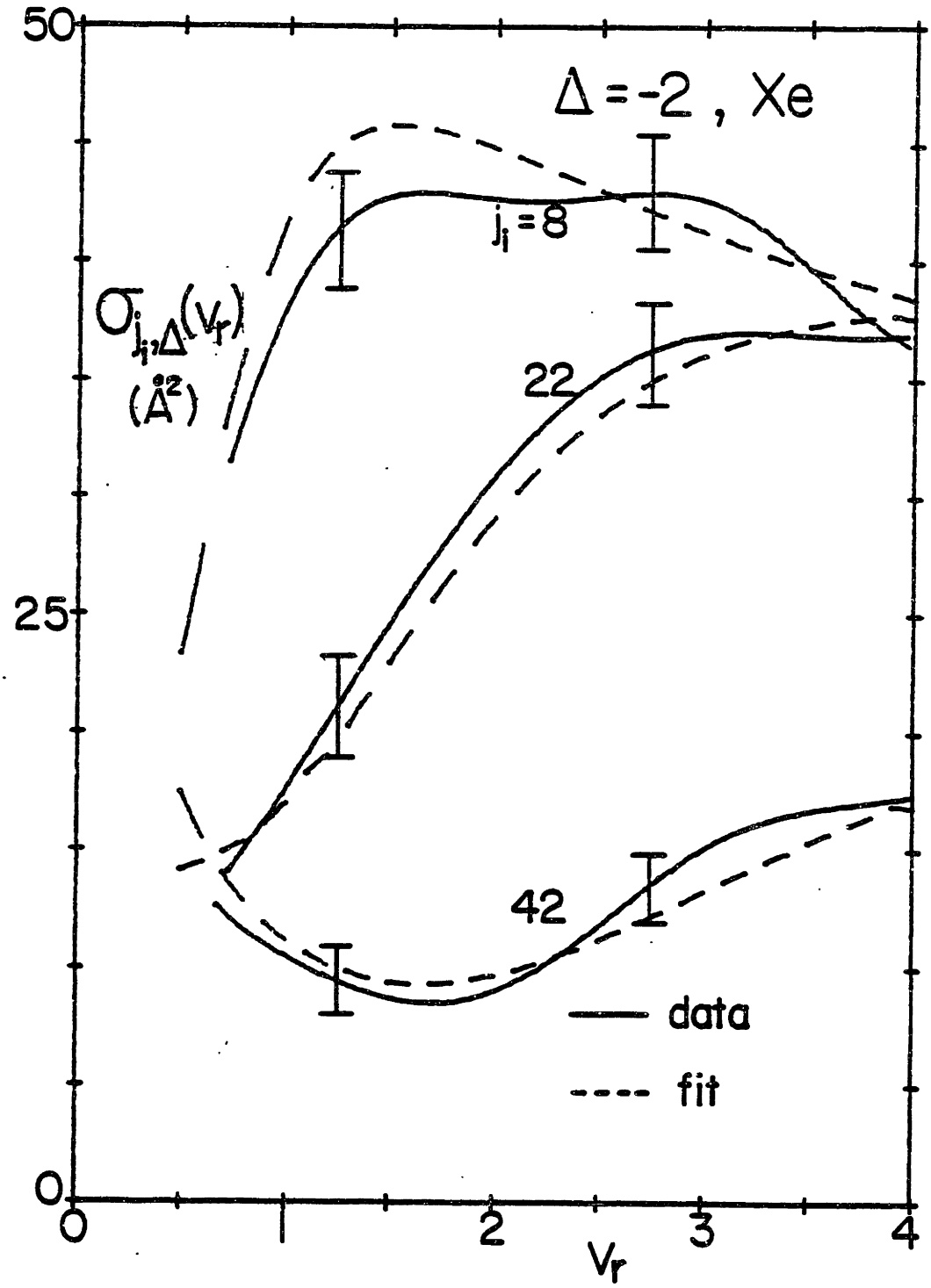

limit" values of l_c obtained with ECS-EP fits to Li_2^*-Xe (as one should expect); in addition, $\bar{b} = 6.7\text{Å}$ is quite consistent with the assumption of a long range collision. We consider the success of this simple theory (eqs. 11) as convincing proof of our repeated contentions that long range collisions dominate the behavior of $\sigma_{j,-2}(v_r)$ in Li_2^*-Xe, and that "torque averaging", epxressed quantitatively by $f^2(\tau)$, is responsible for the unique increasing with v_r behavior of the $|\Delta| = 2$ cross-section.

Attempts at "fitting" the Li_2^*-Ar,Ne $\Delta = -2$ data with the formulas of eqs. 11 showed reasonable agreement could again be obtained, but "best" fits found $\bar{b} \sim 3\text{Å}$, not unlike l_c from ECS-EP. Such a small, value for $\bar{b}$, is unfortunately, inconsistant with the assumptions made concerning the long range nature of the collisions, again reconfirming that long range forces do not play as important roles for Li_2^*-Ar,Ne, and invalidating application of eqs. 11 to these cases. However, as C_6 for Ar is $\simeq 1/3$ that for Xe, eqs. 7,8 would predict $\bar{b} \propto C_6^{1/5} \simeq 5.3\text{Å}$ for Ar if $\bar{b} = 6.7\text{Å}$ for Xe. As the long range attraction goes like R^{-7}, it is not at all unlikely that at $R \simeq 5.3\text{Å}$ short range contributions are of considerable importance, with the straight line trajectory approximation failing, and thus accounting for the fit value $\bar{b} \sim 3\text{Å}$ for Ar, similar (as stated above) to values for l_c found from ECS-EP fits.

2. Classical Trajectory Calculations

The interesting and widely varying v_r, j_i, Δ dependence of our Li_2^*-X results for $\sigma_{j_i,\Delta}(v_r)$ provide substantial motivation to attempt calculations to try and reproduce this behavior (as was done last section for Xe, $\Delta = -2$), and thus gain knowledge about the underlying collision dynamics, as well as the otherwise unknown Li_2^*-X potentials. (The great similarity between velocity averaged $\overline{k}^o_{j_i,\Delta}$ in many past experiments with seemingly widely differing systems would indicate that non v_r dependent, velocity averaged measurements are ineffective for obtaining any detailed knowledge of potentials). Unfortunately, it is impossible to make reasonable analytic calculations (like those in the last section) for RI collisions given general j_i, Δ, and one is then forced to resort to somewhat less informative numerical methods of calculation.

Exact, but extremely long and complicated quantum close-coupling calculations[36] are generally only used for highly quantum systems (i.e. low reduced mass $\mu \backsim 1$ a.m.u., small $j_i \backsim 1$, "weak potentials") where only a relatively few final j_f levels are accessible through RI collision, and where reasonable knowledge (e.g. by a priori calculation) of interaction potentials justifies their use. Several approximations[7,37] to the exact close-coupling equations have been developed to reduce the length and complexity of these quantum calculations, though it is not well understood what are the ranges of their validity, except

perhaps to generally say that they probably work best for purely repulsive[37] potentials (thus inapropriate to Li_2^*-X), with the decoupled L-dominant[37] approximation a probable exception to this.

However, the Li_2^*-X system (take X = Xe for example) we have studied is in fact a very classical system, being reasonably heavy ($\mu \simeq 12$a.m.μ.) with high j_i (average $j_i \simeq 25$ for our data), having a DeBroglie wavelength (for $v_r = 1$) of $\lambda \simeq .08$Å which is much less than range of the potential (certainly $\geq$ 5Å), and a strong enough interaction to couple by RI collision virtually all energetically allowable final j_f levels, as may be seen from our experimental results.

We have thus elected to employ classical trajectory calculations on Li_2^*-Xe for several reasons. The relative numerical simplicity and speed of classical trajectory methods[7,8], coupled with the intuitive and conceptual understandability of classical mechanics, as well as its proven applicability on classical-like systems[38], would appear to make this method an ideal choice for our purposes. More accurate (and complicated) semi-classical methods, such as those of Miller[39], which can include (unlike purely classical methods) quantum interference effects, have shown that these quantal effects are unimportant[39.b] when calculating degeneracy (orientation) averaged cross-sections, which of course is our intention anyway. Further, since the Li_2^*-Xe interaction potential is mostly unknown to start with, the speed of trajectory calculations makes them very suitable for repeated testing (fitting) of trial

potentials. Finally, we chose X = Xe since we feel our Xe results are our most accurate, having the greatest resolution, and exhibit by far the most interesting v_r dependence of the rare gas collision partners we have tried.

As a first stage in developing our calculation methods, we chose to treat Li_2^* as a rigid rotor, neglecting vibrational motion as well as VRI collisions and their influence on the dynamics of the problem. This results in a significant reduction of complexity of the equations of motion, and a large savings in computational time, since the vibrational period for $Li_2^* \simeq 1.3 \times 10^{-13}$ sec, is an order of magnitude faster than the rotational period of 16×10^{-13} sec, (for $j_i = 22$), and thus neglecting vibrational motion will permit a considerable increase in the necessary temporal step size for a predetermined integration accuracy. We will however, have definitely more to say on the important issue of VRI collisions later on.

1. Rigid Rotor Calculations

As in IV.1, we let $\vec{R}$ be the relative position vector, from the center of mass (CM) of the rotor to the target atom (treated as a point mass) with $R \equiv |\vec{R}|$; $\vec{r}$ again describes the orientation of the rotor (internuclear) axis, with $r \equiv |\vec{r}|$ = constant for a rigid rotor (i.e. internuclear separation is assumed fixed). Our coordinate system axis are assumed to have fixed orientation in space, with the origin moving with the constant CM velocity of the collision system, thus removing the

unimportant CM motion from the problem; as $\vec{R}$ is a relative coordinate, the location of the coordinate system origin is irrelevant for our purposes. We again assume (without loss of generality) that initial relative velocity $\vec{v}_r = v_r\hat{y}$ to be along the y axis and in the x-y plane, so (relative) orbital angular momentum $\vec{L}$ is initially along the z axis, $\vec{L} = L\hat{z}$. To avoid confusion with axis unit vectors $\hat{x}$, $\hat{y}$, $\hat{z}$, we will use the notation for Cartesian components of $\vec{R}$ and $\vec{r}$ as $\vec{R} = R\hat{R}$, $\hat{R} = (R_x, R_y, R_z)$ and $\hat{r} = (r_x, r_y, r_z)$.

The following set of equations of motion (our initial choice for developing the method) are a somewhat unusual hybrid mixture of Cartesian, spherical, and angular momentum variables. The equations are derivable directly from Newton's equations, along with the conditions (physically required by total rotational invarience symmetry) that $V(\vec{R},\vec{r}) = V(R,\hat{R}\cdot\hat{r})$ for the interaction potential V, and conservation of total angular momentum $\vec{J} \equiv \vec{j} + \vec{L}$. The equations of motion, along with relevant relations, are given in vector form by

$$a.\ \frac{d\vec{j}}{dt} = (\hat{R}\times\hat{r})\frac{\partial V}{\partial(\hat{R}\cdot\hat{r})},\quad V = V(R,\hat{R}\cdot\hat{r})$$

$$b.\ \frac{d\hat{r}}{dt} = \frac{1}{I}(\vec{j}\times\hat{r}),\quad I \equiv \frac{m_p r^2}{4},\quad r \text{ fixed at } 3.2\text{Å}$$

$$c.\ \frac{dR}{dt} = \frac{1}{\mu}P_R,\quad \mu \equiv m_p m_t/(m_t+m_t)$$

$$d.\ \frac{dP_R}{dt} = \frac{L^2}{2\mu R^3} - \frac{\partial V}{\partial R} \qquad (12.$$

$$e.\ \frac{d\hat{R}}{dt} = \frac{1}{\mu R^2}(\vec{L}\times\hat{R})$$

$$f.\ R_z = \frac{1}{L_z}(L_x R_x + L_y R_y)$$

$$g.\ \vec{L} = \vec{J} - \vec{j}\ ,\ \frac{d\vec{J}}{dt} = 0$$

$$h.\ \vec{j} \equiv I\left(\hat{r} \times \frac{d\hat{r}}{dt}\right),\ j = |\vec{j}|,\ \vec{L} \equiv \mu R^2\left(\hat{R} \times \frac{d\hat{R}}{dt}\right),\ L = |\vec{L}|$$

$$i.\ E = \frac{P_R^2}{2\mu} + \frac{L^2}{2\mu R^2} + \frac{j^2}{2I} + V(R, \hat{R}\cdot\hat{r}),\ \frac{dE}{dt} = 0$$

The orbital angular momentum $\vec{L}$, and the rigid rotor rotational angular momentum $\vec{j}$ are mathematically defined in eq.12.h; I = the (fixed) moment of inertia of the rotor, and (in our usual rotation) m_p, m_t, and μ are the rotor, target and reduced mass respectively. The equations of motion themselves are given explicity in eqs. 12.a-e, a set of 11 1^{st} order, coupled, partial differential equations. We can however, eliminate the z component of eq. 12.e and obtain $R_z(t)$ through eq. 12.f, which employs the identity $\vec{L}\cdot\hat{R} = 0$ (which follows by definition), thus reducing the set of independent variables to 10 - $\vec{j}$, $\hat{r}$, R, P_R, R_x, R_y. The quantity P_R is the linear momentum along the radial direction $\hat{R}$ (i.e. $P_R = \vec{P}\cdot\hat{R}$); equations 12.c,d are the usual equations of orbital mechanics, with $L^2/2\mu R^2$ the "centrifugal potential". The orbital angular momentum (<u>not</u> conserved) is obtained by conservation of $\vec{J}$ through eq. 12.g. The total energy E (conserved) is also given explicitly in eq. 12.i.

Before integrating the above equations of motion, initial conditions for each variable must be specified. Identified by a subscript

"O", they are as follows:

$$\text{a. } J_o = j_i + \tfrac{1}{2}, \quad \vec{J}_o = J_o(\sin\theta\cos\varphi, \sin\theta\sin\varphi, \cos\theta)$$

$$\text{b. } \hat{r}_o = \left(-(\cos\theta\cos\varphi\sin\Psi + \sin\varphi\cos\Psi), -\cos\theta\sin\varphi\sin\Psi + \cos\varphi\cos\Psi, \sin\theta\sin\Psi\right)$$

$$\text{c. } R_o \Longleftrightarrow V(R_o,1) = \tfrac{1}{300}\left(\tfrac{\mu v_r^2}{2}\right)$$

$$\text{d. } P_{R_o} = -\mu v_r\sqrt{1 - b^2/R_o^2}$$

$$\text{e. } \hat{R}_o = \left(b/R_o, \sqrt{1 - b^2/R_o^2}, 0\right)$$

$$\text{f. } \vec{L}_o = \mu v_r b(0,0,1), \quad \vec{J} = \vec{J}_o + \vec{L}_o$$

$$\text{g. } b = b_{max}\sqrt{q}, \quad \cos\theta = 2q - 1, \quad \varphi = 2\pi q, \quad \Psi = 2\pi q, \quad 0 \le q \le 1$$

(13.

Eq. 13c assumes that the trajectory starts when R is effectively infinite, such that the interaction potential is negligible compared to the initial kinetic energy; eqs. 13.d-f then follow from our previously chosen geometry, with b = impact parameter, as usual. Eq. 13.a gives the initial magnitude and direction of rotational angular momentum $\vec{j}$, with $j_o = j_i + 1/2$ the semi-classical prescription[40] for assigning a continuous classical angular momentum j_o to a discrete, integer quantum rotational level j_i; θ, ϕ (the usual spherical angles) give the direction of $\vec{j}_o$. Eq. 13.b then gives the orientation of $\hat{r}$, with ψ the phase of $\hat{r}$ about the $\vec{j}$ direction, and $\theta = \phi = \psi = 0$ has $\hat{r} = \hat{y}$.

To simulate real experimental conditions, we must average over all orientations θ, ϕ, ψ and impact parameters b (we consider j_i, v_r fixed, as is our data for $\sigma_{j_i,\Delta}(v_r)$). We do this by the standard Monte Carlo method, choosing b, θ, ϕ, ψ as in eq. 13.g, with each "q" appearing

there a distinct (pseudo) random number generated by standard congruence methods[41], with q distributed uniform in (0,1). We choose ϕ and ψ uniformly distributed in $(0,2\pi)$ with θ in $(0,\pi)$ but distributed uniform in $\cos\theta$, to assure that $\vec{j}$ points into any solid angle $d\Omega = d\cos\theta d\phi$ with equal probability. We choose b in $(0,b_{max})$ uniformly distributed in b^2 so the # of trajectories per unit area is independent of b (i.e. uniform intensity). The quantity b_{max} is determined from the long range potential, and conservatively chosen so that trajectories with $b > b_{max}$ virtually always result in elastic scattering collisions, yielding no information on RI cross-sections.

It is naturally a great convenience to work with dimensionless dynamical variables, defined in terms of a set of units of appropriate physical scale for the problem at hand. We choose the following system of units:

$$\begin{aligned} &a.\ M = 1.6606\times10^{-24}\ \text{gr.} = 1\ \text{a.m.u.} \\ &b.\ L = 10^{-8}\ \text{c.m.} = 1\text{Å} \\ &c.\ T = 1.5746\times10^{-13}\ \text{sec.} \\ &d.\ \hbar = 1 \\ &e.\ V = L/T = 6.351\ \text{cm/sec} \rightarrow S_p = 1.14 \\ &f.\ E = ML^2/T^2 = 33.72\ \text{cm}^{-1} \end{aligned} \qquad (14.$$

with M, L, T of eq. 14.a-c as the basic units of mass, length, and time respectively. The units are defined (in Eqs. 12 a-c) so that $\hbar \equiv 1$ and M and L are of convenient size; derived units for velocity and energy

are also given in eqs. 12.e,f, with the VSDS velocity unit s_p conveniently $\simeq 1$ in these units. For the rest of this chapter, all quantities and dyamical variables are assumed to be expressed in the above units, unless explicitly specified otherwise.

For numerical integration of our equations of motion, we chose a method developed by Nordsieck[42], and recommended by past authors[8.a]. The Nordsieck method (NM) is applicable to a system of n nonlinear, 1st order coupled differential equations $\frac{dy_i(x)}{dx} = f_i(x, y_1, y_2 \cdots y_n)$, $i = 1, 2, \ldots n$ (or in vector notation, $\frac{d\vec{y}}{dx} = \vec{f}(x,\vec{y})$) with independent variable x, and n coupled, dependent variables y_i $i = 1, 2, \ldots n$. (In our case, x = time = t, and y_i are the 10 dynamical variables given in eqs. 12). The NM method is based on a Taylor series expansion, and is (we feel) superior to the more common Runge-Kutta (R-K) and predictor-corrector (P-C) methods[43]. NM is self-starting (like R-K), has the efficiency and error-estimatimng capability of P-C, and unlike either (because with NM, $\vec{y}(x)$ and higher derivitives at a single previous x yield $\vec{y}(x+h)$) allows for quick and simple automatic variable step-size control, the efficiency of which cannot be too overly emphasized.

In particular, we used what Nordsieck refers to as his 5th order method, which is analyzed in detail in ref. 42. As the truncation error (error incurred from neglect of higher order derivitive terms) per step is shown to be given approximately by

$$\vec{E}_t(x+h/2) = \frac{1}{70} h^7 \vec{y}^{VII}(x) + O(h^8) \qquad (15.$$

which goes like the 7^{th} derivative, this particular case might be more commonly referred to as a 6^{th} order method.

Our automatic step size control algorithm consists of independent tests on both stability (propagation of error) control and truncation error. Our stability test is the same as that recommended by Nordsieck[42], while our truncation error test is similar in nature, but formulated somewhat differently. Having previously calculated and stored $\vec{q}(x)$, an estimator (to order h^5) of $h^5\vec{y}^{VI}(x)$, $\vec{q}(x+h)$ is then calculated during the integration step $x \to x+h$. The difference $\vec{e}(x+h) \equiv \frac{1}{70}(\vec{q}(x+h) - \vec{q}(x)) = h^{-1}\vec{E}(x+h)$ (to order h^6 - see eq. 15) is then the truncation error <u>per unit x interval</u> when integrating $x \to x+h$; our step size control check then consists of the following test:

$$|e_i(x+h)|_{max} \leq \epsilon \quad , \quad 1 \leq i \leq n \qquad (16.$$

where "max" refers to the maximum among all variables y_i ($1 \leq i <= n$), and ε is our chosen upperbound for tolerable error per unit x. If the error test of eq. 16 is failed, we let $h \to h/2$ and repeat integration step $x \to x+h$; failure of the stability test (applied previous to eq. 16) also results in halving the step size h and restarting. If however, the stability test is passed, <u>and</u>, it is then subsequently found that

$$|e_i(x+h)| \geq 100\epsilon \text{, all } i \quad 1 \leq i \leq n \qquad (17.$$

then the integration step $x \to x+h$ is completed, and we let $h \to 2h$ before

proceeding with the next step. Changing the step size h when using NM requires rescaling of the derivative terms stored during integration; we use an improvement to the original rescaling procedure given by Nordsieck as recommended by other workers[44] which reduces rescaling error by an order of h, to $O(h^7)$.

We have found from experience that for our rigid rotor calculations, a value $\varepsilon \simeq 10^{-3}$ will give convergence (i.e. no significant change in final results for $\vec{j}_f$ as ε is further decreased) for $\gtrsim$ 99% of all trajectories, with total energy E (eq. 12.i) found conserved to better than .01%. We have further empirically observed that although the average step size $h \sim .1$ (we restrict $h \leq .5$), it varies (due to automatic step size control) by close to 2 orders of magnitude in the course of a typical collision, indicating that a fixed step size routine would cost about a factor of $\sim$100 in computation time.

Having chosen initial conditions (eqs. 13) at (by definition) $t \equiv 0$ (and using the starting method recommended by Nordsieck), we proceed to integrate the equations of motion (eqs. 12.a-f) checking after $t > R_o/v_r$ to see if $R(t) > R_o$. When the latter is found true, further more sophisticated checks are done to determine whether rotational angular momentum $\vec{j}(t)$ has effectively converged to its asymptotic value (as $R \to \infty$, $P_R > 0$). If determined converged at some time t_f, the calculation is halted, and we assign

$$j_f = \sqrt{j_x^2(t_f) + j_y^2(t_f) + j_z^2(t_f)} - \tfrac{1}{2} \qquad (18.$$

as the final, non integer "quantum rotational level" of the rotor, using the semi-classical prescription (eq. 13.a) in reverse now. To assign an integer value of Δ for each trajectory, we use the prescription

$$\Delta \equiv 2\left[\frac{(j_f - j_i)+1}{2}\right] \qquad (19.$$

$[\ ] \equiv$ greatest integer function

which is equivalent to the standard histogram (bin) method, with bin size = $\pm$ 1 about all integer j_f with identical parity to j_i. The rounding of Δ to the nearest even integer is required by the homonuclear symmetry of the rigid rotor (and Li_2^*) which quantum mechanically requires Δ = even integer. This classical $\rightarrow$ quantum bin assignment procedure for the homonuclear case has been shown to work well in the past[45], and unlike the "near" homonuclear case, where propensity against Δ = odd collisions (a quantum interference effect[39.b]) cannot be classiclaly observed. In any case, after adding another "tally" to the particular Δ value bin, the procedure repeats for a new trajectory with new randomly chosen initial conditions (eqs. 13).

Assuming a total of N trajectories have been run, are if n_Δ is the number of trajectories resulting in particular value Δ (eq. 19) then, we have

$$\sigma_{j_i,\Delta}(v_r) = \pi b_{max}^2 (n_\Delta/N) \qquad (20.$$

as the classical trajectory calculation result for $\sigma_{j_i,\Delta}(v_r)$, where j_i,

v_r have been fixed throughout the calculation. Eq. 20 follows from the basic definition of cross-section ≡ # scattered events ÷ incoming intensity, with n_Δ the number of collisions scattered into the $j_f = j_i + \Delta$ channel, and $N/\pi b_{max}^2$ the uniform intensity (# per unit area) of the incoming initial particle "beam". As the expected statistical <u>fractional</u> error in $\sigma_{j_i,\Delta}(v_r) \simeq 1/\sqrt{n_\Delta}$, one must generally run many trajectories ($N \sim 5{,}000$) to get reasonable ($\sim$10%) convergence of results for all Δ of interest.

A uniform impact parameter selection (UIPS) method, where impact parameter b is chosen uniform in b (and not b^2 as in eq. 13.g) is a possible alternative to improve the rapidity of convergence of trajectory results. Choosing b uniform in b^2 is equivalent to $p(b) \propto b$ as the probability distribution for selected inpact parameters, and thus UIPS with $p(b) = 1/b_{max}$ will give more relative weight to smaller b, resulting in more (fewer) large $|\Delta|$ (elastic) trajectories; the large $|\Delta|$ cross-sections being naturally the smallest have of course the worst convergence problems. As UIPS is <u>not</u> equivalent to a uniform "beam" intensity distribution of b, eq. 20 must be modified as follows[45] ;

$$\sigma_{j_i,\Delta}(v_r) = \frac{2\pi b_{max}}{N}\left(\sum_i b_\Delta^i\right) \qquad (21.$$

where b_Δ^i is the impact parameter for the i^{th} trajectory that resulted in a Δ change in rotational level, with b_Δ^i stored separately. Of course, as $N \to \infty$, both regular (eq. 20) and UIPS (eq. 21) methods are

equivalent. We have empirically found UIPS to result in ∿50% more inelastic trajectories for given N, with results that show no systematic deviations with those obtained otherwise.

Finally, we note a few minor points concerning our method. Firstly, having chosen a suitable b_{max}, we require that R_o (otherwise determined from eq. 13.c) be $\geq 1.5\ b_{max}$ to insure a reasonable trajectory path length. Secondly, we eliminate from consideration very long orbiting collisions where the collision partners become quasi-bound due to translational → rotational energy transfer causing relative energy $E_r = E - j^2/2I$ (eq. 12.i) to become negative, and then undergo multiple collision events with many (generally >5) sign changes of P_R; preliminary tests showed that such collisions are generally hyper-sensitive to initial conditions and numerical error, with results for j_f non-convergent (and thus meaningless) even for $\varepsilon < 10^{-6}$. To eliminate this problem, we impose a maximum collision time (minimum time $\approx 2R_o/v_r$) of $6R_o/v_r$ if $E_r(t=6R_o/v_r) < 0$, and $10R_o/v_r$ otherwise, after which in either case the trajectory is halted, results discarded, and the trajectory re-started with new initial conditions. This trajectory failure is however, a rather rare event, happening in ∿ 0.3% of all trajectories for $v_r \approx 1$ and considerably less as v_r is increased.

As a diagnostic tool, as well as for our own amusement, our trajectories program had been adapted to use the available computer graphics to plot trajectory "movies" on storage scopes by drawing "x" to mark

atom and diatom positions in the x-y plane. The movies were found to be very useful for giving a pictorial understanding of RI collision dynamics, and were also of great aid in debugging our programs in their development stages.

As a final check, we attempted to reproduce earlier rigid-rotor trajectory calculations of Pattengill and Bernstein[8.b] on N_2-Ar using a simple analytical 6-12 type potential which those authors refer to as potential PLBC. Comparison of our results and theirs for $j_i = 10$ $v_r = 5.47$ showed no differences outside of those due to expected statistical error.

Choice of potential.

From a physical viewpoint, the most important step in doing trajectory calculations is the choice of interaction potential $V(R,\hat{R}\cdot\hat{r}) = V(R,\cos\gamma)$. Due to our relative ignorance of Li_2^*-Xe potentials (and for computational efficiency) we decided to try to model the potential with a relatively simple continuous analytical representation which allows rapid calculation of $V(R,\cos\gamma)$ as well as $\frac{\partial V}{\partial r}$, $\frac{\partial V}{\partial \cos\gamma}$ which are needed for integration of the equations of motion. We attempt to incorporate in our model known quantiative experimental or theoretical information that <u>is</u> known about Li_2^*-Xe potentials, as well as qualitative information on $V(R,\cos\gamma)$ expected from similar potentials or form any other sources.

The failure of our first model potential (adapted from simple

well-known analytic representation of atom-atom potentials) to give agreement with our experimental data for $j_i = 22$ led us to make an important modification which substantially improved the quality of agreement between calculations and experiment. Below we will describe our choices for $V(R,\cos\gamma)$ and our motivation behind our proposed modification.

Our first trial model potential $V(R,\cos\gamma)$ was of the form

$$a.\ V(R\cos\gamma) = \frac{\epsilon}{k-6}\left[6e^{k(1-R'/a)} + \frac{k}{R'^6}\left(1 + S(R,\gamma)b_2 P_2(\cos\gamma)\right)\right]$$

$$b.\ S(R,\gamma) = \left[1 + e^{c(d-R'/a)}\right]^{-1} \qquad (22.$$

$$c.\ R' \equiv R/\sigma,\quad a \equiv 1 + a_2 P_2(\cos\gamma),\quad P_2(x) = \frac{3x^2-1}{2}$$

$$d.\ C_6 = \frac{k}{k-6}\epsilon\sigma^6$$

The above potential $V(R,\cos\gamma)$ with free parameters ϵ, σ, k, a_2, b_2, c, d is a simple adaptation of the well known exponential-6 (exp-6) representation of spherical atom-atom potentials. As written, ϵ is the well depth at the minimum occuring at $R = \sigma$, for $\gamma = 55°$ ($P_2(55°) = 0$). The long range (2nd) term in eq. 22.a (for $R \to \infty$ and $S(R,\gamma) \to 1$) is well known from theoretical considerations[28,46], being the leading asymptotic expansion term representing the induced dipole-dipole interaction of Li_2^*-Xe as $R \to \infty$ and electron overlap becomes negligable. Values of the quantities b_2 and also C_6 (eq. 22.d) are given for Li_2^*-Xe in ref. 4

based on calculations and experimental data; the values are $b_2 = .66$ and $C_6 = 1.4 \times 10^7$ erg-Å^6 $= 4.2 \times 10^5$ in our units (eqs. 14).

Unfortunately, information concerning the short range potential is essentially unknown, and so we chose an exponential repulsion known to be a reasonable approximation for atom-atom potentials[47]. We assumed the short range to be simply described by $P_2(\cos\gamma)$, but we unorthodoxly chose to put the $P_2(\cos\gamma)$ dependence in the exponent (more on this shortly). However, one feature of the short and intermediate range potential we strongly expect to be true is that the well depth and potential minimum at $\gamma = 90°$ should be deeper and occur at smaller R than when compared with $\gamma = 0°$. We base this statement on a pictorial model of $Li_2^*(A^1\Sigma)$ as a "combination" of Li(2s) and $Li^*(2p)$ (the asymptotic dissociation limit[15] of $Li_2(A^1\Sigma)$, with p orbital lobes along $\hat{r}$ so $\vec{L}_{electron} \cdot \hat{r} = 0$ as is for Σ states) and calculations by Baylis[28] of Li(2s)-Xe and Li*(2p)-Xe well depths ϵ and well minimum locations R_{min} for $\gamma = 0°$, $90°$ (i.e. Σ and π in standard notation).

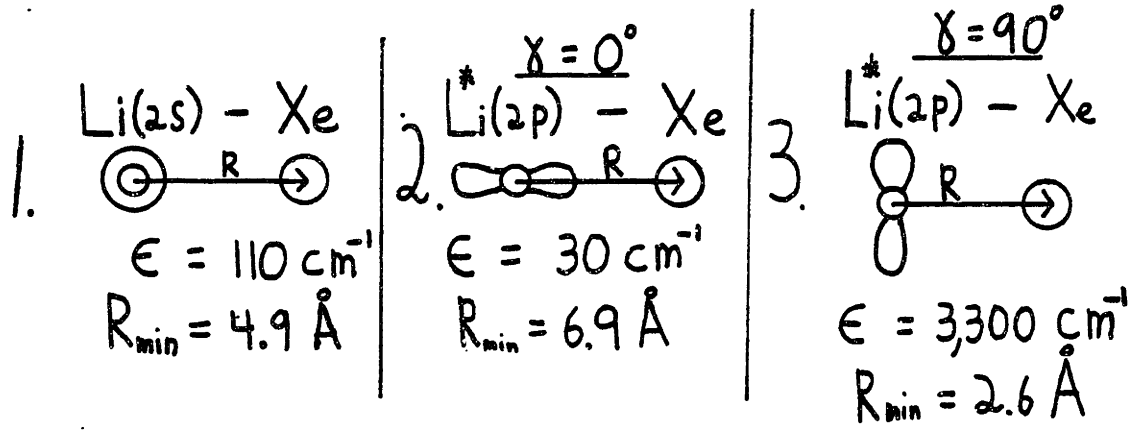

It is clear from the above "sketches" of electron density distributions that even if Baylis' results are only order of magnitude accurate, the simple model of $Li_2^*(A'\Sigma)$-Xe for $\gamma = 0°$, $90°$ as symmetrized combinations of cases 1,2 and 1,3 respectively is compelling evidence backing our earlier statement concerning the γ dependence of $\varepsilon(\gamma)$ and $R_{min}(\gamma)$; we take $\varepsilon(90°) > \varepsilon(0°)$ and $R_{min}(0°) > R_{min}(90°)$ as a <u>constraint</u> on our choice of potentials and potential parameters.

It was this constraint which led us to express the short range $P_2(\cos\gamma)$ asymmetry inside the exponent as in eq. 23.a, as opposed to the more common factorization method, having $V \propto (1+a_2P_2(\cos\gamma))e^{-kR}$ for the short range potential. For relatively large $b_2 \simeq .66$, we found the factorization aproach very inflexible for constraining $\varepsilon(90°) > \varepsilon(0°)$, requiring $a_2 > 1.5$ ($0 \leq a_2 < 2$ always) and giving the short range potential contours an unphysical kink at $\gamma = 90°$. Our choice, (expressed in eq. 23.a) needed only $a_2 \sim 0.2$ to satisfy the previously discussed constraint; further, keeping $P_2(\cos\gamma)$ in the exponent can (in a sense) incorporate higher order terms of an expansion $\Sigma_n C_n V_n(R) P_n(\cos\gamma)$ of the short range potential which in reality must certainly be non-zero.

We note that although the exp-6 type potential is unrealistic at sufficiently small R since $V(R,\cos\gamma) \to -\infty$ as $R \to 0$, if we restrict the parameter $k > 12$ (larger $k \to$ steeper repulsion) the short range <u>maximum</u> of $V(R,\cos\gamma)$ occurs for energies $>>> \frac{1}{2}\mu v_r^2$ for any v_r of interest to us. This will assure the unphysical behavior will be completely inside the

classically forbidden region.

Finally, we include the function $S(R,\gamma)$in our long range potential (see eq. 23.a), with $S(R,\gamma)$ having the property of a "switching function", with $S \to 1$ $R >> d$, and $S \to 0$ $R << d$ (assuming $cd >> 1$), with the rapidity of the switch $0 \to 1$ increasing with increasing c. A physical justification of $S(R,\gamma)$ is the reduction of the long range asymmetry (characterized by b_2) which should hapen as electron overlap and repulsion begins to occur, but where long range forces still dominate; we thus choose the γ dependence of $S(R,\gamma)$ similar to that of our short range repulsive term. Mathematically, $S(R,\gamma)$ with two additional free parameters c,d allows increased freedom in choosing the relative depths and locations of the 0°, 90° well minimums.

Having felt that our data for Xe, $j_i = 22$ was perhaps the most interesting data set from a v_r dependence viewpoint, and being that $j_i = 22$ was the intermediate value of j_i measurements were made for, we chose $j_i = 22$ to try out our model potential of eq. 23.a, using our trajectories program to attempt a determination of a "best" set of potential parameters which would "maximize agreement and thus fit (by trial and error) the potential and the calculations to our experimental results for $\sigma_{22,\Delta}(v_r)$. It would next serve as a strong test of our calculations to see if reasonable agreement could also be achieved for $j_i = 8, 42$ with the same potential.

After extensive calculations ($\sim$100,000 trajectories) for $j_i = 22$,

and fixed $v_r = 2s_p$, using the potential model of eq. 23.3 with a wide range of trial values for the free parameters, our results were disappointing. Our most notable observations are summarized below.

1. General trial ranges for parameters were: $.05 < a_2 < .2$, $.4 < b_2 < 1.0$, $12 < k < 20$, $5 < c < 15$, $.8 < d < 1.25$. The partiuclar values $a_2 = .1$, $b_2 = .8$, $k = 15$, $c = 10$, $d = 1$ were found to work as well or better than other choices, and were generally the values used for the more extensively varied parameters ε,σ, the most important and influential of the potential parameters. Trial ranges were $3 < \varepsilon < 30$, $4 < \sigma < 7$, with perhaps $\varepsilon \backsim 10$, $\sigma \backsim 5.25$ being "average".

2. Using the "best" set of potential parameters (see #1 above) and resticting the value of(see eq. 22.d) $C_6 \propto \varepsilon\sigma^6 \simeq \overline{C}_6 \equiv 4\text{x}10^5$ (the value given in ref. 4), we found we were able to obtain satisfactory agreement between experiment and theory for $\Delta = +-2, -4, -8$, with typical calculated values at $v_r = 2s_p$ of $\sigma_{22,\pm2} = 28\pm2\text{Å}^2$, $\sigma_{22,-4} = 12\pm1.5\text{Å}^2$ and $\sigma_{22,-8} = 6.5\pm1\text{Å}^2$ (see figs. , for comparison with our measurements). However, trajectory results for $\Delta = -16, +6, +12$, and certainly all large positive Δ were systematically overestimating the experimental results by factors $\gtrsim 2$. The extent of this disagreement generally increased with increasing ε, though total cross-section $Q = \Sigma_\Delta \sigma_{j_i,\Delta}$ remained approximately constant for fixed C_6.

3. Reducing C_6 to $\simeq \overline{C}_6/4$ by reduction of ε was found to bring the calculated $\Delta = -16, +6, +12$ cross-sections into reasonable agreement

(≈within error) with experiment, except $\Delta = +12$ was still frequently ∿25% too large. However, this reduction in the value of C_6 also resulted in calculations underestimating the $\Delta = +-2, -4, -8$ cross-sections by factors ≈ 2.

The value of $C_6 \equiv \overline{C}_6$ quoted in ref. 4 was based on experimental measurements of ionization potentials[48] and rare gas polarizabilities[24], and we then expect its value to be within a factor of 2. We thus suspect that the asymmetric (with sign of Δ) disagreement between calculations and data, being worse (by overestimation) for large positive Δ to be a real ,serious inadequacy of our present potential model. This problem seems particularly puzzling for the case $\Delta = +6$, which being a relatively large cross-section, and with $v_r = 2s_p$ substantially above $v_{th} \approx .75s_p$, would thus naturally have been expected to be accurately determined by our classical trajectory calculation, especially when considering the good agreement with experiment found for $\Delta = \pm 2, -4$. For any reasonable choice of $\varepsilon > 100$ cm^{-1} (we speculate ∿ 100 cm^{-1} as an approximate lower bound for ε, based on earlier discussion of Li-Xe well depths), these peculiar, substantial overestimations stubbornly persisted.

Final and convincing proof of the failure of the inadequacy of our present model was found when we subsequently tried varying the initial relative velocity v_r, running additional trajectories at $v_r = 1s_p$ and $v_r = 3s_p$. For $C_6 \approx \overline{C}_6$, we found calculated results for $v_r = 1s_p$ gave worse

agreement than before with calculations overestimating all cross-sections by factors $\gtrsim 2$. However, this same potential gave reasonably good results at $v_r = 3s_p$ for almost all $\Delta \leq 6$, with a notable exception for $\Delta = +12$, still being overestimated by factors greater than 2. Conversely, for $C_6 \approx \overline{C}_6/4$ (see #3 above) calculations for $v_r = 1s_p$ agreed with experiment to roughly within error for all $\Delta \leq 6$, ($v_{th} = 1.04$ for $\Delta = +12$). On the other hand, these latter potentials underestimated the $|\Delta| \leq 4$ cross-section by factors ≈ 2 for $v_r = 3s_p$.

Although it is clear our present potential model is incapable of yielding calculations which accurately describe our data, the manner of its failure and its dependence on v_r offer clues as to what the problem is, as well as possible modifications for its solution. The relatively good agreement found for $|\Delta| = 2$ at $v_r = 3s_p$ for potentials with $C_6 \approx \overline{C}_6$ offers strong indication that $\overline{C}_6$ is in fact a realistic value, and well describes that actual long range potential, and especially the long range torque. The then serious overestimations of cross-sections at $v_r = 1s_p$ indicative of an intermediate potential (at or near the well minimum) which is very likely too strong, with "strength" being characterized by both σ and especially ε. This problem is naturally most severe at low v_r when strong long-intermediate range attraction can pull together collision pairs for even relatively large impact parameter trajectories, which of course give the larger contributions to the cross-sections. The contrasting failure at $v_r = 3s_p$ and success at $v_r = 1s_p$

for potentials with $C_6 << \overline{C}_6$ (e.g. $\overline{C}_6/4$) definitely give even further "proof" of our above contentions.

Mathematically, we would thus wish to modify our potential model so to leave the <u>long</u> range torque $\propto \frac{\partial V}{\partial \cos\gamma}$ relatively unchanged, while simultaneously reducing the long-intermediate range attraction $\propto \frac{\partial V}{\partial R}$. It would be necessary for such a model to allow an additional degree of freedom in choosing ε, σ and a value for C_6; the current potential constrains $C_6 \propto \varepsilon\sigma^6$, with thus only two of these three parameters independent.

We now propose the following modificaion to our previous potential $V(R,\cos\gamma)$ of eq. 22.a

$$a.\ V(R\cos\gamma) = \frac{\epsilon}{k-(6-c_1 S_0 e_0)}\left[(6-c_1 S_0 e_0)e^{k(1-R'/a)} - \frac{k S_1(R,\gamma)}{S_0} R'^{-6}\left(1+S_2(R,\gamma)b_2 P_2(\cos\gamma)\right)\right]$$

$$b.\ S_i(R,\gamma) = \left[1+e^{c_i(d_i - R'/a)}\right]^{-1},\quad e_0 = e^{c_1(d_1-1)},\quad S_0 = (1+e_0)^{-1}$$

$$c.\ R' = R/\sigma,\quad a = 1+a_2 P_2(\cos\gamma) \qquad (23.$$

$$d.\ C_6 = \frac{k}{k-(6-c_1 S_0 e_0)}\,\frac{\epsilon\sigma^6}{S_0}$$

$$e.\ c_1 S_0 e_0 < 6$$

The only real change in the new potential $V(R,\cos\gamma)$ of eq.23.a is the inclusion of the switching function $S_1(R,\gamma)$ which multiplies the entire long range term, in addition to the earlier one (now called

$S_2(R,\gamma)$) which only affected the long range asymmetry b_2. Additional multiplication factors which now appear are chosen so that ε and σ retain their origianl meaning. Asymmptotically, as $R \to \infty$, we now have $C_6 \propto \varepsilon\sigma^6/S_o$ (with S_o determined by c_1, d_1) which allows near independent selection of ε, σ and C_6; c_1 and d_1 must however, not be chosen too large as to cause unphysical behavior - see eq.23.e. Our new potential thus allows us to keep the <u>long</u> range potential ($\propto C_6R^{-6}(1+b_2P_2)$) fixed, while reducing ε, σ and thus the strength of the potential in the intermediate regions. In particular, this enables us to adjustably decrease the depth and steepness of the potential well, and thus reduce $\frac{\partial V}{\partial R}$ in this region, which we believe will reduce or eliminate the previous cross-section overestimation at low v_r. Similar to $S_2(R,\gamma)$, the inclusion of $S_1(R,\gamma)$ may be justified physically as accounting for partial electron overlap which decreases the pure dipole-dipole R^{-6} long range attraction, which is especially plausible for the electron orbital configuration of $Li_2^*(A^1\Sigma)$ and the relatively large many electron rare gas Xe atom.

Our new potential model (eq. 23.a) for $V(R,\cos\gamma)$ confirmed our above speculations and yielded markedly better agreement between calculations and measurements for $j_i = 22$ cross-sectons, especially for $v_r < 2s_p$. In fact, rigid rotor trajectory calculations with the new potential (eq. 23.a) can reproduce quantitatively the <u>magnitude and v_r dependence</u> of the $\sigma_{22,\Delta}(v_r)$ to very often within expected error, includ-

Fig. 2 "Best" rigid-rotor Li_2^*-Xe interaction potential (eq. 23 - Table 1) as a funtion of R, for γ = 0,90 degrees.

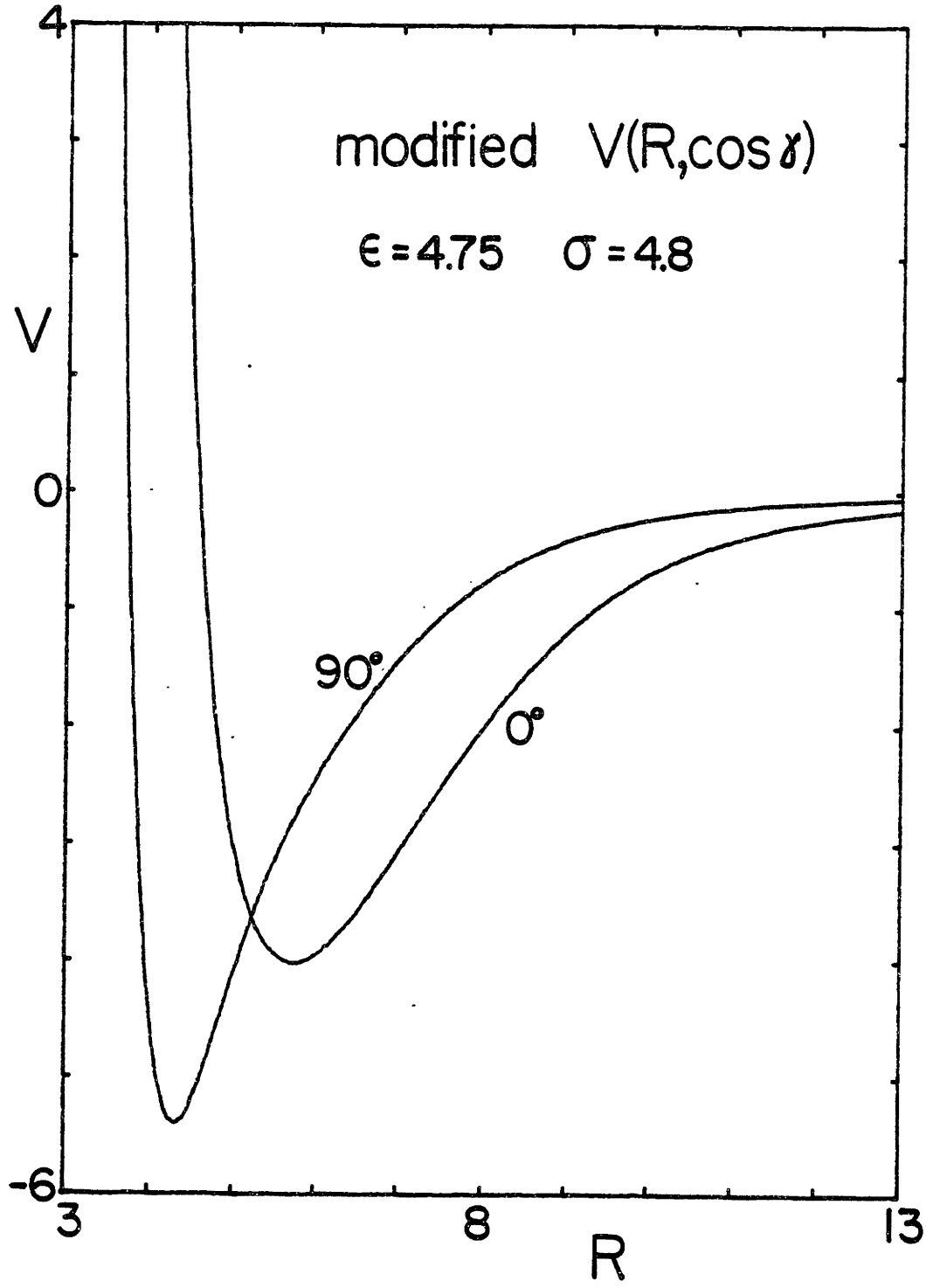

Table IV.1

"Best" Fit Rigid Rotor Potential Parameters

parameter	"best" value ± range
ε	4.75 ± .75
σ	4.8 ± .2
a_2	1.0 ± .05
b_2	.85 ± .10
k	15. +5,-2
c_1	5.0 ± .50
d_1	1.32 ± .05
c_2	10. ± 2
d_2	1.0 ± .10

Fig. 3 Comparison of unmodified exp-6 potentials (eq. 22) with equal ε or σ of the potential of fig. 2 (also shown).

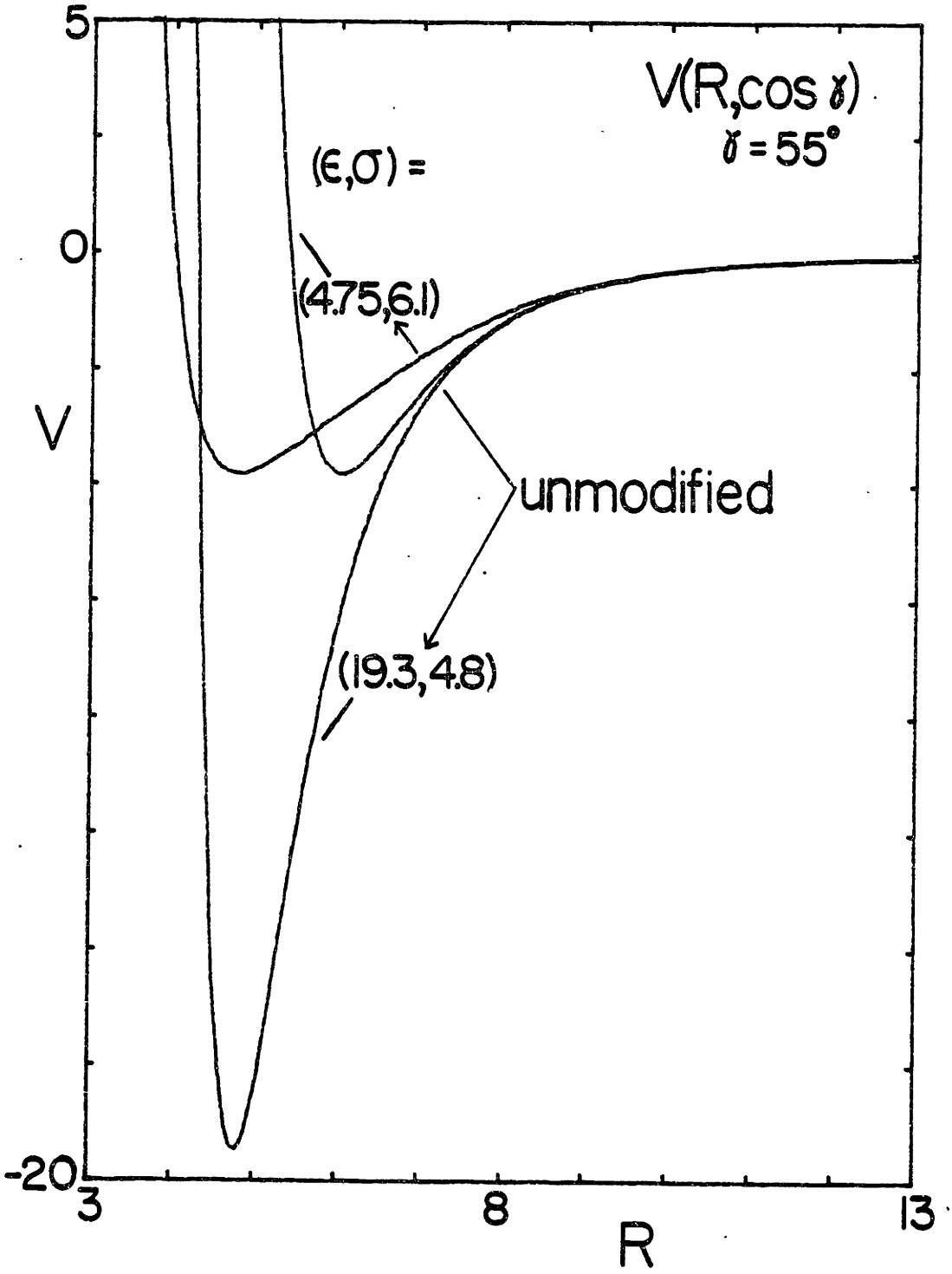

ing the rise of the $\sigma_{22,\pm2}(v_r)$ as well as the unusual and rapid v_r dependence of $\sigma_{22,-16}(v_r)$! In Table 1 we give the nine parameter values for the new potential which gave "best" results for the $\sigma_{22,\Delta}(v_r)$ at v_r = 1, 2, and $3s_p$; the ± values indicate "uncertainties" in these parameter values over which variation of parameters showed little or no significant or obvious systematic differences in calculated results.

In fig. 2, we plot our new potential $V(R,\cos\gamma)$ as a function of R for $\gamma = 0°$ and 90°, using the parameter values given in Table 1. For comparison, we show in fig. 3 the new and corresponding old, unmodified potentials at $\gamma = 55°$ for equal values of ε or σ, with C_6 the same for all. It is easily seen that while old and new potentials become identical in the asymptotic limit $R \to \infty$, comparison (especially of the equal σ cases) shows the new potential to have a much broader and shallower well, a feature crucial for obtaining the measured v_r dependence of the $\sigma_{22,\Delta}(v_r)$. As stated earlier, this substantially reduces the intermediate range attraction while maintaining the long range torque. Even for the equal ε comparison, the new potential has a less sharply varying well minimum, and of course a much smaller repulsive contour radius.

In figs. 4 and 5, we reproduce the deconvoluted results for $\sigma_{22,\Delta}(v_r)$ from chap. III, along with the trajectory calculations (symbols - see figs. for the key) of these cross-sections for v_r = 1, 2, and $3s_p$. The calculated values represent averages obtained from 5-10 different trajectory runs using slightly different potentials through small

Fig. 4 Experimental results for $\sigma_{22,\Delta}(v_r)$ (solid lines) and rigid-rotor trajectory results (symbols). Δ (and scaling) as shown.

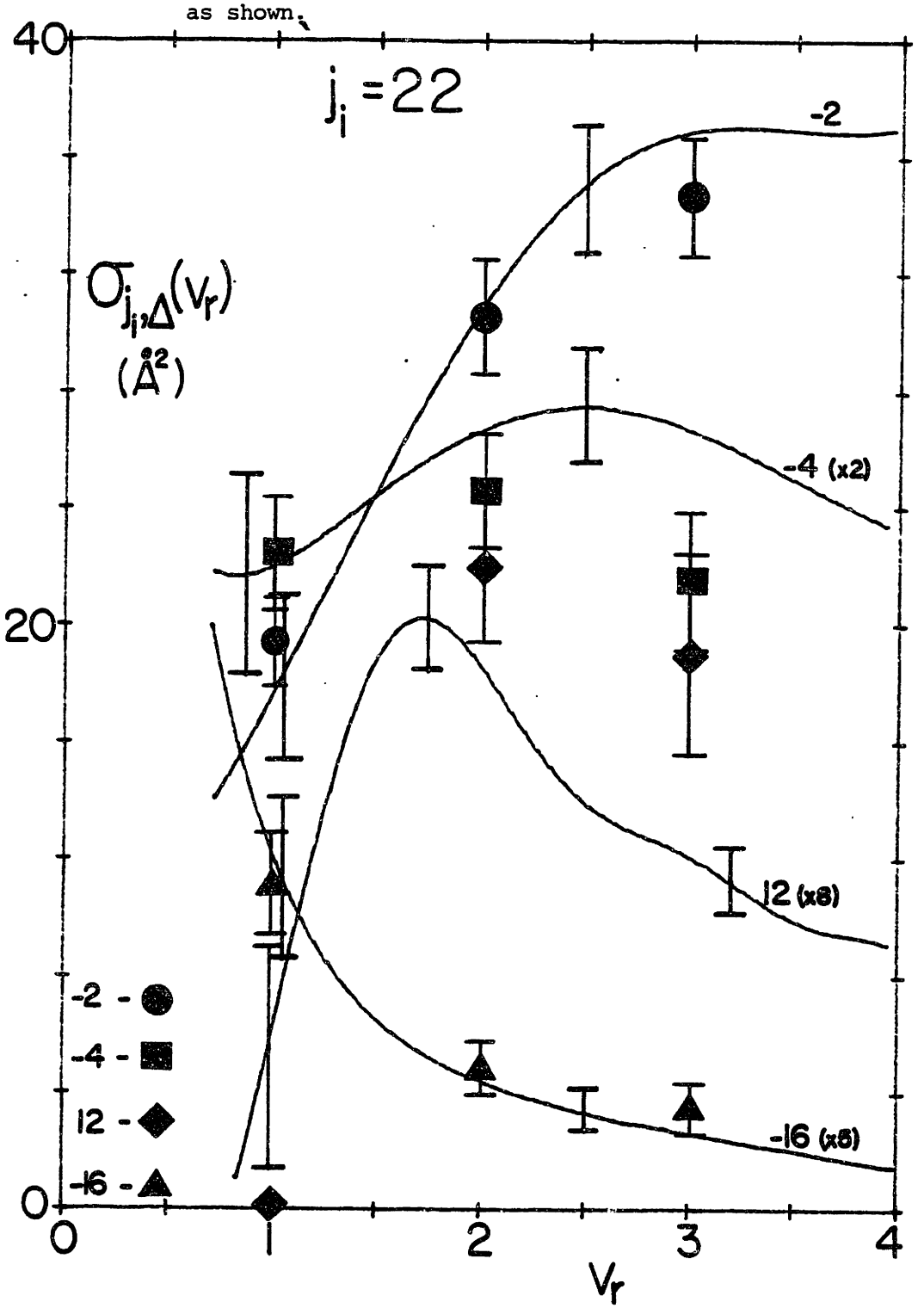

Fig. 5 Experimental results for $\sigma_{22,\Delta}(v_r)$ (solid lines) and rigid-rotor trajectory results (symbols). Δ (and scaling) as shown.

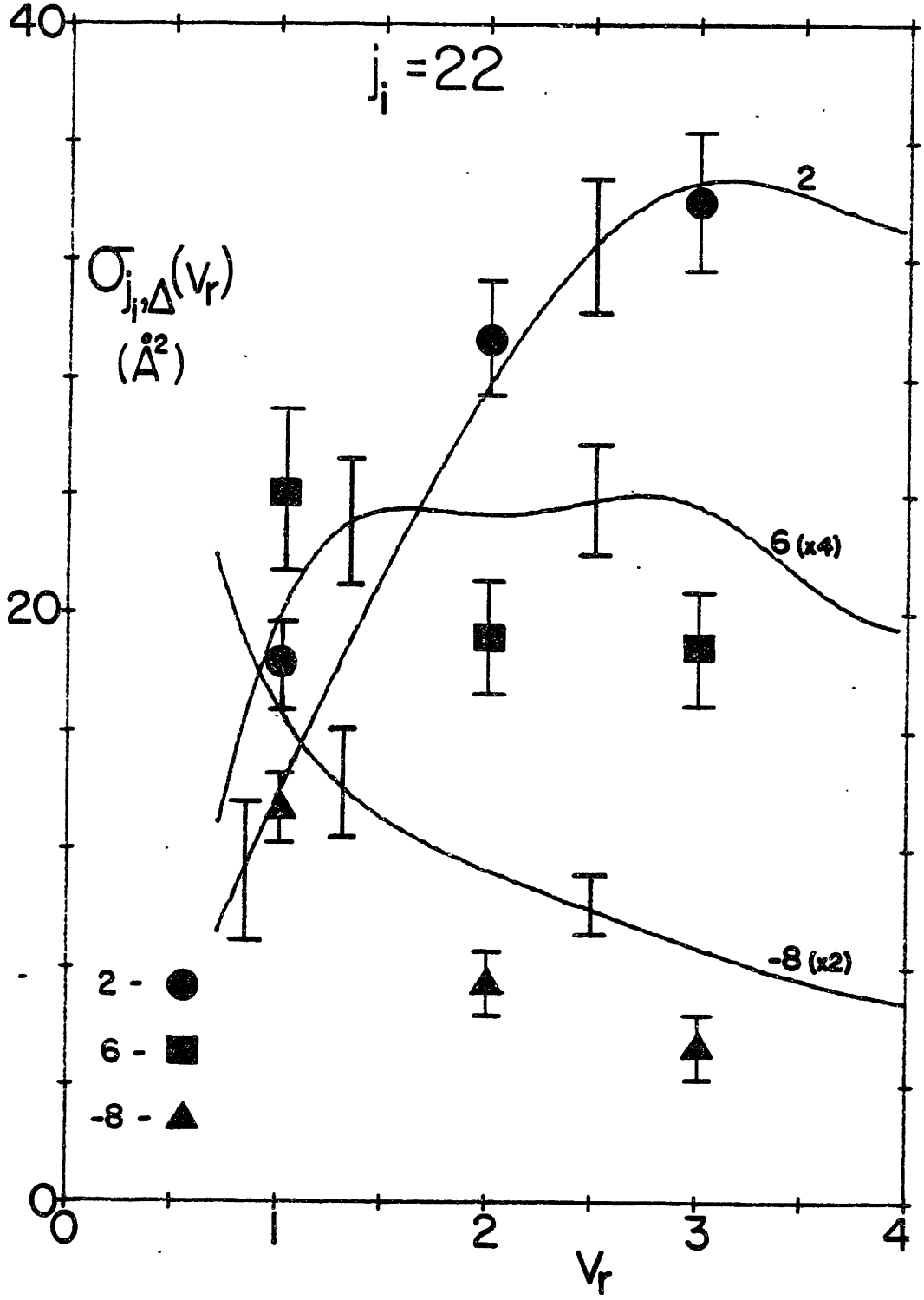

variations in the parameters (primarily ϵ and σ) over the ranges given in Table 1. The resuts were computed from a total of $\sim$ 30,000 trajectories run, with typically 55% inelastic (UIPS) and $b_{max} \simeq 10\text{Å}$. Error bars on the calculated values represent variations between the different potentials used (probably mostly statistical), as well as the expected statistical error incurred for any Monte-Carlo type calculation, going like $\delta\sigma_{22,\Delta} = \sigma_{22,\Delta}/\sqrt{n_\Delta}$, with n_Δ being the # of trajectories yielding a particular Δ result. We note that in addition to the shown deconvolution error bars, there is a 7-10% overall normalization uncertainty for each experimental result - see Table III.2.

We consider the agreement between theory and experiment in fig. 4 to be excellent, with $\Delta = +12$, $v_r = 3s_p$ a notable exception. In particular, the calculations agree with the (widely different) measurements of $\sigma_{22,-2}(v_r)$ and $\sigma_{22,-16}(v_r)$ to within error for all v_r; the v_r dependence of the $\Delta = -4$ cross-section is also fairly well reproduced, with the calculation appearing to be systematically low in magnitude by only about 20%. While the calculation is fairly accurate for $\Delta = +12$, $v_r = 2s_p$, the overestimation at $v_r = 3s_p$ appears to indicate that our calculations do fail to reproduce the rapid ($\sim v_r^{-1}$) fall-off seen experimentally for $\sigma_{22,12}(v_r)$ at larger v_r.

In fig. 5, we compare results for $\Delta = +2$, +6 and -8, the agreement for these cases being good, but somewhat less than the other cross-sections. The calculated results for $\Delta = +2$ (being very similar to

calculations for $\Delta = -2$) agree with experiment except for $v_r = 1s_p$, where the trajectories result overestimates the data. The calculations of $v_r = 1s_p$ also slightly overestimate the $\Delta = +6$ cross-section, while slightly underestimating the experimental values for $v_r \geq 2s_p$, but agrees with the experimental result that $\sigma_{22,6}(v_r)$ is basically constant over the measured velocity range. The v_r dependence of $\sigma_{22,-8}(v_r)$ is also reproduced reasonable well by our trajectory calculations (though perhaps somewhat overestimating the rapidity of the fall-off with increasing v_r), but like $\Delta = -4$, the calculations uniformly underestimate the measured values, in this case by about 30%.

Overall, considering the wide range of magnitudes and v_r dependences of the $\sigma_{22,\Delta}(v_r)$, as well as the virtually complete lack of a priori information available to us about the interaction potential, we feel our trajectory calculations have been surprisingly successful thus far in giving agreement with our measurements for $j_i = 22$, reproducing the v_r behavior of $\sigma_{22,\Delta}(v_r)$, and in the majority of cases give agreement of the cross-section magnitudes to within error. Since we however, essentially "fit" our potential to the $j_i = 22$ data, a final and more rigorous test of our model would be to compare calculations against measurements for the $j_i = 8$ and $j_i = 42$ data, without of course, any further modifications or change of parameters from our present potential - eq. 23.a and Table 1.

Unfortunately, as can be seen from fig. 6, the calculations for j_i = 8 do not agree with the data as well as for the j_i = 22 case. Somewhat surprising is the overestimation of ≃ 20% of the $|\Delta| = 2$ measurements (-2 not shown), especially for $v_r = 1s_p$, where the calculations do not exhibit quite as strongly the considerable reduction in cross-section shown by our data and predicted theoretically (sec. IV.1) on the basis of "torque averaging." This is perhaps due to the overestimation by the calculations of smaller Δ short range contributions, as is evidenced by the somewhat overly large values for Δ = -4 and -6 at $v_r = 1s_p$. As with $|\Delta| = 2$, the overall calculated v_r dependence of the Δ = +6 (not shown) and Δ = +12 cross-sections are also in good agreement with the deconvolutions, with magnitudes uniformly low by only ≃ 10% for Δ = +6, and essentially within error for Δ = +12. On the other hand, calculations for Δ = -4 and Δ = -6 (not shown) exaggerate the mild decrease with v_r of the measured $\sigma_{8,-4}(v_r)$ and $\sigma_{8,-6}(v_r)$.

The worst disagrement between calculations and experiment occurs for the Δ = +24 results, and to a lesser extent Δ = +18. Not unlike our earler finding for j_i = 22, Δ=+12, these calculations systematically and significantly overestimate the large positive Δ cross-sections at larger $v_r \geq 2s_p$ and additionally fail to reproduce the experimentally observed rapid fall-off with increasing v_r these cross-sections exhibit at large v_r. It also appears that this type of overestimation for the large positive Δ cross-sections at larger v_r (above threshold) is perhaps more

Fig. 6 Experimental results for $\sigma_{8,\Delta}(v_r)$ (solid lines) and rigid-rotor trajectory results (symbols). Δ (and scaling) as shown.

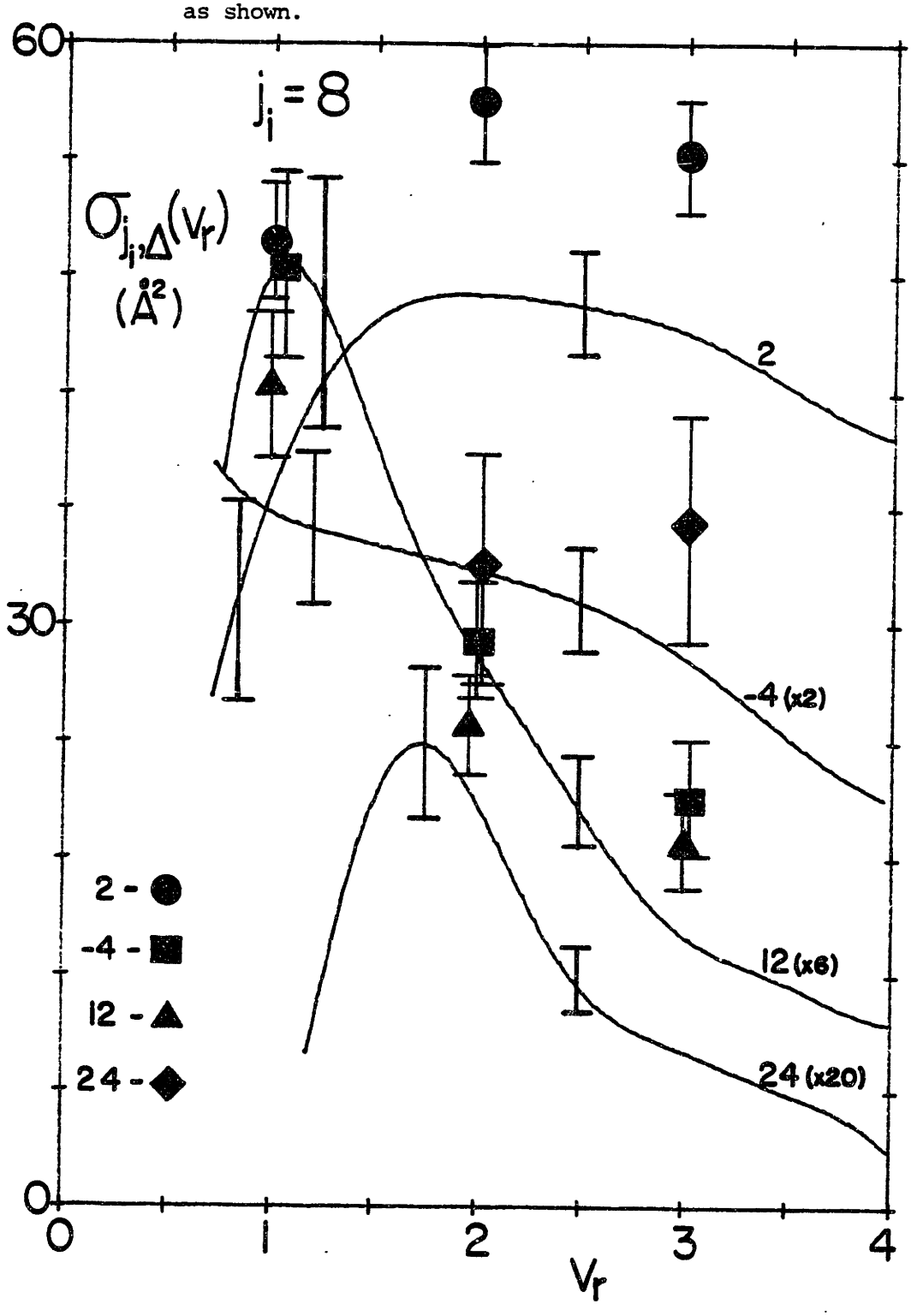

correlated with the size of the energy threshold ΔE for the particular collision process, than with simply the size of Δ; e.g. $\Delta = +12$ calculated cross-sections for $j_i = 8$ are considerably better in these regards than those for $j_i = 22$, while for $\sigma_{8,18}$, $\Delta E = 8.25$ is quite similar to $\Delta E = 8.83$ for $\sigma_{22,12}$, with $\Delta E = 12.8$ for $\sigma_{8,24}$.

We note that our trajectory results for $j_i = 42$ in fig. 7 do give better overall agreement with experiment than those for $j_i = 8$, but still not quite as good as the original results for $j_i = 22$. Calculations for $v_r = 1s_p$ are systematicaly too large, almost uniformly by factors between 1.2 and 1.5 for all Δ (we do not consider $\Delta = +6$, since the very close thereshold $v_{th} = .91$ makes both deconvolution and trajectory results unreliable). Similar to $j_i = 8$ results for $|\Delta| = 2$, the calculations for $j_i = 42$ overestimate the $\sigma_{42,\pm 2}(v_r)$ (+2 not shown) at lower v_r, yet do definitely reproduce the "torque averaging" infuenced rise in $\sigma_{42,\pm 2}(v_r)$ for $v_r \geq 2s_p$.

For $v_r = 2$ and $3s_p$, calculations for <u>all</u> Δ (shown and not shown) actually give quite good reproduction of the <u>v_r dependence</u> of the corresponding measurement, the calculated cross-sections being generally somewhat overly large in magnitude but often in agreement to within or near expected error. Not unexpectedly, the worst case occurs for $\Delta = +12$, being overestimated by factors ≥ 2.

In order to investiage the "torque prevention" effect (discussed in sec. III.6) for $j_i = 42$, $\Delta \leq -16$ and $v_r \leq 1s_p$, we ran additional calcu-

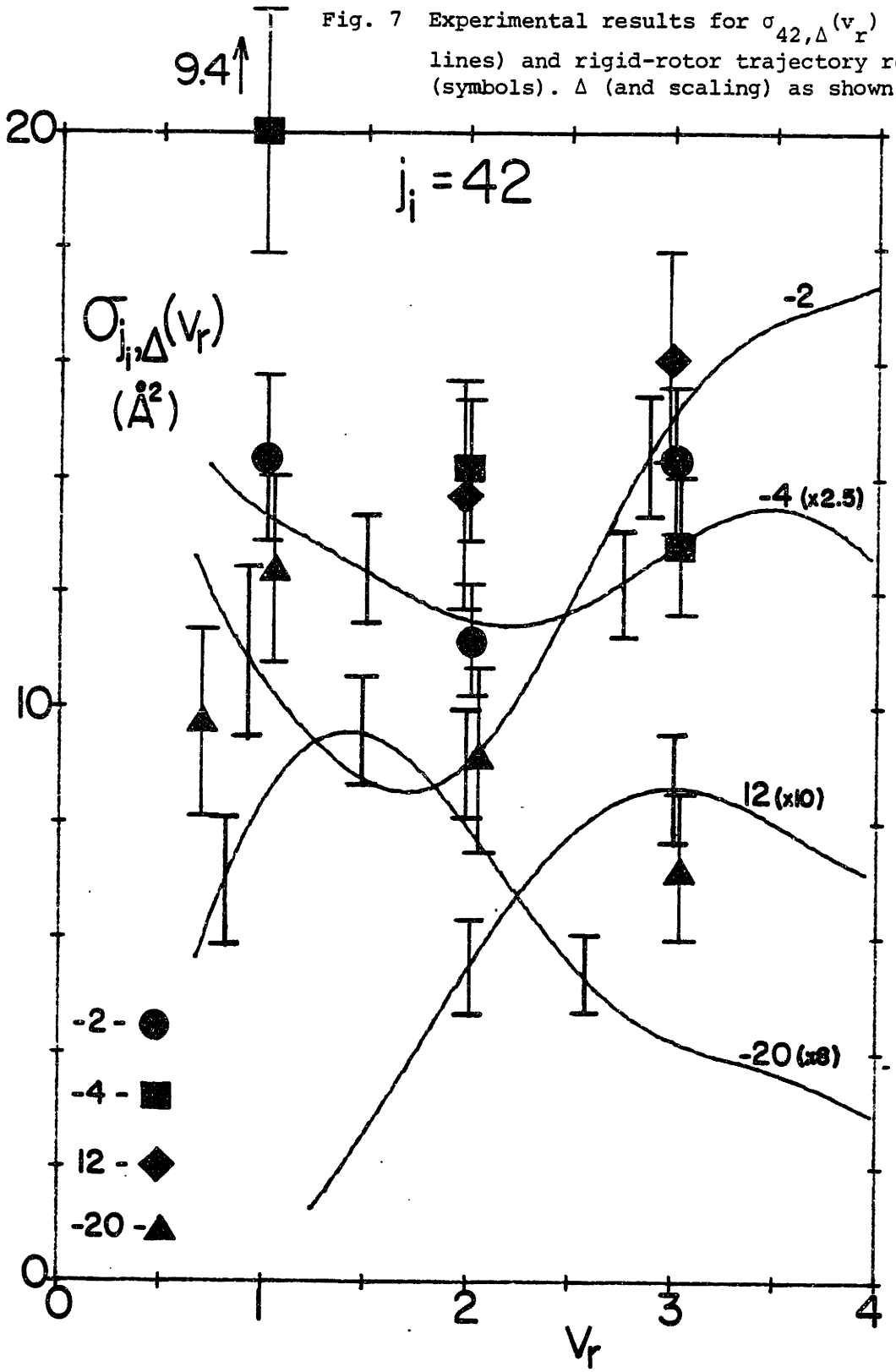

Fig. 7 Experimental results for $\sigma_{42,\Delta}(v_r)$ (solid lines) and rigid-rotor trajectory results (symbols). Δ (and scaling) as shown.

lations at $v_r = 0.7s_p$, the results for $\Delta = -20$ being also shown in fig. 7. These results clearly show that the steady increase in cross-section as v_r decreases does not continue for $v_r < 1s_p$, and the calculations definitely appear to show the decrease in $\sigma_{42,-20}(v_r)$ as v_r become small. Although not shown, trajectory results for $\Delta \leq -24$ actually show $\sigma_{42,\Delta}(v_r)$ decreasing by factors <u>greater</u> than 2 as v_r goes from 1 to $.7s_p$, presumably validating our "torque prevention" dynamical constraint theory, the influence of which (as expected from our earlier arguments and indicated by our data) increases as Δ becomes more largely negative.

Summarizing the results of our rigid-rotor classical trajectory calculations for Li_2^*-Xe, we feel justified in concluding that the overall agreement between calculations and experimental measurements was surprisingly good. The scale or magnitude of the numerial calculations was almost always within a factor of 2 of the measured values, and was in fact in agreement to ≈ within error for nearly half of the 69 data points, i.e. 23 j_i, Δ pairs at 3 valus of v_r; the trajectory results being presumably continuous in v_r would then of course give as good agreement at many more values of $v_r \leq 4s_p$. The v_r dependence of our measured RI cross-sections (excluding scaling factors) is even more often accurately predicted by our calculations, including the "torque averaging" effects for $|\Delta| = 2$, the unusual v_r dependene of $\sigma_{22,-16}(v_r)$, as well as the "dynamical threshold-torque prevention" effect observed

for $\sigma_{42,\Delta}(v_r)$, $\Delta \leq -16$ and $v_r \leq 1s_p$.

Checking the v_r dependence as well as the magnitude of the trajectory calculations vs. experiment enabled us to more sucessfully distinguish between different potential models, motivating our substantial modification to our original atom-atom like exp-6 potential. This modification led us to use a potential with a substantially shallower and broader well minimum then first anticipated, in order to obtain the resulting much improved agreement with our data. We feel that velocity dependent measurements can provide a much more sensitive test of potential models than the more common velocity averaged measurements of many past experiments.

However, as pointed out earlier, our calculations generally agreed poorly with experiment for large $+\Delta$ cross-sections, often overestimating the magnitudes by factors ≥ 2, and usually failing badly to predict the typical rapid fall-off of the cross-sections at large v_r. Best (or worst) examples of this failure are $j_i = 8$, $\Delta = +18$ and $+24$, and $j_i = 22$, $\Delta = +12$. Inspection of the $\overline{k}_{j_i,\Delta}(v_L)$ for these cases indicates clearly that deconvoution error cannot be responsible for these inaccuracies.

Considering more generally results for all j_i, Δ, worst agreement between calculations and measurements apparently occurs at low v_r. While it is conceivable that this can be in part due to the less than usual velocity resolution of the deconvolutions at low $v_r = 1s_p$, which are then subject to larger error, it is extremely unlikely this could

solely explain this problem.

That both the above discrepancies were observed to be substantially worse for our 1st potential model (eq. 22.a) may indicate that either further modifications beyond those included in our 2nd potential model (eq. 23.a) are necessary, or even perhaps only a considerably more complicated and sophisticated potential model would or could be able to significantly better explain the observed $\sigma_{j_i,\Delta}(v_r)$ for Li_2^*-Xe. However, a completely different, alternative explanation and/or solution might be the need for a more realistic dynamical model than that of the rigid rotor; we will consider this possibility in the next section.

2. Vibrating Rotor Calculations

The remainder of chap. IV will be devoted to discussion and calculation of the effects of vibrational motion and the possibility of vibrationally inelastic collisions on RI cross-sections. We will use the self-explanatory notation $\sigma(v_i,j_i;v_f,j_f)$ for individual VRI cross-sections, and $Q(v_i,j_i;\Delta v) \equiv \sum_{j_f} \sigma(v_i,j_i;v_f,j_f)$ of the total VRI cross-section for fixed $\Delta v = v_f - v_i$ out of level (v_i,j_i); we replace $\Delta = j_f - j_i$ by Δj to avoid confusion.

There is considerable experimental evidence that even though the individual $\sigma(v_i,j_i;v_f,j_f)$ are small (<1 Å^2) for $\Delta v \neq 0$, the $Q(v_i,j_i;\Delta v)$ and their sum over all $\Delta v \neq 0$, are large enough to substantially influence the collision dynamics and final outcome of inelastic collision processes by effectively removing cross-sectional area from pure RI collisions. Indeed this removal may serve as an alternative explanation of the substantial overestimation of the $\sigma_{j_i,\Delta}$ for large Δ by our rigid-rotor model. For example, a past study of Ennen and Ottinger[2.b] or VRI collisions in $Li_2^*(B^1\Sigma)$-Xe found that the velocity averaged cross-section $\overline{Q}(4,24;-1) = 15$Å^2, and the total VRI cross-section $\sum_{\Delta v \neq 0} \overline{Q}(4,24;\Delta v) \approx \underline{50\text{Å}^2}$, <u>more than 1/3 the total RI cross-section</u>! The j_f distribution of $\sigma(v_i,j_i;v_f,j_f)$ for $v_i \neq v_f$ was found to be quite broad and relatively flat, having a FWHM in j_f of $\approx$ 20 with a maximum occuring at $j_{fmax} > j_i$ for $\Delta v < 0$, thus favoring <u>positive</u> Δj (visa-versa for $\Delta v > 0$). Very similar results for $Li_2^*(A^1\Sigma)$-Xe have in fact been

observed in very recent spx-type experiments in our lab measuring VRI cross-sections, where preliminary results showed[49] $\overline{Q}(4,28;-1) \approx 15\text{Å}^2$, $\overline{Q}(4,28;+1) \approx 10\text{Å}^2$, and $\overline{Q}(4,28;-2) \approx 5\text{Å}^2$, with the j_f distribution of $\sigma(4,28;4\pm1,j_f)$ having a FWHM of ≈ 24, with peak values $j_{fmax} = 34,26$ for $\Delta v = -1,+1$ respectively.

The empirical fact that $j_{fmax} > j_i$ for $\Delta v < 0$ may explain our puzzling observation that our rigid rotor calculations at <u>lower</u> v_r preferentially overestimated the <u>positive</u> Δj experimental cross-sections considerably worse than for $\Delta j < 0$, the reason being that vibrational inelasticity preferentially reduces the probability of pure RI $\Delta j > 0$ collisions at low v_r where $\Delta v < 0$ collisions are energetically strongly favored ($\Delta v = +n$ has $v_{th} \approx .96\sqrt{n}s_p$). The experimentally observed <u>large</u> total VRI cross-sections provide ample motivation to attempt trajectory calculations with a <u>vibrating</u>-rotor model, and strongly question the validity of the rigid-rotor approximation for the Li_2^*-Xe system. As vibrational inelasticity offers an alternative explanation of some of the failures of the <u>rigid</u>-rotor model, vibrating-rotor calculations can serve as a check on the reality of <u>both</u> our earlier proposed interaction potential (eq.23.a) <u>and</u> its <u>modification</u> from the simpler exp-6 model.

The discussion below will first concentrate on the development of practical techniques and equations of motion for a vibrating-rotor model, to be then followed by presentation of preliminary results, along with an evaluation of how important a role vibrational motion and

inelasticity play in the v_r dependence of our experimental results for $\sigma_{j_i,\Delta}(v_r)$.

To account for effects of vibrational motion and VRI collisions, we must include two additional equations of motion to describe the time dependence of the internuclear separation r(t) (formally a constant r_o), as well as introduce an r dependence to the interaction potential $V(R,r,\cos\gamma)$, which is <u>necessary</u> to provide the vibrational coupling of the atom-rotor interaction making vibrational inelasticity possible. The equations of motion are

$$a.\ \frac{dr}{dt} = \frac{1}{m_p} p_r$$

$$b.\ \frac{dp_r}{dt} = \frac{-\partial}{\partial r}\left[V(R,r,\cos\delta) + U(r) + \frac{2j^2}{m_p r^2}\right] = \frac{4j^2}{m_p r^3} - \frac{\partial U}{\partial r} - \frac{\partial V}{\partial r} \qquad (24.$$

with p_r = vibrational momentum along the internuclear axis, and U(r) is the interatomic molecular potential (of Li_2^* in our case). For mathematical simplicity we will assume the well known harmonic oscillator (H.O.) approximation

$$U(r) = \frac{m_p}{8}\omega^2(r-r_o)^2 \qquad (25.$$

where ω is the vibration frequency (radians/time) of the pure vibrational motion, and r_o is now the equilibrium inter-nuclear separation for zero rotation. Previous <u>3</u> dimensional classical calculations[50] of VRI collisions showed that the H.O. approximation yielded similar

results to the much more realistic Morse potential approximation.

Unfortunately, preliminary testing of our trajectories program with additional eqs. 24 found that even neglecting the vibrational coupling term $\frac{\partial V}{\partial r}$ (using rigid rotor potentials V(R,cosγ)), the inclusion of the rapid vibrational motion increased trajectory calculation time by more than an order of magnitude, resulting in generally $\leq$ 1 trajectory/min. We felt that this extremely long computation time per trajectory made the vibrating rotor calculations too impractical on our computer system.

However, our interest in the non-rigid rotor was re-kindled by a series of interesting articles[39] by Miller concerning semi-classical evaluation of scattering amplitudes for VRI collisions, among others. Miller makes extensive use of the Hamiltonian formalism of classical mechanics, and in particular classical generators of canonical transformations and action-angle variable descriptions of classical dynamics.[51] Action-angle variables, combined with the WKB (Bohr-Sommerfeld) quantization rule are particularly useful as a bridge between the classical and quantum mechanics of systems undergoing bound, periodic motion. For periodic motion describable by generalized Hamiltonian conjugate momentum-coordinates p, q, the action A and the WKB quantization condition are[52] given by

$$A \equiv \frac{1}{2\pi}\oint p\,dq = (n+\tfrac{1}{2})\hbar \qquad (26.$$

where the path integral refers to integration over one complete period

of the motion. The dimensionless variable n is then the classical analogue of the quantum number characterizing the quantized quantum mechanical motion of the system; for simplicity we refer to both A and n as action variables. For example, letting $A = |\vec{j}|$ the classical angular momentum, and $n = j$ the rotational quantum number, then eq.26 is just the semi-classical prescription used earler (eq. 13.a) for relating quantum and classical angular momentum variables. Choosing in eq.26 $p = p_r$ and $q = r$ (the variables from eqs.24), n would then be the classical analogue of the vibrational quantum number v; for further discussion in this context we let $n \to v$.

The great advantage of using action-angle variables v, ψ_v (ψ_v as we shall show, is the phase of the vibrational motion) over the usual p_r,r to describe vibrational motion is that both v and ψ_v have a much less rapid time dependence, and thus will not slow trajectory calculation time nearly as much as use of p_r,r did. For example, in the asymptotic limit $R \to \infty$ and $V \to 0$, and assuming an H.O. U(r), both p_r and r vary in time like $\sin(\omega t+\phi)$; in the identical limit, v(t) is in fact <u>constant</u>, while $\psi_v(t) \propto \omega t$ varies only <u>linearly</u> with time t. Additionally, calculations done using v, ψ_v allow immediate assignment of $v_f = v(t\to\infty)$ as well as an essentially exact treatment of the coupling between rotational-vibrational motion.

We will now briefly develop the action-angle Hamiltonian for the vibrating rotor, as well as describe the canonical transformation to

action angle variables for the vibrational motion. As was originally done for programming development we will first derive the Hamiltonian formulation for the rigid rotor, which will then serve as a basis for developing the full vibrating rotor Hamiltonian.

As is well known from general Hamiltonian mechanics, if generalized coordinate θ is the azimuthal angle describing the orientation of a particle (or rigid body) with respect to a fixed axis along direction $\hat{n}$, and $\vec{I}$ is the angular momentum of the particle, then in general $(\vec{I}\cdot\hat{n},\theta)$ are generalized conjugate momentum-coordinate (i.e. action-angle) variables in the Hamiltonian sense. As an example of current interest, both (j_z,ϕ) and (j,ψ) are conjugate action-angle variables, with $j_z = j\cos\theta$, $j = |\vec{j}|$, and θ, ϕ, ψ are the orientation angles previously introduced in eq. 13. Conversely, letting $\cos\theta = j_z/j$, it follows from eqs. 13.a,b that $\vec{j}$ and $\hat{r}$ (and thus the motion of the rigid rotor) can be completely described in terms of the action-angle conjugates j_z, ϕ_j and j, ψ_j; (the subscript "j" is added for notational purposes). Similarly, relative motion variables $\vec{L}$ and $\hat{R}$ can be analogously described in terms of the corresponding conjugates (L_z,ϕ_L) and (L,ψ_L) with $L \equiv |\vec{L}|$. We have

$$a.\ \hat{r} = \left(\frac{-j_z}{j}\cos\varphi_j\sin\psi_j - \sin\varphi_j\cos\psi_j,\ \frac{-j_z}{j}\sin\varphi_j\sin\psi_j + \cos\varphi_j\cos\psi_j,\ \sqrt{1-j_z^2/j^2}\,\sin\psi_j\right)$$

$$b.\ \vec{j} = \left(\sqrt{j^2-j_z^2}\cos\varphi_j,\ \sqrt{j^2-j_z^2}\sin\varphi_j,\ j_z\right) \qquad (Q7.)$$

c. $\hat{R},\hat{L}$ same as above, $j_z \to L_z$, $j \to L$, $\varphi_j \to \varphi_L$, $\psi_j \to \psi_L$

As can be readily shown using eq. 27 the quantity $\hat{R}\cdot\hat{r}$, needed for evaluation of $V(R,\hat{R}\cdot\hat{r})$, depends on ϕ_j,ϕ_L only through a factor $\cos(\phi_j-\phi_L)$, motivating the change to new conjugate variables (J_z,Σ) and (Δ,δ) defined through

$$\text{a. } J_z = j_z + L_z\,,\quad \Sigma = \tfrac{1}{2}(\varphi_j+\varphi_L) \qquad (28.$$

$$\text{b. } \Delta = j_z - L_z\,,\quad \delta = \tfrac{1}{2}(\varphi_j-\varphi_L)$$

It then immediately follows that the Hamiltonian will not depend on Σ, which being an ignorable coordinate implies that $\frac{d}{dt}\,j_z = 0$, which follows simply from conservation of total angular momentum $\vec{J} = \vec{j} + \vec{L}$. Without loss of generality, we set $J_x = J_y = 0$, which means we define a new coordinate system with $\hat{z}$ axis chosen along the direction of $\vec{J}$. From eqs. 27,28.

$$\text{a. } J_x = j_x + L_x = \sqrt{j^2-j_z^2}\cos\varphi_j + \sqrt{L^2-L_z^2}\cos\varphi_L = 0$$

$$\text{b. } J_y = j_y + L_y = \sqrt{j^2-j_z^2}\sin\varphi_j + \sqrt{L^2-L_z^2}\sin\varphi_L = 0 \qquad (29.$$

$$\text{c. } \Rightarrow \varphi_j - \varphi_L = \pi \quad \text{or} \quad \delta = \pi/2$$

$$\text{d. } j^2 - j_z^2 = L^2 - L_z^2 \quad \text{or} \quad \Delta = \frac{1}{J_z}(j^2-L^2)$$

Thus, the conjugate variables (Δ,δ) may be completely removed from the Hamiltonian by substitution of eq. 29, since $\delta = \pi/2$ is strictly constant, and $\frac{\partial H}{\partial \Delta} = \dot{\delta} = 0$. Re-using the previous conjugate variables P_R, R, the rigid-rotor Hamiltonian is (see eq. 12.i)

$$H = \frac{P_R^2}{2\mu} + \frac{L^2}{2\mu R^2} + \frac{j^2}{2I} + V(R,\cos\gamma),\quad I = \frac{m_p r_0^2}{4} \qquad (30.$$

$$\cos\gamma = -\left[\cos\varphi_j\cos\varphi_L + \left(\frac{J^2-j^2-L^2}{2jL}\right)\sin\varphi_j\sin\varphi_L\right]$$

We have let $J_z \to J$ and $\Sigma \to \psi_J$ for convenience as well as consistancy in notation since $\vec{J} = |\vec{J}|\hat{z}$ in our new coordinate system. Integration of $\frac{d\psi_J}{dt} = \frac{\partial H}{\partial J}$ is unnecessary for trajectory computations since all other equations of motion are independent of ψ_J; of course, $\frac{dJ}{dt} = 0$ also requires no computational effort. Thus the Hamiltonian formulation above has effectively reduced the atom-rigid rotor system to a set of 6 coupled differential equations of motion in conjugate variables (P_R,R), (L,ψ_L) and (j,ψ_j), which is a sizable reduction from the 10 equations of our previous set, eqs. 12.

The extension of eq. 30.a, to a vibrating-rotor Hamiltonian may be written down by inspection as

$$H = \frac{P_R^2}{2\mu} + \frac{L^2}{2\mu R^2} + \frac{2j^2}{m_p r^2} + \frac{2p_r^2}{m_p} + U(r) + V(R,r,\cos\gamma) \quad (31.$$

which still uses variable p_r,r. To develop the action-angle Hamiltonian, we will employ a suitable canonical transformation[51] $p_i,q_i \to P_i,Q_i$ from an old → new set of conjugate variables. Formally, for the generator of a canonical transformation of the second type $F_2(q_i,P_i)$, a function of <u>both</u> old and new variables, the canonical transformation generated by $F_2(q_i,P_i)$ is given by[51]

$$a.\ Q_i = \frac{\partial F_2(q_i,P_i)}{\partial P_i}\ ,\quad P_i = \frac{\partial F_2(q_i,P_i)}{\partial q_i} \quad (32.$$

$$b.\ \frac{dQ_i}{dt} = \frac{\partial H}{\partial P_i}\ ,\quad \frac{dP_i}{dt} = \frac{-\partial H}{\partial Q_i}\ ,\quad H(P_i,q_i) = H(P_i,Q_i)$$

which generally defines the transfomration only implicity; eq. 32.a must generally be inverted to give $q_i(Q_i,P_i)$ and $p_i(Q_i,P_i)$, with the possibility of multiple roots.

Employing our usual set of units (eqs. 14) in which h = 1, we define the vibrational action variable v using the WKB correspondence rule (eq. 25) as follows

$$a.\quad E' = \frac{2}{m_p}P_r^2 + U_{eff}(r) = \frac{2}{m_p}P_r^2 + U(r) + \frac{2j^2}{m_p r^2}$$

$$b.\quad \oint p_r\,dr = 2\pi(v+\tfrac{1}{2}) = 2\int_{r_<}^{r_>}\sqrt{\frac{m_p}{2}\left[E'(v,j)-\left(U(r)+\frac{2j^2}{m_p r^2}\right)\right]}\,dr \qquad (33.$$

where E' = E'(v,j) is the internal vibrotational energy (defined implicityly in eq. 33.b) with the vibrational-rotational coupling accounted for in the usual way by inclusion of the "centrifugal" term $\frac{2j^2}{m_p r^2}$ in the effective potential $U_{eff}(r)$ (eq. 33.a). We define $r_<$, $r_>$ as the inner, outer classical turning points of the vibrotational motion. Again assuming an H.O. potential for U(r), eqs. 33 may be cast in the more useful form

$$a.\quad U(r) = \frac{m_p}{8}\omega^2(r-r_0)^2,\quad e \equiv E'/\omega,\quad \lambda \equiv \frac{2}{m_p r_0^2 \omega},\quad z \equiv \frac{1}{\sqrt{\lambda}}\left(\frac{r}{r_0}-1\right)$$

$$b.\quad (v+\tfrac{1}{2})\pi = \frac{1}{2}\int_{z_<}^{z_>}\sqrt{4e - z^2 - \frac{4\lambda j^2}{(1+\sqrt{\lambda}z)^2}}\,dz \qquad (34.$$

As $h = 1$ in our units, and $I = \frac{m_p r_o^2}{4}$, then $\lambda = \frac{2}{m_p r_o^2 \omega} = \frac{h^2}{2I}(\frac{1}{h\omega})$, and thus $\lambda = B/\omega_e$ where B and ω_e are the rotational and vibrational molecular constants. For $Li_2^*(A'\Sigma)$, we have( ) $B = .49\ cm^{-1}$, $\omega_e = 255\ cm^{-1}$, and thus $\lambda \approx 1/520$; this (generally for all diatomics) very small value of parameter λ makes possible further approximations to eq. 34.b to allow analytic inversion to determine e(v,j). We make the following important expansion approximation.

$$\frac{\lambda}{(1+\sqrt{\lambda}z)^2} = \lambda - 2\lambda^{3/2}z + 3\lambda^2 z^2 + O(\lambda^{5/2}) \quad (35.$$

Substitution of the above approximation into eq. 34.b results in a standard inverse trigonometric integral which may be performed analytically, yielding the following result for e(v,j).

$$e(v,j) = (v+\tfrac{1}{2}) + \lambda j^2 + 6\lambda^2(v+\tfrac{1}{2})j^2 - 4\lambda^3 j^4 + O(\lambda^4) \quad (36.$$

Eq. 36 gives explicitly the vibrational-rotational coupling in determining the internal molecular energy, something not easily determined using p_r, r variables as in eq. 24.

Finally, to transform to vibrational action-angle variables, we use the following generator, similar to that recommended by Miller(39.a)

$$\begin{aligned} &a.\ (P_1,q_1)\equiv(P_R,R),\ (P_2,q_2)\equiv(P_r,q_r),\ (P_3,q_3)\equiv(L,\psi_L),\ (P_4,q_4)\equiv(j,\psi_j) \\ &b.\ P_2 \equiv V \\ &c.\ F_2(q_i,P_i) = q_1P_1 + q_3P_3 + q_4P_4 + \int_{r_e}^{q_2}\sqrt{\tfrac{m_p}{2}\left[E'(P_2,P_4)-\left(U(x)+\tfrac{2P_4}{m_p x^2}\right)\right]}\,dx \end{aligned} \quad (37.$$

with the integral in eq. 37.c chosen to conform to $p_2 = p_r = \frac{\partial F_2}{\partial q_2}$ as in eq. 33.a; the quantity $r_e \equiv \frac{\partial}{\partial r} U_{eff}(r)|_{r_e} = 0$ = the equilibrium separation of the rotating H.O. ($r_e = r_o$ if $j = 0$). The basic transformation eqs.32 then yield the following result for (P_i, Q_i):

$$a.\ P_1 = \frac{\partial F_2}{\partial q_1} = P_1 = P_R,\quad P_3 = \frac{\partial F_2}{\partial q_3} = P_3 = L,\quad P_4 = \frac{\partial F_2}{\partial q_4} = P_4 = j,\quad P_2 \equiv V$$

$$b.\ Q_1 = \frac{\partial F_2}{\partial P_1} = q_1 = R,\quad Q_3 = \frac{\partial F_2}{\partial P_3} = q_3 = \Psi_L \qquad (38.$$

$$c.\ \frac{\partial F_2}{\partial P_2} = Q_2 \rightarrow \cos^{-1}[\cos(Q_2 - n\pi)] = \frac{\partial e}{\partial V}\int_{z_e}^{z} \frac{dx}{\sqrt{4e - x^2 - 4\lambda j^2(1+\sqrt{\lambda}x)^{-2}}}$$

$$\hookrightarrow n = 1 \text{ if } z < z_e,\ n = 0 \text{ if } z > z_e$$

$$d.\ \frac{\partial F_2}{\partial P_4} = Q_4 = \Psi_j + \Delta\Psi_j,\quad \Delta\Psi_j = \int_{z_e}^{z} \frac{\left[\frac{\partial e}{\partial j} - 2\lambda j(1+\sqrt{\lambda}x)^{-2}\right]}{\sqrt{4e - z^2 - 4x^2 j^2(1+\sqrt{\lambda}x)^{-2}}}\, dx$$

Eqs. 38c,d are expressed in the dimensionless variables of eq. 34.a, and are valid when using the H.O. approximation for U(r).

In eq. 38.c, we uniquely define $Q_2 \rightarrow 2\pi n$ ($n = 1,2, \ldots$) for $r = r_e - \delta$ and $\delta \rightarrow 0$, the $\cos^{-1}[\quad]$ allowing Q_2 to take on any value $0 \leq Q_2 \leq \infty$. Physically, $\Delta\psi_j$ in eq. 38.d is a "centrifugal distortion correction", for the changing rotational speed of the vibrating rotor as r(t) changes (thus conserving rotational angular momentum).

Even with the simple H.O. approximation for U(r), eq. 38 cannot be solved analytically for general $j \neq 0$, so we again employ the expansion approximation of eq. 35, as well as our earlier result for e(n,j), to analytically invert eqs. to solve for z (or $r = 1 + \sqrt{\lambda} r_o z$) and $\Delta\psi$ in terms of the new action-angle variables v, Q_2. These last results (given

below in eqs. 39.c,d) as well as those of eqs.38.a,b will, when substituted into the Hamiltonian of eq. 31, (letting $Q_2 \leftarrow \beta_v$ and $Q_4 \leftarrow \beta_j$, for consistancy with earlier notation) then yield the following action-angle Hamiltonian and equations of motion for the vibrating rotor:

(39.

a. $$H = \frac{P_R^2}{2\mu} + \frac{L^2}{2\mu R^2} + E'(v,j) + V(R,r,\cos\gamma)$$

b. $$E'(v,j) = \omega\left[(v+\tfrac{1}{2}) + \lambda j^2 + 6(v+\tfrac{1}{2})\lambda^2 j^2 - 4\lambda^3 j^4\right] + O(\lambda^4), \quad \lambda \equiv \frac{2}{m_p r_0^2 \omega}$$

c. $$r(v,j,\psi_v) = r_0\left[(1+4\lambda^2 j^2) + 2\sqrt{\lambda(v+\tfrac{1}{2})}(1-3\lambda^2 j^2)\sin\psi_v\right] + O(\lambda^3)$$

d. $$\Delta\psi_j(v,j,\psi_v) = 2j\lambda^{3/2}\sqrt{v+\tfrac{1}{2}}\left[4(1-\cos\psi_v) + 3\sqrt{\lambda(v+\tfrac{1}{2})}\sin(2\psi_v)\right] + O(\lambda^{5/2})$$

e. $$\cos\gamma = -\left[\cos\psi_L\cos(\psi_j - \Delta\psi_j) + C\sin\psi_L\sin(\psi_j - \Delta\psi_j)\right]$$

f. $$C \equiv \frac{J^2-(j^2+L^2)}{2jL}, \quad Q \equiv \frac{J}{jL}\frac{\partial V}{\partial\cos\gamma}\sin(\psi_j-\Delta\psi_j)\sin\psi_L, \quad j_z = \frac{j(j+CL)}{J}, \quad L_z = J - j_z$$

g. $$\frac{dR}{dt} = \frac{\partial H}{\partial P_R} = P_R/\mu$$

h. $$\frac{dP_R}{dt} = \frac{-\partial H}{\partial R} = L^2/\mu R^3 - \frac{\partial V}{\partial R}$$

i. $$\frac{dL}{dt} = \frac{-\partial H}{\partial\psi_L} = \frac{\partial V}{\partial\cos\gamma}\left[C\sin(\psi_j-\Delta\psi_j)\cos\psi_L - \cos(\psi_j-\Delta\psi_j)\sin\psi_L\right]$$

j. $$\frac{d\psi_L}{dt} = \frac{\partial H}{\partial L} = L/\mu R^2 + Q\,L_z/L$$

k. $$\frac{dj}{dt} = \frac{-\partial H}{\partial\psi_j} = \frac{\partial V}{\partial\cos\gamma}\left[C\cos(\psi_j-\Delta\psi_j)\sin\psi_L - \sin(\psi_j-\Delta\psi_j)\cos\psi_L\right]$$

l. $$\frac{d\psi_j}{dt} = \frac{\partial H}{\partial j} = \frac{\partial E'}{\partial j} + \frac{\partial V}{\partial r}\frac{\partial r}{\partial j} + Q\,j_z/j + \frac{\partial\Delta\psi_j}{\partial j}\frac{dj}{dt}$$

m. $$\frac{dV}{dt} = \frac{-\partial H}{\partial\psi_v} = -\left[\frac{\partial V}{\partial r}\frac{\partial r}{\partial\psi_v} + \frac{\partial\Delta\psi_j}{\partial\psi_v}\frac{dj}{dt}\right]$$

n. $$\frac{d\psi_v}{dt} = \frac{\partial H}{\partial V} = \frac{\partial E'}{\partial V} + \frac{\partial V}{\partial r}\frac{\partial r}{\partial V} + \frac{\partial\Delta\psi_j}{\partial V}\frac{dj}{dt}$$

o. $$\frac{dJ}{dt} = \frac{-\partial H}{\partial\psi_J} = 0, \quad \frac{d\psi_J}{dt} = \frac{\partial H}{\partial J} = -Q$$

We again emphasize that eqs. 39.b-d apply for a H.O. potential $U(r) = \frac{m_o}{8}\omega^2(r-r_o) = \frac{1}{4\lambda}\left(\frac{r}{r_o}-1\right)^2$. Setting $v = -1/2$ and letting $\omega \to \infty$ ($\lambda \to 0$) recovers the rigid rotor limit. As eq. 39.o is ignorable for our purposes, this formulation has reduced the vibrating-rotor problem to a system of 8 coupled equations - eqs. 39.g-n.

Since the new coordinate system to which the above equations apply has $\hat{J} \| \hat{z}$, its orientation is not fixed in space as we average over all possible rotor orientations. We then define our initial conditions exactly as was done in our original coordinate system (with $\vec{L}_o = L_o\hat{z}$, $\vec{v}_r = v_r\hat{y}$) using Euler angles θ, ϕ, ψ introduced earlier (eqs. 13) and finally transform these conditions to our new variables. The results are:

a. $j_o = j_i + 1/2$

b. $\psi_{jo} = \psi$

c. $R_o \Rightarrow V(R_o, r_o, 1) = \frac{1}{300}\mu V_r^2$, r_o fixed at 3.2 for $Li_2^*(A^1\Sigma)$

d. $P_{Ro} = -\mu V_r\sqrt{1 - b^2/R_o^2}$

e. $L_o = \mu V_r b$

f. $\psi_{Lo} = \tan^{-1}\left[(1 - b^2/R_o^2)^{-1/2}\right]$

g. $J = \sqrt{j_o^2 + L_o^2 + 2j_oL_o\cos\theta}$

h. $\psi_J = -\pi/2$ (arbitrary)

i. $V_o = V_i$, ψ_v uniform in $(0, 2\pi)$

(40.

with b, θ, ϕ, ψ chosen as before (eq. 13.g), and ψ_v also uniformly random

in $(0,2\pi)$; the intial vibrational quantum # $v_i = 9$ for all of our experimental data.

The convergence testing procedure is the same as done earlier, and having found convergence at time t_f, assignment of Δj are Δv are simply given by

$$a.\ j_f = j(t_f) - \tfrac{1}{2},\quad \Delta j = 2\left[\frac{(j_f - j_i)+1}{2}\right] \qquad (41.$$

$$b.\ V_f = V(t_f),\quad \Delta V = \left[(v_f - v_i) + \tfrac{1}{2}\right]$$

$$[\ ] = \text{greatest integer function}$$

with j_f binned as before, and v_f binned $\pm 1/2$ about all integer values. The major difference from rigid rotor calculations is that only trajectories with $\Delta v = 0$ are counted towards caluclation of RI cross-sections $\sigma_{j_i,\Delta}$, with all trajectories with $|\Delta v| \geq 1$ counted separately, thus in general reducing the calculated values of $\sigma_{j_i,\Delta}$ in comparison with the rigid rotor model; these latter trajectories are used to compute $Q(v_i, j_i; \Delta v)$ for a comparison with experiment[41] and a check on our method and potential.

Initial testing of our new action-angle Hamiltonian equations of motion showed that trajectory computation time was longer only by a factor ≈ 3 form that of the rigid rotor model, computing ≈300 trajectories/hour for $v_r = 2s_p$, at least 4 times faster than our original model using p_r, r to describe vibrational motion. This substantial

increase in computational efficiency (potentially saving weeks of computation time) combined with the much more accurate treatment of vibrational-rotational energy coupling, well establish the merit of the action-angle variable approach to classical treatment of the vibrating rotor.

The above Hamiltonian equations appear at first sight to have numerical difficulties[39.b] as j or L become very small, since both appear in the denominator of the quantities C, Q defined above. An example of such a possibility would be a hard near planar collision ($\vec{j},\vec{L}$ ≈ antiparallel) which results in a near 180° flip in the direction of $\vec{j}$, implying the action variable j is ≈ instanteously zero, with a near discontinuity in $\frac{dj}{dt}$ at this point; both j and L are physically positive definite.

We have found a method of avoiding these numerical problems by exploiting the fact that the equations of motion (eqs. 39) are mathematically invariant under the switch $(j,\psi_j) \rightarrow (-j,-\psi_j)$ or $(L,\psi_L) \rightarrow (-L,-\psi_L)$. We have observed during testing that as j or L $\rightarrow \leq .1$, the integration step size h rapidly decreases due to the automatic step size control "sensing" the numerical difficulties. When either j or L is found $\leq .01$, we freeze the step size h at its present value, and continue fixed h integration until j (or L) $\geq .01$ again, or until either one takes on a negative value, as our integration routine cannot "know" the physically required positive definiteness of j and L.

In this latter case, we make the "change of variable" $(j,\psi_j) \to (-j,-\psi_j)$ (and similarly for L,ψ_L) by switching sign of the presently stored values of j, ψ_j, and all stored higher derivitives (up to 5th derivitives for our 5th order Nordsieck method), and continue fixed h integration until j (or L) $\geq .01$, at which time we resume automatic step size control. This technique of allowing $j(t)$ (or $L(t)$) to become negative for short times $t_1 \leq t \leq t_2$ avoids the near discontinuity of $\frac{d}{dt} j(t_1)$ for the physical solution $j(t) \geq 0$, $j(t_1) \approx 0$, and only resumes the physical solution by letting $(j,\psi_j) \to (-j,-\psi_j)$ at time $t_2 > t_1$ when the numerical discontinuity problem has passed (see sketch below).

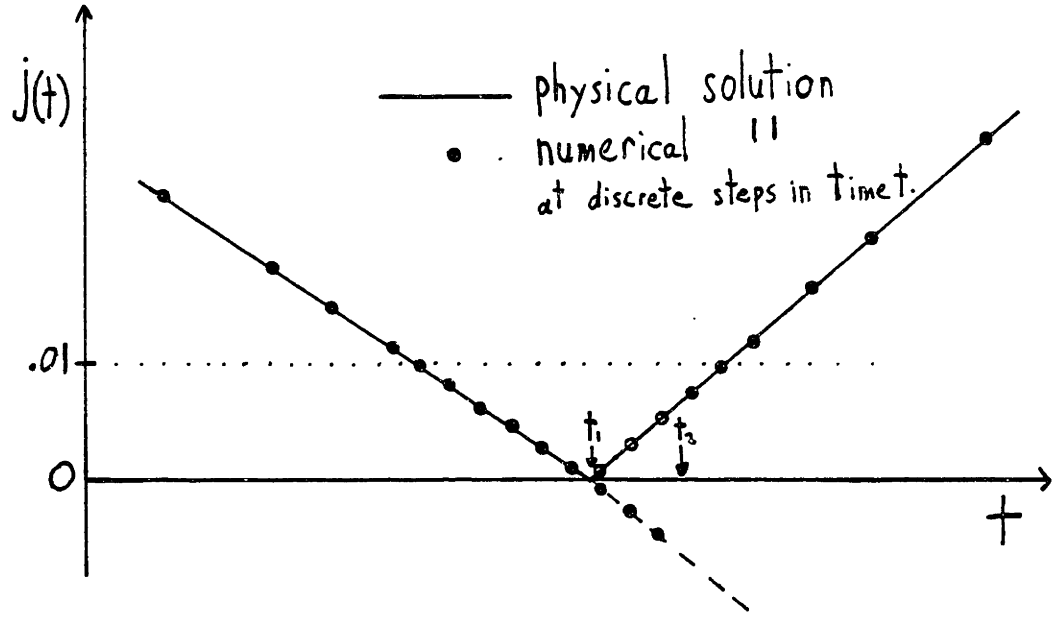

We point out that the necessity of employing this step-size and/or sign change of variables proceedure(s) occurs quite infrequently, probably less than 1% of all trajectories for $j_i \geq 8$. Testing of the tech-

nique in the rigid-rotor limit with many trajectories having $\vec{J}_o$ at or near anti-parallel to $\vec{L}_o$, showed negligable differences of only $\sim .01$ in the determination of j_f from that obtained by our former method (eqs.12) For extra assurance we restrict $L_o \geq .05$ ($b \geq .002$, $v_r = 2s_p$); trajectories with smaller b contribute virtually zero to any Δ cross-section.

Unfortunately, despite the elegance, computational efficiency, and classical↔quantum compatibility of the action-angle variable method, its increased mathematical complexity does not in general allow exact application to arbitrary potentials U(r) without further approximation; we feel our choice of an H.O. U(r), and the excellent (as $\lambda < 1/500$) expansion approximation in parameter λ (eq. 35) made earlier, are more than sufficiently accurate for our limited purpose of determining the effect of vibrational inelasticity on pure RI cross-sections. Regarding in particular the slight inexactness of the eqs. 39.b-d, we found total energy conserved to $\leq .1\%$ for all trajectories, and to $\leq .01\%$ for those with $\Delta v = 0$, (which are of course of greatest interest to us), giving us confidence that the classical accuracy of our trajectory results is sufficient.

Finally, we must include an r dependence to the interaction potential $V(R,r,\hat{R}\cdot\hat{r})$; $\frac{\partial V}{\partial r}$ is by far the dominant term in eq.39.m for $\frac{d}{dt} v(t)$ and thus necessary to account for vibrational inelasticity. As the parameter a_2 of our previous potentials describes the shape of the short range repulsive contours, we expect a_2 to vary with inter-nuclear

separation r so to have the contours "breathe" in and out with the vibrational motion of the rotor. It is also natural that the long range asymmetry also increase with increasing r, being that b_2 goes like the difference of the (0°-90°) polarizabilities of the Li_2^*. We then assume the following simple yet qualitatively reasonable modification to our earlier exp. 6 type potentials to allow a non-zero $\frac{\partial V}{\partial r}$

$$a. \quad a_2 \rightarrow a_2\left(1+\alpha\left(\frac{r-r_0}{r_0}\right)\right) \qquad \alpha \text{ and } \beta \geq 0 \qquad (42.$$

$$b. \quad b_2 \rightarrow b_2\left(1+\beta\left(\frac{r-r_0}{r_0}\right)\right)$$

with two additional free parameters α and β; a_2 and b_2 are now simply interpreted as the value of the asymmetry paramters when $r \rightarrow r_0$, the equilibrium separation for $j \rightarrow 0$.

The calculational approach for our vibrating-rotor work went along similar lines to that used for the previous rigid-rotor work. Fixing $v_r = 2s_p$ and $j_i = 22$, we then proceeded to do parameter fitting by "trial and error", but now using the knowledge gained previously as a very useful starting point. In a departure from our ealier approach, we waited far less time before branching out to $j_i = 8$ and 42, and then $v_r = 1$ and $3s_p$, since we now know this to be more critical test of trial potentials. Further, we tried throughout this work to constrain our potentials so that results for $Q(9, j_i=22, \Delta v)$ were in reasonable agreement with experimental values[49] discussed at the beginning of IV.2.

Due to the now increased calculational time required, as well as

other constraining factors, we were unfortunately unable (as of this writing) to obtain calculations and potential "fits" as precise as previous rigid-rotor results; we must therefore refer to the results that will be presented as "preliminary". However, we feel we have found rather unmistakable evidence to lend solid support to the following observations-conclusions:

1. The $Q(9,j_i;\Delta v)$ and $Q_V(9,j_i) \equiv \sum_{\Delta v} Q(9,j_i;\Delta v)$ are fairly sensitive to the value of k, the parameter controlling the steepness of the exponential repulsion (see eq. 22.a or 23.a). As the total inelastic cross-sections $Q_T(v,j) \equiv Q_V(v,j) + Q_R(v,j)$ (where Q_R is the total RI cross-sections) is not as sensitive, this implies that Q_R is also more sensitive to k than previously expected from the rigid-rotor work. Further, this sensitivity was found to substantially increase both with smaller j_i and especially smaller v_r. Using other potential parameters similar to those to be given in table 2, we found $Q_V(9,8)$ to increase by 30 (from $\approx .8\text{Å}^2 \approx 25\text{Å}^2$) as k varied between 20 and 25, while $Q_V(9,42)$ increased by $\approx$ 50%, from $\approx 40\text{Å}^2$ to $\approx 60\text{Å}^2$.

2. Similar to #1 above, we found increasing j_i substantially increased the probability for vibrational inelasticity, the effect again being greater at lower v_r. A very similar vibrational-rotational coupling has also been observed in previous vibrating-rotor studies.[53] This could also explain a heretofor unmentioned

experimental observation of spx scan spectrums for Xe and Ar, j_i = 42, were (compared to 8,22) noticably more "dirty", i.e. having a greater density of non-RI satellite lines presumably populated through VRI collisions. This effect was considerably greater for Xe than Ar (and more so Ne) which is even further evidence that its origin lies in vibrational inelasticity, and not from fluorescence due to another excited foreign line spectrum. (Note also in table III.2 that very much unlike 8 and 22, $\bar{k}^{o}_{42,\Delta}$ are basically uniformly low for Xe in comparison with Ar and Ne, suggesting reduction due to increased vibrational inelasticity in Xe). We finally note that for a given j_i (in particular for 8 and 22), $Q_V(9,j_i)$ generally increased with increasing v_r (especially for $v_r = 1s_p$ compared to $v_r \geq 2s_p$).

3. Hypothesizing that our potential modification of eq. 23 was an artifact required to give agreement with experiment when using an invalid rigid-rotor model, we were <u>unable</u> to obtain satisfactory theory-experiment agreement with the simple exp-6 potentiasl of eq. 22. For $\varepsilon \simeq 5$ (table 1) and $\sigma \simeq 6$ (so $C_6 \simeq \bar{C}_6$) with moderate coupling parameters $\alpha,\beta \lesssim 1$, these potentials again substantially over-estimated the $\sigma_{22,\Delta}(2s_p)$ for large Δ, apparently at the expense of the smaller $|\Delta| \leq 4$ cross-sections. For $\sigma \simeq 5$ (table 1) requiring $\varepsilon \simeq 15$, the $Q(9,22;\Delta v)$ were (we assume) highly overestimated at the expense of underestimating many of the RI cross-

sections for both large and small Δ. (This likely happens because the usual exp-6 is more sharply, steeply varying at or inside the well minimum). We feel at this point that this is strong further evidence that our proposed modification to the exp-6 potential may well bear a resemblance to realty.

In figs. 8-10 we present our best to date vibrating-rotor trajectory results, the style of presentation being the same as was done earlier. The results represent trajectory runs from 2 to 5 slightly varied potentials, with the range of parameters used given in table 2; we cannot as of yet state "best" potential values as was done for table 1. We emphasize that our uncertainty in σ and (especially) ε is potentially larger than table 2 might indicate. In any case, the new potentials are similar to the rigid-rotor ones, though they have a deeper, somewhat narrower well, and a steeper repulsion.

The values for $v_r = 2s_p$, all j_i and $v_r = 1s_p$, $j_i = 8$ were computed from a total of ≈ 15,000 trajectories run (with ≈ 60% inelastic); values for other v_r, j_i were computed with only ≈ 5000 total trajectories. The reader should bear in mind that one cannot reach very satisfactory convergence of results with as few as ∿ 5000 (or probably not even after ∿ 15,000) trajectories run. We believe fluctuations exceeding those based simply on statistical grounds occur because of incomplete averaging (integration) over all possible initial conditions.

Table IV.2

Vibrating- Rotor Potential Parameters

parameter	value range
ε	8.0 - 9.0
σ	4.7 - 4.8
a_2	1.0
b_2	.85
k	20. - 22
c_1	6.0 - 6.5
d_1	1.15 - 1.17
c_2	10.
d_2	1.0
α	1.0 - 1.5
β	1.0 - 1.25

The values we present represent averages and/or "best eyeball estimations" based upon comparison of the different trajectory runs. For the smaller cross-sections of about $1\mathring{A}^2$ or less (generally for large $|\Delta|$), statistical fluctuations were severe enough so that we usually chose to "average" trajectory values from each individual run over the particular Δ of interest and its two adjacent Δ values; as results for large Δ generally vary reasonably slowly with Δ at large ($\gtrsim 12$) Δ (no thresholds), then this should not be a bad approximation. In these cases and indeed most others the error bars given are not precise, but represent variations of results between different potential runs as well as our "best estimate" as to the expected range cross-section values would fall in if sufficiently many more trajectories were run (with the same choice of potentials) to give adequate convergence. Having now stated the above cautionary remarks, we will now briefly discuss the results.

Considering the $j_i = 8$ results in fig. 8, the agreement between the experimental deconvolutions and the calculations is little short of phenomenal. All trajectory points shown are in agreement to within deconvolution + estimated calculation error (range); agreement for Δ = -6, -2, +12, +18 (all not shown) was basically just as good, except for $\Delta = +12$, $v_r = 1s_p$, which though 40% high has a $v_{th} = .75s_p$, making suspect both deconvolution and especially classical results. This last case aside, we note that agreement for all other cases is as good as or even better than all rigid-rotor results (fig. 6). Most impressive how-

Fig. 8 Experimental results for $\sigma_{8,\Delta}(v_r)$ (solid lines) and vibrating-rotor trajectory results (symbols). Δ (and scaling) as shown.

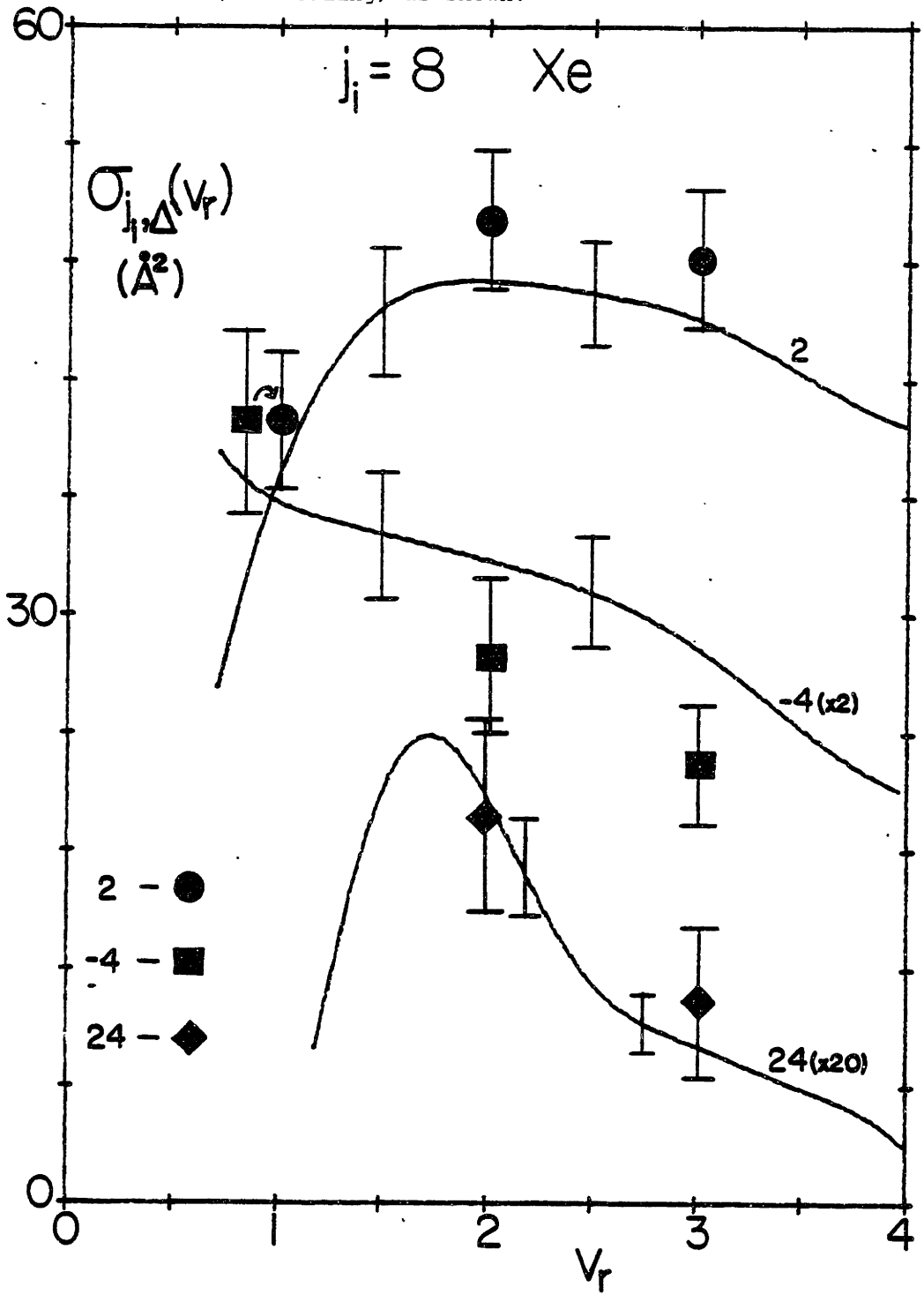

ever is that the vibrating-rotor results now give an excellent description of both magnitude and v_r dependence of $\Delta = +24$ (and +18), where rigid-rotor calculations had previously failed badly. Lastly, we also note that the "torque averaging" behavior of $\sigma_{8,-2}(v_r)$ is also noticably more accurately representd than previously (fig. 6), probably due to VRI collisions reducing the short range contribution at lower v_r, which is also in evidence by the comparitivly better agreement also obtained for $\Delta = -4$, $v_r = 1s_p$.

Considering fig. 9 here (and figs. 4 and 5 earlier), it is seen that for $\Delta = -2$ and -16 rigid and vibrating-rotor cross-section results are essentially the same, giving strong evidence that the big rise in $\sigma_{22,-2}(v_r)$ due to torque averaging and the unusual v_r dependence of $\Delta = -16$ are essentially due to rotational- dynamical effects only (which of course is already well understood in the case of torque averaging). For $v_r \geq 2s_p$, calculations for $\Delta = +6$ are somewhat larger than before, thus giving even better agreement than the +6 rigid-rotor calculations; like the +12 result, $\Delta = +6$ at $v_r = 1s_p$ is too large, and probably again due to threshold inaccuracies. Similar to +6, $\Delta = -4$ and -8 results (not shown) are uniformly larger by 5-10% than previously for all v_r and thus somewhat more accurate, though the size of the error bars negates any real meaning to the improvement. As with $j_i = 8$, we once again find the new results for $\Delta = +12$ demonstrating the rapid fall-off with increasing v_r typical of measured large $+\Delta$ cross-sections, but consistantly absent

Fig. 9 Experimental results for $\sigma_{22,\Delta}(v_r)$ (solid lines) and vibrating-rotor trajectory results (symbols). Δ (and scaling) as shown.

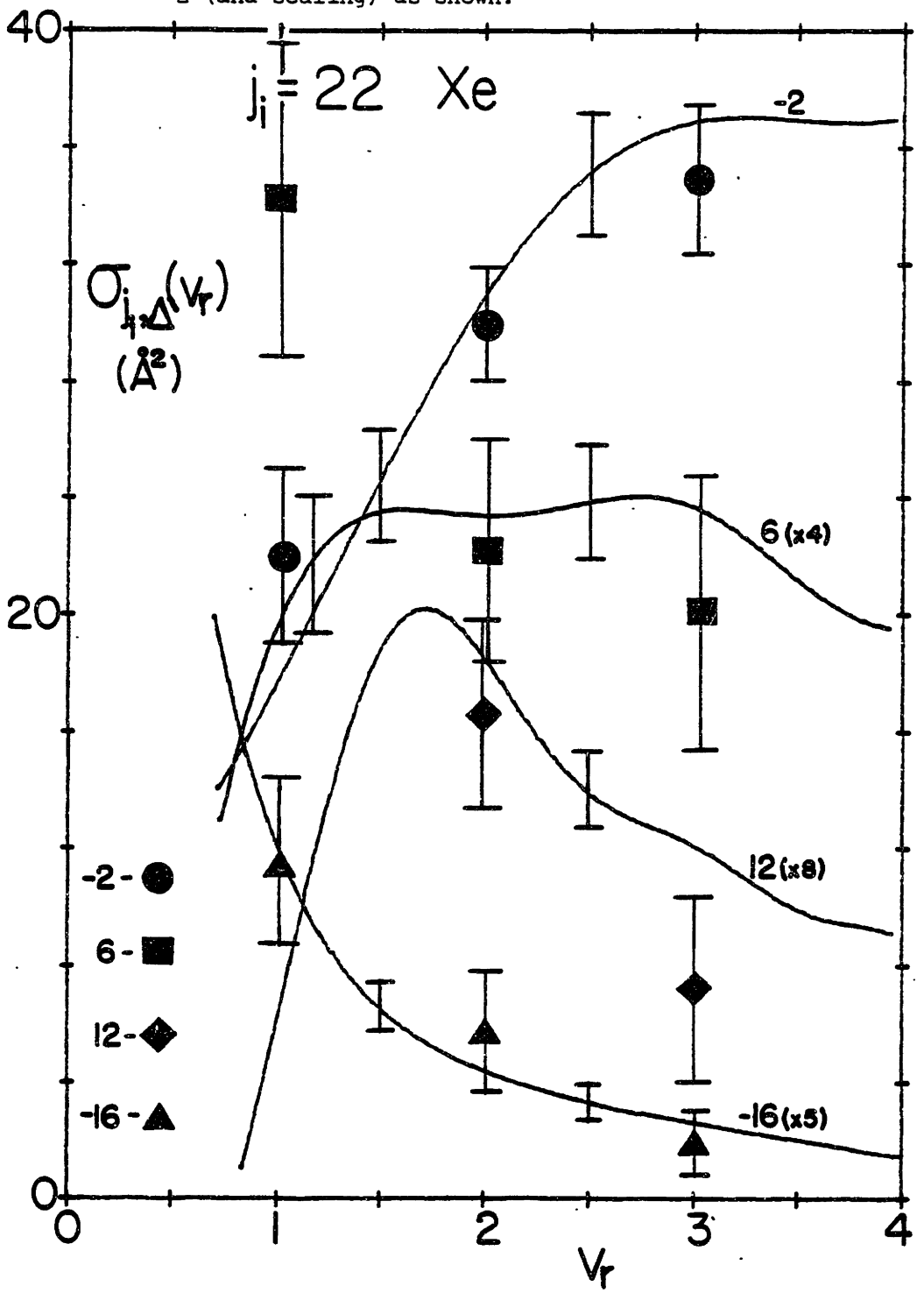

Fig. 10 Experimental results for $\sigma_{42,\Delta}(v_r)$ (solid lines) and vibrating-rotor trajectory results (symbols). Δ (and scaling) as shown.

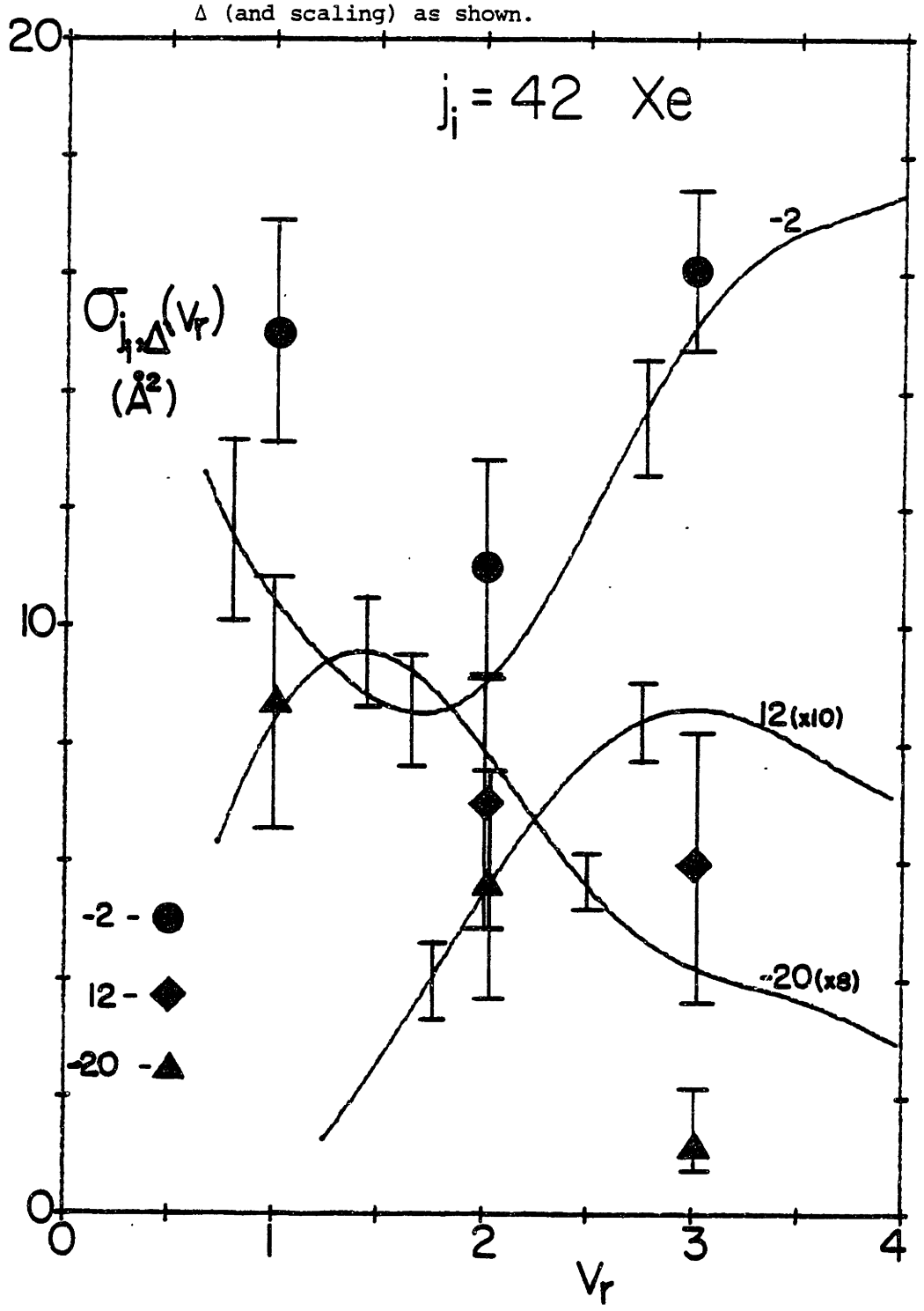

in our rigid-rotor predictions. In this case, the trajectory result over-estimates the rapidity of the drop-off, likely due to substantial removal of Δ = +12 cross-section lost to vibrational inelasticity.

The above observation that our vibrating- rotor model may in some cases actually over-reduce the large Δ cross-section at high v_r due to presumably excessivly high vibrational inelasticity is further confirmed in fig. 10 for both Δ =12 and -20. It is evident this underestimation is worst at $v_r = 3s_p$, and progressively decreases or is completely eliminated as v_r decreases. This is not at all suprising in light of our earlier general observations (#1 and #2 above) that VRI collision probabilities are enhanced at high v_r and high j_i.

Finally, we note that as with the rigid-rotor results, the calculated velocity dependence of $\sigma_{42,-2}$ (as with +2 - not shown) agrees well with experiment, though it overestimates the rise at low v_r like before (fig. 7). Likewise, the obvious "torque-averaging effects for $v_r \geq 2s_p$ are also very well reproduced by both rigid and vibrating-rotor models. The Δ = -4 calculation (not shown) again overestimates the $v_r = 1s_p$ experimental value of 5.5Å^2, though the present value of 8.1Å^2 is an improvement on the earlier calculated value of 9.4Å^2. This disagreement for high j_i, low $v_r \approx 1s_p$, and small Δ remains less than satisfactorilly explained.

Vibrationally inelastic cross-sections.

In table 3 we present values for $Q_V(9,j_i)$, as well as $Q(9,22;\pm1)$,

Table IV.3

	$Q_V(9,j_i)$ (Å^2), as a function of v_r		
j_i	$v_r = 1s_p$	$v_r = 2s_p$	$v_r = 3s_p$
8	10 ± 2	30 ± 3	38 ± 5
22	15 ± 5	33 ± 3	37 ± 5
42	45 ± 5	44 ± 3	45 ± 5

Δv	$Q(9,22;\Delta v)$ (Å^2), for $v_r = 2s_p$
+1	14.5 ± 1.5
-1	9.5 ± 1.5

the latter for comparison with experimental values of $\overline{Q}(4,28;\pm1) \simeq 10\pm2\text{Å}^2$ for $\Delta v = +1$, and $\simeq 15\pm3\text{Å}^2$ for $\Delta v = -1$. A very brief study of trajectory runs at $v_i = 4$, $j_i = 28$, and $v_r = 2s_p$ did not however show any large, obvious deviations from values typically found for $v_i = 9$, $j_i = 22$, and $v_r = 2\ s_p$. For table 3 approximate the velocity averaged $\overline{Q}$ by results for $v_r = 2s_p$. As is readily seen, these values well reproduce the experimental values for $\overline{Q}(4,28;\pm1)$ as expected. As mentioned previously, we assumed these values as a rough guide in fitting the vibrational results of our trial potentials. We do speculate, however, that this latter proceedure might possibly result in an under-estimation of the real $\overline{Q}(9,j_i;\Delta v)$ by our calculation. If true, this could mean that ε may in fact be somewhat larger than our present estimate of 8-10 (i.e. 270-340 cm^{-1}), though very unlikely by more than a factor of 1.5-2. The $Q_V(9,j_i)$ as a funtion of v_r are seen to confirm our observations stated in #1 and #2 above.

Summary

Our vibrating-rotor calculations show that for the majority of (j_i,Δ) pairs we have made measurements for, the v_r dependence, as well as the j_i,Δ dependence, is determined primarily by rotational dynamics of the Li_2^*-Xe collision system, with the vibrational motion of Li_2^* and vibrational inelasticity playing a relatively "minor" role; of course inclusion of vibrational effects did require a non-negligable change in our initial rigid-rotor potential to obtain agreement with the data as a

whole.

With a very few isolated exceptions (most with v_r near v_{th}, and thus unreliable anyway) our vibrating-rotor model gave equally good or better agreement with experiment (i.e. 23 j_i,Δ pairs at 3 distinct v_r) than did results of our rigid-rotor calculations. This was especially and most importantly true for $\Delta \geq +12$, where rigid-rotor results failed very distinctly (often by factors $\gtrsim 2$), in stark contrast to the vibrating-rotor results which gave agreement within expected error for the majority of these large $+\Delta$ cross-sections. Further, the vibrating-rotor results agreed fairly well (to the best of our knowledge) for the calculation of $Q(9,j_i;\Delta v)$, which of course a rigid-rotor model is incapable of.

Despite our earlier warnings about the "preliminary" nature of the vibrational calculations, not to mention the unknown error incurred by using a H.O. approximation for U(r),it seems extremely unlikely that we could obtain agreement of the unexpected high quality we have indeed found, as the result of several or many fortuitious coincidences. We stand convinced that vibrational inelasticity is responsible for the characteristic velocity dependence of the large $+\Delta$ RI cross-sections in Li_2^*-Xe.

Most important of all, we feel we have greatly increased the available knowledge of Li_2^*-Xe interaction potentials (and indeed excited alkali-rare gas potentials) relative to that known prior to this work.

While we will not claim our potentials are precisely correct or unique, we feel the "inversion" of our data to yield information on the potential was done to a degree of accuracy far beyond that possible using only velocity averaged data, and even perhaps beyond that possible with fixed energy differential scattering data.

Hopefully, the future will see a more complete vibrating-rotor trajectory study in Li_2^*-Xe where many more trajectories are run to give much more satisfactory convergence and confidence of results. Admittedly, our PDP 11/34 computer is not well suited for this task - although our vibrational trajectories run with an average step size of about 10^{-14} sec, $\approx$ 100 times more efficient than other workers[53], our user time is only just comparable to theirs due to the $\sim$ 100 times faster computing speed of their CDC 7600 computer.

Another possible outgrowth of the present work would be a study of <u>both</u> rigid <u>and</u> vibrating-rotor trajectory calculations on Li_2^*-Ar and Ne. It would be interesting to compare sucess of the two dynamical models in these cases, as we expect vibration to play a less important role than in the case of Xe. Finally, for all future calculation purposes, it would be of great aid if more experimental data on VRI cross-sections, especially for $v_i = 9$, could be obtained in the future.

APPENDIX A

MATHEMATICS OF VSDS DECONVOLUTIONS

Deconvolution of thermal averaging in scattering experiments using integral transform methods[a)]

Neil Smith,[b)] Timothy A. Brunner, Richard D. Driver, and David E. Pritchard

Research Laboratory of Electronics and Department of Physics, Massachusetts Institute of Technology, Cambridge, Massachusetts 02139
(Received 2 May 1978)

In several distinct types of scattering experiments the velocity distribution of some components of velocity of the primary and/or target particles is a Maxwell–Boltzmann distribution of known width, while other velocity components are known to far better precision. We derive inversion procedures using Fourier and Laplace transforms which permit the detailed microscopic rate constant $k(V_{rel})$ to be recovered from the measured quantities. Experiments using the beam–gas arrangement, velocity selection (of one component) by Doppler shift, and experiments conducted in complete thermal equilibrium are considered. Practical applications and limitations are discussed.

I. INTRODUCTION

The objective of many types of scattering experiments is to measure the dependence of the microscopic rate constant

$$k(v_r) = v_r Q(v_r)$$

on the relative speed v_r of the colliding partners, where $Q(v_r)$ is the cross section for the particular process of interest. In a wide variety of such experiments some or all of the velocity components of the primary and target collision partners are distributed with a Maxwell-Boltzmann (M–B) velocity distribution characterized by a known temperature, while other velocity components are known to much better precision. The measured quantity in such cases is essentially an average of $k(v_r)$ over all thermal (M–B distributed) velocity components.

In this paper we present mathematical methods for deconvoluting data characterized by thermal averaging of this sort, to obtain the unaveraged quantity $k(v_r)$. We treat, in subsequent sections, averaging occurring in experiments employing the beam–gas (BG) technique, velocity selection by Doppler shift (VSDS), and measurements made with all velocity components in thermal equilibrium (TE) over a range of temperatures. A final section is devoted to a discussion of the practical application of these techniques. The cross section Q may depend on the initial and final states of the collision partners but we assume that it does not depend on the orientation of v_r.

This paper is inspired by Kinsey's recent paper on Fourier transform Doppler spectroscopy,[1] as well as experiments in our laboratory using the VSDS technique.[2–4] Fourier transform methods are especially well suited to situations involving convolution integrals and Fourier methods are employed in deconvoluting the thermally averaged data in the BG and VSDS experiments. Laplace transforms are used in the case of the TE experiments.

For simplicity we use the following notation:

(1) Subscripts p, t refer to primary, target collision partners.

(2) Subscripts b, d, e refer to BG, VSDS, and TE experiments.

(3) $s_t = \sqrt{k_B T/M_t}$, $s_p = \sqrt{k_B T/M_p}$, where k_B is Boltzmann's constant. These will be used as velocity units in Secs. III and IV.

(4) Unprimed functions are functions of velocity variables. The corresponding function of the corresponding dimensionless variable is denoted by a prime [i.e., if $v/S_t = x$ $F(v) = F(S_t x) = F'(x)$].

(5) $\bar{k}_x$ is the thermal average of $k(v_r)$, where x takes on one of the subscripts in (2) above for the three cases considered.

II. BEAM–GAS EXPERIMENT

In a beam–gas experiment, a well-collimated beam of primary particles with a monochromatic speed v_b scatters from a target gas in thermal equilibrium. What is inferred experimentally is the rate constant $\bar{k}_b(v_b)$, the average of $k(v_r)$ over the M–B velocity distribution of the target particles, as a function of v_b:

$$\bar{k}_b(v_b) = (2\pi s_t^2)^{-3/2} \times \int_{-\infty}^{\infty} d^3 v_t \exp(-v_t^2/2s_t^2)\, k[(v_t^2 + v_b^2 - 2v_{tz}v_b)^{1/2}] \,. \tag{II.1}$$

We have chosen a coordinate system so that the beam travels along the $\hat{z}$ axis, thus $\mathbf{v}_b = v_b \hat{z}$, and we use the notation $v^2 = |\mathbf{v}|^2$. Switching to a relative coordinate system $\mathbf{v}_r = \mathbf{v}_b - \mathbf{v}_t = v_b\hat{z} - \mathbf{v}_t$, this equation becomes

$$\bar{k}_b(v_b) = (2\pi s_t^2)^{-3/2} \int_{-\infty}^{\infty} \exp\left(\frac{-(v_{rz}^2 + v_{rz})^2}{2s_t^2}\right) \times \exp\left(\frac{-(v_b - v_{rz})^2}{2s_t^2}\right) k[(\mathbf{v}_r^2)^{1/2}]\, d^3 v_r \,. \tag{II.2}$$

Making the substitution $\mathbf{z} = \mathbf{v}_r/s_t$, $x_b = v_b/s_t$, switching to the spherical coordinates (z, θ, ϕ) and carrying out the integrals over θ and ϕ, we obtain

[a)]Work supported by the Joint Services Electronics Program, Contract No. DAAB07-76-C-1400.
[b)]Part of work completed while in M.I.T. Undergraduate Research Opportunities Program.

 0021-9606/78/6904-1498$01.00

$$x_b\bar{k}'_b(x_b) = (2\pi)^{-1/2}\int_0^\infty z k'_b(z)\left[\exp\left(\frac{-(x_b-z)^2}{2}\right) - \exp\left(\frac{-(x_b+z)^2}{2}\right)\right] dz \ . \tag{II. 3}$$

We now wish to consider the more general quantity $\exp(-\alpha x_b^2/2)\bar{k}'_b(x_b)$, where $\alpha \geq 0$ is an unspecified parameter whose usefulness will be discussed later. By completing the square in the exponents [and replacing z by $(\alpha+1)z$] we find that

$$e^{-\alpha x_b^2/2} x_b \bar{k}'_b(x_b) = (\alpha+1)(2\pi)^{-1/2}\int_0^\infty z\, dz k'[(\alpha+1)z]\exp\left(\frac{-\alpha(\alpha+1)z^2}{2}\right)\left[\exp\left(\frac{-(\alpha+1)(x_b-z)^2}{2}\right) - \exp\left(\frac{-(\alpha+1)(x_b+z)^2}{2}\right)\right]. \tag{II. 4}$$

The resulting equation is of the same form as Eq. (A3) of Appendix A, with $h(x_b) = \exp(-\alpha x_b^2/2)\, x_b \bar{k}'_b(x_b)$, $f(z) = zk'[(\alpha+1)z]\exp[-\frac{1}{2}\alpha(\alpha+1)z^2]$, and $g(u) = (\alpha+1)(2\pi)^{-1/2}\exp[-\frac{1}{2}(\alpha+1)u^2] = g(-u)$. Using the fact from Eq. B1 that $\mathfrak{F}_{(\alpha)}[g] = (\alpha+1)^{3/2}\exp[-2\pi^2\kappa/(\alpha+1)]$, we can invert Eq. (II. 4) by using Eq. (A5) of Appendix A to give

$$k'[(\alpha+1)z] = k[(\alpha+1)s_t z] = \frac{\exp[\frac{1}{2}\alpha(\alpha+1)z^2]}{z(\alpha+1)^{3/2}}\ \mathfrak{F}^{-1}_{(z)}\left[\exp\left(\frac{2\pi^2\kappa^2}{\alpha+1}\right)\mathfrak{F}_{(\alpha)}[e^{-\alpha x_b^2/2} x_b \bar{k}'(x_b)]\right]. \tag{II. 5}$$

Thus, knowledge of the thermally averaged rate constant measured in a BG experiment as a function of initial primary beam velocity is sufficient for a unique determination of the relative velocity dependence of the true microscopic rate constant $k(v_r)$.

From a physical standpoint, we can only measure $\bar{k}'_b(x_b)$ for $x_b \geq 0$. However, mathematically speaking, $\bar{k}'_b(-x_b) = \bar{k}'_b(x_b)$, as can be seen from Eq. (II. 3), and so we take $\bar{k}'_b(-x_b) = k'_b(x_b)$ when taking the Fourier transform of $\bar{k}'_b(x_b)$.

III. THE VSDS EXPERIMENT

In the VSDS technique[2,3] both the primary and target particles are contained within a gas, or vapor cell. The technique allows for the selection of one velocity component of the primary particle to a very high degree of accuracy. Again, we choose a coordinate system so that the selected velocity component is the $\hat{z}$ component, whose magnitude we denote by v_d (i.e., $v_{pz} = v_d$). The experimentally measured quantities are proportional to $\bar{k}_d(v_d)$, the thermal average of the microscopic rate constant $k_d(v_r)$ over the five unselected M–B distributed velocity components of the target and primary particles. Thus $\bar{k}_d(v_d)$, as a function of selected speed v_d, is given by

$$\bar{k}_d(v_d) = \left(\frac{1}{2\pi s_t^2}\right)^{3/2}\left(\frac{1}{2\pi s_p^2}\right)\int_{-\infty}^{\infty} dv_{px}\, dv_{py} \exp\left(\frac{-(v_{px}^2+v_{py}^2)}{2s_p^2}\right) \times \int_{-\infty}^{\infty} k_d[(\mathbf{v}_p^2 + \mathbf{v}_t^2 - 2\mathbf{v}_p\cdot\mathbf{v}_t)^{1/2}]\exp\left(\frac{-\mathbf{v}_t^2}{2s_t^2}\right) d^3v_t \ . \tag{III. 1}$$

Using the relative velocity $\mathbf{v}_r = \mathbf{v}_p - \mathbf{v}_t$, we substitute $\mathbf{v}_t = \mathbf{v}_p - \mathbf{v}_r$ and integrate over v_{px} and v_{py}. The result is, in terms of relative velocities,

$$\bar{k}_d(v_d) = \frac{1}{2\pi(s_p^2+s_t^2)}\left(\frac{1}{2\pi s_t^2}\right)^{1/2}\int_{-\infty}^{\infty} d^3v_r \exp\left(\frac{-(v_{rx}^2+v_{ry}^2)}{2(s_p^2+s_t^2)}\right) \times \exp\left(\frac{-(v_d - v_{rz})^2}{2s_t^2}\right) k_d[(\mathbf{v}_r^2)^{1/2}] \ . \tag{III. 2}$$

Switching to spherical coordinates (v_r, θ, ϕ), integrating over ϕ, and letting $a = \cos\theta$, the above equation yields

$$\bar{k}_d(v_d) = \frac{1}{s_p^2+s_t^2}\left(\frac{1}{2\pi s_t^2}\right)^{1/2}\int_0^\infty v_r^2 \exp\left(\frac{-v_r^2}{2(s_p^2+s_t^2)}\right) k_d(v_r) dv_r \times \int_{-1}^{1}\exp\left(\frac{-(v_d - v_r a)^2}{2s_t^2}\right)\exp\left(\frac{v_r^2 a^2}{2(s_t^2+s_p^2)}\right) da \ . \tag{III. 3}$$

We now make the substitution $x_d = v_d/s_p$, $y = v_r/s_p$, and defining $\tau = s_t^2/s_p^2$, the above equation gives, after rearranging the integral over a,

$$\bar{k}_d(x_d) = \frac{1}{\tau+1}\left(\frac{1}{2\pi\tau}\right)^{1/2}\int_0^\infty y^2 \exp\left(\frac{-y^2}{2(\tau+1)}\right) k_d(y)\, dy \times \int_{-1}^{1} e^{\tau a^2/2}\exp\left[-\left(\frac{\tau+1}{2\tau}\right)\left(x_d - \frac{ya}{\tau+1}\right)^2\right] da. \tag{III. 4}$$

Using Eq. (III. 4), it is straightforward to show that

$$x_d\bar{k}'(x_d) - \frac{d\bar{k}'(x_d)}{dx_d} = \left(\frac{1}{2\pi\tau}\right)^{1/2}\int_0^\infty y\exp\left(\frac{-y^2}{2(\tau+1)}\right) k'_d(y)\, dy \int_{-1}^{1} e^{\tau a^2/2}\ \frac{d}{da}\left\{\exp\left[\frac{-(\tau+1)}{2\tau}\left(x - \frac{ya}{\tau+1}\right)^2\right]\right\} da$$
$$= \left(\frac{1}{2\pi\tau}\right)^{1/2}\int_0^\infty y k'_d(y)\left[\exp\left(\frac{-(x_d-y)^2}{2\tau}\right) - \exp\left(\frac{-(x_d+y)^2}{2\tau}\right)\right] dy \ , \tag{III. 5}$$

the last equation being obtained after performing the integral over a, and rearranging the result.

Comparison of Eqs. (II. 3) and (III. 5) shows that $[k_d(x_d) - (1/x_d)(d\bar{k}_d/dx_d)]$ can be considered to be the average of the microscopic rate constant in a BG experiment with beam speed $= v_d$. This interesting result, in a slightly different form, was first shown by Kinsey,[1] through independent means.

Considering the more general quantity $\exp(-\delta x_d^2/2\tau^2)(x_d\bar{k}_d' - d\bar{k}_d'/dx_d)$, in analogy with Sec. II, we obtain the following result [similar to Eq. (II. 4)] after replacing y by $(1+\delta)y$:

$$e^{-\delta x_d^2/2\tau}\left(x_d\bar{k}_d' - \frac{d\bar{k}_d'}{dx_d}\right) = \left(1-\frac{\delta}{\tau}\right)x_d\bar{k}_d' e^{-\delta x_d^2/2\tau} - \frac{d}{dx_d}\left(e^{\delta x_d^2/2\tau}\bar{k}_d'\right)$$

$$= \frac{(\delta+1)^2}{(2\pi\tau)^{1/2}}\int_0^\infty y\exp\left(\frac{-\delta(\delta+1)y^2}{2\tau}\right)k_d'[(1+\delta)y]\left[\exp\left(\frac{-(\delta+1)}{2\tau}(x_d-y)^2\right) - \exp\left(\frac{-(\delta+1)}{2\tau}(x_d+y)^2\right)\right] . \quad \text{(III. 6)}$$

Equation (III. 6) is of the same form as Eq. (A3), with

$$h(x_b) = \left[\left(1-\frac{\delta}{\tau}\right)x_d\bar{k}_d' e^{-\delta x_d^2/2\tau} - \frac{d}{dx}\left(e^{-\delta x_d^2/2\tau}\bar{k}_d'\right)\right] ,$$

$$f(y) = y\exp\left(\frac{-\delta(\delta+1)y^2}{2\tau}\right)k_d'[(1+\delta)x_d] ,$$

and

$$g(u) = \frac{(\delta+1)^2}{(2\pi\tau)^{1/2}}\exp\frac{-(\delta+1)u^2}{2\tau} = g(-u) .$$

Thus, using the results of Eqs. (A5) and (A6), and the fact from Eq. B1 that $\mathcal{F}(\kappa)[g] = (\delta+1)^{3/2}\exp[-2\tau\pi^2\kappa/(\delta+1)]$, we have

$$k_d'[(1+\delta)y] = k_d[(1+\delta)s_p y]$$

$$= \frac{\exp[\delta(\delta+1)y^2/2\tau]}{y(\delta+1)^{3/2}}\left(\mathcal{F}_{(y)}^{-1}\left\{\exp\left(\frac{2\tau\pi^2\kappa}{\delta+1}\right)\left[\left(1-\frac{\delta}{\tau}\right)\right.\right.\right.$$

$$\left.\left.\left.\times\mathcal{F}_{(x)}[x_d e^{-\delta x_d^2/2\tau}\bar{k}_d'(x_d)] + 2\pi i\kappa\,\mathcal{F}_{(x)}[e^{-\delta x_d^2/2\tau}\bar{k}_d'(x_d)]\right]\right\}\right) . \quad \text{(III. 7)}$$

For the special case $\delta = \tau$, we have the simpler result

$$k_d'[(1+\tau)y] = k_d[(1+\tau)s_p y]$$

$$= \frac{\exp[\frac{1}{2}(\tau+1)y^2]}{y(\tau+1)^{3/2}}\left\{\mathcal{F}_{(y)}^{-1}\left[2\pi i\kappa\right.\right.$$

$$\left.\left.\times\exp\left(\frac{2\tau\pi^2\kappa^2}{\tau+1}\right)\mathcal{F}_{(x)}[e^{-x_d^2/2}\bar{k}_d'(x_d)]\right]\right\} \quad \text{(III. 8)}$$

involving only one transform. A physical explanation of why $\delta = \tau$ is an exceptional case is that $\exp(-\delta x_d^2/2\tau)|_{\delta=\tau} = \exp(-x_d^2/2)$ is proportional to the number of primary particles in the gas whose z velocity is equal to the selected speed $v_d = s_p x$, as can be determined by the form of the Maxwell–Boltzmann distribution.

IV. THERMALLY AVERAGED DATA

In this section we show that it is in principle possible to infer the microscopic rate constant from data taken under conditions of complete thermal equilibrium (but of course measurements must be made over a wide range of temperatures). In such a system, each component of the relative velocity has a M–B distribution characterized by a width $s_\tau = \sqrt{s_p^2 + s_t^2} = \sqrt{k_B T/\mu}$, where μ is the reduced mass of the system. The mean rate constant is then given by the well-known expression

$$\bar{k}_t(T) = (2/\pi)^{1/2}s_\tau^{-3}\int_0^\infty v_\tau^2 e^{-v_\tau^2/2s_\tau^2}k(v_\tau)\,dv_\tau , \quad \text{(IV. 1)}$$

where we are working in terms of the relative velocity $v_\tau = v_p - v_t$. We can put this integral in terms of the dimensionless variables $p = v_\tau^2/2s_0^2$ and $\tau = s_0^2/s_\tau^2$, where $s_0 = (kT_0/\mu)^{1/2}$ and T_0 is a reference temperature, thus

$$(\pi/2)^{1/2}\tau^{-3/2}\bar{k}_d(\tau) = \int_0^\infty dp(2p)^{1/2}k_d'[(2p)^{1/2}]e^{-\tau p}$$

$$= \mathcal{L}_{(\tau)}\{(2p)^{1/2}k_d'[(2p)^{1/2}]\} , \quad \text{(IV. 2)}$$

where

$$\mathcal{L}_{(\tau)}[f(x)] = \int_0^\infty e^{-\tau x}f(x)\,dx$$

$$= \text{Laplace transform of } f(x) .$$

Thus (if we can invert the Laplace transform) we have that

$$k_d'[(2p)^{1/2}] = (2p)^{-1/2}\mathcal{L}_{(p)}^{-1}[\sqrt{\pi/2}\,\tau^{-3/2}\bar{k}_d(\tau)] . \quad \text{(IV. 3)}$$

Unlike the previous two cases, the procedure involves only an inverse transformation. We shall not discuss this procedure further, since its practicality is considerably limited by the instabilities and uncertainties in inverting Laplace transforms with values known only along the real axis,[5] as well as the problem of obtaining wide ranges of temperature over which to take data.

V. DISCUSSION

The mathematical deconvolution procedure developed in the preceding sections are all designed to extract the microscopic rate constant from real thermally averaged data. As such, it is appropriate to consider some of the problems and limitations that will be encountered in the practical applications of these techniques, and how, to at least some extent, they may be overcome.

There are three fundamental problems which in practice limit the accuracy and validity of "unaveraged" rate constants obtained using our deconvolution techniques. Firstly, in any real experiment (BG or VSDS), data can be measured only over a limited range of selected speed, or velocity (v_b or v_d). This creates problems in applying the deconvolution procedures (which demand data over the range 0 to ∞), and at the very least will prevent one from obtaining accurate information of $k(v)$ for values of v well outside the range of values of the selected velocity. Secondly, real data contain noise, and this noise generally has a roughly flat spectral density. This is especially troublesome because the essence of deconvolution is to multiply the Fourier transform of the data by a function which increases rapidly at high frequencies in order to compensate for the falloff of

response of the measurement process at these frequencies. In order to prevent the deconvoluted rate constant from containing unacceptably large amplitudes of high frequency components, some procedure must be devised to remove this noise from the deconvoluted rate constant which neither looses valuable information from the data nor generates unphysical high frequency structure in the result. Thirdly, data are generally taken only at discrete points, and not over a continuous velocity range. This puts an upper limit to the resolution of the data, but since the spacing between points can usually be controlled by the experimenter, it should never be the dominant practical limitation. Another possible limitation may arise from the fact that in real BG or VSDS experiments, data must be taken with only finite resolution of the selected velocity. The effects of this finite resolution can usually be expressed as a convolution integral involving some resolution function of the experiment, which can generally be measured or calculated. Thus, in principle, such effects can be deconvolved simultaneously with the deconvolution procedures discussed above. In any event, these effects should generally be small compared to the thermal averaging.

In this section we shall discuss two practical techniques for applying the mathematical deconvolution methods we have presented in this paper to real data, by which we mean a finite set of data points, with noise, taken over a finite velocity range at discrete points. We shall discuss how the fundamental limitations mentioned above affect the accuracy and validity of these practical techniques.

The first technique involves the use of finite discrete Fourier transforms,[6-8] which can be used to approximate the Fourier transformation $\mathcal{F}_{(\kappa)}[f]$ of a function $f(x)$, whose values are known only for $x = n\Delta (n = 0, \pm 1, \pm 2, \ldots \pm N)$. The approximation is valid for $|\kappa| \leq 1/2\Delta$ and the subsequent inversion for $|x| \leq N\Delta$. The discrete transform approximation cannot distinguish between $\mathcal{F}_{(\kappa)}[f]$ and $\mathcal{F}_{(\kappa \pm m/\Delta)}[f]$ (integer m), a problem known as aliasing. If $\mathcal{F}_{(\kappa)}[f]$ is negligible for $|\kappa| > 1/2\Delta$, then this is not a significant source of error. The most troublesome limitation of the discrete transform approach results from the finite range of the data: the discrete transform approximation to $\mathcal{F}_{(\kappa)}[f]$ will be (neglecting aliasing) the convolution of $\mathcal{F}_{(\kappa)}[f]$ and $\mathcal{F}_{(\kappa)}[W]$ where $W(x)$ is a "data window" function[6,7] which is zero for $|x| > N\Delta$, and is a constant (unity) or smoothly tapering function for $|x| \leq N\Delta$. In general, $\mathcal{F}_{(\kappa)}[W]$ has a FWHM $\approx 1/N\Delta$ in κ space, so the larger $N\Delta$ (the larger the range of data) the smaller the error. More importantly, $\mathcal{F}_{(\kappa)}[W]$ falls off as κ^{-n} for large κ and so the discrete transform approximation to $\mathcal{F}_{(\kappa)}[f]$ cannot fall off faster than κ^{-n}. This has serious consequences, since we must multiply the transform of the data by a factor $e^{B\kappa^2} (B > 0)$ for both the BG and VSDS deconvolution procedures. Application of smoothing techniques such as digital filtering, or fitting, before carrying out the discrete transform alleviates to a certain extent this problem (and may also limit the noise in the data). In any case, to prevent the transforms from blowing up for "large" κ, the transform can be multiplied by a cutoff filter $C(\kappa)$ [the κ space analogue of $W(x)$, which is identically zero for $|\kappa| > \kappa_{\max}$]. After multiplication by $C(\kappa)$, the inverse transform can be carried out. However, use of $C(\kappa)$ results in a final resolution of $\Delta x \approx 1/\kappa_{\max} \{= \text{FWHM}\, \mathcal{F}^{-1}_{(x)}[C(\kappa)]\}$ in the deconvoluted result. This can still be a significant improvement over the experimental resolution, which is about $\Delta z \approx 2.4$, for BG, and $\Delta y \approx 2.4 r^{1/2}$ for VSDS (FWHM $e^{-x^2}/2\sigma^2 \approx 2.4\sigma$). The functions $\exp(-\alpha x_b^2/2)$, $\exp(-\delta x_d^2/2r)$ in Eqs. (II. 4) and (III. 6) may in a sense be considered as variable window function depending on α, or δ, which may help reduce the aliasing and especially the data window convolution problem, resulting in higher resolution and more accurate results. Further important discussion about the effects and choices for window functions can be found in references.[6,7]

The second practical technique for implementing our deconvolution procedures is to fit the data with analytic functions which allow the entire Fourier transform deconvolution procedure to be carried out analytically. A specific example describing suitable functions is described in Appendix B, using fitting functions of the form $\exp(-cx^2/2) \sum_{n=0}^{N} a_n x^{2n}$. In the discussion here we shall consider the more general aspects of such a procedure.

The fit, like the analytic functions which comprise it, is defined over the entire velocity range, thus preventing problems arising from the finite numbers or range of the data points from interfering with the Fourier transform deconvolution process. These problems now appear as the question "does the fit accurately represent reality in regions where no data were taken?" This question is most troublesome in the velocity range(s) not experimentally accessible, and the variation of the deconvoluted result with respect to plausible extensions of the data must be considered an error in this result. Generally speaking, the term in Eqs. (II. 3) and (III. 5) which goes like $\exp[-(\omega \pm u)/2\sigma^2]$ assures that the data and the deconvolution are relatively independent when their arguments (u and w here) differ by more than 2σ. If the highest datum is at u_0 then the deconvolution should be relatively independent of the extension when $w < u_0 - 2\sigma$ and relatively independent of the data (and hence reality) for $w > u_0 + 2\sigma$. Further, inspection of these same equations reveals that the data $\bar{k}'(u)$ are relatively insensitive to $k'(w)$, for $w \lesssim \sigma$, due to the substantial cancellation of the two exponential terms of the integrand. Physically, this results from the fact that there are comparatively few collision partners with relative velocities w much less than σ. Thus, it is unlikely that any deconvolution procedure can obtain accurate information for $k(w)$, for $w \ll \sigma$.

Problems due to the enhancement of high frequency components are manifest in two ways when using the fitting approach. If too few fitting functions are used to fit the data, it is probable that the fit will not reproduce small high frequency structure in the data, resulting in a loss of this information in the deconvolution. If too many fitting functions are used, the most probable result is a small high frequency oscillation of the fit about the data which will become considerably amplified

in the deconvolution. Close attention to the reduction in the χ^2 of the fit with increases in the number of fitting functions employed is necessary to avoid these extremes.

We shall present a further discussion, including several examples, of the application of the above technique to VSDS data in a future publication.

APPENDIX A: SOME PROPERTIES OF FOURIER TRANSFORMS

In this section we define some properties of Four.er transforms which are useful in the analysis.

We use the following convention:

$$\mathfrak{F}_{(x)}[b(x)] = \mathfrak{F}_{(x)}[b] = \int_{-\infty}^{\infty} e^{2\pi i x\kappa} b(x)\,dx$$

—Fourier transform of b , (A1)

$$\mathfrak{F}^{-1}_{(y)}[\mathfrak{F}_{(x)}[b]] = \int_{-\infty}^{\infty} e^{-2\pi i \kappa y} \mathfrak{F}_{(x)}[b]\,d\kappa = b(y) - \text{inverse Fourier transform} . \quad (A2)$$

Next consider an integral equation of the form

$$h(p) = \int_0^{\infty} f(q)[g(p-q) - g(p+q)]\,dq , \quad (A3)$$

where $f(q)$ is defined for $0 \le q \le \infty$ and $h(p)$ and $g(u)$ are defined for $-\infty \le p \le \infty$ and $-\infty \le u \le \infty$, respectively. The object is to solve for $f(q)$ when $h(p)$ and $g(u)$ are known.

In the case that $g(u)$ is an even function [i.e., $g(-u) = g(u)$], we can extend the domain of $f(q)$ over the interval $-\infty \le q \le \infty$ by defining $f(-q) = -f(q)$. Equation (A3) may then be rewritten as

$$h(p) = \int_{-\infty}^{\infty} f(q) g(p-q)\,dq . \quad (A4)$$

This may be inverted by the familiar convolution theorem of Fourier analysis[9] to give

$$f(q) = \mathfrak{F}^{-1}_{(q)}\left[\frac{\mathfrak{F}_{(x)}[h]}{\mathfrak{F}_{(x)}[g]}\right]. \quad (A5)$$

Other important relations can be derived from Eqs. (A1) and (A2):

$$\mathfrak{F}_{(x)}\left[\frac{db(x)}{dx}\right] = -2\pi i \kappa \mathfrak{F}_{(x)}[b] ,$$

$$\mathfrak{F}^{-1}_{(\kappa)}\left[\frac{dc(\kappa)}{d\kappa}\right] = 2\pi i x\, \mathfrak{F}^{-1}_{(\kappa)}[c] , \quad (A6)$$

$$\mathfrak{F}_{(x)}[xb(x)] = 1/2\pi i \frac{d}{d\kappa}\{\mathfrak{F}_{(x)}[b(x)]\} ,$$

$$\mathfrak{F}^{-1}_{(\kappa)}[\kappa c(\kappa)] = i/2\pi \frac{d}{dx}\{\mathfrak{F}^{-1}_{(\kappa)}[c(\kappa)]\} . \quad (A7)$$

APPENDIX B: ONE EXAMPLE OF A FAMILY OF FITTING FUNCTIONS

In this Appendix we will show one example of a family of fitting functions, whose Fourier transforms can be done analytically. They are of the form $x^{2n} e^{-cx^2/2}$, with n integer ≥ 0, and $c \ge 0$. These functions are even functions of their arguments, to be mathematically consistent with Eqs. (II. 2) and (III. 5), which demand $\bar{k}_b(x_b)$ and $\bar{k}'_d(x_d)$ to be even functions. The following results will be useful when evaluating Fourier transforms of these functions:

$$\mathfrak{F}^{-1}_{(x)}[e^{-ax^2}] = (\pi/a)^{1/2} e^{-\pi^2\kappa^2/a}$$

$$\mathfrak{F}^{-1}_{(x)}[e^{-a\kappa^2}] = (\pi/a)^{1/2} e^{-\pi^2 x^2/a} , \quad (B1)$$

$$\mathfrak{F}_{(\kappa)}[x^n f(x)] = (1/2\pi i)^n \frac{d^n}{d\kappa^n}\{\mathfrak{F}_{(\kappa)}[f(x)]\} ,$$

$$\mathfrak{F}^{-1}_{(x)}[\kappa^n g(\kappa)] = (1/2\pi i)^n \frac{d^n}{dx^n}\{\mathfrak{F}^{-1}_{(x)}[g(\kappa)]\} , \quad (B2)$$

where Eq. (B2) is a generalization of Eq. (A7). A third very useful result can be found from expressions for the Hermite polynomials $H_n(x) = (-1)^n e^{x^2}(d^n/dx^n)e^{-x^2}$. Equating this expression, and the following power series form of $H_{n(x)}$,[10]

$$\text{For } n \text{ even} \quad H_n(x) = n! \sum_{m=0}^{n/2} \frac{(-1)^m (2x)^{n-2m}}{m!\,(n-2m)!} , \quad (B3)$$

$$\text{For } n \text{ odd} \quad H_n(x) = n! \sum_{m=0}^{n/2-1} \frac{(-1)^m (2x)^{n-2m}}{m!\,(n-2m)!}$$

yields the following useful result:

$$\text{For } n \text{ even} \quad \frac{d^n}{dx^n} e^{-ax^2} = e^{-ax^2} \sum_{m=0}^{n/2} \frac{(-1)^m n!\, a^{n-m}(2x)^{n-2m}}{m!\,(n-2m)!} \quad (B4)$$

$$\text{For } n \text{ odd} \quad \frac{d^n}{dx^n} e^{-ax^2} \sum_{m=0}^{n/2-1} \frac{(-1)^{m+1} n!\, a^{n-m}(2x)^{n-2m}}{m!\,(n-2m)!} .$$

To deconvolute a BG experiment using these functions, we first approximate (fit) $\bar{k}_b(x_b)$:

$$\bar{k}_b(x_b) = e^{-c_b x_b^2/2} \sum_{n=0}^{N} B_n x_b^{2n} . \quad (B5)$$

Substituting this equation into Eq. (II. 5), we can then derive an expression for $k'_b(z)$ with the aid of Eqs. (B1), (B2), and (B4). After considerable manipulations one can obtain the result

$$k'_b(z) = \frac{\exp[-c_b z^2/2(1-c_b)]}{(1-c_b)^{1/2}} \sum_{p=0}^{N} \frac{z^{2p}}{(2p+1)!} \times \sum_{n=p}^{N} \frac{B_n (2n+1)!\,(-1)^{n-p}}{2^{n-p}(1-c_b)^{n-p}(n-p)!} \quad (B6)$$

with the restriction that $0 \le C_b < 1$. The result, as it must be, is independent of the parameter α in Eq. (II. 4).

Application of these fitting functions to the VSDS case proceeds in a similar fashion. The approximation to $k'_d(x_d)$ is of the form

$$\bar{k}'_d(x_d) = e^{-c_d x_d^2/2} \sum_{n=0}^{N} A_n x_d^{2n} . \quad (B7)$$

This equation is then substituted into Eq. (III. 8) (we take the case $\delta = \tau$, for simplicity), and one can now solve for $k'_d(y)$, again utilizing Eqs. (B1), (B2), and (B4). The result one obtains after much calculation and manipulation is

$$k'_d(y) = \frac{\exp[-c_d y^2/2(1-c_d\tau)]}{(1-c_d\tau)} \sum_{p=0}^{N} \frac{y^{2p}}{(2p+1)!} \sum_{n=p}^{N} \frac{A_n(2n)!\,(-1)^{n-p}\tau^{2n-(p+1)}\{(2n+1)[\tau(1+c_d)/(1-c_d\tau)]+2(n-p)\}}{(1-c_d\tau)^{n-p}\,2^{n-p}\,(n-p)!}\,, \quad \text{(B8)}$$

with the restriction that $0 \leq c_d < 1/\tau$. That τ appears in the final result is not because we chose $\delta = \tau$ when doing the calculation, but because it is a fundamental parameter in the VSDS integrals. The restriction on the values at c_b and c_d stem from the fact that the Gaussian part of our fitting approximation to the convoluted data cannot in principle be "narrower" then the Gaussian function inside the convolution integrals.

The parameter c_b or c_d may be used to partially control the behavior of the approximating fit to $\bar{k}'_b$ or k'_d, outside the range of data, and prevent it from blowing up like x^n, which is entirely unphysical. A possible procedure when applying the above technique is to multiply the measured data $\bar{k}'_b(x_b)[k'_d(x_d)]$ by the function $\exp(c_b x_b^2/2^n)[\exp(c_d x_d^2/2^{2n}]$, having made an *a priori* choice for $c_b(c_d)$, and then fit the result with the polynomial $\sum_{n=0}^{N} B_n x_b^{2n}[\sum_{n=0}^{N} A_n x_b^{2n}]$, over the available range of data using standard fitting procedures (e.g., linear least squares, orthogonal polynomials, etc.).

An alternative procedure is to extend artificially the data over a greater range of velocity, before fitting, thus forcing the fit to follow this extension and removing the unphysical part of the fit from regions where it may influence the deconvolution in the original data range. To this end, a sufficient extension length should be $\Delta u = 2 - 3\sigma$ (see Sec. V). This procedure can be done with c_b or $c_d = 0$, thus simplifying the above deconvolution formulas. Examination of the variation of the deconvolution result with respect to changes in the extension should serve as a check to the validity of such an approach.

[1] J. L. Kinsey, J. Chem. Phys. 66, 2560 (1977).
[2] W. D. Phillips and D. E. Pritchard, Phys. Rev. Lett. 33, 1254 (1975).
[3] J. Apt and D. E. Pritchard, Phys. Rev. Lett. 37, 91 (1976).
[4] T. Brunner, R. D. Driver, D. E. Pritchard, and N. Smith (in preparation).
[5] R. E. Bellman, *Numerical Inversion of the Laplace Transform* (American Elsevier, New York, 1966).
[6] R. B. Blackman, and J. W. Tukey, *The Measurment of Power Spectra* (Dover, New York, 1958).
[7] G. M. Jenkins, *Spectral Analysis and its Applications* (Holden-Day, San Francisco, 1968).
[8] E. O. Brigham, *The Fast Fourier Transform* (Prentice-Hall, Englewood Cliffs, NJ, 1974).
[9] E. Butkov, *Mathematical Physics* (Addison-Wesley, Reading, MA, 1968), Chap. 7.
[10] *Handbook of Mathematical Functions*, edited by M. Abramowitz and I. Stegun (National Bureau of Standards, Washington, DC, 1970), p. 775.

APPENDIX B

A PREVIOUS VSDS EXPERIMENT IN $Na_2^*(A^1\Sigma)$-Xe

Velocity dependence of rates for rotationally inelastic collisions in Na_2^*–Xe using velocity selection by Doppler shift

Neil Smith, Timothy A. Brunner, and David E. Pritchard

Research Laboratory of Electronics and Department of Physics, Massachusetts Institute of Technology, Cambridge, Massachusetts 02139
(Received 29 July 1980; accepted 23 September 1980)

We have measured the velocity dependence of rotational energy transfer (RET) rate constants for $Na_2^*(A\,^1\Sigma_u^+)$–Xe collisions over an order of magnitude range in relative kinetic energy. Measurements were made for initial rotational levels $j_i = 16, 38$, and 66 for four different values of $\Delta = j_f - j_i$. The present data are analyzed in terms of the energy corrected sudden (ECS) scaling approximation and determine the velocity dependence of both the "adiabatic correction" factor of the ECS theory, and the parameters a and γ which appear in the power law expression for the basis rates $k_{i\to f}(v_r) = a(v_r)[l(l+1)]^{-\gamma(v_r)}$, an expression shown to be valid at all relative velocities studied. These measurements were made in a gas cell using the velocity selection by Doppler shift (VSDS) technique. Full details of analysis and deconvolution procedures used to isolate the relative velocity dependence are given.

I. INTRODUCTION

This paper contains measurements of the velocity dependence of rates for rotationally inelastic collisions made on a level to level basis in the system Na_2^*–Xe, where the Na_2^* is in the $v' = 18$ vibrational level of the $A\,\Sigma$ electronic state. For historical reasons this collision process—whose inelasticity is purely rotational — translational—will be termed rotational energy transfer (RET). Our earlier report of this work[1] was the first study of the velocity dependence of RET on a level to level basis, but there has recently been another one in HF–Ar.[2] Our experiment was conducted in a gas cell rather than a molecular beam machine, and velocity selection was achieved using the Doppler shift (VSDS). In earlier work[3] this method has been applied to fine-structure-changing collisions of Na(3p) with several targets, and it was possible to show ±5% agreement with suitably averaged measurements made by conventional molecular beams machines.

The present study, however, represents a major advance in the VSDS technique in two important respects: The experimental data are carefully corrected for contributions due to virtually excited molecules and also for multiple collisions by procedures described in Sec. III, and these data—which give the rate as a function of the one velocity component of the Na_2^* selected by the laser—are then analyzed using a method based on Fourier transforms[4] to give the level-to-level rate constants as a function of *relative* velocity. An extensive discussion of this procedure, together with some numerical examples, is given in Sec. IV. The result of this analysis is to extend the VSDS technique both in range and resolution: It is now possible to measure over a relative velocity range of about 4 to 1.

Data were obtained for roughly four different final values of rotational quantum number j_f for each of three initial values $j_i = 16$, 38, and 66. These data are presented in Sec. V. In Sec. VI we discuss these results in terms of recently developed[5,6] fitting laws for RET. We find that our rate constants can be well represented by a simple three parameter fitting law which assumes a power law for the rate constants $k_{i\to 0}$ into the $j_f = 0$ level at each relative velocity and also uses the energy corrected sudden (ECS) scaling law[5,6] to relate all other rate constants to these.

II. APPARATUS

A schematic diagram of our apparatus is shown in Fig. 1, and was described in detail earlier.[7] An important addition is photomultiplier tube PMT2 (RCA 31034, as is PMT3) which provides a second fluorescence analysis channel, allowing for simultaneous fluorescence intensity measurements at two different wavelengths. PMT2 is attached to an optics tower with translational capability to allow for wavelength selectivity. The base of this tower extends inside our Spex double monochromator. Attached to the base is a 7% pellicle beam splitter which intercepts focused light diffracted off the first grating of the monochromator and reflects some of it up

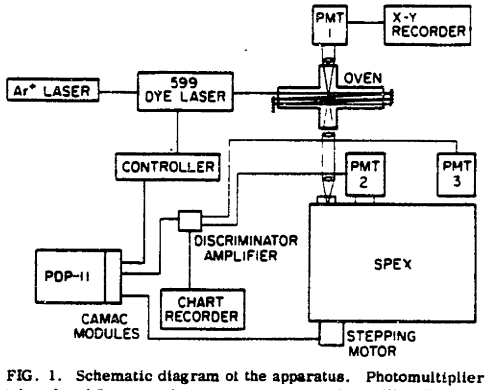

FIG. 1. Schematic diagram of the apparatus. Photomultiplier tubes 2 and 3 are used to monitor parent and satellite fluorescence, respectively.

 0021-9606/81/010467-16$01.00

and out of the monochromator and through a slit of ~150 μ width mounted directly in front of the PMT2 housing window.

Our electrically heated oven contains sodium vapor (Na pressure ~0.08 Torr and Na_2 pressure of $\sim 10^{-3}$ Torr at typical operating temperature of 350 °C) and xenon gas. A Coherent 599-21 single mode cw dye laser is used to populate the initial rovibronic level (v_i, j_i) in the $A\,\Sigma$ electronic state. Fluorescence from the transition $(v_i, j_i + \Delta) - (v'', j_i + \Delta \pm 1)$ (collisional satellite) is monitored by PMT3 mounted at the exit slit of the double monochromator, and more intense fluorescence $(v_i, j_i) - (v'', j_i \pm 1)$ from the laser populated level (parent) is monitored with PMT2. Techniques used to determine excited state quantum numbers, and to measure the thermally averaged rate constant at zero detuning for various j_i, Δ combinations, have been discussed earlier.[7]

The essential procedure in the VSDS technique is the measurement of the intensity ratio of fluorescence from the satellite line to that of the parent as a function of detuning of the laser from line center. This ratio is proportional to the thermally averaged rate constant in the single collision regime, and the detuning controls the velocity component of the excited molecules along the laser beam, hence determining the average relative velocity of the collision partners.

We begin to take data by tuning our dye laser to excite a chosen particular initial rovibronic level,[7] and setting the monochromator and tower to observe decay fluorescence from the satellite and parent lines, respectively. We then simultaneously measure the satellite and parent line intensities (and thus the intensity ratio) as a function of laser detuning for typically 200 equally spaced intervals spanning a 7 GHz frequency range, centered on the resonance frequency.

The frequency sweeping of the 599 dye laser is controlled by our PDP-11/20 computer using a 12 bit CAMAC output register and a digital-to-analog converter, which outputs to the 599 frequency controller. The counting time at each frequency (typically 1 sec), number of points to be taken, frequency step size, and laser settling time between successive data points are input to the data-taking program. The satellite and parent line intensities, in counts per second, as well as the intensity ratio, are stored on computer disk files at each frequency point. This procedure is repeated 3–4 times at a fixed Xe pressure, for at least two Xe pressures. The repetitions allow us to average results and improve the statistical quality of our data; the results for two different Xe pressures are later subtracted to remove contributions from Na_2–Na collisions (the temperature and thus the Na density being fixed).

Before proceeding with the procedure described above, we have found it useful to check for foreign lines appearing in our parent and satellite profiles at large laser detuning. This is done by scanning our monochromator at fixed laser frequency, and using PMT3 to measure fluorescence intensity vs frequency. These fluorescence scans were taken at three laser frequencies: line center, 2 GHz red, and 2 GHz blue. Comparison of the red and blue wing scans to that at line center will determine if other weak parent–satellite progressions are excited off line center, overlapping with a given satellite of interest, and rendering it useless for VSDS analysis. If this is the case, we then look at other v'' progressions to try to find one where this problem occurs for at most only one side of line center. In any event, as a further check we record a longer 10 GHz width laser scan for each satellite observed to see if any foreign lines are present in the far wings of the scan.

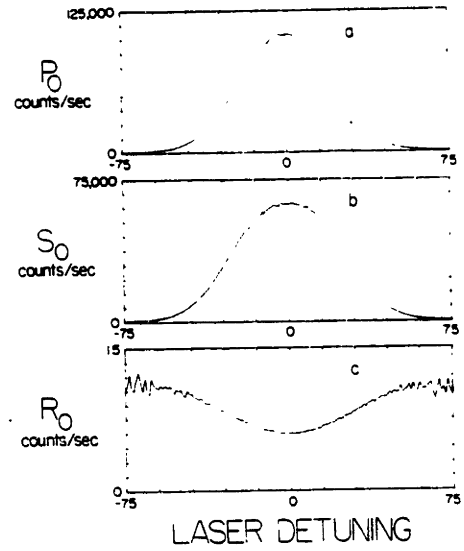

FIG. 2. (a), (b), and (c) are raw parent P_0, satellite S_0, and ratio $R_0 (\approx S_0/P_0)$ line shapes, respectively. The horizontal axis measures frequency detuning in experimental units (1 exp. unit ≈30 MHz) from line center (resonance). The scaling of the vertical axes was done for convenience in data storage.

Typical operating conditions for the experiment are an oven temperature of 350 °C, incident laser power of 20 mW, and Xe pressure of both 0.2 and 1.2 Torr. As shown in Fig. 1, we have used mirrors located outside the end of our oven to provide four to five passes of the laser beam through the oven, increasing the optical depth of the interaction region as viewed from the monochromator. These passes are mostly nonoverlapping and can provide a factor of more than 3 increase in signal. Because the average relative velocity depends on the magnitude of the selected velocity and not its direction, using laser beams traveling at 180° with respect to one another does not affect the validity of the VSDS technique. The slight overlap of the counterpropagating beams sometimes produces a small Lamb dip at the line center, but has not been observed to affect the fluorescence ratio.

In Fig. 2 are samples of raw parent and satellite lines, as well as their intensity ratio, as a function of

laser detuning, or selected speed along the laser beam axis, for the $\Delta J = +2$ satellite of a $J_i = 38$ parent with $v'' = 10$.

III. DATA ANALYSIS AND CORRECTION

In an ideal VSDS experiment to study the process

$$Na_2^*(v_i, J_i) + Xe \rightarrow Na_2^*(v_f, J_f) + Xe, \tag{1}$$

one measures the ratio of the population N_f in level J_f to population N_i in J_i as a function of v_r, the selected component of velocity of Na_2^* along the laser beam (z axis):

$$\frac{N_f(v_r)}{N_i(v_r)} = n_{Xe}\tau \bar{k}_{i\to f}(v_r) \,. \tag{2a}$$

with

$$\bar{k}_{i\to f}(v_r) = n_{Xe}\tau \int dv_r F(v_r; v_r) k_{i\to f}(v_r) \,. \tag{2b}$$

where τ is the radiative lifetime (assumed to be the same for level J_i and level J_f), $k_{i\to f}(v_r) = v_r \sigma_{i\to f}(v_r)$, and $\sigma_{i\to f}(v_r)$ is the cross section for process (1) at relative velocity v_r. $F(v_r; v_r)$, the distribution of relative velocities for fixed laser selected velocity $v_r = v_r$ yields unity when integrated over v_r [see Eq. (15)]. Once we obtain $\bar{k}_{i\to f}(v_r)$, the deconvolution procedures in Sec. IV allow us to find $k_{i\to f}(v_r)$.

Our real experiment differs from the ideal in several ways:

(1) $Na_2^* + Na$ collisions contribute to the J_f population.

(2) The experiment is done at finite Xe pressure so that more than one collision is possible (though not probable).

(3) Because of the finite homogeneous width of the radiative excitation process, the velocity distribution of excited molecules is not a delta function in v_z [i.e., $\delta(v_z - v_r)$].

In this section we describe how our raw experimental population ratios are analyzed and corrected to obtain a ratio that approximates the ideal one. The data are stored in disk files and a computer program performs these corrections.

The raw data consist of the number of photomultiplier counts per second in the parent channel and satellite channel as a function of laser frequency. The dark counts (typically $\simeq 20$ counts per sec) are first subtracted from each channel. Next, a dead time correction which accounts for pulse overlap in the photon counting electronics[7] is applied. Sweeps taken under the same conditions are then averaged together. Each sweep is centered by calculating the centroid of the parent profile to eliminate any problems due to laser mode jumps or frequency drift between sweeps. The centered sweeps are displayed on a storage scope one on top of another, so that bad sweeps (roughly 10% of all sweeps) are easily seen and thrown out.

The averaged parent profile as a function of laser frequency ν_l is then fit to determine the Gaussian width $\Gamma_G = (1/2\sqrt{2\ln 2})$ FWHM, and Lorentzian width $\Gamma_L = \frac{1}{2}$ FWHM of the convolution. Using

$$V = V(\nu_l, \Gamma_G; \Gamma) = \frac{\Gamma}{\pi}\int_{-\infty}^{\infty} d\nu' \exp(\nu'^2/2\Gamma_G^2)[(\nu_l - \nu')^2 + \Gamma_L^2 - \Gamma^2]^{-1} \tag{3}$$

as the Voigt profile function, we fit the parent line shape with the function $hVe^{-a\nu}$, where h is an amplitude, a is an absorption parameter, $\Gamma = \Gamma_L, \Gamma_G$, and h, a, Γ_G, and Γ are free parameters. We use a 0.1% accurate approximation to the Voigt profile for $\Gamma \ll 1$ (see the Appendix). Our simple exponential absorption factor is reasonable because we are looking at fluorescence from a relative short length of the Na_2 vapor and because the absorption is small, at most 20% on line center. Each data point in the fit is given an error of $\sqrt{\text{counts}}$ because we have found that Poisson noise dominates. The resulting reduced chi-squared[8] range from 0.7 to 2, indicating that the fit is within our assumed error. Over the experimental range of interest the fit can barely be distinguished from the data.

The frequency offset and laser selected velocity are linearly related by the first order Doppler shift formula $v_l/c = (\nu_l - \nu_0)/\nu_0$. We routinely measure the frequency offset $\nu_l - \nu_0$ in arbitrary experimental units and use Γ_G (determined in these same units) to define a velocity scale. If we call the unit of this velocity scale s_p, then s_p is empirically defined by the relation

$$v_l/s_p = \frac{\nu_l - \nu_0}{\Gamma_G} \,. \tag{4}$$

From the Maxwell–Boltzmann velocity distribution, we know in principle $s_p = \sqrt{RT/m}$, where R is the gas constant, T the temperature, and m is the mass of Na_2 in amu. We have confirmed this experimentally by using a calibrated spectrum analyzer to measure the absolute frequency offset $\nu_l - \nu_0$, and thus Γ_G in absolute units. Using $s_p = c\Gamma_G/\nu_0$, we calculated the temperature; it was found to agree to within 2% with the measured cell temperature. (The agreement between our several thermocouples was also about 2%.) *In all subsequent expressions and formulas all velocities (e.g., v_l) are dimensionless and expressed in units of s_p.*

Next we correct for the effects of finite Xe pressure by using a slight generalization of the matrix approach used in our previous study[7] to solve the steady state rate equations exactly. At each ν_l the rate constant $k_{i\to f}$ is related to the population ratio by

$$n_{Xe}\tau k_{i\to f} = \frac{n_f}{n_i}\left[1 + n_{Xe}\tau\left(\sum_{g\neq f} k_{f\to g} - \sum_{g\neq f}\frac{n_g}{n_f}k_{g\to f}\right)\right] \,. \tag{5}$$

an expression which follows from the steady state rate equations. We assume that the rate constants appearing in the two summations are proportional to the average relative velocity, an assumption supported by our final results, which show a linearly rising rate constant for the $\Delta = 2$ and 4 collisions which dominate the multiple collision correction sums. We rewrite Eq. (5) in the form

$$R_2(v_l) = R_1(v_l)[1 + \epsilon n_{Xe}\bar{v}_r(v_l)/\bar{v}_r(0)] \,, \tag{6}$$

where R_1 is the averaged raw ratio, R_2 is the multiple collision corrected ratio, ϵ is determined from our matrix solution at $v_l = 0$,[7] and $\bar{v}_r(v_l)$ is the average relative

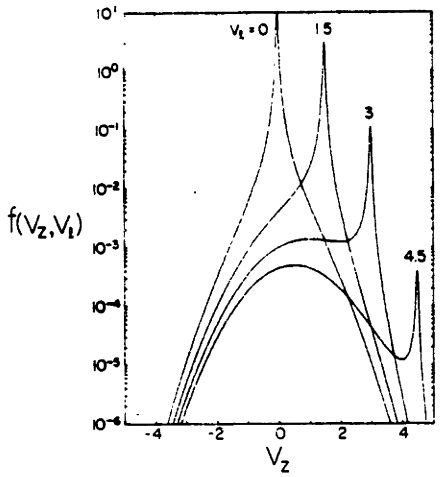

FIG. 3. Semilog plot of the excited state v_z velocity distribution $f(v_z; v_l)$ [Eq. (7) with $\Gamma = 0.03$] for several values of the laser selected velocity v_l, as a function of v_z.

velocity of Xe and Na_2 at v_l [see Eq. (2b)]. At the low pressures used in this experiment the correction is less than 15%.

Next a correction is applied which takes into account the finite homogeneous width of the distribution of v_z for a given v_l. If we assume that each excited molecule lives for the natural lifetime of 12 nsec[9] and that significant hole burning does not occur in the ground state velocity distribution, then

$$f(v_z; v_l) = \frac{\Gamma}{\pi} \exp(-v_z^2/2)[(v_l - v_z)^2 + \Gamma^2]^{-1} , \qquad (7)$$

where v_z is the velocity of the unexcited molecule. At first glance this correction would seem to be small since the homogeneous width is typically less than 4% of the Doppler width (i.e., $\Gamma \leq 0.04$) and this is the case for small v_l. However, at large v_l the excited state distribution of v_z, i.e., $f(v_z; v_l)$, shows that very few of the excited molecules have a z velocity v_z near v_l. Figure 3 shows a semilog plot of $f(v_z; v_l)$ at four different laser detunings with $\Gamma = 0.03$. For low v_l (0 and 1.5) the function is quite sharply peaked with almost all of the excited molecules near $v_z = v_l$. However, as v_l increases (i.e., detuning from line center increases) the population from molecules at low v_z rapidly becomes more important, an effect due to the tail of the Lorentzian overwhelming the tail of the Gaussian. These observations show that the correction in the ratio due to contributions from molecules with v_z not close to v_l will be appreciable only for $v_l \geq 3$.

The ratio of satellite to parent intensity for fixed laser velocity v_l (in the single collision limit) may be expressed in terms of the rate constant:

$$R_2(v_l) = \frac{\int_{-\infty}^{\infty} dv_z f(v_z; v) \bar{k}(v_r)}{\int_{-\infty}^{\infty} dv_z f(v_z; v_l)} \equiv \frac{S_2(v_l)}{P_2(v_l)} , \qquad (8)$$

where $S_2(v_l)$ and $P_2(v_l)$ are proportional to the satellite and parent intensities, and $\bar{k}(v_r)$ is the average rate constant with $v_r = v_z$ for the ideal VSDS experiment with $f(v_z; v_l) = \delta(v_z - v_l)\exp(-v_l^2/2)$. Figure 4 shows $R_2(v_l)$ calculated numerically assuming $k(v_r) = v_r$ (i.e., cross section independent of velocity) and $\Gamma = 0.03$. The dotted curve in the same figure is $\bar{k}(v_l)$ and agrees quite closely with $R_2(v_l)$ for $v_l < 2$. As we suggested from examination of $f(v_z; v_l)$, the curves differ more and more for larger v_l. As v_l increases, $\bar{k}(v_l)$ goes up linearly while $R_2(v_l)$ will level off and approach $\bar{k}_{\text{thermal}}$ since as $v_l \to \infty$, $f(v_z; v_l)$ becomes $\exp(-v_z^2/2)$ (i.e., thermal distribution).

Our correction procedure is equivalent to subtracting, from both the parent and satellite, contributions due to molecules with $|v_z - v_l| > \Delta$, where Δ represents a small velocity "window" about $v_z = v_l$. We define the corrected ratio R_3 to be

$$R_3(v_l) \equiv \frac{\int_1 f(v_z; v_l)\bar{k}(v_r)dv_z}{\int_1 f(v_z; v_l)dv_z} = \frac{S_2(v_l) - \int_2 f(v_z; v_l)\bar{k}(v_r)dv_z}{P_2(v_l) - \int_2 f(v_z; v_l)dv_z} \equiv \frac{S_3(v_l)}{P_3(v_l)} , \qquad (9)$$

where $\int_1$ denotes integration over v_z such that $|v_z - v_l| < \Delta$ and $\int_2$ denotes integration over $|v_z - v_l| > \Delta$. Since we know Γ from fitting the average parent profile, we know $f(v_z; v_l)$ and can therefore calculate the corrected parent. The integral P_3 can be approximated to within 0.5% by expanding the exponential factor in a power series of $(v_l - v_z)$ and keeping all terms to third order. The result is

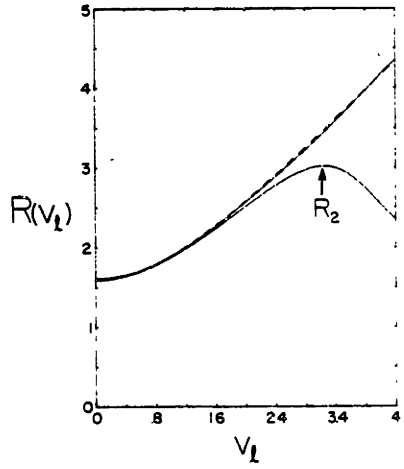

FIG. 4. The effect of the non-resonantly excited molecules is to produce the measured ratio $R_2(v_l)$ [Eq. (8), solid line] from the rate constant $\bar{k}(v_l)$ [Eq. (15), dashed line]. The correction procedure regains $R_3(v_l)$ [Eq. (9), solid line]. All curves were numerically generated assuming $k(v_r) = v_r$, with $r = 0.3502$ and $\Gamma = 0.03$.

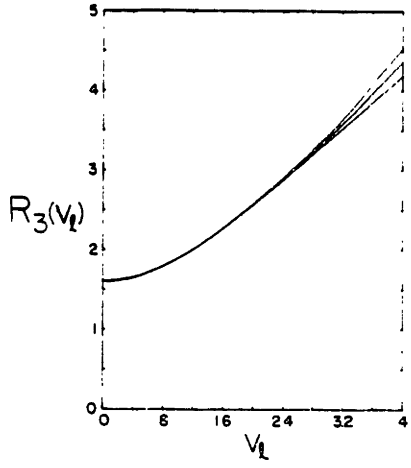

FIG. 5. Effect of a 10% error in the Lorentz width Γ on the recovered ratio: $R_3(v_t)$ as a function of v_t using $\Gamma = 0.03$ (middle), $\Gamma = 0.027$ (lower), and $\Gamma = 0.033$ (upper). All curves result from corrections applied to $R_2(v_t)$ (see Fig. 4), which was generated with $\Gamma = 0.03$.

$$P_3(v_t) = \int_1 f(v_s; v_t)\,dv_s$$
$$= 2\Gamma \exp(-v_t^2/2)\left\{\tan^{-1}(\Delta\Gamma)\left[1 - \left(\frac{v_t^2-1}{2}\right)\Gamma^2\right] + \Gamma\Delta(v_t^2-1)\right\}. \quad (10)$$

The corrected satellite is calculated by a fast converging interative technique in which we first approximate $\bar{k}(v_s)$ by $R_2(v_s)$. The iteration procedure is given by

$$S_3^{i+1}(v_t) = S_2(v_t) - \int_2 dv_s f(v_s; v_t) S_3^i(v_s)/P_3(v_s)\,, \quad (11)$$

with

$$S_3^{i=0}(v_t) = S_2(v_t) - \int_2 dv_s f(v_s; v_t) R_2(v_s) \quad (12)$$

and converges to within 0.1% after the first two iterations.

In practice, we make the approximation (i.e., for $v_t \geq 0$)

$$\int_2 dv_s \cong \int_{-\infty}^{v_t-\Delta} dv_s + \int_{v_t+\Delta}^{\infty} dv_s \simeq \int_{-v_{max}}^{v_t-0.5} dv_s\,, \quad (13)$$

where v_{max} is the largest laser velocity where $R_2(v_t)$ is measured, and the value $\Delta = 0.5$ is used. Replacing $-\infty$ by $-v_{max}$ is generally an excellent approximation, and with $\Delta = 0.5$, neglecting the second integral above induces an error of less than 1% in the final result for any v_t. Further, the choice of 0.5 for the value of Δ allows sufficient smoothing to avoid introducing undesirable noise into $R_3(v_t)$, yet is sufficiently small to eliminate contributions from slow molecules when these are nonnegligible (see Fig. 3). In Fig. 4 we have applied this correction procedure using two iterations to a numerically simulated "measured" ratio R_2. The resulting corrected ratio $R_3(v_t) = S_3^{i=2}(v_t)/P_3(v_t)$ is plotted as a solid line and coincides with $\bar{k}(v_t)$ to better than 0.3%.

Since the values for Γ and Γ_G (or s_p) result from fits to the parent line, they are subject to experimental error. Therefore, we have applied the correction procedure with Γ higher or lower than that used to calculate R_3. Figure 5 shows how the corrected ratio changes when Γ changes by ±10%. Similarly, we have approximately simulated a ±2% error in Γ_G (or S_p) by replacing v_t with $v_{t'}/(1 \pm 0.02)$ in $f(v_s; v_t)$ of the rhs of Eq. (9) *only* [not in Eq. (8)]. The resulting variation in the corrected ratio $R_3(v_t)$ is shown in Fig. 6. (Measurements of Γ_G varied less than 2% at fixed temperature.) In the data presented in this paper, the Lorentz correction is always less than 15% and the estimated errors in R_3 generated by uncertainties in the correction are less than 10% of that.

Finally, we eliminate the effects of Na_2^*-Na collisions by subtracting the corrected ratio at two different Xe pressures p_1 and p_2:

$$R_{final}(v_t) = \frac{R_3(v_t; p_2) - R_3(v_t; p_1)}{p_2 - p_1} \quad (14)$$

and from this point on take $\bar{k}(v_t) \simeq R_{final}(v_t)$.

IV. DECONVOLUTION

A. Mathematical procedure

In this section we discuss the deconvolution procedures which we use to obtain an approximation to the unaveraged rate constant $k(v_r)$ from the measured rate constant

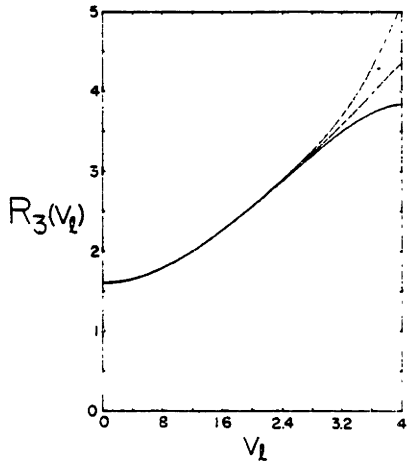

FIG. 6. Effect of errors in the Gaussian (Doppler) width parameter on recovered ratio: $R_3(v_t)$ as a function of v_t, when replacing v_t with $v_t/1.02$ (lower curve) and v_t 0 98 (upper curve) in the integral correction term to $R_2(v_t)$ [see Eq. (9)]. The third (middle) curve is corrected properly.

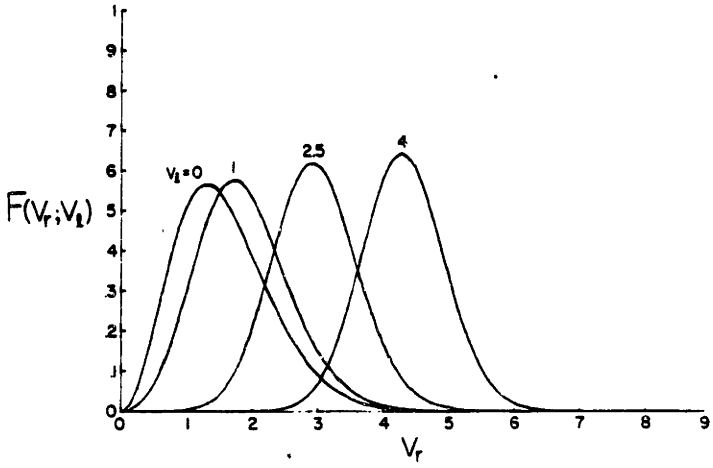

FIG. 7. The VSDS relative velocity distribution function $F(v_r; v_l)$ [Eq. (15) with $\gamma = 0.3502$] as a function of v_r, for several values of v_l indicated. Here, v_l is the magnitude of the laser selected velocity along the z (laser) axis of the laser excited collision partner (Na_2^*).

$\bar{k}(v_l)$. In order to give the reader a feel for the power and limitations of these procedures, we apply them first to numerically generated simulations of data, thus permitting comparison of the deconvoluted $k(v_r)$ to the true $k(v_r)$ from which the simulated data were generated.

The mathematical relationship between the two quantities $\bar{k}(v_l)$ and $k(v_r)$, under ideal VSDS conditions, is given by[4]

$$\bar{k}(v_l) = \int_0^\infty k(v_r) F(v_r; v_l) dv_r \,, \tag{15}$$

with

$$F(v_r; v_l) = v_r/2(\gamma+1)^{1/2} \exp\{-[v_r^2 - (\gamma+1)v_l^2]/2(\gamma+1)\} \times \left(\operatorname{erf}\left\{\frac{v_r + (\gamma+1)v_l}{[2\gamma(\gamma+1)]^{1/2}}\right\} + \operatorname{erf}\left\{\frac{v_r - (\gamma+1)v_l}{[2\gamma(\gamma+1)]^{1/2}}\right\}\right)$$

and γ = mass of Na_2^* + mass of xenon = 0.3502. Examples of $F(v_r; v_l)$ as a function of v_r for several fixed values of v_l are shown in Fig. 7.

In this work, the deconvolution of $\bar{k}(v_l)$ is carried out using a procedure similar to that described in Appendix B of Ref. 4. The data $\bar{k}(v_l)$ are first least squares fit by computer to an even polynomial function

$$\bar{k}(v_l) = \sum_{n=0}^{N} b_n P_n(v_l) \,, \tag{16}$$

where $P_n(v_l)$ is an even polynomial in v_l of order 2^n. The set of polynomials P_n are not standard polynomial functions, but a set of mutually orthogonal polynomials[10,11] defined so that the weighted sum $\sum_i \sigma_i^{-2} P_m(v_l) P_n(v_l) = 0$ $(m \neq n)$, where $\sum_i$ is a sum over all data points and σ_i is the error assigned to the ith data point. The orthogonal polynomials can be written

$$P_n(v_l) = \sum_{m=0}^{n} c_{nm} v_l^{2m} \,, \tag{17}$$

where the coefficients c_{nm} are generated using recursion relations described in Refs. 10 and 11. Using Eqs. (16) and (17), the fit to $\bar{k}(v_l)$ may be written

$$\bar{k}(v_l) = \sum_{m=0}^{N} \left(\sum_{n=m}^{N} c_{nm} b_n \right) v_l^{2m} \,, \tag{18}$$

i.e., as an even power series in v_l. We have previously shown that $\bar{k}(v_l)$ expressed in such a power series can be deconvoluted to give $k(v_r)$. This is done in practice using Eq. (B8) of Ref. 4 with $c_q = 0$ and $A_m = \sum_{n=m}^{N} c_{nm} b_n$.

Because the deconvolution in general involves a sum of relatively large terms, often alternating in sign, we found it advisable to do all calculations in double precision, especially for $N \gtrsim 10$.

In principle, the quantities A_m could be computed directly by least squares fitting $\bar{k}(v_l)$ to the form $\sum_{m=0}^{N} A_m v_l^{2m}$, but evaluation of the A_m's require the inversion of the $(N+1)\times(N+1)$ matrix which becomes highly ill conditioned as N increases.[10] However, due to the orthogonality properties of the P_n's the corresponding matrix in this case is diagonal; thus, the b_n's can be solved for immediately. Further, the b_n's are independent of each other, making statistical and error analysis considerably simpler.

In our procedure, as in any other deconvolution technique, a fundamental limitation is lack of information. In our experiment, the lack of information is due to the finite range of v_l over which $\bar{k}(v_l)$ is measured, as well as to noise and other errors that might be present. In principle, a deconvolution of $\bar{k}(v_l)$ to get $k(v_r)$ requires exact knowledge of $\bar{k}(v_l)$ for $0 \leq v_l \leq \infty$. In practice, though, the finite range problem need not be a severe limitation to obtaining $k(v_r)$ over a correspondingly limited range of v_r. This can be seen qualitatively from the relative velocity distribution plots of $F(v_r; v_l)$ in Fig. 7. Roughly speaking, all distributions shown for various v_l have a FWHM of about 1–1.5 about their peak, outside of which these distributions go to zero rapidly. Thus, if $\bar{k}(v_l)$ could be determined exactly for $v_l \leq (v_l)_{max}$ (typically 3.5), then one should be able to make an accurate determination of $k(v_r)$ for at worst $v_r \leq (v_l)_{max} - 1$.

This should be true because $\bar{k}(v_t)$ for $v_t \geq (v_t)_{max}$ contains very little "information" about $k(v_r)$ for $v_r \leq [(v_t)_{max} - 1]$. However, $\bar{k}(v_t)$ for $[(v_t)_{max} - 1] \leq v_t \leq (v_t)_{max}$ is strongly dependent on $k(v_r)$ for $v_r \sim (v_t)_{max}$ and so it is not unrealistic to expect to recover $k(v_r)$ for $v_r \leq (v_t)_{max}$ with reasonable accuracy. This has been empirically verified using a variety of computer simulated data, some examples of which will be discussed later.

The most serious practical difficulty to overcome is noise and/or uncertainty in the measurement of $\bar{k}(v_t)$. Structure such as narrow peaks or rapid oscillations in $k(v_r)$ will appear in $\bar{k}(v_t)$ with greatly reduced magnitude due to the convolution with $F(v_r, v_t)$, and this structure may be partially or completely obscured by noise. Ideally, one wishes the deconvolution procedure to recover the structure of $k(v_r)$ using $\bar{k}(v_t)$, without generating erroneous structure from the noise. In our method, this dilemma is manifest in the selection of the number of polynomials used to fit the measured $\bar{k}(v_t)$. If too many polynomials are used, the fit will tend to follow the noise structure in $\bar{k}(v_t)$ resulting in artificial structure in the deconvolution. Using too few polynomials will result in a loss of resolution and accuracy in both fit and deconvolution.

We employ a statistical test[11] to determine the "optimum" number of terms in the polynomial fit to $\bar{k}(v_t)$; basically, it tests the hypothesis that the fit coefficient b_n is truly zero, i.e., that the finite value obtained is due solely to noise. Our test is based on the assumptions of normal error analysis, for which $t_n = b_n\sqrt{[\#-(n+1)]\sum_t (1/\sigma_t^2)P_n^2(v_t)/\chi_n^2}$ (with $\# =$ number of data points, and $\chi_n^2 =$ sum of the squares of deviations from fit to data, for $n+1$ term fit) will be distributed according to Student's "t" distribution, with $\# - (n+1)$ degrees of freedom, if the hypothesis that b_n is in reality zero is true. A significance level of 0.01 is employed, so that if $|t_n|$ is large enough so that the probability that b_n is zero is less than 1%, the hypothesis is assumed false, P_n is kept in the fit, b_{n+1} is calculated, and the "t" test is then applied to b_{n+1}. We have found in almost all cases that there exists a number N such that b_n is statistically significant at the 99% confidence level for all $n \leq N$, and for no $n > N$. In such cases, we feel that the fit $\sum_{n=0}^{N} b_n P_n(v_t)$ represents in a practical sense all the information obtainable from the given set of data. Our somewhat conservative choice of a 0.01 significance level reflects our desire to avoid "recovering" unreal structure in the deconvolution and the above truncation procedure has mostly eliminated this problem for both real and computer simulated data, even when such simulated $\bar{k}(v_t)$ could not be exactly expressed by a finite polynomial.

Having discussed our deconvolution method, we now discuss our procedure for assigning errors to our results. Substituting $A_m = \sum_{n=m}^{N} c_{nm} b_n$ and putting $c_d = 0$ in Eq. (B8) of Ref. 4, it follows that the deconvolution result $k(v_r)$ can be expressed as

$$k(v_r) = \sum_{n=0}^{N} b_n G_n(v_r) , \tag{19}$$

where $G_n(v_r)$ is a triple sum expression obtained by interchanging the order of the summations in the resulting equation. It can be shown[11] that $\delta_n^2 = [\sum_t (1/\sigma_t) P_n^2(v_t)]^{-1}$ is the variance of b_n, if $\sigma_t =$ error in tth data point. From the statistical independence of the b_n's it follows that

$$\delta_k^2(v_r) = \sum_{n=0}^{N} \delta_n^2 G_n(v_r) \tag{20}$$

is the variance in the deconvolution result $k(v_r)$.

This result includes only errors due to statistical uncertainty in the b_n's kept in the fit, and does not include errors incurred due to truncating our fitting function to a finite polynomial, or error from the fact that the fitting function is unrealistic outside the available range of data. There is no reason to expect that these errors have the same v_r dependence as $\delta_k(v_r)$, but due to a lack of further information, we make this assumption and take $\sqrt{2\delta_k(v_r)}$ to calculate error bars for our deconvolution results. A justification for this is that we have found in the many computer simulated examples studied that these error bars fairly accurately measure the magnitude in the error between actual and deconvoluted $k(v_r)$, and that such error falls within the error bars roughly $\frac{2}{3}$ the time, as would statistically be expected (see Figs. 8–10).

B. Numerical examples

We shall now present some numerical examples to illustrate the above discussion. The procedure consists of choosing a trial $k(v_r)$ and numerically calculating the integral in Eq. (1) to obtain $\bar{k}(v_t)$ for typically 100 equally spaced values of v_t, up to some $(v_t)_{max}$. The mass ratio parameter used was $r = 0.3502$. The deconvolution procedure is then applied to $\bar{k}(v_t)$; the results will be referred to as $k^{N+1}(v_r)$, where $N+1$ is the number of terms in the fit to $\bar{k}(v_t)$ [see Eq. (2)]. In addition, we create a noisy analog of $\bar{k}(v_t)$, referred to as $\bar{k}'(v_t)$, with $\bar{k}'(v_t) = \bar{k}(v_t) + n(v_t)$ and $n(v_t)$ is a "noise function" consisting of computer generated numbers following a Gaussian distribution with zero mean and standard deviation $\sigma(v_t) = (0.0075v_t^2 + 0.01)k(v_t)$, chosen to roughly simulate the pattern of uncertainty in our actual VSDS data. The result of the deconvolution procedure applied to $\bar{k}'(v_t)$ will be referred to as $k'^{N+1}(v_r)$. The values of N used in all cases were those determined by the t test described earlier. For the case of the $\bar{k}(v_t)$ without noise, each point was assigned an error $\sigma = 1$; this magnitude however has no bearing on the results of the t test.

The computer integrations to get $\bar{k}(v_t)$ were done using Simpson's rule with a step size of 0.04 in v_r, and an upper limit of integration chosen so that $F(v_r, v_t)$ at that point has value $\sim 10^{-20}$. Using this method the normalization integral of $F(v_r, v_t)$ was found to be unity within 0.1%.

The first example considered was that of a linear rate constant with a finite threshold at $v_r = 0.75$, and $(v_t)_{max} = 3.5$:

$$k(v_r) = \begin{cases} 0 , & v_r < 0.75 , \\ 0.35v_r - 0.2625 , & v_r \geq 0.75 . \end{cases} \tag{21}$$

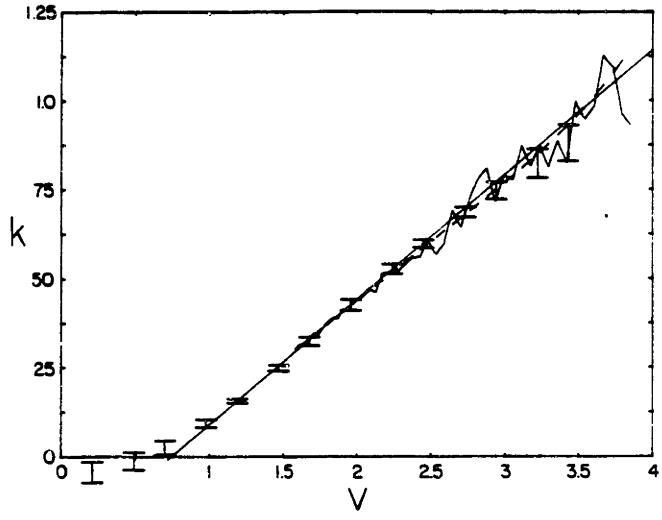

FIG. 8. Deconvolution of a linear rate constant with threshold at $v_r = 0.75$. The true rate constant $k(v_r)$ (solid line) and the deconvolution result $k'^4(v_r)$ (error bars) are shown plotted against relative velocity v_r. Also shown are the simulated data $\bar{k}'(v_l)$ (solid line) and the four term polynomial fit to it (dashed line), with the horizontal axis now measuring $\bar{v}_r(v_l)$, the average relative velocity for selected laser velocity v_l. Note that $\bar{v}_r(v_l = 0) \simeq 1.0$, thus setting a lower bound on the relative velocity accessible without deconvolution.

A plot of $k(v_r)$ as well as the result $k'^4(v_r)$ is shown in Fig. 8. The fit to $\bar{k}'(v_r)$ was limited to four terms by the t test, but it is seen that $k'^4(v_r)$ agrees with $k(v_r)$ within error bars for all $v_r \geq 0.5$. For no noise, $k^9(v_r)$ (not shown) was determined "best" by the t test, and was very similar to $k^4(v_r)$ for $v_r \leq 1$, but was considerably more accurate for larger v_r.

This, and other, examples show that with or without noise the deconvolution results for $v_r \leq 0.5$ were not highly accurate, probably for two basic reasons. Firstly, one could not expect a finite polynomial to converge accurately to the threshold behavior and discontinuity for $v_r \leq 0.75$. Secondly, and more generally, $\bar{k}(v_l)$ will usually not be highly dependent on or sensitive to $k(v_r)$ for low v_r since $F(v_r; v_l) \to 0$ as $v_r \to 0$ for all v_l. Even for $v_l = 0$, $F(v_r; v_l) \propto v_r^2$ for small v_r, and as can be seen from Fig. 7, $F(v_r; v_l = 0)$ is rapidly vanishing for $v_r \leq 0.5$; it is therefore unlikely that the VSDS method will ever accurately recover $k(v_r)$ for $0 \leq v_r \leq 0.5$, with $r \geq 0.35$.

For an interesting comparison, we have also shown in Fig. 8 a plot of $\bar{k}'(v_l)$ vs $\bar{v}_r(v_l)$, i.e., the horizontal axis

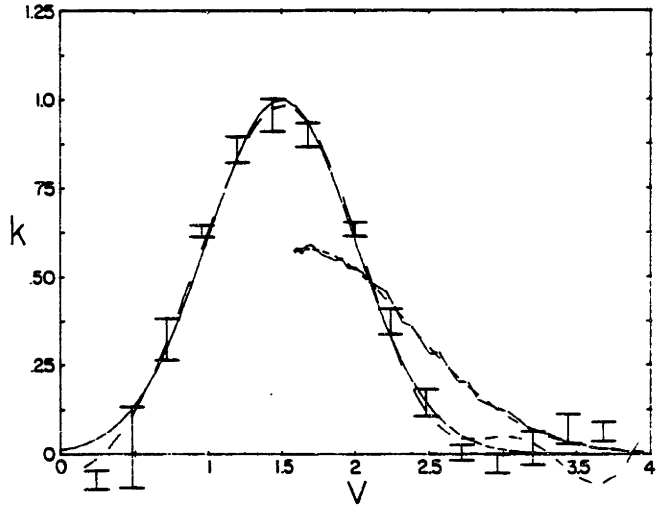

FIG. 9. The true rate constant $k(v_r) = \exp[-(v_r - 1.5)^2/0.5]$ (solid line) and the deconvolution results $k'^{12}(v_r)$ (dashed line) and $k'^8(v_r)$ (error bars) are shown plotted as a function of v_r. Also shown are the simulated data $\bar{k}'(v_l)$ (solid line) and its eight-term polynomial fit (dashed line) plotted as a function of $\bar{v}_r(v_l)$.

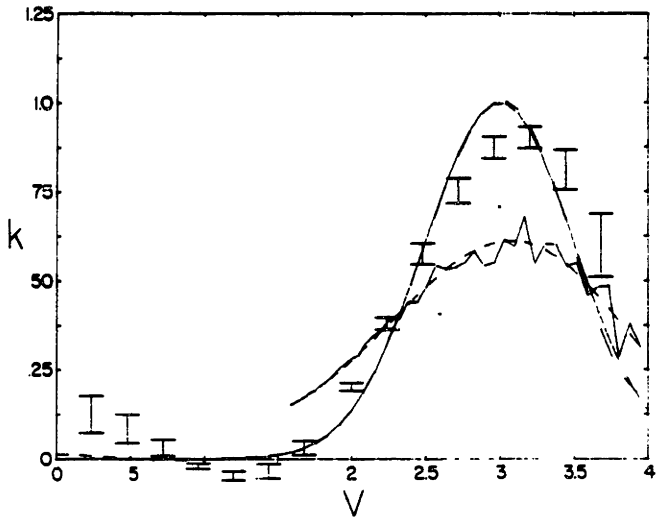

FIG. 10. The true rate constant $k(v_r) = \exp[-(v_r-3)/0.05]$ (solid line) and the deconvolution results $k^{12}(v_r)$ (dashed line) and $k'^6(v_r)$ (error bars) are shown plotted as a function of v_r. Also shown are the simulated data $\bar{k}'(v_t)$ (solid line) and its six-term polynomial fit (dashed line) plotted as a function of $\bar{v}_r(v_t)$.

now measures the average relative velocity $\bar{v}_r(v_t)$. $\bar{v}_r(v_t) = \int_0^\infty F(v_r; v_t)dv_r$ has been tabulated and stored by our computer. This is simply a plot of the average rate constant vs average relative velocity, and has been used as a sort of "first order" approximation to $k(v_r)$ in earlier VSDS work in our laboratory.[3] This quantity contains only experimental errors, not deconvolution errors, and thus may be more useful for comparison of a theoretical $k(v_r)$ (after being averaged) with our experimental results. However, as demonstrated in the upcoming examples, the resolution of this method is inferior to that of the deconvolution, and it cannot provide information for $v_r < \bar{v}_r(v_t=0)$. For the Na_2–Xe system this cutoff is at $v_r \simeq 1.6$ as opposed to $v_r \simeq 0.5$, the practical lower limit with the deconvolution method.

The next trial example we consider is of a substantially different nature than before:

$$k(v_r) = \exp[-(v_r-1.5)^2/2(0.5)^2]\,, \quad (v_t)_{\max} = 4\,, \qquad (22)$$

a Gaussian centered at $v_r = 1.5$ with a standard deviation of 0.5. Shown in Fig. 9 are $k(v_r)$, $k^{12}(v_r)$, $k'^6(v_r)$, as well as $\bar{k}'(v_t)$ (along with the 8 term fit to it) plotted vs $\bar{v}_r(v_t)$, the so called first order approximation. We point out that $\bar{k}'(v_t)$ was generated several times [$n(v_t)$ being random, it is never the same twice] and we consistently found that an eight term fit was appropriate using the t test criterion. Both $k^{12}(v_r)$ and $k'^6(v_r)$ are good approximations to $k(v_r)$ to $0.5 \leq v_r \leq 3$, confirming general statements made to this effect in the previous sections. For $3 \leq v_r \leq 4$ both results tend to oscillate about zero, a convergence problem not surprising and almost certainly due to the finite degree of the polynomials representing these functions. In any case both $k^{12}(v_r)$ and more significantly $k'^6(v_r)$ give very accurate information as to the location, height, and width of the Gaussian peak of $k(v_r)$, and the error bars on $k'^6(v_r)$ reasonably accurately reflect the true deviations for $v_r \geq 0.5$.

This case also serves as a dramatic example of the increase in accuracy and information gained when using the deconvolution technique over the simple first order approximation of plotting $\bar{k}'(v_t)$ vs $\bar{v}_r(v_t)$. From this approximation one cannot accurately determine the height or width of the Gaussian peak, and from observation of $\bar{k}'(v_t)$ vs $\bar{v}_r(v_t)$ alone, it is not even clear whether $k(v_r)$ has a peak, or roughly levels off to a constant value for $v_r \lesssim 1.5$. Lastly, we should point out that when experimenting with a similar Gaussian peak with mean $\leq v_r = 1$ (not shown), we found that the deconvolution procedure gave results which also tended to level off rather than display the peak, another manifestation of the problems at low v_r mentioned earlier.

The final example considered is again a Gaussian peak centered at $v_r = 3$:

$$k(v_r) = \exp[-(v_r-3)^2/2(0.5)^2]\,, \quad (v_t)_{\max} = 4\,. \qquad (23)$$

As before, $\bar{k}'(v_t)$ was generated several times, and each time it was found that six terms gave the best fit.

Shown in Fig. 10 are $k(v_r)k^{12}(v_r)$ and $k'^6(v_r)$ with error bars as well as $\bar{k}'(v_t)$ and its six term fit plotted vs $\bar{v}_r(v_t)$. It is seen that $k^{12}(v_r)$ (no noise) is noticeably more accurate than the corresponding case in the previous Gaussian example, and is a very good approximation to $k(v_r)$ for all v_r shown. This is probably due to the fact that the peak occurs at higher v_r [and thus v_t for $k(v_t)$] than in the last example, and thus where the averaged rate constant has more intrinsic resolution. The result $k'^6(v_r)$ for the noise case is somewhat less accurate than $k'^6(v_r)$ of the last example, a result probably due to the increased noise at higher v_t where the peak of $k'(v_t)$ is now located, causing a limit of six on the number of recoverable terms in the fit. In any event, the height, width, and location of the peak of $k(v_r)$ can probably be determined to within 10%–15% from $k'^6(v_r)$,

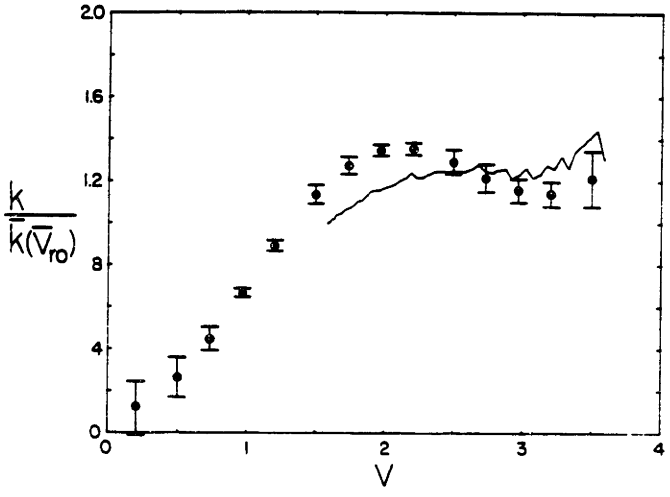

FIG. 11. Normalized rate constants $\bar{k}(\bar{v}_r)/\bar{k}(\bar{v}_{r0})$ (solid line) and $k(v_r)/\bar{k}(\bar{v}_{r0})$ (error bars associated with points) as functions of $\bar{v}_r(v_l)$ and v_r, respectively. In both cases, rates constants are for $j_l = 16$, $\Delta = +16$.

which is still a significant improvement over the first order approximation also shown. However, it seems that the error bars on $k'^6(v_r)$ are small, the cause of which is most likely an underestimation of the error incurred by those unknown terms not included in the fit.

We feel the above three examples demonstrate most of the relevant points made in the previous discussion section. The first example is similar in form to some of the rate constants we have seen experimentally, while the second and third examples help to demonstrate qualitatively the improvement in resolution afforded by the deconvolution method, and how this may vary with v_l. Further, for reasons of brevity and clarity of the figures we have not here shown comparisons of $k^4(v_r)$ with $k'^4(v_r)$, $k^8(v_r)$ with $k'^8(v_r)$, and $k^6(v_r)$ with $k'^6(v_r)$ for the three examples, respectively. However, for each of the above-mentioned pairs, the deviations between them were fairly minor, and considerably smaller than the corresponding error bars. From this, as well as other studies of trial examples not discussed here, we have concluded the following: The main effect of the type of noise considered here (and thus presumably for real VSDS experiments) on our deconvolution procedure is to limit the number of fitting terms that can be used to recover $k(v_r)$; noise does not significantly distort results obtained with those terms kept. In relation to this, we have observed for all real VSDS experiments we have done that the signal is greatest and thus the noise is relatively minimized at small v_l, where the intrinsic resolution of the experiment is worst (and *vice versa*). This fortuitous "balancing" of noise provides the most (least) accurate values of $k(v_l)$ where it is most (least) needed to help minimize inversion errors.

Lastly, we mention some other techniques tried to improve upon the procedures discussed above. We have tried to alter the behavior of the fitting function (in a region roughly 1 velocity unit long) for $v_l > (v_l)_{max}$, by artificially extending $k(v_l)$ in some plausible manner, to prevent the fit from assuming highly unrealistic and inaccurate behavior immediately outside of $v_l = (v_l)_{max}$. Using numerical examples, this was found to have only relatively minor effects on the deconvoluted result, and only for v_r near $(v_l)_{max}$. This method has proved useful when treating measured $k(v_l)$ which are adversely affected in the vicinity of $(v_l)_{max}$ by perturbing satellite lines.

We have also adapted our fitting program to perform least squares fits with the constraint that the deconvoluted rate constant vanish at $v_r = 0$ [a physical necessity since $\sigma(v_r = 0)$ is finite]. This constraint was used only on the $j_l = 68$ data, where applying the constraint made very little difference in the χ^2 (goodness) of the fit.

V. EXPERIMENTAL RESULTS

In this section we present and discuss our VSDS results for $Na_2^*(A\,^1\Sigma)$–Xe. In Fig. 11 we show both $k(v_r)/\bar{k}(\bar{v}_{r0})$ and $\bar{k}(\bar{v}_r)/\bar{k}(\bar{v}_{r0})$ (the so called first order deconvolution) for $j_l = 16$, $\Delta = 16$, where $\bar{v}_r = \bar{v}_r(v_l)$, $\bar{v}_{r0} = \bar{v}_r(v_l = 0)$, and $\bar{k}(v_{r0})$ is used as a convenient scaling factor (having been measured absolutely in Ref. 7).

We show the case $j_l = 16$, $\Delta = +16$ because of its interesting and unexpected velocity dependence (discussed qualitatively below); in addition, it serves as a good example for demonstrating the improved resolution, velocity range, and information gained by our deconvolution technique over the first order approximation also shown. The error bars on $\bar{k}(\bar{v}_r)$ (not shown) include estimated errors incurred from our data correction procedures discussed in Sec. III, as well as errors due to counting noise and experimental fluctuations, and their size is well described by the magnitude of the noise function of Sec. IV B. These errors in turn are used to generate error bars for $k(v_r)$ (shown) by the procedure described at the end of Sec. IV A. A similar plot for $j_l = 38$, $\Delta = +2$ can be found in Ref. 1.

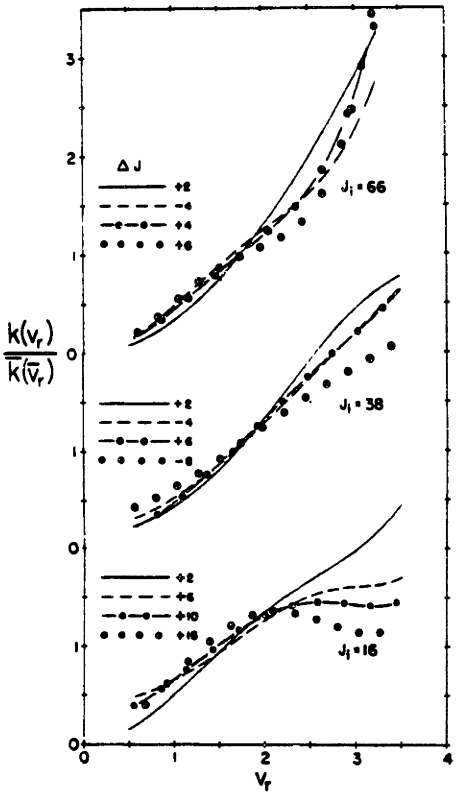

FIG. 12. Rate constants $k(v_r)/\bar{k}(\bar{v}_r)$ for $j_i = 16$, 38, and 66, for values of Δ indicated.

Figure 12 shows our complete set of deconvoluted results for $j_i = 16$, 38, and 66 for the various values of Δ shown. Error bars (not shown) are roughly as large as those of Fig. 11 for $j_i = 16$ and 38, and about 50% larger for $j_i = 66$. One can note some interesting systematic trends from these results. For $j_i = 16$, the rate constants systematically decrease with increasing v_r (at least for $2 \leq v_r \leq 3$), the amount of decrease increasing steadily with increasing $|\Delta|$. For $j_i = 38$, all rate constants are roughly linear over the velocity range shown, with the slope apparently decreasing slightly with increasing $|\Delta|$. Unlike the previous cases, rate constants for $j_i = 66$ appear to increase at a faster than linear rate with increasing v_r, but the size of error precludes observation of systematic trends as $|\Delta|$ varies.

VI. DISCUSSION

In this section we discuss our results from three perspectives. These data offer a chance to see if fitting laws for RET (expressions which fit many thermally averaged rate constants with a few parameters) can fit velocity selected RET rates (they do) and thus reveal the velocity dependence of the parameters. Secondly, the velocity dependence displays several qualitative features which beg qualitative, if speculative, explanations. Finally, this experiment offers an opportunity to assess the strengths and weaknesses of the VSDS technique.

A. Velocity dependence of the ECS–P fitting law

Recent work in our group has shown that the energy corrected sudden (ECS) scaling approximation,[5] coupled with the power law assumption $k_{l\to 0} = a[l(l+1)]^{-\gamma(4-16}$ for the basis rates $k_{l\to 0}$, can accurately represent all thermally averaged RET rate constants for Na_2^+ with a variety of targets. We call the coupling of these concepts the ECS–P fitting law.[16] The present VSDS data allow a test of the ECS scaling theory over a range of selected relative velocities in the same system. The first issue is whether this fitting law works at all selected velocities. We find the ECS–P law fits the data at all velocities within error; hence, the velocity dependence of the three parameters of this theory represents all the information in our data.

The ECS–P fitting law for RET data begins with the assumption (previously applied only to thermally averaged data) that the basis rate constants follow a power law

$$k_{l\to 0}(v_r) = a(v_r)[l(l+1)]^{-\gamma(v_r)} . \tag{24}$$

Rate constants for other values of angular momentum are obtained from the ECS scaling law[6]

$$k_{j_i\to j_f}(E_r + \epsilon_{j_>} - \epsilon_{j_i}) = [1 + (\epsilon_{j_>} - \epsilon_{j_i})/E_r]^{-1/2}(2j_f+1)\sum_l (2l+1) \times \begin{pmatrix} j_i & j_f & l \\ 0 & 0 & 0 \end{pmatrix}^2 |A_l^{j_>}|^2 k_{l\to 0}(E_r) . \tag{25}$$

In this expression, E_r = initial relative kinetic energy, ϵ_j = the energy of the jth rotational level, $j_>$ = the greater of j_i or j_f, and $k_{j_1\to j_2}(E)$ is the rate constant at relative energy E. The quantity $A_l^{j_>}$ is known as the "adiabaticity," or "adiabatic correction" factor, and is given by

$$A_l^j = \frac{6 + [(\epsilon_j - \epsilon_{j-2})(l_c/2v_r\hbar)]^2}{6 + [(\epsilon_j - \epsilon_{j-2})(l_c/2v_r\hbar)]^2} , \tag{26}$$

with v_r the initial relative velocity and l_c representing an "effective collisional length." The presence of the adiabaticity factor extends the range of validity of the well-known energy sudden[13,17] scaling approximation (which is regained in the limit $A_l^{j>} \to 1$) to cases where a sudden approximation cannot be justified because the molecule rotates appreciably during the collision. It reduces the magnitude of the predicted rate as the ratio of the duration of the collision to the rotational period increases.

To write the above ECS approximation in terms of our more usual velocity notation for VSDS,[4] we take $\epsilon_j = Bj(j+1)$ (B = rotational constant = 0.10 cm^{-1} for $A\,^1\Sigma$ Na_2, $v = 18$) and note that $E_r = \mu s_\theta^2 v_r^2/2 = kTv_r^2/2(1+\gamma)$. The result (applied to rate constants with the same kinetic energy above threshold) is

TABLE I. The χ^2/ν for the least squares fits of our data to ECS as a function of velocity.

v_r	χ^2/ν
0.75	0.47
1.1	0.37
1.5	0.61
1.9	1.4
2.25	2.7
2.6	1.2
3.0	1.5

$$k_{j_i\to j_f}(v_r') = \left(\frac{v_r'}{v_r}\right)(2j_f+1)\sum_l (2l+1) \times \begin{pmatrix} j_i & j_f & l \\ 0 & 0 & 0 \end{pmatrix}^2 |A_l^{j_f}|^2 k_{l,0}(v_r') , \quad (27)$$

with $v_r' = v_r\{1+(\alpha/v_r^2)[j_>(j_>+1) - j_i(j_i+1)]\}^{1/2}$, $\alpha = 2(1+\gamma)B/kT$ ($=6.27\times10^{-4}$ for the Na_2–Xe system at $T=620$ K). To fit our velocity-dependent rate constants we determine the three parameters a, γ, and l_c, the effective collision length appearing in $A_l^{j_f}$, using a nonlinear least square fitting to data at fixed total energy. For several distinct v_r (and thus E_r), we obtained values of $k_{j_i\to j_f}(v_r')$ from the data points of the deconvolution results stored in our computer (using linear interpolation when necessary with 64 data points in the range $0 \le v_r \le 3.5$). Using each j_i and Δ shown in Fig. 12 (a total of 13 data points) we fit the values obtained from the deconvolutions for $v_r = 0.75$, 1.1, 1.5, 1.9, 2.25, 2.6, and 3.0. The fitting routine used, as well as the method for assigning errors to the values obtained for the fitting parameters, is described in Ref. 8.

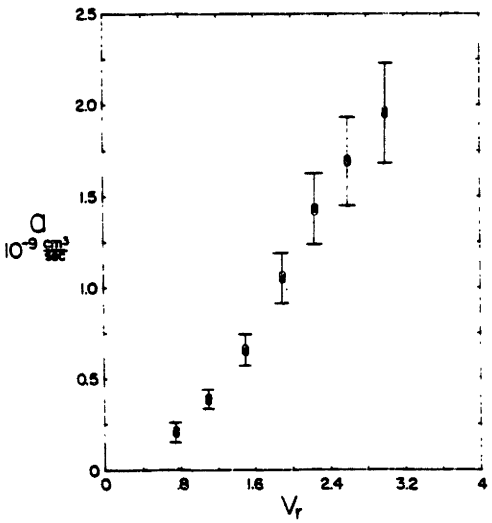

FIG. 13. Values for the parameter "a" (with error bars) as a function of v_r, obtained by least squares fitting with $k_{l\to0} = a[l(l+1)]^{-\gamma}$.

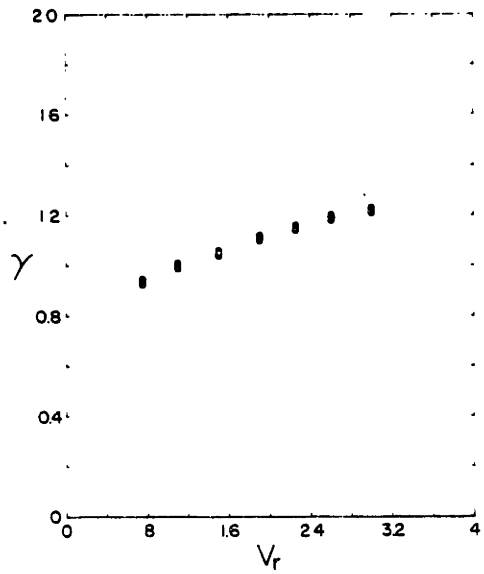

FIG. 14. Values for the parameter γ as a function of v_r, obtained by least squares fitting with $k_{l\to0} = a[l(l+1)]^{-\gamma}$. The size of the error bars is approximately the height of the points.

Table I gives a list of χ^2/ν[8,11] for the fits at each velocity; errors on the data points determined by the deconvolution procedure were augmented by a 5% error due to uncertainties in the line center rate constant used for normalization. We used 13 data points and a fitting function with three parameters, so the number of data points less free parameters is $\nu = 10$ and statistically one would expect $\chi^2/\nu = 1 \pm \sqrt{(2/\nu)} = 1 \pm 0.45$.[11] Thus, it seems clear that ECS with $k_{l\to0} = a(v_r)[l(l+1)]^{-\gamma(v_r)}$ does in fact fit our data quite well (the large χ^2/ν for $v_r = 2.25$ in puzzling, but perhaps is due to an underestimate by our deconvolution procedure for the error at this v_r) and is further evidence of the wide applicability of this approach. However, we point out that this does not substantiate the ECS approximation independent of an assumption for $k_l - 0$; in fact, two out of three of our fitting parameters, namely, a and γ, do not emerge from ECS, but rather the energy gap power law [Eq. (24)].

In Figs. 13–15 are plots of a, γ, and l_c vs v_r, the relative velocity. The parameter l_c is the only one pertaining to the ECS scaling law and will be discussed first. The dependence of l_c on v_r is rather surprising, and appears inconsistent with the simple physical picture of a collision length as put forward by DePristo *et al.*[8] From this picture, one would expect l_c to remain constant, or decrease slightly. For example, if one takes $t_c = l_c/v_r$ as a "collision time" and assumes the anisotropic part of the Na_2^*–Xe potential gives rise to a force

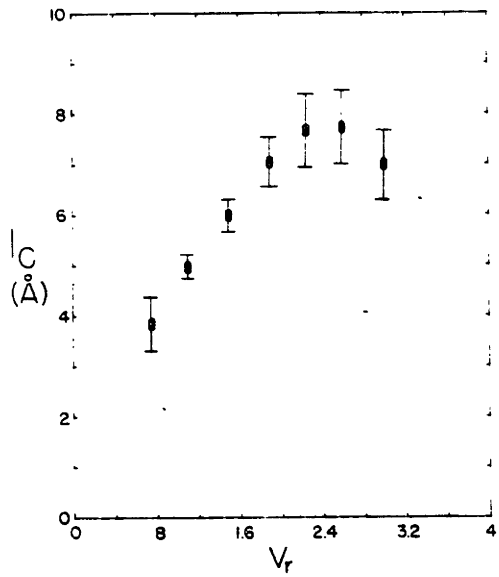

FIG. 15. Least squares fitted values for the "collison length" l_c, appearing in Eq. (25), as a function of v_r.

and thus torque $\propto l_c^n$, then to provide a constant (torque $\times t_c) = \Delta j$ independent of v_r, one expects $l_c \propto v_r^{-1/(n+1)}$. Alternatively, one might expect $l_c \propto Q^{1/2}$, where Q is the total (sum over j_f) RET collision cross section. This expectation would predict $l_c \sim$ constant except decreasing at large v_r. Thus, while the fact that the ECS–P fitting law fits data at different velocities is a victory for that law, the somewhat puzzling behavior of l_c clouds its physical interpretation and suggests difficulties in extending the theory to calculate l_c from a given potential.

In addition to testing the ECS, the present data provide important evidence about the velocity dependence of the basis rate constants, the $k_{i\to 0}(v_r)$. The first significant finding is that the power law form for $k_{i\to 0}$ [Eq. (27)] works at all measured velocities, just as it does for thermally averaged $k_{i\to 0}$ in many different collision systems. This corroborates the recent finding that cross sections for RET in velocity selected HF–Ar collisions fit a power law at all studied velocities.[2] The χ^2/ν is at most 2.25, with a similar quality to that observed in our work on Na_2^*–X systems with different target gases; it must be noted, however, that the fractional errors in the rate constants at different v_r are about 1.5 times larger than those thermally averaged measurements. There is presently no theoretical prediction or justification of power law behavior; however, the existence of two systems (HF–Ar and Na_2^*–Xe) in which the behavior extends over different velocities should serve as a stimulus to finding one, and the manner in which α and γ depend on velocity may serve as a clue. This velocity dependence is shown in Figs. 13 and 14: α increases rapidly and somewhat nonlinearly with increasing v_r, while γ is slowly decreasing and may well be linear. Moreover, γ lies in the range observed for collisions of Na_2^* with a host of other targets.[14,15]

Lastly, shown in Fig. 16 is the total rate constant for rotational relaxation of molecules initially with $j_i = 0$: $K(v_r) = \sum_{l\,\text{even}} k_{0\to l}(v_r)$, where $k_{0\to l}(v_r)$ is obtained from $k_{l\to 0}(v_r)$ using microreversibility and is given by $k_{0\to l}(v_r) = (2l+1)(v_r''/v_r)k_{l\to 0}(v_r'')$ with $v_r'' = v_r[1-(\alpha/v_r^2)l(l-1)]^{1/2}$ and $k_{l\to 0}(v_r'') = a(v_r'')[l(l+1)]^{-\gamma(v_r'')}$. Values for $a(v_r'')$ and $\gamma(v_r'')$ were obtained by linear interpolation using known values obtained earlier. We see that $K(v_r)$ is quite linear at lower velocities and quickly levels off for $v_r \gtrsim 2.5$. This implies that the RET relaxation cross section is roughly constant at thermal velocities but begins to decrease for $v_r > 2.5$.

B. Trends in data

The most significant feature of the data is that the majority of the rate constants are nearly linear in velocity, implying that the associated level-to-level cross section is essentially constant. This was also the conclusion of a recent experiment on HF–Ar.[2] We now discuss the exceptions to this behavior: The *decrease* with increasing v_r of the rates for the largest Δ from $j_i = 16$, the faster than linear increase of the rates for $j_i = 66$.

The observation that $k(v_r)$ [or $\sigma(v_r)$] rolls off with increasing v_r for large Δ and $j_i = 16$ is counter to one's classical intuition that more angular momentum can be transferred by increasing the relative velocity. Nevertheless, it can be rationalized classically by the following considerations: (1) The molecular potential is stronger and more anisotropic at small atom–molecular separations, so that the torque grows rapidly with decreasing separation and (2) there is a strong long-range

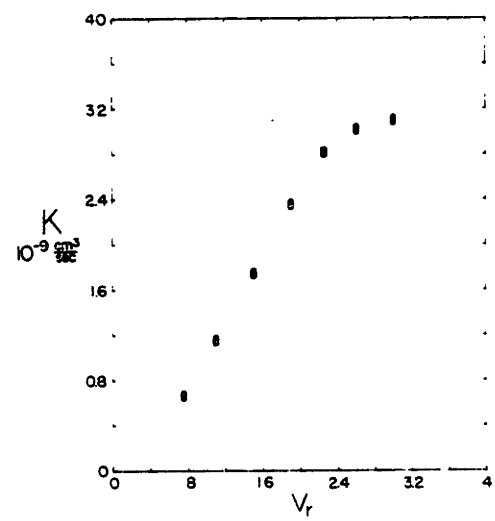

FIG. 16. $K(v_r) = \sum_{l\,\text{even}} k_{0\to l}(v_r)$, the total rate constant for all energetically allowed transitions out of the zeroth rotational level, as a function of v_r (no errors given).

attraction between Na_2^* and Xe (the potential probably has a well depth of at least 1000 cm^{-1}, the well depth for NaXe in the $A\,^2\Pi$ state[12]) which is relatively less anisotropic. The lack of strong long range anisotropy means that large Δ will most likely result only from collision trajectories where Xe passes relatively close to Na_2^*; and, because of long range attraction, a slower atom is more likely than a faster atom to be drawn in to these small separations. These considerations imply smaller cross sections at higher velocity, for larger Δ, as observed. However, it is difficult to account for the fact that $\sigma(v_r)$ decreases more rapidly than v_r^{-1} with this argument alone.

The only deviation from constancy of the HF–Ar RET cross section studied by Barnes *et al.*[2] was also attributed to the long range portion of the potential (but it was for *small* Δ). This suggests that RET in systems with strong long range forces ought to exhibit interesting behavior.

The relatively fast increase in $k(v_r)$ with increasing v_r for $j_i = 66$, or the faster increase in $j_i = 66$ compared to $j_i = 38$, may reflect the reduction of averaging of the torque due to the rotation of Na_2^* as Xe passes. For $v_r = 1$, $l_c = 4$ Å (see Fig. 15), and for $j_i = 66$ the Na_2^* molecule will rotate $\simeq \pi$ rad in the collision time l_c/v_r, thus averaging the potential over one period (since Na_2^* is homonuclear), and reducing the "sudden" rate by a factor of 7.7 [calculated from the square of the denominator of A_1^2, Eq. (26)]. This reduction factor is roughly 3 times smaller than the corresponding factor for initial $j_i = 38$ at the same velocity, or for $j_i = 66$ at $v_r = 3$. Thus, it may be more correct to view the steeper velocity dependence of the $j_i = 66$ rates as a reflection of lowering $k(v_r)$ at small v_r caused by rotational averaging.

The above discussions are qualitative arguments which give simple explanations of the general features of our data; they are by no means complete. For example, we have not considered the possibility of vibrational energy transfer or electronic quenching, both of which can reduce the rate of pure RET processes discussed here, and both of which may have strong velocity dependences.

Accurate *ab initio* calculation of potentials for Na_2^*–Xe as well as complete and accurate close-coupling calculations of the dynamics would be prohibitively expensive with present computational methods. There may be, however, alternative routes to the theoretical prediction of our results. One possibility is to accept the ECS scaling laws so that only the basis set $k_{j=0}$ need be calculated. Since these are generally in the sudden regime, it may be possible to use the infinite order sudden[13] (IOS) approximation to make calculation of $k_{j=0}$ quick and simple. Another approach is to use classical or semiclassical methods which are, in general, well suited to heavy systems such as Na_2–Xe.

C. The VSDS method

The present experiment represents, in our opinion, the most careful and fruitful application of Doppler-based velocity selection techniques to determine the velocity dependence of collisions occurring in a gas. While the present application contains new data correction and deconvolution procedures which have not been tested against other experiments, these are basically improvements and refinements on our earlier VSDS work[3] which was shown to agree with independent (and subsequent) molecular beams results within 5%. In addition, any uncertainties which they introduce are confined to the lowest and highest relative velocities.

In general, we feel that there is not much room for undetected systematic errors in our VSDS measurements. The basic experimental variables—laser frequency and light intensity ratios—can be determined reliably. There is no reliance on dimensional stability and reproducible mechanical action as there is in a molecular beams machine, for example—the only movable mechanical items in our experiment are the pressure gauge and the spectrometer. We feel that the most serious cause of systematic error in our experiment is the possibility of light of unknown physical origin (collisional transfer from extraneous weakly excited lines, for example) adding to the satellite intensity. This causes an increase in the associated rate constant which is strongest at large v_i (where the parent intensity is smallest). As indicated in Sec. II, we took careful precautions to guard against this type of error. The general smoothness with respect to Δ of the trends of k for large v_r in our data furnish additional evidence that this source of error has been eliminated. Certainly, the dramatic decrease in k at large v_r in the $j_i = 16$ large Δ data can not originate from this source.

The present experiment has a S/N ratio which has typically allowed recovery of four or five ($=N+1$) coefficients in the expansion of the velocity dependence. Roughly speaking, this results in a FWHM resolution of $\simeq [(v_i)_{max}/N+1]$ or $\simeq 0.75$ in our experiment. Simulations suggest that a S/N ratio 100 times better would roughly double the number of recoverable coefficients. Thus, it is not likely that the VSDS method will ever approach the resolution typical of molecular beams. On the other hand, the velocity range demonstrated here ($\simeq 0.75$ to $\simeq 3.5$ sp) corresponds to a 20:1 range of relative kinetic energy (cf. 4:1 in Ref. 2 using molecular beams). The VSDS method also offers the possibility of selecting molecules with large internal energies, and it measures the rate constants absolutely. The VSDS method has been described (by someone unfamiliar with the cost of single frequency dye lasers) as "the poor man's molecular beams machine"—we feel that this experiment opens the way for VSDS to achieve middle class respectability.

ACKNOWLEDGMENTS

We wish to thank D. Driver and R. Suchannek for help in the initial stages of this experiment. We also wish to thank A. Karp for help in taking and analyzing the data reported here. This work was sponsored by the U.S. Air Force Office of Scientific Research Grant No. AFOSR76-2972E.

APPENDIX

In this Appendix, we briefly outline our method for obtaining approximations to the Voigt function

$$V(x,y)=\frac{y}{\pi}\int_{-\infty}^{\infty}\frac{e^{-t^2}dt}{(x-t)^2+y^2}\,. \tag{A1}$$

The above definition seems to be standard in the literature,[18] and differs only slightly with that given in Eq. (3) [they are equivalent if one identifies $x=(1/\sqrt{2})v_t/\Gamma_G$, $y=(1/\sqrt{2})\Gamma$] and so we will consider the above definition for use here.

The Voigt function may be alternatively expressed in complex variable notation as[18]

$$\text{(a)}\quad V(x,y)=\mathrm{Re}\left[e^{-z^2}+\frac{2i}{\sqrt{\pi}}D(z)\right]\,,$$

$$\text{(b)}\quad z=x+iy\,,\quad y\geq 0\,, \tag{A2}$$

$$\text{(c)}\quad D(z)=e^{-z^2}\int_0^z e^{u^2}du\,,$$

and $D(x)$ is known as Dawson's integral. We are here interested in the case $y\ll 1$ corresponding to our physical condition that $\Gamma\ll 1$, i.e., the homogeneous linewidth is small compared to the Doppler width. Thus, for $y\ll 1$, we can Taylor expand $D(z)$ (analytic for all z) about the point $z=x$. If one then substitutes this expansion[18] into Eq. (A2a) and truncates the sum at the y^{2N+1} term, the resulting approximation to $V(x,y)$ can be shown to be

$$V(x,y)\simeq V(x,y;N)=\exp(y^2-x^2)\cos(2xy)-\frac{2y}{\sqrt{\pi}}\sum_{n=0}^{N}d_{2n+1}(x)(-y^2)^n\,, \tag{A3}$$

where

$$d_n(x)\equiv\frac{1}{n!}\frac{d^n}{dx^n}D(x) \tag{A4}$$

and the $d_n(x)$ satisfy the following recursion relation[18]

$$\text{(a)}\quad d_{n+2}(x)=\frac{-2}{n+2}[xd_{n+1}(x)+d_n(x)]\,,$$

$$\text{(b)}\quad d_0(x)=D(x)\,, \tag{A5}$$

$$\text{(c)}\quad d_1(x)=1-2xd_0(x)\,.$$

To find $d_0(x)=D(x)$ we use the following rational approximation for $D(x)$ good to ~1 part in 10^4 for $0\leq x\leq\infty$:

$$D(x)\simeq\frac{\sum_{n=0}^{4}c_n x^{2n+1}}{\sum_{n=0}^{5}d_n x^{2n}}\,, \tag{A6}$$

$$c_0=1\,,\quad d_0=1\,,$$

$$c_1=1.41845\,2\times10^{-1}\,,\quad d_1=c_1+\tfrac{2}{3}\,,$$

$$c_2=4.91080\,3\times10^{-2}\,,\quad d_2=3.179982\times10^{-1}\,,$$

$$c_3=4.99103\,0\times10^{-3}\,,\quad d_3=8.824410\times10^{-2}\,,$$

$$c_4=2.31111\,6\times10^{-3}\,,\quad d_4=2c_3-c_4\,,\quad d_5=2c_4\,.$$

The values for c_0, d_0, as well as the constraints on d_1, d_4, d_5, were chosen so that our approximation, when expanded in powers of x $(1/x)$ as $x-0(\infty)$, agrees exactly with Taylor (asymptotic) expansions[19] of the function $D(x)$ up to terms x^3 $(1/x^3)$. The other coefficients were obtained by nonlinear least square fitting to values of $D(x)$ given in Ref. 20.

Assuming no convergence or computation (e.g., roundoff error) problems, the error in approximation (A3) generated from an initial error in $D(x)$ can be accurately estimated by the following argument[21]: Let $D'(z)$ $(z=x+iy)$ be the value obtained for $D(z)$ by expansion about the point $z=x$ when using $D'(x)$ as an approximation to $D(x)$; let $\delta=D(x)-D'(x)$, and let $\delta(z)=D(z)-D'(z)$. Using Eq. (A5c) (valid for $z-z$), it is simply shown that $d\delta(z)/dz=-2z\delta(z)$, and thus $\delta(z)=\exp(x^2-z^2)\delta$. From this it follows that the final error in the Voigt function $\Delta V(x,y)$ is given by [see Eq. (A2a)]

$$\Delta V(x,y)=\frac{2\delta}{\sqrt{\pi}}e^{y^2}\sin(2xy)\,. \tag{A7}$$

For our own application of Eq. (A3), with $y=\Gamma/\sqrt{2}\simeq 0.03$, $0\leq x=v_t/\sqrt{2}\leq 3$ and $D'(x)$ given by Eq. (A6), we find $V(x,y;N=1)$ accurate to better than 0.1%.

[1] N. Smith, T. A. Brunner, A. W. Karp, and D. E. Pritchard, Phys. Rev. Lett. 43, 693 (1979).

[2] J. A. Barnes, M. Keil, R. E. Kutina, and J. C. Polanyi, J. Chem. Phys. 72, 6306 (1980). These authors find that their data fit a power law in transferred energy (see Ref. 7) rather than for the basis rate constants. These are equivalent findings in many circumstances, however—see Ref. 22.

[3] J. Apt and D. E. Pritchard, Phys. Rev. Lett. 37, 91 (1976).

[4] N. Smith, T. A. Brunner, R. D. Driver, and D. E. Pritchard, J. Chem. Phys. 69, 1498 (1978).

[5] R. Ramaswamy, A. E. DePristo, and H. Rabitz, Chem. Phys. Lett. 61, 495 (1979).

[6] A. E. DePristo, S. D. Augustin, R. Ramawamy, and H. Rabitz, J. Chem. Phys. 71, 850 (1979).

[7] T. A. Brunner, R. D. Driver, N. Smith, and D. E. Pritchard, J. Chem. Phys. 70, 4155 (1979).

[8] P. R. Bevington, *Data Reduction and Error Analysis for the Physical Sciences* (McGraw-Hill, New York, 1969).

[9] We have performed a separate experiment to treat virtually excited atoms using this assumption. R. Walkup and D. E. Pritchard (to be submitted).

[10] G. E. Forsythe, J. Soc. Ind. Appl. Math. 5, 74 (1957).

[11] P. G. Guest, *Numerical Methods of Curve Fitting* (Cambridge University, New York, 1967).

[12] G. York, R. Scheps, and A. Gallagher, J. Chem. Phys. 63, 1052 (1975).

[13] R. Goldflam, S. Green, and D. J. Kouri, J. Chem. Phys. 67, 4149 (1976); G. A. Parker and R. T Pack, J. Chem. Phys. 68, 1585 (1978); *Atom–Molecule Collision Theory*, edited by R. B. Bernstein (Plenum, New York, 1979).

[14] M. Wainger, I. Al-Agil, T. A. Brunner, A. W. Karp, N. Smith, and D. E. Pritchard, J. Chem. Phys. 71, 1977 (1979).

[15] T. A. Brunner, N. Smith, and D. E. Pritchard, Chem. Phys. Lett. 71, 358 (1980).

[16] T. A. Brunner, Ph.D. Thesis, Massachusetts Institute of Technology (1980); T. A. Brunner, N. Smith, A. Karp, and D. E. Pritchard, J. Chem. Phys. (to be published).

[17] V. Khare, J. Chem. Phys. 68, 4631 (1978). This work demonstrates that the scaling law [Eq. (24) with A_j^j-1] follows *only* from the "rotational sudden" approximation $J^2-k^2j_0(j_0+1)$ (i.e., replacing the rotor angular momentum operator J by an eigenvalue, for some fixed j_0), and that the addition of the "centrifugal sudden" approximation [$L^2-k^2l_0(l_0+1)$, with L orbital angular momentum operator] which when combined with "rotational sudden" yields the IOS approximation[13] [with which one can also derive Eq. (24) with A_j^j-1] is unessential. The rotational sudden approximation ignores rotational level spacing and is often assumed equivalent to the energy sudden approximation, i.e., that the relative kinetic energy $\gg$ rotational energies. However, what we have observed empirical-

ly[14–16] and what is immediately suggested by ECS is that the most important criterion, in these regards, is that the molecule does not appreciably rotate during the collision, i.e., that the reduced collision duration $U_c = v_0[2B\hbar^{-1}\sqrt{J_0(J_0+1)}] \ll 1$ so $A_1^1 = 1$.

[13]B. H. Armstrong, J. Quant. Spectrosc. Radiat. Transfer 7, 61 (1967).

[14]W. J. Cody, K. A. Paciorek, and H. C. Thacher, Jr., Math. Comp. **24**, 171 (1970).

[15]J. B. Rosser, *Theory and Application of* $\int e^{-x^2} dx$ and $\int_0^z e^{-p^2 x^2} dx$ $\int e^{-x^2} dx$ (Mapleton, Brooklyn, 1948).

[16]V. N. Faddeeva and N. M. Terentex, *Tables of the Function* $w(z) = e^{-z^2}(1 + (2i^{1/2}/\sqrt{\pi}) \int_0^z e^{t^2} dt)$ *for Complex Argument* (translated) (Pergamon, New York, 1961).

[17]N. Smith and D. E. Pritchard, J. Chem. Phys. (to be published).

References

1. N. Smith, T.A. Brunner, and D.E. Pritchard, J. Chem. Phys. 74, 467 (1981). This reference is reproduced in Appendix B, and will also be referred to as App. B.

2. a) K. Bergmann and W. Demtröder, Z. Physik. 243, 1 (1971).
b) G. Ennen and C. Ottinger, Chem. Phys. 3, 404 (1974).
c) R.K. Lengel and D.R. Crosley, J. Chem. Phys. 67, 2085 (1977).
d) B.E. Wilcomb and P.J. Dagdigian, J. Chem. Phys. 67, 3829 (1977).
P.J. Dagdigian and B.E. Wilcomb, J. Chem. Phys. 67, 6462 (1977).
e) C.R. Vidal, Chem. Phys. 35, 215 (1978).

3. a) T.A. Brunner, R.D. Driver, N. Smith, and D.E. Pritchard, J. Chem. Phys. 70, 4155 (1979).
b) T.A. Brunner, N. Smith, A.W. Karp, and D.E. Pritchard, J. Chem. Phys. 74, 3324 (1981).

4. C. Ottinger and M. Schröder, J. Phys. B. 13, 4163 (1980).

5. J.A. Barnes, M. Keil, R.E. Kutina, and J.C. Polanyi, J. Chem. Phys. 76, 913 (1982).

6. A good review of RI collision theory, as well as a vast list of references can be found in Atom-Molecule Collision Theory, edited by R.B. Bernstein (Plenum Press, New York, 1979), chaps. 8,9,10.

7. j_z consrvng: P.McGuire and D.J. Kouri, J. Chem. Phys. 60, 2488 (1974).
R. T Pack, J. Chem. Phys. 60, 633 (1974);
ℓ_z consrvng: V. Khare, J. Chem. Phys. 68, 4631 (1978);

IOS: G.A. Parker and R. T Pack, J. Chem. Phys. 68, 1585 (1978);
semi-classical: W.H. Miller, in Advances in Chemical Physics, edited by I. Prigogine and S.A. Rice, Vol. 25 (Interscience, New York, 1974). pp. 67-177.
A.P. Clark, A.S. Dickenson, and D. Richards, in Advances in Chemical Physics, ed. by I. Prigogine and S.A. Rice, Vol. 36 (Interscience, New York, 1977). pp. 63-139.
(see chap. 9 of ref. 6 for reviews of these and other methods).
classical: chap. 10 of ref. 6, and refs. 8 below.

8. a) R.A. Labudde and R.B. Bernstein, J. Chem. Phys. 55, 5499 (1971).
b) M.D. Pattengill and R.B. Bernstein, J. Chem. Phys. 65, 4007 (1976).
c) D.L. Thompson, J. Chem. Phys. 77, 1286 (1982) - this reference also considers the possibility of VRIC.

9. a) D.E. Pritchard, N. Smith, R.D. Driver, and T.A. Brunner, J, Chem. Phys. 70, 2115 (1979).
b) ref. 3b
c) for a general survey of scaling-fitting laws for RIC, see T.A. Brunner and D.E. Pritchard in Dynamics of the Excited State, edited by K.P. Lawley (John Wiley & sons Ltd, New York, 1982) pp. 590-641.

10. A.E. DePristo, S.D. Augustin, R. Ramaswamy, and H. Rabitz, J. Chem. Phys. 71, 850 (1979).

11. W.D. Phillips and D.E. Pritchrad, Phys. Rev. Lett. 33, 1254 (1975).

12. R. Walkup, A. Spielfiedel, D. Ely, W.D. Phillips, and D.E. Pritchard, J. Phys. B 14, 1953 (1981).

13. see any probability-statistics text, such as Mathematical Statistics by J.E. Freund, (Prentice-Hall, New Jersey, 1962).

14. P.D. Dunn and D.A. Reay, Heat Pipes (Pergamon, Oxford, 1978).

15. G. Herzberg, Spectra of Diatomic Molecules, (Van Nostrand, New York, 1950) 2nd ed.

16. P.H. Wine and L.A. Melton, Chem. Phys. Lett. 45, 509 (1977).

17. While the lifetime τ was seen in ref. 16 to be independent of upper state (v,j), the transition rate Γ for a particular fluorescence transition goes as the cube of the transition frequency ν, and depends also on Franck-Condon and Honl-London factors (ref. 15). Measured intensity I_Δ also depends on the frequency responce of our detection apparatus. In the past, we have accounted for Honl-London factors and ignored any Δ dependence to the Franck-Condon factors (which primarily depend only on v' and v''. The ν dependence of transmission of our detection system (Spex + PMT's) has recently been measured, and incorporating this as well as the ν^3 factor into our analysis has resulted in $\leq$ 10% correction to measured rate constants as analyzed using our previous assumption that Γ is independent of Δ - see also ref. 19.

18. P. Kusch and M.M. Hessel, J. Chem. Phys. 67, 586 (1977).

19. T. Scott, N. Smith, and D.E. Pritchard, to be submitted.

20. P.R. Bevington, Data Reduction and Error Analysis for the Physical Sciences, (McGraw-Hill, New York, 1969) - Chap. 11, pp. 235+. This is the basic type routine used for all non-linear fitting we do.

21. A.N. Nesmeyanov, Vapor Pressure of the Elements, (Elsevier, Amsterdam, 1963).

22. P.G. Guest, Numerical Methods of Curve Fitting, (Cambridge University Press, New York, 1967).

23. a) J. Apt and D.E. Pritchard, Phys. Rev. Lett. 37, 91 (1976).
b) see also App. B, Sec. IV.B.

24. A. Dalgarno and A.E. Kingston, Proc. R. Soc. A 259, 424 (1961).

25. N. Smith, T.P. Scott, and D.E. Pritchard, Chem. Phys. Let.

26. It is understood that the rapidly decreasing sensitivity of $\bar{K}(v_L)$ to $\sigma(v_r)$ for $v_r << .7$ prevents us from concluding positively that the v_r^{-p} behavior does in fact continue in the actual limit $v_r \to 0$.

27. The $j_i = 100$ data of ref.3.b had a $\tau = 3.4$ for the same v_r and b, but its range was only for $|\Delta| \leq 6$.

28. W.E. Baylis, J. Chem. Phys. 51, 2665 (1969).

29. N. Smith and D.E. Pritchard, J. Chem. Phys. 74, 3939 (1981).

30. T.A. Brunner, N. Smith, and D.E. Pritchard, Chem. Phys. Lett. 71, 358 (1980).

31. S.L. Dexheimer, M. Durand, T.A. Brunner, and D.E. Pritchard, J. Chem. Phys. 76, 4996 (1982).

32. See any quantum mechanics text, such as A. Messiah, Quantum Mechanics, (North-Holland, Amsterdam 1962). Vol. II, pp. 724-225. see also ref. 10.

33. a) E. Merzbacher, Quantum Mechanics, 2nd ed. (John Wiley and Sons, New York, 1970), pp. 186-187.
b) ref. 32, Vol. II, App. C, eqs. C.14-C.17.

34. T.A. Brunner, T.P. Scott, and D.E. Pritchard, J. Chem. Phys. 76, 5641 (1982).

35. The function $f^2(\tau)$ has been derived earlier, though used in a somewhat different context; see ref. 4.

36. ref. 6, chap. 8.

37. ref. 6, chap. 9

38. a) R.T. Pack, J. Chem. Phys. 62, 3143 (1975).
b) S. Chapman and S. Green, J. Chem. Phys. 67, 2317 (1977).

39. a) W.H. Miller, J. Chem. Phys. 53, 1949 (1970).
b) W.H. Miller, J. Chem. Phys. 54, 5386 (1971).
c) See also Miller's article given in ref. 7.

40. R.E. Langer, Phys. Rev., 51, 669 (1937).

41. Handbook of Mathematical Functions, ed. by M. Abramowitz and I.A. Stegun, (Dover, New York, 1972), 9th edition, pp. 949-950.

42. A. Nordsieck, Math. Comp. 16, 22 (1962).

43. For a discussion of R-K and P-C methods, see for example A. Ralston,
A First Course in Numerical Analysis, (McGraw-Hill, New York, 1965). chap. 5.

44. J.J. Kohfeld and G.T. Thompson, J. Assoc, Comp. Mech. 15, 390 (1968).

45. Ref. 38.b, eq. 6.

46. J. Pascale and J. Vandeplanque, J. Chem. Phys. 60, 2278 (1974).

47. ref. 6, chap. 4.

48. Handbood of Chemistry and Physics, ed. by R.C. Weast (CRC Press, Florida, 1980) p. E-69.

49. S. Dexheimer, C. Engelke, and K. Saenger, private communication.

50. J.D. Kelly and M. Wolfsberg, J. Chem. Phys. 53, 2967 (1970).

51. H. Goldstein, Classical Mechanics, (Addison-Wesley, Mass., 1950)

chaps. 9,10.

52. ref. 33, pp. 122-125.

53. a) J.W. Duff, N.C. Blais, and D.G. Truhlar, J. Chem. Phys. 71, 4304 (1979).
b) N.C. Blais and D.G. Truhlar, J. Chem. Phys. 69, 846 (1978).

ACKNOWLEDGEMENTS

I would like to thank my research advisor Dave Pritchard for providing the means, financial and otherwise, which have allowed me to have experienced both enjoyable and productive years as a graduate student. I would also like to thank Rudy Sucannek, Dick Driver, and Tim Brunner for help and good will given to me during our collaborations in the earlier years prior to this work. This thanks extends to those people who, in one way or another, have also provided help and assistance to me during my years here.

I would like to acknowledge the many hours of assistance of Tom Scott during the long, into the night (morning) data-taking sessions during which we made all of the raw Spx and VSDS measurements used for this work. Finally, I wish to extend my thanks to Dave Pritchard and Jim Kinsey for a constructively critical reading of the manuscript and many suggestions for its improvement. Special thanks goes to Andrea Gelinas for her very fast, efficient typing and friendly cooperation during the long months of preparation of of this thesis.